Boron Dye-Polymer Materials for Oxygen Sensing and Imaging

Meng Zhuang
Deyang, Sichuan, China

B.S., University of Science and Technology of China, 2015

A Dissertation Presented to the Graduate Faculty
of the University of Virginia in Candidacy for the Degree of
Doctor of Philosophy

Department of Chemistry

University of Virginia
April 2020

Abstract

Bioimaging based on luminescence has brought revolutionary advancement in studying biology and biomedicine. The family of difluoroboron β-diketones (BF_2bdks) dye polymeric materials has been widely used as imaging and sensing reagents. These materials possess unique dual-emissive properties, that is, fluorescence (F) and oxygen sensitive room temperature phosphorescence (RTP), making them ideal for ratiometric oxygen sensing where the fluorescence serves as an internal standard and the phosphorescence is the oxygen sensor. The properties including emission, lifetime, and oxygen sensitivity are tunable by boron dye modification and polymer conjugation, which provides a wide range of potential biological applications for the dye polymer materials.

The material behaviors in relevant biological environment are studied, and material engineering and optimization for multiple biological purpose are discussed. First, the blue boron nanoparticles were optimized as cell tracking reagents in immunology. Second, active targeting was achieved by appropriate surface modification with biomolecules to improve delivery and tumor accumulation. For example, folic acid was conjugated to fabricate multi-color and oxygen sensing nanoparticles. Then, new oxygen sensing dyes were designed to be used with red/green/blue (RGB) color camera, and their utilities were demonstrated in murine wound oxygen imaging. Finally, oxygen sensing method was established to study oxygen consumption and brain activity in the brain slices.

Table of Contents

Acknowledgements

The accomplishment of this dissertation would not have been possible without the support and help from people around me. First of all, I wish to express the special thanks to my advisor, Prof. Cassandra Fraser. Her guidance and financial support made me achieve my graduate career. Throughout the years, she encouraged me to explore the science and taught me the importance of innovation and being meticulous. She is always supportive, offering me the opportunities to learn new techniques and to develop my own career goal.

I thank every individual that I have worked with in Fraser Lab. The help from senior graduates, Dr. Christopher DeRosa and Dr. Tristan Butler was really appreciated during the earlier years. Big thanks to Chris, who was my mentor and guided me to get started on the road of scientific research. He has always been patient showing me every single step in a reaction, answering my annoying questions, and giving me ideas when I got stuck. It was from his passion, creativity, and diligent towards science that I realized what a real chemist would be. I also want to thank my colleague and friend, Fang Wang. We had many discussions about life and science; we shared thoughts on projects and experiments. We learned together and we solved problems together. Thanks to the undergrads, Nidhi Manu and Sammie Chung, and junior graduate Parris Anbaei, who have been really great. Nidhi is quiet and focused when doing experiments, while Sammie is always attentive with curiosity. Parris is no doubt a hard worker. I will definitely miss those long and good days we spent together.

My deepest gratitude also goes to Prof. Jaideep Kapur in Department of Neurology and his group, where I learned neuroscience and imaging during the past two years. I was so lucky to work in an interdisciplinary environment and to extend my research experience beyond the chemistry laboratory. Prof. Kapur's guidance and encouragement provided me the confidence of never giving

up. I want to specially thank lab members from his group: Dr. Tanveer Sigh, Dr. Huayu Sun, Dr. Suchitra Joshi, and Dr. Tamal Batabyal for their assistance in the brain project, Diane Payne for scheduling appointments whenever I needed, and John Williamson for taking care of my animals and orders. It was truly a valuable memory throughout my graduate career.

Thank you for every collaborator in the past five years. Big thanks to Prof. Rebecca Pompano at UVA Chemistry. Her insights in imaging has made my first project be fulfilled. I also thank Prof. James Demas at UVA Chemistry, Prof. Palmer Gregory at Duke Radiology, Prof. Shayn Peirce at UVA Biomedical Engineering, Dr. Patrick Cottler at UVA Plastic Surgery Clinic. I have learned imaging techniques in Keck Center, and special thanks to Dr. Ammasi Periasamy and Dr. Ruofan Cao for their training. In addition, I need to thank many staff in the Chemistry Department. Danny and Debbie from stockroom are always patient dealing with ordering chemicals and supplies, and Michael is super nice to help with any shipments. Thanks Dr. Jeff Elena for solving my problems if I had when running NMR, Susie for assisting with any questions related to graduate studies.

I also thank my friends, old and new, back in China and here in Charlottesville. I will be sure to remember every great moment we share together. Thanks to my family, my dear dad and mom, for their unconditional love and support no matter where I am and what I do. Thanks to our lovely dog JJ, for always sitting next to me while I am writing the hundreds of pages in the dissertation. Finally, the biggest thanks to my husband Gengyu. None of these would ever happen without your love and accompany during the past seven years. Your integrity, compassion, and ingenuity will always inspire me. We have gone through a lot, and I am sure there are more adventures awaiting us to explore in the future.

Dedication

This thesis is dedicated to Dad and Mom.

Thank you for giving me the courage to explore the world and to become who I am.

List of Tables

List of Figures

Chapter 1: Introduction to Luminescence, Polymeric Materials and Bioimaging

As one of the most important techniques during the past decades, fluorescence imaging brings new insight and understanding to biology and medicine.[1] Revolutionary advances are due to a combination of novel fluorophores, modern instrumentation and software, and multiplex biological models.[2–9] Among fluorescent probes, small organic fluorophores are of interest, such as the difluroboron β-diketones (BF_2bdks) dye family, which is the focus of this thesis. In this research, BF_2bdk polymers were functionalized and optimized for applications in oxygen sensing and imaging. Luminescence, organic and polymer synthesis, and material design (e.g., nanofabrication), along with current biological issues will be covered in this introductory chapter.

1.1 Photoluminescence

Luminescence is the emission of light from a substance.[1] There are several different ways that the light can be produced. For example, the energy released from chemical reactions leads to chemiluminescence (e.g., bioluminescence or eletrochemiluminescence). Application of heat can produce thermoluminescence, and absorption of photons results in photoluminescence. Designing luminescent materials requires an understanding of the mechanism and applications of interest, which underlies the optical characteristics of each type of luminescence. In terms of photoluminescence, extinction coefficient (ε), excitation (λ_{ex}) and emission (λ_{em}), lifetime (τ), and quantum yield (Φ) are important parameters.

1.1.1 Fluorescence and Phosphorescence

Photoluminescence is a result of radiative relaxation of an electron from an excited state (S_1) to the ground state (S_0) after photon absorption. Depending on the electronic configuration of the excited state, photoluminescence can be further divided into two categories, fluorescence (F) and phosphorescence (P). A simple Jablonski Diagram is shown in Figure 1.1 to illustrate these radiative decay processes. Typically, a molecule is excited to a higher vibrational level of either

S_1 or S_2 by light irradiation. Following by photon absorption, most of the molecules rapidly relax back to the lowest vibrational level of S_1 through a process called internal conversion (IC). This process usually occurs within 10^{-12} s or less and is much shorter than the lifetime of fluorescence, therefore it is complete prior to emission. Fluorescence emission is the radiative decay from the thermally equilibrated excited state (i.e., the lowest vibrational level of S_1) where the electron is repaired with the electron in the S_0 orbital. Because spin is paired, fluorescence usually occurs rapidly within nanoseconds.[10,11] In certain cases, the molecule can undergo a spin conversion to the triplet excited state (T_1) by intersystem crossing (ISC). The emission from T_1 is known as phosphorescence. Because the relative energy gap between T_1 and S_0 is smaller than that of S_1 and S_0, phosphorescence is longer in wavelength than fluorescence. Transition from T_1 to S_0 states is spin forbidden, and as a result the triplet emission is normally several orders slower than fluorescence. When the molecule is in the triplet state, there is also possible to back populate the singlet state. This process is called reverse intersystem crossing and is thermally allowed, and subsequent emission is referred to as thermally activated delayed fluorescence (TADF).[12]

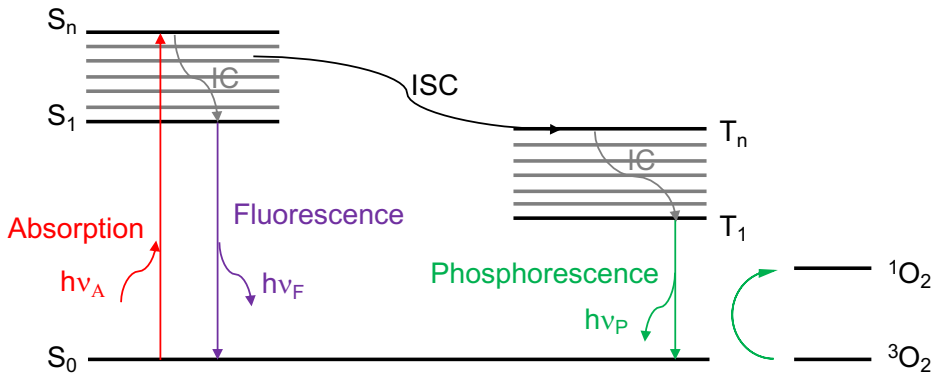

Figure 1. 1. Jablonski Diagram. S0 = singlet ground state, Sn = singlet excited state, S1 = lowest energy singlet excited state, Ex = excitation, IC = internal conversion, F = fluorescence, ISC = intersystem crossing, Tn = triplet excited state, T1 = lowest energy triplet excited state, P = phosphorescence.

1.1.2 Spectroscopic Parameters

Based on the mechanism of photoluminescence illustrated above, the production of light can be generally divided into two processes: photon irradiation (absorption) and radiative relaxation (emission). The main spectroscopy instruments that are involved in analyzing photoluminescence materials are a UV-Vis spectrophotometer and a spectrofluorometer. The light absorption of a molecule is measured by UV-Vis spectroscopy where the sample is scanned through a range of wavelengths and the transmitted light is detected. The intensity and corresponding wavelength of transmitted light is compared to a blank control, which provides information on the molar extinction coefficient (ε) and maximum absorption (λ_{abs}). According to the Beer-Lambert Law (Eq. 1.1), the molar extinction coefficient (in $cm^{-1}M^{-1}$) can be determined by the optical density (A, absorption value at λ_{abs}), the path length of the sample (b), and the molar concentration (c).[13] The absorption spectrum is indicative of molecular electronic transitions from the ground state to the singlet excited state, an important feature associated with the chemical structure. In particular, the extinction coefficient and maximal absorption must be matched to the application of interest, and can be further tuned by chemical modification.

$$A = \varepsilon bc \qquad \textbf{Equation 1.1}$$

A spectrofluorometer, on the other hand, is the instrument used to monitor radiative decay from excited state to ground state. Generally, the components include a light source to yield a constant photon output with all wavelengths, the monochromators that select excitation and emission wavelength, a photomultiplier tube to detect fluorescence, and appropriate electronic devices to quantify the spectrum. The spectrofluorometer is usually able to record both excitation and emission spectra. While an emission spectrum is the wavelength distribution of an emission at a fixed excitation wavelength, an excitation spectrum is the opposite. It measures emission intensity at a fixed emission wavelength under a range of excitation wavelengths. Absorption (λ_{abs})

in conjunction with emission maxima (λ_{em}) are valuable parameters describing the optical properties of luminescent materials, and are normally reported for newly designed fluorophores. An illustration of absorption and emission spectra is shown in Figure 1.2. A Jablonski diagram reveals that emission energy of fluorescence is generally lower than that of absorption due to internal conversion and nonradiative decay. The wavelength difference between absorption and emission is called the Stokes Shift. Also, because of the rapid decay to the lowest vibrational level of S_1, the observed emission spectrum is independent of excitation wavelength. This additionally leads to another important feature: for most fluorophores, the emission is the mirror image of S_0 → S_1 transition, not of total absorption.

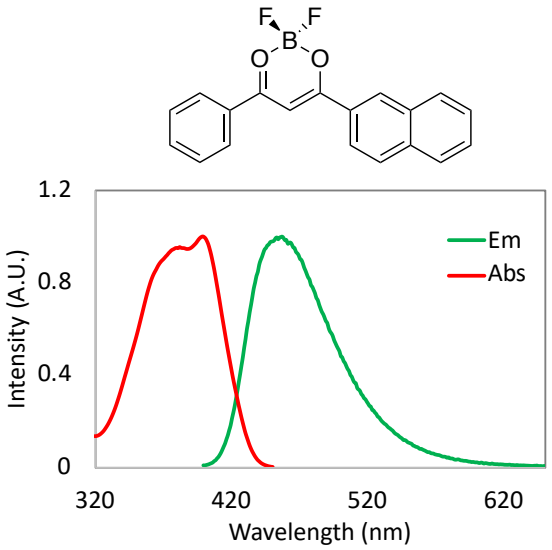

Figure 1. 2. Absorption and emission spectra of difluoroboron benzoylnaphthoylmethane in dioxane (1 x 10-5 M; λ_{ex} = 369 nm).

Fluorescence measurements can be generally classified into steady-state and time-resolved methods. Steady-state, the most common way to monitor excitation and emission spectra, requires constant illumination and observation. While for time-resolved measurement, the sample is exposed to a pulse of light, where the pulse width is usually shorter than the decay time. Time-

resolved techniques are useful in tracking intensity decays or fluorescence anisotropy. In steady-state (constant illumination), fluorescence and lower energy phosphorescence (if present) can both be observed in a total emission spectrum. To isolate phosphorescence, time-resolved (gated technique) may be conducted by applying a gate between the time scale of fluorescence (ns) and phosphorescence (ms) while the sample is excited, typically with a flash lamp.

$$Q = Q_R \frac{I}{I_R}\frac{OD_R}{OD}\frac{n^2}{n_R^2} \qquad \textbf{Equation 1.2}$$

Two other important characteristics of fluorophores are lifetime (τ) and quantum yield (Φ).[1] The lifetime of the excited state is defined as the average time the molecule spends in the excited state before emitting a photon and returning back to ground state. The measurement of lifetime is a time-resolved method. When the sample is illuminated with a short pulse of light, emission intensity versus time is recorded with a detector, typically time-correlated single photon counting (TCSPC).[14] Fluorescence lifetime (τ_F) and phosphorescence lifetime (τ_P) are then determined from the slope of intensity decay. Lifetime is an intrinsic property of the fluorophore, independent of external factors. Therefore, it has found important applications in lifetime-based assays, sensing, and imaging.[15] Quantum yield is a measure of photon efficiency defined by the ratio of the number of emitted photons to the number of absorbed photons. For quantum yield measurement, a reference fluorophore (e.g. quinine sulfate, anthracene, or Rhodamine G6) with an excitation wavelength compatible to the sample is generally required.[16] Both absorption and emission need to be recorded for the reference and the sample, and the quantum yield is given by Eq.1.2 where Q is the quantum yield of the sample and Q_R is the quantum yield of the reference (note: variables with subscript R refer to the reference). I is the integration of emission, OD is the optical density or absorbance, and n is the refractive index of the solvent. Quantum yield along with extinction coefficient determine fluorescence intensity of a molecule, and the brightness of a

fluorophore is defined by multiplying quantum yield and extinction coefficient. Brighter fluorescence is desirable in cellular and tissue imaging to efficiently label region of interests.

All of these spectroscopic parameters of a fluorophore are related to the chemical structure and should be considered in designing materials. For example, fluorophores with emission beyond 700 nm are desirable because the light has its maximum depth penetration within the tissue in this longer wavelength range. To illustrate how the emission of a fluorophore is optimized by chemical modification, an example of red-shifting a new class of rhodamine-based fluorophores to achieve near infrared (NIR) emission was shown in Figure 1.3.[17] The design strategy originates from the understanding of fluorescence on-off observed for malachite green (MG) dye. That is, when the MG dye binds to RNA aptamers or cell surface proteins, the molecule is locked in a rigid planar configuration, thereby inhibiting vibrational deexcitation and activating fluorescence. As shown in Figure 3, by replacing the rhodamine 10-position O atom with a sulfone group, the absorption and maxima emission of SO_2R analogs is much longer than OR, CR, and SIR derivatives and reaches up to 750 nm. This is due to unusual d*-π* conjugation and smaller energy gap between HOMO and LUMO.

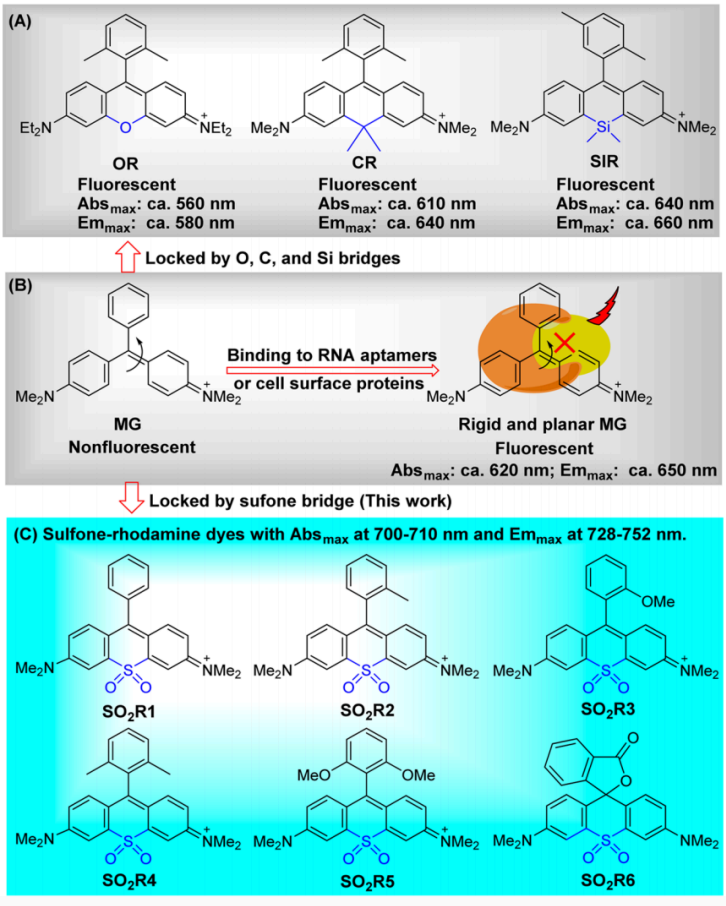

Figure 1. 3. Comparison of Photophysical Properties of OR, CR, and SIR Dyes (A) with Those of MG (B) and Sulfone Rhodamine SO_2R Derivatives (C). This figure was reproduced from Liu et al., *ACS Appl. Mater. Interfaces* **2016**, *8*, 22953–22962.[17] Copyright American Chemical Society.

1.2 Biomedical Oxygen Sensing and Imaging

1.2.1 Fluorescence Imaging

Fluorescent dyes play important roles in biological and biochemical imaging.[18] Cell and tissue imaging with distinctly emitting fluorophores are versatile tools to locate subcellular and multicellular structures.[19–21] Tracking fluorescently labelled cells is a common strategy to assess cell behavior *in vitro* and *in vivo*. Moreover, based on fluorescence quenching or enhancement, the fluorescence imaging can be used to quantify pH, enzyme substrates concentration, protein binding, O_2 level, and more.[22,23] Cultured cells are simple and useful models to evaluate fluorescent dyes

from traditional organic dyes to novel nanomaterials. By binding to cellular organelles, fluorophores with distinct wavelengths can be used and detected simultaneously for visualizing colocalization of cell division. For example, in *in vitro* imaging, muntjac skin fibroblast cells were imaged by using green fluorescent Alex Fluor 488 Phalloidin to label F-action, orange fluorescent Alex Fluor 555 goat anti-mouse secondary antibody to label mitochondria, and TO-PRO-3 far-red fluorescence to label nuclei (Figure 1.4).[24]

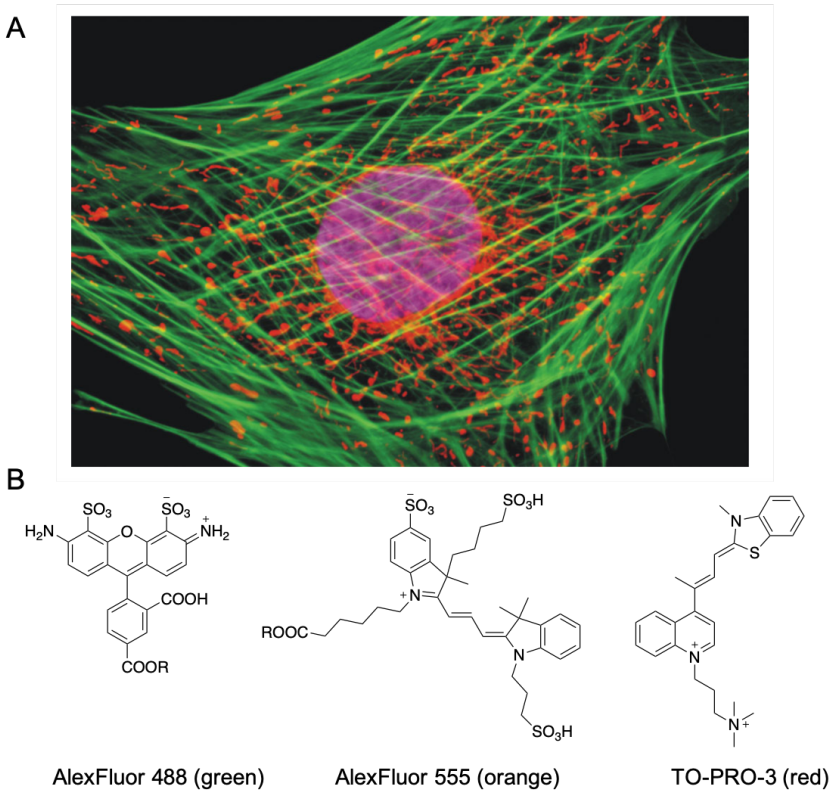

Figure 1. 4. Intracellular Imaging. A) Multiplexed confocal imaging of fixed and permeabilized muntjac skin fibroblast cell. B) Chemical structures of fluorescent labels used in cellular imaging: green dye AlexFluor 488, orange dye AlexFluor 555, and far red dye TO-PRO-3. Images reproduced from Kilgore et al., *Curr. Protoc. Cytom.* **2014**, *67*, 12.32.1-12.32.17.[24] Copyright John Wiley & Sons, Inc.

Small organic dyes have attracted research interest over the past decades, given their tunable chemical structures. Moreover, nanosized fluorescent reagents are becoming more and more attractive candidates for biological labeling owing to their unique physical properties,

including polymer-based nanoparticles, inorganic nanocrystal quantum dots, and carbon dots. Polymeric nanoparticles are usually fabricated from hydrophobic or amphiphilic chain polymers or branched dendrimers. While possessing cell-membrane penetrating features, these materials shield the traditional fluorophore from interacting with biological components and provide improved biodegradability and with decreased cytotoxicity. Fluorescent quantum dots and carbon dots are also commonly used in cancer imaging and therapy, especially for multimodal biomedical imaging such as NIR fluorescence-magnetic resonance imaging.[25] For example, an approach of generating carbon dots (CDs) emitting red, green, and blue (RGB) colors based on three isomers of phenylenediamines was demonstrated, and a full-color emissive film can be achieved by mixing any of those carbon dots.[26] This class of fluorescent carbon dots is applicable in live cells for multicolor imaging as shown in Figure 1.5.

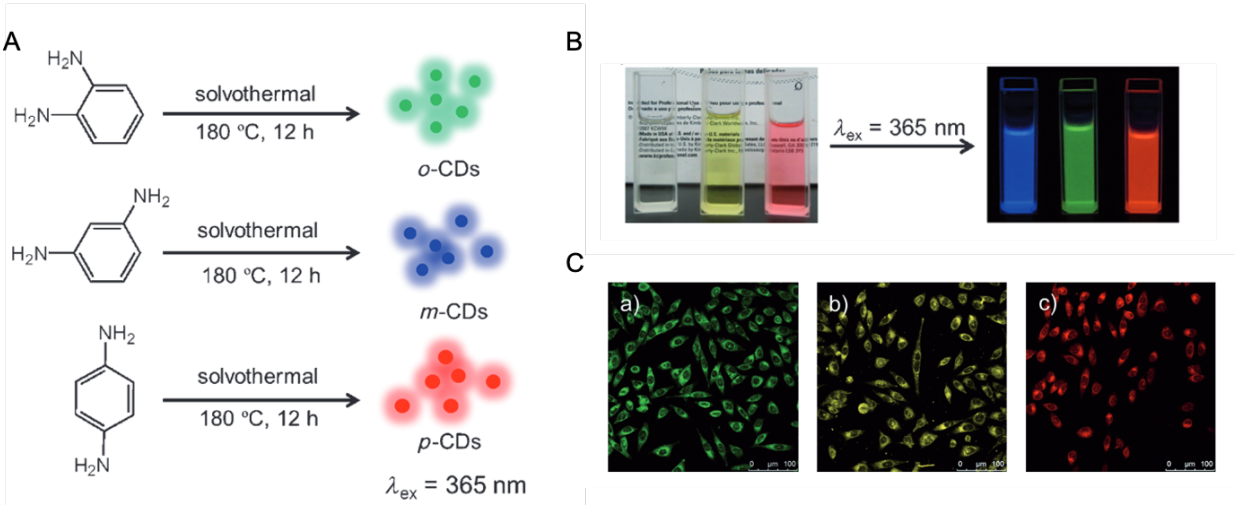

Figure 1. 5. Multicolor Fluorescent Carbon Dots. A) Preparation of RGB CDs from three different phenylenediamine isomers. B) Visualization of *o*-CDs, *m*-CDs, *p*-CDs under UV excitation. C) Confocal fluorescence imaging of *o*-CDs, *m*-CDs, *p*-CDs in MCF-7 cells. Images reproduced from Jiang et al., *Angew. Chemie Int. Ed.* **2015**, *54*, 5360–5363.[26] Copyright John Wiley & Sons, Inc.

Photostability and cytotoxicity are two major obstacles that need to be addressed in fluorescence imaging. Photobleaching is a common problem for fluorophore molecules where

excitation exposure necessary to stimulate them to fluorescent results in chemical damage of the molecules. Other than chemically modifying the sensor to a more stable structure, there is the possibility to circumvent photobleaching by using excitation sources of lower energy (e.g., two photon microscopy) and filtering out the light source that cannot excite the sample. The toxicity of fluorescent dyes to cells or tissue limits the application in biological aimaging. To minimize cytotoxicity of fluorophores, chemicals that are biocompatible and biodegradable are preferred in material engineering. This ensures the cells are unaffected by labelling and generates accurate results in tracking cellular activity and in *in vivo* labeling, especially for long-term imaging.

1.2.2 Phosphorescence Quenching

As illustrated by a Jablonski diagram, phosphorescence is the emission from the triplet state. The transition from singlet state to the triplet state via ISC requires a spin conversion and takes a much longer time, which gives the molecule enough time to interact with the environment. Oxygen is one of the molecules that can quench phosphorescence. When molecular oxygen, a triplet molecule in the ground state, collides with phosphor in its triplet-excited state, the energy can be easily transferred from the phosphor to oxygen, leading to phosphorescence quenching.[27] Oxygen concentration or partial pressure is correlated to phosphorescence. In particular, the relationship between phosphorescence and the oxygen level can be described by the Stern Volmer equation (Eq. 1.3-1.4):

$$\frac{I_0}{I} = \frac{\tau_0}{\tau} = 1 + K_{SV}[Q] \qquad \textbf{Equation 1.3}$$

$$K_{SV} = k_q \tau_0 \qquad \textbf{Equation 1.4}$$

where I_0 and τ_0 are the unquenched phosphorescence intensity and lifetime, and I and τ are the intensity and lifetime of the sensor response. The quenching constant Ksv is a combination of unquenched lifetime and oxygen diffusion through the matrix, and a longer lifetime is related to

higher sensitivity.[28] Phosphorescence imaging provides an effective way for oxygen measurement in both spatial and temporal resolution.

Room temperature phosphorescence (RTP) is rare in purely organic materials, therefore efforts have been made to enhance phosphorescence intensity for more accurate oxygen detection.[29–31] In quantum mechanics, the perturbation factor δ describing singlet-triplet mixing by first order spin-orbit coupling can be illustrated as Eq. 1.5 where Ψ^1 and Ψ^3 represent wavefunctions of singlet and triplet states, H_{so} refers to spin-orbit Hamiltonian, and E_1 and E_3 are energy levels for singlet and triplet states. As spin-orbit interactions are substantial, a change in spin is thus more favorable. It is known that H_{so} is greater with heavier elements, therefore heavy atoms (e.g., metal, halogen) are usually introduced to increase the rate of intersystem crossing and to enhance phosphorescence intensity (heavy atom effect).[32,33]

$$\delta = \frac{\langle \psi^3 | H_{SO} | \psi^1 \rangle}{|E_1 - E_3|} \qquad \textbf{Equation 1.5}$$

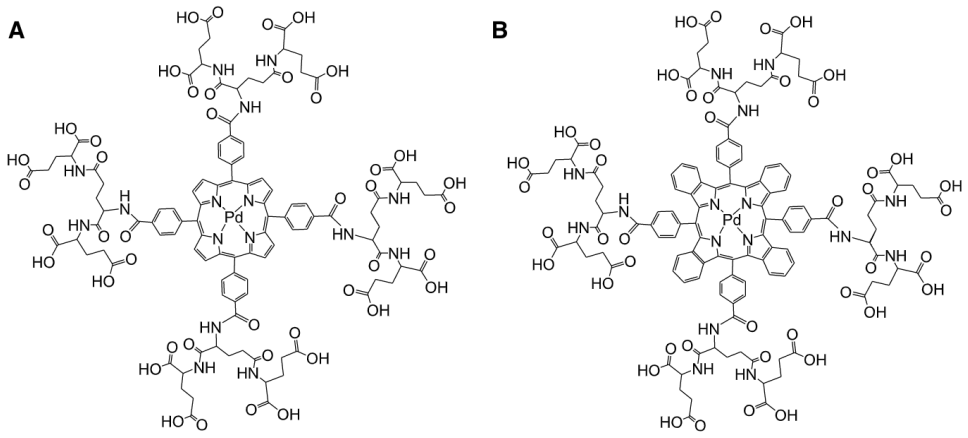

Figure 1. 6. Chemical Structure of Oxyphor R2 (A) and Oxyphor G2 (B). The second generation of glutamate dendrimers of Pd-meso-tetra-(4-carboxyphenyl)porphyrin and Pd-meso-tetra-(4-carboxyphenyl)tetrabenzoporphyrin.

Metalloporphyrin derivatives are a class of phosphors that are most commonly used in oxygen sensing.[34–37] These compounds have merits in significantly high RTP quantum yield, red emission, and long phosphorescence lifetime. Early reports of phosphors Oxyphor R2 and Oxyphor G2 (Figure 1.6) based on Pd-meso-tetra-(4-carboxyphenyl)porphyrin and Pd-meso-tetra-(4-carboxyphenyl)tetrabenzoporphyrin, respectively, have found successful application in living tissue oxygen measurement. [38] The diverse end groups of porphyrin-based dyes enable further functionalization for improved properties and advanced material fabrication. For example, the addition of poly (ethylene glycol) (PEG) has increased sensor stability as well as minimized interference from albumin binding.[39] To enhance cell penetration, the Evans group designed porphyrin dendrimers G3-CAOS that can spontaneously penetrate multiple cell layers in a 3D model (Figure 1.7).[40] The authors synthesized azido-functionalized analogues of platinum meso-tetraphenyltetrabenzoporphyrin (PtTBP) surrounded by poly (amidoamine) (PAMAM) like dendritic units, and demonstrated the ability of this NIR phosphorescent sensor in lifetime oxygen sensing. Other metal containing phosphors, such as ruthenium and iridium complexes are also popular as oxygen sensing reagents. Although metal complexes are often expensive and may introduce toxicity in biological samples, these issues can be overcome by metal-free compounds having halogen substitutions (i.e., Br, I). For example, the Kim group achieved bright RTP from purely organic crystals by combing aromatic carbonyls, the heavy atom effect, and halogen bonding.[41]

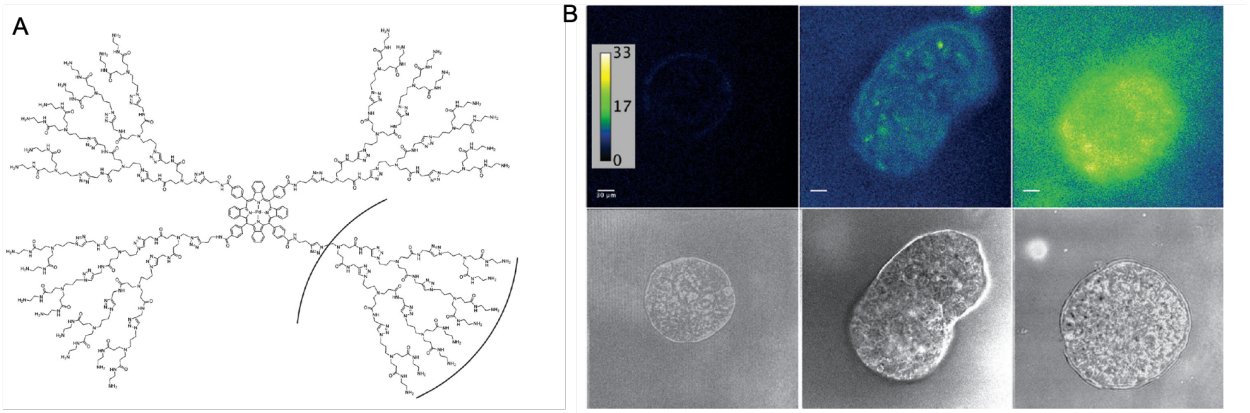

Figure 1. 7. Oxygen Sensing Porphyrin Dendrimers. A) Structure of the third generation click-assembled oxygen sensor (G3-CAOS). B) NIR phosphorescence confocal imaging shows that G3-CAOS could spontaneously penetrate 3D ovarian cancer spheroids; from left to right is no treatment control (bottom/gray panels: transmission channel), G3-CAOS treated for 4 h and imaged under air, and G3-CAOS treated for 4 h and imaged under nitrogen. Images were reproduced by Nichols et al., *Angew. Chem. Int. Ed*. **2014**, *53*, 3671 –3674.[40] Copyright John Wiley & Sons, Inc.

Phosphorescence lifetime and emission are important characteristics to consider when designing, optimizing, and engineering phosphors, as they are directly related to oxygen sensing applications. Recently developed phosphors are listed in Table 1.1, with optical properties listeds. For efficient delivery and localization, traditional phosphors are developed into nanoconjugates, bioconjugates, films, and fibers in combination with advanced material engineering and nanotechnology.

Table 1. 1. Commonly used O_2 sensitive phosphorescent dyes and their optical characteristics

Phosphor Dye	λ_{ex} (nm)	λ_{em} (nm)	τ_0 (μs)	Brightness $\varepsilon\Phi$ ($M^{-1}cm^{-1}$)	Photostability	Refs
PdTCPTBP	442, 632	790	251	6000	Moderate	[38]
PtPFPP	390, 504, 538	647, 710	60	28 424	High	[42,43]
PtTPTBPF	430, 615	773	50	87 600	High	[44]
$[Ru(dpp)_3]^{2+}Cl_2$	463	618	6.4	10 467	High	[45,46]
PtCP	380, 535	650	67	56 000	Modest	[47]
$[Ir(btp)_2(acac)]^{3+}$	408	596	6.4	50 112	Modest	[48,49]

PdTCPTBP: Pd-meso-tetra-(4-carboxyphenyl)tetrabenzoporphyrin; PtPFPP: Pt(II)-tetrakis(pentafluorophenyl)porphine; PtTPTBPF: Pt-meso-tetra-(4-fluorophenyl)tetrabenzoporphyrin; $Ru(dpp)_3$: tris(4,7-diphenyl-1,10-phenanthroline)ruthenium(II)

chloride; PtCP: Pt-coproporphyrin; $[Ir(btp)_2(acac)]^{3+}$: Iridium (III) bis(2'-benzothienyl)-pyridinato-N,C) (acetylacetonate)] trichloride; $(Ir(btp)_2(acac)\lambda_{ex}$: maxima excitation wavelength; λ_{em}: maxima emission wavelength; ε: molar absorptivity; Φ: phosphorescence quantum yield; τ_0: unquenched phosphorescence lifetime.

1.2.3 Phosphorescence Oxygen Sensing

An important applications of phosphorescence imaging is oxygen sensing.[28,48] Molecular oxygen (O_2) plays an essential role in living creatures.[49,50] In eukaryotic cells, oxygen is required as a terminal electron acceptor in the aerobic metabolic process known as oxidative phosphorylation.[51] This reaction takes place in mitochondria, during which the electrons transfer from electron donor to electron acceptor or oxygen, and energy released from electrons flowing is used to transform adenosine diphosphate (ADP) to adenosine triphosphate (ATP). The ATP generated during phosphorylation drives many cellular activities and processes and maintains biochemical function. For example, ATP is involved in DNA and RNA synthesis, amino acid activation, nerve impulse propagation, and other processes.

The percentage of oxygen is 21% or 160 mmHg in ambient atmosphere, namely, air. During human aerobic respiration, oxygen is carried by red blood cells and is delivered throughout the body. The oxygen level is highest in the respiratory system and decreases along venous and arterial systems. Downstream of arteries, cells and tissues have very different intracellular and extracellular oxygen levels that are highly regulated within physiological and pathological ranges. For example, the oxygen partial pressure is 33.8±2.6 mmHg in brain and 40.6±5.4 mmHg in liver. In cells, the numbers are smaller and are varied from 9.9 to 19 mmHg. Though oxygen levels are in a dynamic range, fluctuation beyond this range could result in cellular dysfunction and organ damage. An inadequate oxygen supply is known as hypoxia, and it is associated with pathological disorders and many diseases including strokes, seizures, chronic wounds, and cancer.

Based on the Stern-Volmer equation, the measurement of oxygen based on phosphorescence quenching can be generally conducted by intensity or lifetime. Intensity-based oxygen sensing is fairly simple. By comparing the quenched intensity to the unquenched intensity, oxygen concentration can be detected qualitatively or quantitatively. Also, most of the imaging systems can be readily adapted for intensity measurement. Although phosphorescence intensity is concentration dependent, a reference fluorescent dye that is oxygen-insensitive is typically involved as an internal standard. The ratio of fluorescence to phosphorescence is used to generate a ratiometric image and to correlate with oxygen levels. The signal from the reference and the sensor can be detected by a color RGB camera. As shown in Figure 1.8, a general strategy for designing ratiometric oxygen nanosensors requires an oxygen-insensitive fluorophore and an oxygen quenchable phosphor.[52] Unlike phosphorescence intensity measurements, lifetime-based oxygen sensing is independent of phosphor concentration or intensity of excitation light.[34,53] The instrumentation of phosphorescence lifetime imaging microscopy (PLIM) is either a time-domain or frequency-domain method. Lifetime measurement is often more accurate than using intensity for the reasons that phosphorescent dyes may distribute unevenly and autofluorescence is difficult to separate from the sensor response.[36,54,55]

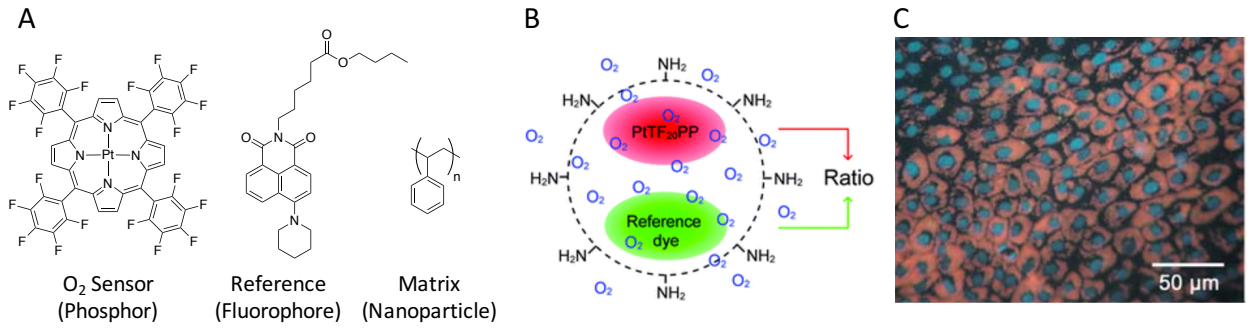

Figure 1. 8. Ratiometric O_2 Sensors Nanoprobes. A) Materials in Nanoparobes including Platinum(II) 5, 10, 15, 20-tetrakis(pentafluorophenyl)porphyrin; (PtTFPP) (Phosphor), N-(5-carboxypentyl)-4-piperidino-1,8-naphthalimide butyl ester (fluorophore), and the matrix is a polystyrene bead functionalized with amine groups to facilitate cell uptake. B) Schematic of the

ratiometric nanoprobe. C) Optical oxygen sensing in normal rat kidney cells (NRK-52 E). Images reproduced from Wang et al. *Chem. Sci.* **2011**, *2*, 901.[52] Copyright Royal Society of Chemistry.

Phosphorescence oxygen sensing provides direct information in cellular level, and it has important applications in a variety of biomedical fields (Figure 1.9). In cancer cells, solid tumors become hypoxia as they grow beyond the diffusion distances of oxygen, as the demand for oxygen exceeds the supply of oxygen. Hypoxia-inducible factor 1 (HIF-1) is triggered, leading to transcription of several genes, including the vascular endothelial growth factor (VEGF), to promote survival under hypoxic conditions. The presence of VEGF promotes angiogenesis, and thereby renders the formation of heterogeneous regions, or microenvironments of hypoxia. Hypoxia is directly related to cancer resistance to radiotherapy and chemotherapy, and being able to understand hypoxia and how it relates to physiological disorders and abnormalities can provide information for cancer treatment and diagnosis.[56] Dermatologists are also interested in oxygen sensing methods, as hypoxia often occurs during skin inflammation and the inflamed skin consumes more oxygen than healthy tissue. The skin inflammation can cause many diseases including acne, wounds, and chronic diabetic ulcers.[57,58] Mapping skin condition by phosphorescence imaging could provide spatiotemporal information on tissue oxygenation such as monitoring wound healing. Moreover, in neuroscience, oxygen sensing offers new fundamental insight into brain function. Brain consumes oxygen expensively, such as maintaining electrochemical gradients, and releasing and recycling synaptic vesicles. [59–61] A slight fluctuation in oxygen levels in the brain might lead to severe neurological disorders. For example, hypoxia-ischemia is a major cause of brain injury in humans including conditions such as hypoxic-ischemic encephalopathy,[62] stroke,[63,64] seizures,[63,65,66] periventricular leukomalacia,[67] and even Alzheimer's disease.[68,69]

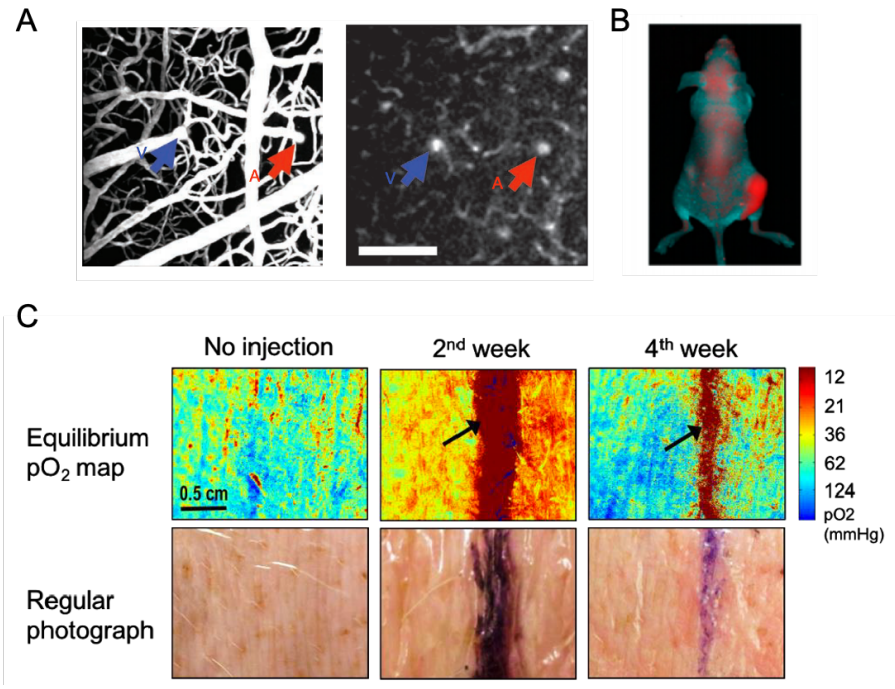

Figure 1. 9. Oxygen Sensing in Biomedical Applications. A) Partial pressure of oxygen in cerebral vasculature was measured by phosphorescence lifetime where maximum intensity projection of mouse cortex (left) and phosphorescence intensity of microvasculature (right) are shown. Two phosphorescence decays from the diving arteriole (A) and the ascending venule (V), with positions marked as arrows were analyzed by single exponential fits. Scale bar = 100 mm. Images were reproduced from Sakadžić et al., *Nat. Methods* **2010**, *7*, 755-759.[34] Copyright Springer Nature. B) *In vivo* imaging of a tumor-bearing nude mouse where the phosphorescence was observed in the center of tumor. Images were reproduced from Yoshihara et al., *Anal. Chem.* **2015**, *87*, 2710-2717.[70] Copyright American Chemical Society. C) Tracking the skin inflammation using an oxygen-sensing paint-on bandage. Top: equilibrium pO_2 map generated by oxygen-sensing bandage. Bottom: regular photograph of skin. Images were reproduced from Li et al., *Biomed. Opt. Express* **2017**, *8* (10), 4640.[71] Copyright the Optical Society.

1.3 Polymeric Materials

Polymers are molecules of high molecular weight, composing of repeated subunits. They have a unique and broad range of properties compared with small molecules. Synthetic polymers can be produced from monomers, and natural polymers including DNA and proteins are basic structure in biology, both of which find numerous applications in research and industry, ranging from food packaging to electronic devices.[5,8,72–80]

1.3.1 Polymer Characteristics

In macromolecular chemistry, average molecular weight (M) and polydispersity (Đ) are two major characteristics to evaluate polymerization and to analyze the final products. These can be measured by the technique of gel permeation chromatography (GPC), sometimes combined with multi-angle light scattering (MALS). Parameters including number average molecular weight (M_n), weight average molecular weight (M_w), and polydispersity index (Đ) can be determined. In GPC, a column filled with porous beads of a polymeric gel or silica beads will admit the ions or small molecules into their pores, allowing excluded large molecules to move more rapidly through the column and get separated into components. The resulting mixture of large molecules will be collected, and the elution volume of a molecule is related to its hydrodynamic volume. Molecular weight determination relies on a calibration standard, and combining GPC with MALS will ensure the absolute measurement of molecular weight, independent from instrument calibration. This is due to the fact that light scattering is able to retrieve molar mass for a solute in solution. For each measurement, the distribution of polymers will be shown in the GPC traces where each time slice can be assigned to a molecular weight. The concentration for each slice of the chromatogram is measured by the concentration detector, normally the refractive index or UV detector. The molar mass for each slice in then calculated based on the intensity of the scattered light and the concentration.

The number average molecular weight (M_n) is the average of molar masses of the individual macromolecules. It is calculated by summing all the polymers of a given molecular weight (M_i) and dividing by the number (n_i) of polymers (Eq. 2.1). In the weighted average molecular weight (M_w), the M_i values are squared, and it is dominated by the high molar mass fraction of the polymer (Eq. 2.2). From these two measurements, the polydispersity index (Đ) is defined as M_w/ M_n (Eq. 2.3). The value of polydispersity is used to evaluate the uniformity of the

polymer sample. For a perfectly monodisperse sample, all molar mass averages have the same value and the polydispersity will be 1.000.

$$M_n = \frac{\sum n_i M_i}{\sum n_i} \qquad \textbf{Equation 2.1}$$

$$M_w = \frac{\sum n_i M_i^2}{\sum n_i M_i} \qquad \textbf{Equation 2.2}$$

$$Đ = M_w / M_n \qquad \textbf{Equation 2.3}$$

A controlled polymerization, which yields narrow distribution of polymers (Đ < 1.3), is desired for synthesis of well-defined polymers and advanced structures including block co-polymers.[75,81–83] For example, synthesis of certain polyesters may be achieved by living ring-opening polymerization (ROP) of lactones, as shown in Figure 1.10A for reaction of difluroboron dibenzoylmethane poly(lactic acid) (BF_2dbmPLA). In biomedical research and clinics, polyesters are important for medical devices and sensor development.[84–86] The structures of polymers explored in this research and their respective monomers are illustrated in Figure 1.10B. The polymer PLA is frequently used as a matrix or carrier for biomaterial formulation because it is biocompatible, biodegradable, and bioderived. Poly (L-lactic acid) (PLLA), a stereoisomer of PLA, offers a higher degree of crystallinity, which may slow the rate of hydrolysis in aqueous solution and is more stable. Poly (ε-caprolactone) (PCL), synthesized from caprolactone, is a more hydrophobic polyester that is even slower to degrade than PLLA, making it useful for extended retention and slower release of loaded cargo. Blends of other polymers with PCL provide tunable properties useful for drug delivery and tissue engineering applications. Water soluble segments, such as poly (ethylene glycol) (PEG), are often incorporated to enhance the stability for biological imaging and drug delivery.

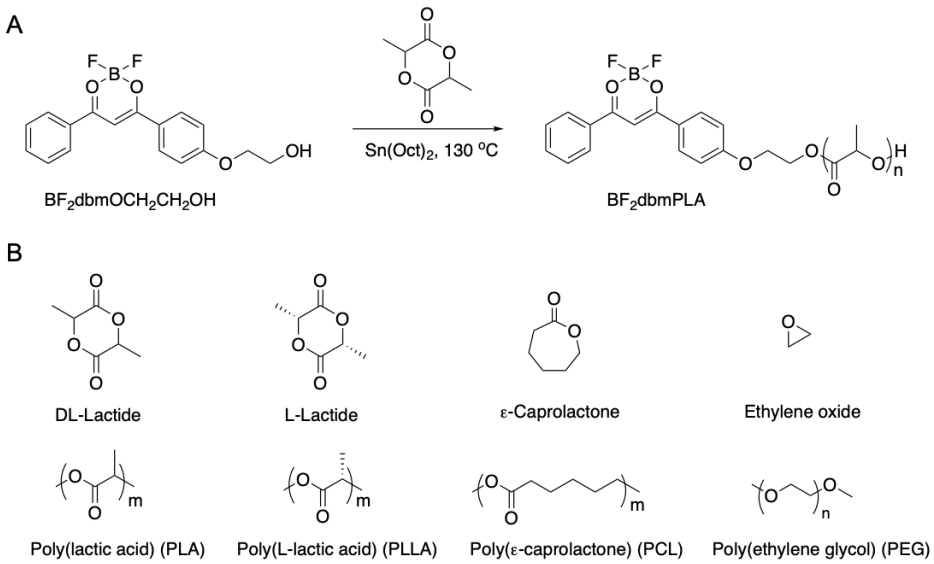

Figure 1. 10. Demonstration of Polymerization and Commonly Used Polymers. A) ROP of BF_2dbmPLA from boron dye initiator and lactide using tin catalyst $Sn(Oct)_2$. B) Chemical structures of commonly used biopolymers and their corresponding monomers.

1.3.2 Nanomaterials

In medicine and biotechnology, polymeric nanomaterials made by self-assembly are among the most common colloidal carriers for delivery (e.g., drug, imaging reagents).[87,88] Hydrophobic polyesters (e.g., PLA, PCL) can form nanoparticle suspensions in aqueous solutions by spontaneous emulsification. Nanoprecipitation is a facile and well-suited way for preparing hydrophobic polymeric nanoparticles.[87,89] It is based on interfacial deposition due to displacement of solvent with the non-solvent. As shown in Figure 1.11, a standard procedure to fabricate boron dye polymer nanoparticles is demonstrated. The polymer (and an organic drug or dye, if desired) is dissolved an organic solvent that is water miscible. The polymer/drug solution is added dropwise to water with continuous stirring. Surfactants or polymer stabilizers may be added to during the nanoparticle formation. The solvent is typically removed by evaporation, or dialysis.

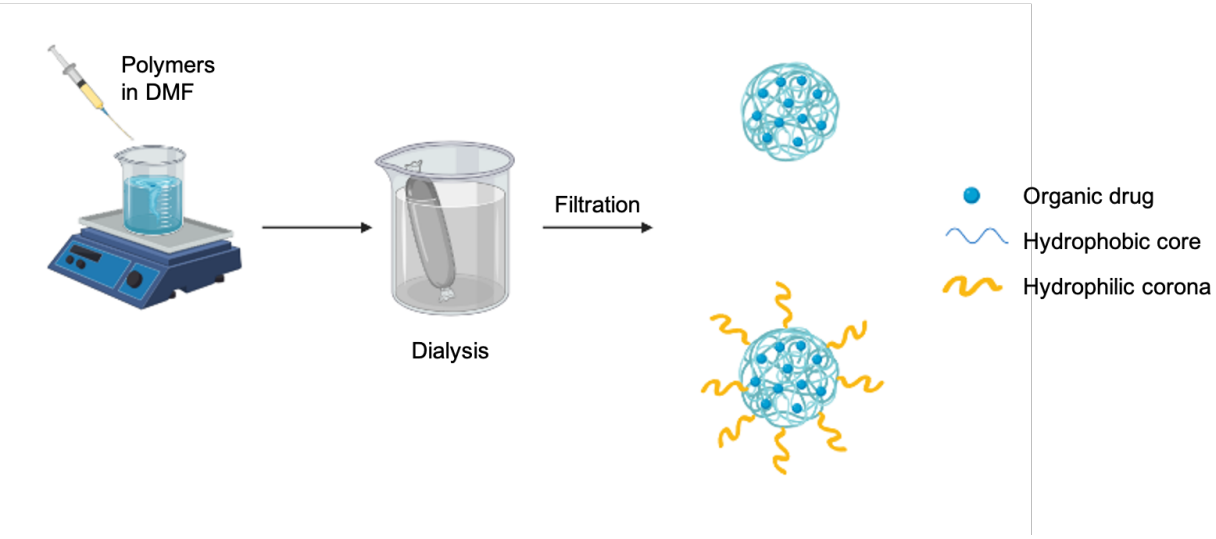

Figure 1. 11. Nanoprecipitation of polymeric nanoparticles.

In evaluating the physical properties of polymeric nanoparticles, radii and zeta potentials are typically analyzed, both of which can be measured by dynamic light scattering (DLS). When a beam of light passes through particles, some of the light is scattered into new directions. A careful analysis of scattered light provides important information about the scattering particles. Dynamic light scattering determines the translational diffusion coefficient for the particle, which is converted to hydrodynamic radius (R_h) based on the assumption that the particle is a sphere undergoing Brownian motion. Because of the dynamic movement of the polymeric nanoparticles, R_h takes not only particle size but also solvent effects into account, which provides a useful method to monitor aggregation and stability in aqueous solution. Zeta potential (ζ) can be measured by phase analysis light scattering (PALS), where an external electric field of a particle is detected.

The macromolecular nanomaterials have significant importance as delivery vehicles for imaging agents or drugs to cells and tissues. The delivery mechanism that involves membrane transport is highly dependent on particle chemistry and other characteristics (e.g. size, solubility, surface charge, molecular weight, and surface functional groups). The cell membrane separates intracellular compartments from the extracellular environment (i.e., interstitial, intravascular, and

transcellular compartments), and it makes delivery of substances (e.g., imaging reagents, oxygen sensors or drugs) into the cytosol challenging. Cells may take up substances by either passive or active targeting. Although no ATP is necessary, passive transport is limited to materials that are lipophilic and have desired chemical structure and surface functionalities. Active targeting involves ion channels or binding to specific protein transporters, and this pathway requires ATP and is often more efficient and selective. Substances can also pass through cell membranes by diffusion or passive transport, for example, by endocytosis, the mechanism of which can vary by cell type. The physical properties of nanomaterials also have direct effect on biodegradation and toxicity.

In solid tumors, nanoparticles and liposomes tend to accumulate in the tumor area by the enhanced permeability and retention (EPR) effect, as shown in Figure 1.12. When tumor cells start to grow quickly, they stimulate the growth factors (e.g., VEGF) that leads to cancer angiogenesis. Tumor cells are dependent on the newly formed blood vessels for nutrition and oxygen supply. This neovasculature, however, is often morphologically poorly-organized and leaky, consisting of abnormal endothelial cells with wide infenestrations. The capillary permeability in tumor vasculature is greater than those in healthy tissues, leading to a higher probability of molecules accumulating in the tumor area, especially for macromolecular drugs. Furthermore, tumor cells usually lack of effective lymphatics that clear and filter out particles under normal conditions, which results in increased retention.

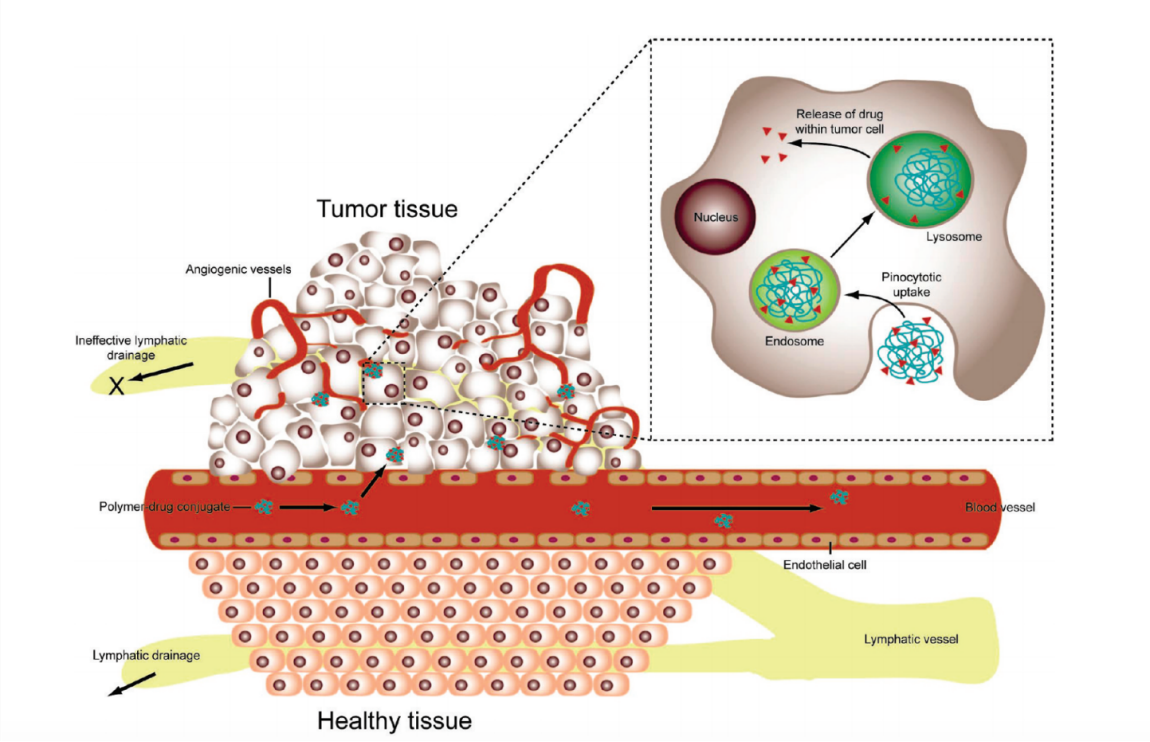

Figure 1. 12. Schematic Illustration of EPR Effect in Solid Tumor. Image was reproduced with permission from Fox et al., *Acc. Chem. Res.* **2009**, *42*, 1141–1151.[90] Copyright American Chemical Society.

Although pure hydrophobic polymeric nanoparticles are usually stable in aqueous solution for a short time, they are prone to form aggregates over a long period of time, which limits the applications to those involving long-term imaging. For example, long-term (e.g., over days) *in vitro* cell tracking can provide information on its process, cell therapy, and cellular pathogenesis.[91] Micelles from amphiphilic block copolymers can improve the aqueous stability due to a corona structure that is highly water soluble while still maintaining a hydrophobic core (Figure 1.11). For this purpose, hydrophilic polymers such as polyethylene glycol (PEG) are often incorporated to form block copolymers with improved aqueous solubility.[92–95] The hydrophilicity of PEG also prevents cellular uptake (e.g., phagocytic cells in the immune system), known as stealth properties, compared with non-PEGylated hydrophobic PLA nanoparticles, the latter of which can be quickly

recognized and cleared as foreign bodies by immune system. Consequently, PEGylated nanoparticles may circulate in the blood stream for a prolonged time. This is beneficial for drugs to be delivered to a target site without unwanted macrophage uptake, and also for improved tumor accumulation by EPR (Figure 1.13).[96] Moreover, the hydroxy terminus of PEG can be easily functionalized with a variety of groups, including alkoxy, amide (e.g., NHS, maleimide), and azide moieties, all of which allow further modification with biomolecules such as peptides and antibodies.

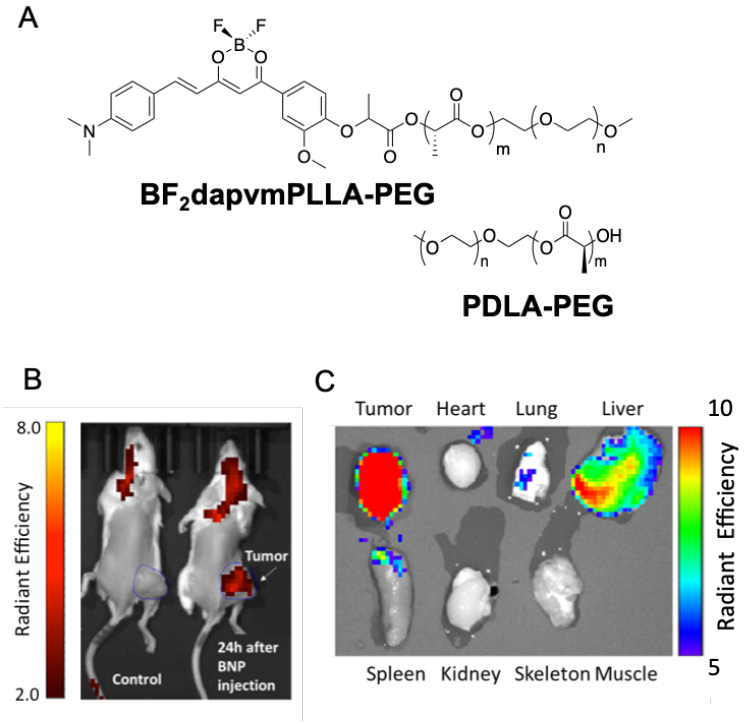

Figure 1. 13. PEGylated Stereocomplexed Nanoparticles in Passive Tumor Targeting. A) The chemical structure of boron dye polymers. B) Epifluorescence images of nanoparticles accumulation in a flank tumor 24 h after IV injection. A negative control mouse with saline injection is shown on the left. C) Radiant efficiency of harvested organs where the nanoparticles have good accumulation in the tumor. The presence of nanoparticles in the liver indicates metabolism in that organ. No significant accumulation was detected in other organs. Images were reproduced from Kerr et al., American Chemical Society.

The design of nanomaterials as drug delivery carriers for biological systems, intracellular or extracellular, to healthy cells or tumor cells, passively or actively, requires a thorough

understanding of physiological properties of biological models, and interactions between these models and materials. Taking advantage of the unique properties of individual biological systems would ensure the efficiency and specificity of delivery in various applications.

1.4 Luminescent Difluoroboron β-Diketone Polylactic Acid Materials

1.4.1 Dual-Emissive Properties

Many difluroboron β-diketones (BF_2bdks) compounds have excellent luminescence properties including large extinction coefficients, high quantum yields, and two-photon absorption.[97–99] Their emission is easily tunable by chemical structure to span across the visible range, making them useful as bioimaging reagents.[100–103] The exploration of boron dye-polymers in the Fraser lab started with the discovery of dual-emissive BF_2dbmPLA.[104] When the boron dye BF_2dbm is confined in a rigid PLA matrix, the fluorescence is retained and room temperature phosphorescence (RTP) is observed in the solid state (Figure 1.14). The long-lived, oxygen-sensitive phosphorescence is rare in organic compounds. In a rigid matrix where the molecular rotation and vibration are restricted, the non-radiative decay is slowed down and the rate of intersystem crossing is increased, consequently the phosphorescence can be greatly enhanced. To our knowledge, this was the first report of RTP in the BF_2bdk family of dyes. As the fluorescence, the phosphorescence, and the matrix are arise from a single component dye-polymer material, this feature offers an excellent opportunity for boron dye polymers to serve as ratiometric oxygen sensors, where the oxygen-insensitive fluorescence is the internal standard for self-calibration, and the oxygen quenching phosphorescence is the sensor to respond on local oxygen level changes.

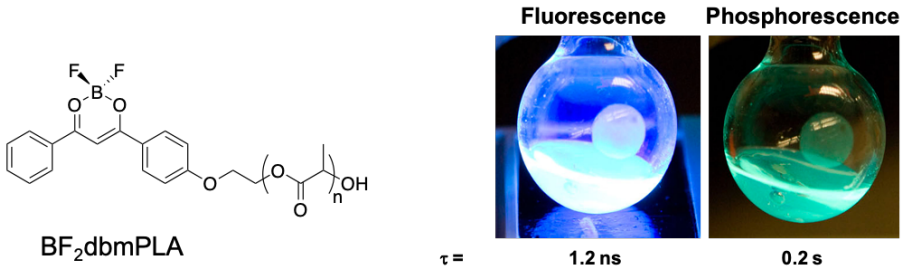

Figure 1. 14. Dual emissive BF_2dbmPLA with blue fluorescence and green long-lived room temperature phosphorescence.[104]

The preparation of boron dye-polymers can be achieved in a number of steps. In general, the boron dye is synthesized from the β-diketone ligand, which is formed via condensation of an ester and a ketone. This means that the boron dye can be easily substituted with different aromatic groups with different substitutions (e.g., halides, donating and withdrawing groups; positions) to tune properties (e.g., emission, lifetime) for multiple applications (Figure 1.15).[105] To synthesize polymers, the boron dye is functionalized with a primary alcohol to act as the initiator for the reaction with lactide by ROP. The polymerization is also able to accommodate a unique combination of boron dyes and polyesters (e.g., block copolymers), to form a large library of materials of interest. The dual-emissive properties and easy modification of BF_2dbmPLA laid a foundation for the continued and exciting research during the past years.

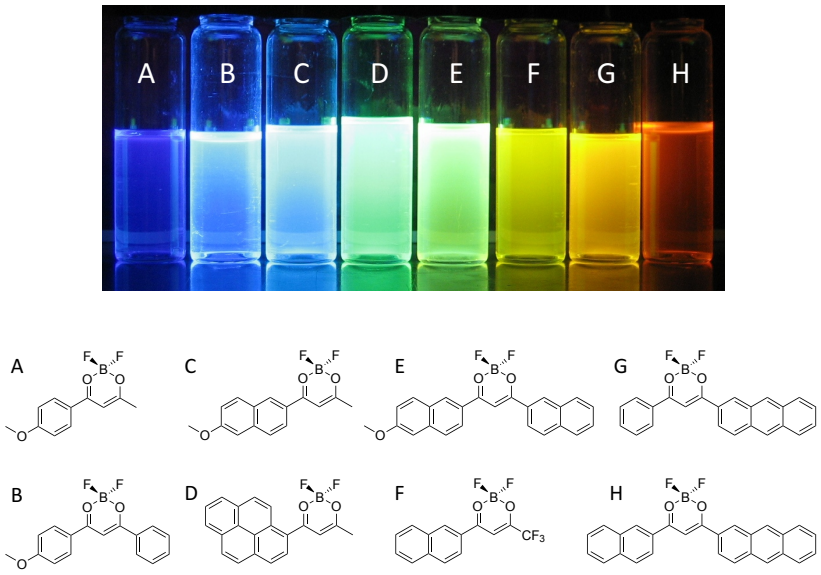

Figure 1. 15. Structure and design of difluoroboron β-diketonate materials.[105]

1.4.2 Polymer and Heavy Atom Effects

As mentioned above, fluorescence and room temperature phosphorescence of boron dye polymers are both observed in the solid state. These properties are well maintained when dye polymers are assembled into nanoparticles, thin films, and nanofibers.[106] With the presence of biocompatible and biodegradable PLA, the fabrication is feasible without the need for adding another matrix. Most importantly, this opens a window for biological applications because the nanomaterial can be suspended in aqueous solution, the necessary environment for biological samples, and the size of nanomaterial (diameter = 20 - 250 nm) is beneficial for cellular uptake and renal clearance.

In the previous studies, it was demonstrated that polymer properties (i.e., molecular weight and composition) can affect the optical properties on the boron dyes.[101,107–109] The fluorescence emission is sensitive to local concentration of dyes, known as the dye loading effect. As molecular weight decreases, dye-dye interaction increases, which could stabilize the excited state by lowering the energy level. The energy gap between the excited state and ground state is decreased, red-

shifting the emission. For BF_2dbmPLA around 10 kDa, the emission is blue (Figure 1.16A). Varying the polymer MW also affects phosphorescence intensity and the fluorescence to phosphorescence intensity ratio. Higher MW polymers expand the singlet-triplet energy gap, and decrease the rate of intersystem crossing, leading to longer phosphorescence lifetimes and decreased phosphorescence intensity. Taking into account the polymer MW effect on both fluorescence maxima and phosphorescence intensity, it was concluded that longer polymers resulting in weaker phosphorescence and but improved fluorescence and phosphorescence peak resolution.

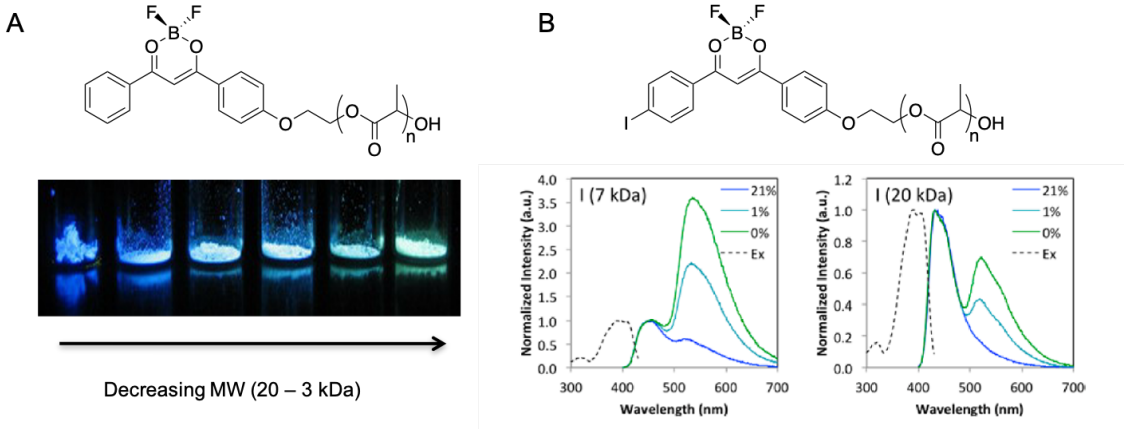

Figure 1. 16. Polymer Molecular Weight Effect. A) Fluorescence emission color green shifted by decreasing MW of BF2dbmPLA. Image adapted with permission from Zhang et al., *Adv. Mater.* **2008**, *20*, 2099–2104.[101] Copyright John Wiley & Sons, Inc. B) Phosphorescence intensity and fluorescence to phosphorescence gap were compared between a shorter (7 kDa) polymer and a longer (20 kDa) polymer of BF_2dbm(I)PLA. Image adapted with permission from DeRosa et al., *ACS Appl. Mater. Interfaces* **2015**, *7*, 23633-23643.[110] Copyright American Chemical Society.

Although singlet and triplet emissions are clearly distinguished by wavelength and lifetime, a stronger phosphorescence intensity is desired for practical oxygen sensing. Heavy atom can be introduced to enhance spin-orbit coupling and increase the rate of intersystem crossing via the heavy atom effect. This was demonstrated by studying optical properties and oxygen sensitivity of a series of halide substituted boron dyes BF_2nbm(X)PLA (X = H, Br, I) (Figure 1.17). Heavier

halides resulted in increased phosphorescence intensities and shorter phosphorescence lifetimes. Lifetime is directly related to oxygen sensitivity, as shown in Equation 1.1 and 1.2. Materials with the longest unquenched lifetimes and fastest diffusion of oxygen through the matrix are the most sensitive. For different biological applications, the sensitivity must be well-matched to the expected oxygen levels for imaging and sensing.

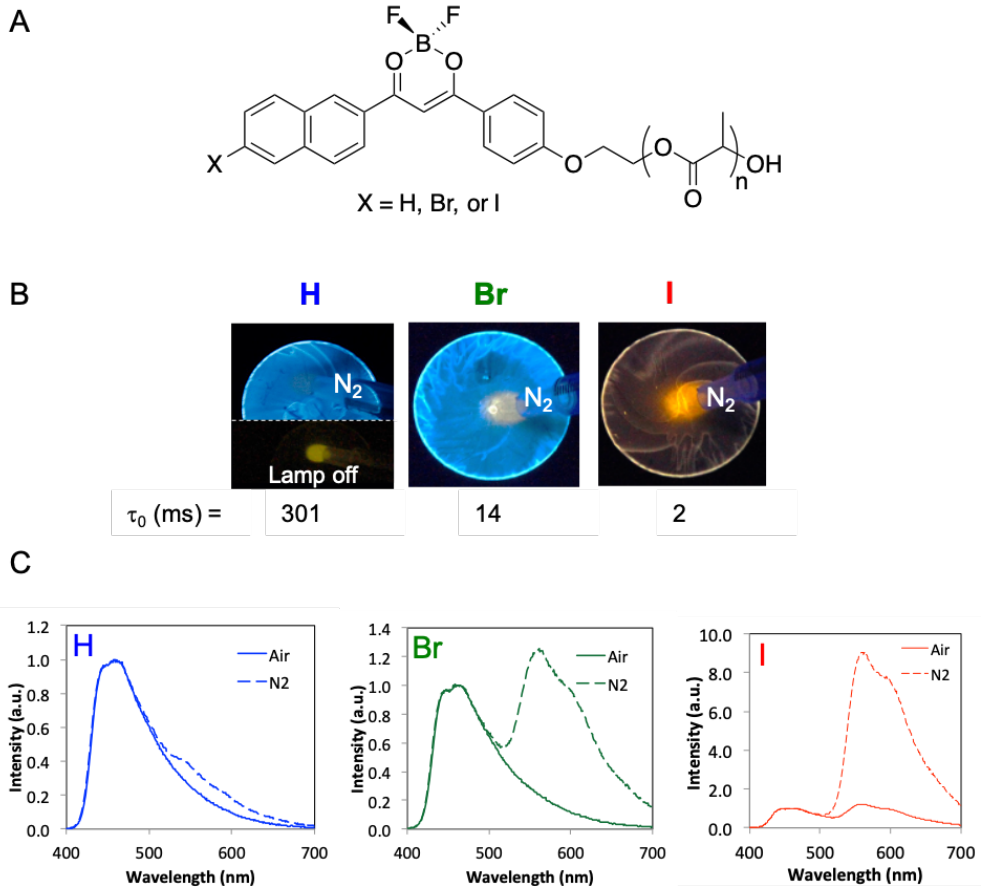

Figure 1. 17. Heavy Atom Effect. A) Chemical structures of BF_2nbm(X)PLA. B) Images showing phosphorescence emission under a N_2 gas stream for polymer films. C). Total emission spectra under air and nitrogen. Images were reproduced from DeRosa et al., *ACS Sensors*, **2016**. *1*, 1366-1373.[111] Copyright American Chemical Society.

1.4.3 Oxygen Sensing

The two most common methods for phosphorescence-based oxygen sensing rely on lifetime measurement and ratiometric imaging. Dyes substituted with heavier halides and shorter

polymers are suitable for ratiometric sensing, and the long phosphorescence lifetimes associated with the lighter halide substituted dye-polymers are promising candidates for lifetime sensing. In 2009, the boron dye oxygen sensor BF_2dbm(I)PLA, developed by Guoqing Zhang, was applied to ratiometric tumor hypoxia imaging (Figure 1.18). A tissue oxygen map was generated using the F/P ratio, and showed excellent contrast between vasculature (indicated as red) and tumor tissue (indicated as blue). By extending π conjugation from benzene to naphthalene, Christopher DeRosa designed a full range oxygen sensor with 0-100% oxygen sensitivity, wherein the blue fluorescence and yellow phosphorescence are well separated. This oxygen sensor has demonstrated utility in wound oxygenation imaging and healing combined with an RGB color camera.

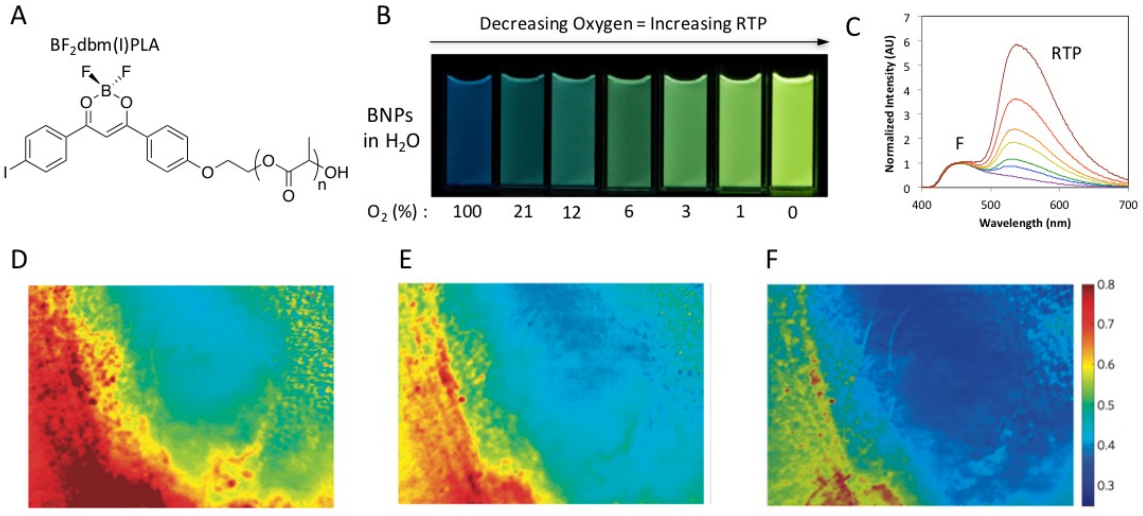

Figure 1. 18. Dual-Emissive BF_2dbm(I)PLA for Tumor Hypoxia. A) Chemical structure. B) Images under UV light of nanoparticles at varying oxygen concentration. C) Total emission spectra of nanoparticles at various oxygen concentrations. D-E) *In vivo* imaging of the breast cancer 4T1 mammary carcinoma tumor region in a mouse window chamber model in carbogen (D; 95% O_2), room air (E; 21% O_2) and nitrogen (F; 0% O_2). Emission intensity was averaged from 430 to 480 nm (fluorescence) and 530 to 600 nm (phosphorescence) then plotted ratios are shown. Images were adapted with permission from Zhang et al., *Nat. Mater.* **2009**, *8*, 747–751.[112]

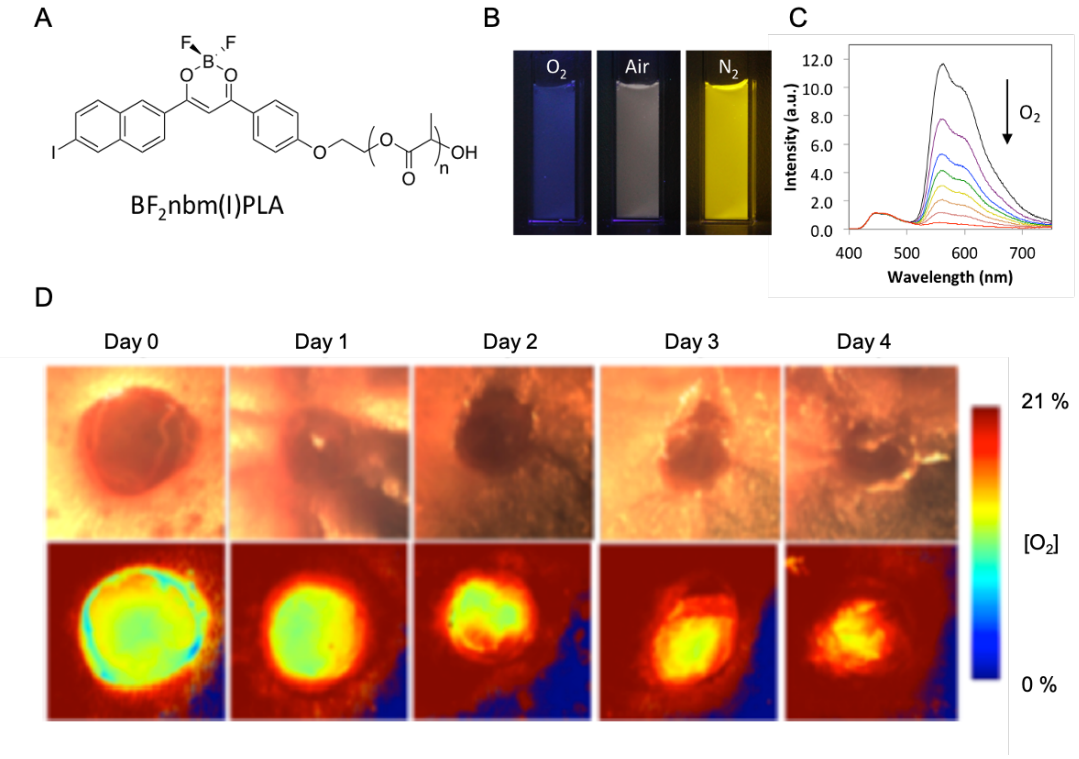

Figure 1. 19. Full Range Oxygen Sensor for Wound Imaging. A) Chemical structure of BF_2nbm(I)PLA. B) Images of nanoparticles under UV excitation at oxygen, air, and nitrogen. C) Total emission spectra of nanoparticles at various oxygen concentrations. D) Wound oxygenation and healing time course. Top: brightfield of wound beds. Bottom: ratiometric images generated via nanoparticles. Images were reproduced from DeRosa et al., *ACS Sensors*, **2016**. *1*, 1366-1373.[111] Copyright American Chemical Society.

Over the past years, the Fraser lab has developed methods to systematically tune the phosphorescence lifetime and to modulate the oxygen sensing range. Properties of four iodide-substituted boron dye polymers were listed in Table 1.2. Their distinct features enabled multiple biological applications in wound hypoxia imaging, cellular imaging, nanoparticle biodistribution, and radiation therapy efficacy.

Table 1. 2. Optical Properties of BF_2bdkPLA Nanoparticles.

Sample	λ_{abs} (nm)	λ_F (nm)	λ_P (nm)	τ_p (ms)	F to P	O2 Range (%)	Refs
BF_2dbm(I)PLA	407	437	525	4.5	F = P	0-21	112
BF_2nbm(I)PLA	417	460	562	1.9	F << P	0-100	111
BF_2dnm(I)PLA	433	503	575	6.0	F < P	0-5	113

BF_2tbm(I)PLA	433	449	581	2.1	F = P	0-21	[114]

1.4.4 Goal of this Research

The previous work in Fraser lab established a library of boron dyes and dye polymers, thoroughly studied their optical properties, and demonstrated fascinating advancements in biological applications. From here, the goal of this research is to further develop these dye-polymers as versatile reagents for imaging and sensing in biomedicine, in order to be adapted in translational clinical fields and to compete commercially in the market. Because each biological context is unique, interactions between biological samples and the dye polymer materials are unknown. Successful application requires understanding of material behaviors in relevant biological environments and adapting materials for specific, unique purposes. It also relies on the optimization of materials, instrumentation and software, and biological models altogether, for each given imaging or sensing goal.

Appropriate surface modification by polymer chemistry allows the conjugation of nanoparticles to a wide range of biomolecules, enabling their delivery and preferential accumulation at the site of action. This can be achieved by active targeting. Adapting materials for commonly used instrumentation makes them more convenient, broadly applicable, and cost effective. In particular, this research involved tailoring the emissions of boron nanoparticles to be well aligned with RGB camera channels. Extending the application of boron nanoprobes to immunology and neuroscience are other important goals of this research. All of these studies help to advance understanding of boron dye materials and promote their use as versatile imaging tools in research and clinical fields.

1.5 References

(1) Lakowicz, J. R. *Principles of Fluorescence Spectroscopy*; Springer: New York, 2006.

(2) Berezin, M. Y.; Achilefu, S. Fluorescence Lifetime Measurements and Biological Imaging. *Chem. Rev.* **2010**, *110*, 2641–2684.

(3) Sarder, P.; Maji, D.; Achilefu, S. Molecular Probes for Fluorescence Lifetime Imaging. *Bioconjug. Chem.* **2015**, *26*, 963–974.

(4) Lavis, L. D.; Raines, R. T. Bright Ideas for Chemical Biology. *ACS Chem. Biol.* **2008**, *3*, 142–155.

(5) Reisch, A.; Klymchenko, A. S. Fluorescent Polymer Nanoparticles Based on Dyes: Seeking Brighter Tools for Bioimaging. *Small* **2016**, *12*, 1968–1992.

(6) Li, D.; Zhang, H.; Wang, Y. Four-Coordinate Organoboron Compounds for Organic Light-Emitting Diodes (OLEDs). *Chem. Soc. Rev.* **2013**, *42*, 8416–8433.

(7) Kwon, J. E.; Park, S. Y. Advanced Organic Optoelectronic Materials: Harnessing Excited-State Intramolecular Proton Transfer (ESIPT) Process. *Adv. Mater.* **2011**, *23*, 3615–3642.

(8) Ding, D.; Li, K.; Liu, B.; Tang, B. Z. Bioprobes Based on AIE Fluorogens. *Acc. Chem. Res.* **2013**, *46*, 2441–2453.

(9) Mei, J.; Leung, N. L. C.; Kwok, R. T. K.; Lam, J. W. Y.; Tang, B. Z. Aggregation-Induced Emission: Together We Shine, United We Soar! *Chem. Rev.* **2015**, *115*, 11718–11940.

(10) Lewis, G. N.; Kasha, M. Phosphorescence and the Triplet State. *J. Am. Chem. Soc.* **1944**, *66*, 2100–2116.

(11) Lower, S. K.; El-Sayed, M. A. The Triplet State and Molecular Electronic Processes in Organic Molecules. *Chem. Rev.* **1966**, *66*, 199–241.

(12) Reineke, S. Organic Light-Emitting Diodes: Phosphorescence Meets Its Match. *Nat. Photonics* **2014**, *8*, 269–270.

(13) Perkampus, H.-H. *UV-VIS Spectroscopy and Its Applications*; Springer Berlin Heidelberg: Berlin, Heidelberg, 1992.

(14) O'Connor, D. V.; Phillips, D. Time-Correlated Single Photon Counting. *IUPAC Compend. Chem. Terminol.* **2008**, *25*, 460–463.

(15) Kuimova, M. K.; Yahioglu, G.; Levitt, J. A.; Suhling, K. Molecular Rotor Measures Viscosity of Live Cells via Fluorescence Lifetime Imaging. *J. Am. Chem. Soc.* **2008**, *130*, 6672–6673.

(16) Crosby, G. A.; Demas, J. N. Measurement of Photoluminescence Quantum Yields. Review. *J. Phys. Chem.* **1971**, *75*, 991–1024.

(17) Liu, J.; Sun, Y. Q.; Zhang, H.; Shi, H.; Shi, Y.; Guo, W. Sulfone-Rhodamines: A New Class of near-Infrared Fluorescent Dyes for Bioimaging. *ACS Appl. Mater. Interfaces* **2016**, *8*, 22953–22962.

(18) Lavis, L. D.; Raines, R. T. Bright Building Blocks for Chemical Biology. *ACS Chem. Biol.* **2014**, *9*, 855–866.

(19) Antaris, A. L.; Chen, H.; Cheng, K.; Sun, Y.; Hong, G.; Qu, C.; Diao, S.; Deng, Z.; Hu, X.; Zhang, B.; et al. A Small-Molecule Dye for NIR-II Imaging. *Nat. Mater.* **2015**, *15*, 235–242.

(20) Haran, G.; Haas, E.; Szpikowskat, B. K.; Maso, M. T. Domain Motions in Phosphoglycerate Kinase: Determination of Interdomain Distance Distributions by Site-Specific Labeling and Time-Resolved Fluorescence Energy Transfer. *Biophysics (Oxf).* **1992**, *89*, 11764–11768.

(21) Greenspan, P.; Mayer, E. P.; Fowler, S. D. Nile Red: A Selective Fluorescent Stain for Intracellular Lipid Droplets. *J. Cell Biol.* **1985**, *100*, 965–973.

(22) Hennig, A.; Bakirci, H.; Nau, W. M. Label-Free Continuous Enzyme Assays with Macrocycle-Fluorescent Dye Complexes. *Nat. Methods* **2007**, *4*, 629–632.

(23) Schreiber, U.; Bilger, W.; Neubauer, C. Chlorophyll Fluorescence as a Nonintrusive Indicator for Rapid Assessment of In Vivo Photosynthesis. *Ecophysiol. Photosynth.* **1995**, 49–70.

(24) Kilgore, J. A.; Dolman, N. J.; Davidson, M. W. A Review of Reagents for Fluorescence Microscopy of Cellular Compartments and Structures, Part III: Reagents for Actin, Tubulin, Cellular Membranes, and Whole Cell and Cytoplasm. *Curr. Protoc. Cytom.* **2014**, *67*, 12.32.1-12.32.17.

(25) Resch-Genger, U.; Grabolle, M.; Cavaliere-Jaricot, S.; Nitschke, R.; Nann, T. Quantum Dots versus Organic Dyes as Fluorescent Labels. *Nat. Methods* **2008**, *5*, 763–775.

(26) Jiang, K.; Sun, S.; Zhang, L.; Lu, Y.; Wu, A.; Cai, C.; Lin, H. Red, Green, and Blue Luminescence by Carbon Dots: Full-Color Emission Tuning and Multicolor Cellular Imaging. *Angew. Chemie Int. Ed.* **2015**, *54*, 5360–5363.

(27) Hasebe, N.; Suzuki, K.; Horiuchi, H.; Suzuki, H.; Yoshihara, T.; Okutsu, T.; Tobita, S. Absolute Phosphorescence Quantum Yields of Singlet Molecular Oxygen in Solution Determined Using an Integrating Sphere Instrument. *Anal. Chem.* **2015**, *87*, 2360–2366.

(28) Wang, X. D.; Wolfbeis, O. S. Optical Methods for Sensing and Imaging Oxygen: Materials, Spectroscopies and Applications. *Chem. Soc. Rev.* **2014**, *43*, 3666–3761.

(29) Zhang, X.; Xie, T.; Cui, M.; Yang, L.; Sun, X.; Jiang, J.; Zhang, G. General Design Strategy for Aromatic Ketone-Based Single-Component Dual-Emissive Materials. *ACS Appl. Mater. Interfaces* **2014**, *6*, 2279–2284.

(30) Gutierrez, G. D.; Sazama, G. T.; Wu, T.; Baldo, M. A.; Swager, T. M. Red Phosphorescence from Benzo[2,1,3]Thiadiazoles at Room Temperature. *J. Org. Chem.* **2016**, *81*, 4789–4796.

(31) Cheng, X.; Wang, K.; Huang, S.; Zhang, H.; Zhang, H.; Wang, Y. Organic Crystals with Near-Infrared Amplified Spontaneous Emissions Based on 2′-Hydroxychalcone Derivatives: Subtle Structure Modification but Great Property Change. *Angew. Chemie* **2015**, *127*, 8489–8493.

(32) Borisov, S. M.; Fischer, R.; Saf, R.; Klimant, I. Exceptional Oxygen Sensing Properties of New Blue Light-Excitable Highly Luminescent Europium(III) and Gadolinium(III) Complexes. *Adv. Funct. Mater.* **2014**, *24*, 6548–6560.

(33) Quaranta, M.; Borisov, S. M.; Klimant, I. Indicators for Optical Oxygen Sensors. *Bioanal. Rev.* **2012**, *4*, 115–157.

(34) Sakadžić, S.; Roussakis, E.; Yaseen, M. A.; Mandeville, E. T.; Srinivasan, V. J.; Arai, K.; Ruvinskaya, S.; Devor, A.; Lo, E. H.; Vinogradov, S. A.; et al. Two-Photon High-Resolution Measurement of Partial Pressure of Oxygen in Cerebral Vasculature and Tissue. *Nat. Methods* **2010**, *7*, 755–759.

(35) Esipova, T. V.; Karagodov, A.; Miller, J.; Wilson, D. F.; Busch, T. M.; Vinogradov, S. A. Two New “Protected” Oxyphors for Biological Oximetry: Properties and Application in Tumor Imaging. *Anal. Chem.* **2011**, *83*, 8756–8765.

(36) Lecoq, J.; Parpaleix, A.; Roussakis, E.; Ducros, M.; Houssen, Y. G.; Vinogradov, S. a; Charpak, S. Simultaneous Two-Photon Imaging of Oxygen and Blood Flow in Deep Cerebral Vessels. *Nat. Med.* **2011**, *17*, 893–898.

(37) Finikova, O. S.; Lebedev, A. Y.; Aprelev, A.; Troxler, T.; Gao, F.; Garnacho, C.; Muro, S.; Hochstrasser, R. M.; Vinogradov, S. A. Oxygen Microscopy by Two-Photon-Excited Phosphorescence. *ChemPhysChem* **2008**, *9*, 1673–1679.

(38) Dunphy, I.; Vinogradov, S. A.; Wilson, D. F. Oxyphor R2 and G2: Phosphors for Measuring Oxygen by Oxygen-Dependent Quenching of Phosphorescence. *Anal. Biochem.* **2002**, *310*, 191–198.

(39) Wilson, D. F.; Lee, W. M. F.; Makonnen, S.; Finikova, O.; Apreleva, S.; Vinogradov, S. A. Oxygen Pressures in the Interstitial Space and Their Relationship to Those in the Blood Plasma in Resting Skeletal Muscle. *J. Appl. Physiol.* **2006**, *101*, 1648–1656.

(40) Nichols, A. J.; Roussakis, E.; Klein, O. J.; Evans, C. L. Click-Assembled, Oxygen-Sensing Nanoconjugates for Depth-Resolved, near-Infrared Imaging in a 3-D Cancer Model. *Angew. Chemie - Int. Ed.* **2014**, *53*, 3671–3674.

(41) Bolton, O.; Lee, K.; Kim, H. J.; Lin, K. Y.; Kim, J. Activating Efficient Phosphorescence from Purely Organic Materials by Crystal Design. *Nat. Chem.* **2011**, *3*, 205–210.

(42) Lee, S.-K.; Okura, I. Photostable Optical Oxygen Sensing Material: Platinum Tetrakis(Pentafluorophenyl)Porphyrin Immobilized in Polystyrene. *Anal. Commun.* **1997**, *34*, 185–188.

(43) Lai, S. W.; Hou, Y. J.; Che, C. M.; Pang, H. L.; Wong, K. Y.; Chang, C. K.; Zhu, N. Electronic Spectroscopy, Photophysical Properties, and Emission Quenching Studies of an Oxidatively Robust Perfluorinated Platinum Porphyrin. *Inorg. Chem.* **2004**, *43*, 3724–3732.

(44) Ehgartner, J.; Sulzer, P.; Burger, T.; Kasjanow, A.; Bouwes, D.; Krühne, U.; Klimant, I.; Mayr, T. Online Analysis of Oxygen inside Silicon-Glass Microreactors with Integrated Optical Sensors. *Sensors Actuators, B Chem.* **2016**, *228*, 748–757.

(45) Liu, J.; Liu, Y.; Bu, W.; Bu, J.; Sun, Y.; Du, J.; Shi, J. Ultrasensitive Nanosensors Based on Upconversion Nanoparticles for Selective Hypoxia Imaging in Vivo upon Near-Infrared Excitation. *J. Am. Chem. Soc.* **2014**, *136*, 9701–9709.

(46) Alford, P. C.; Cook, M. J.; Lewis, A. P.; McAuliffe, G. S. G.; Skarda, V.; Thomson, A. J.; Glasper, J. L.; Robbins, D. J. Luminescent Metal Complexes. Part 5.1 Luminescence Properties of Ring-Substituted 1, 10-Phenanthroline Tris-Complexes of Ruthenium(II). *J. Chem. Soc. Perkin Trans. 2* **1985**, No. 5, 705–709.

(47) Fercher, A.; Ponomarev, G. V.; Yashunski, D.; Papkovsky, D. Evaluation of the Derivates of Phosphorescent Pt-Coproporphyrin as Intracellular Oxygen-Sensitive Probes. *Anal. Bioanal. Chem.* **2010**, *396*, 1793–1803.

(48) Roussakis, E.; Li, Z.; Nichols, A. J.; Evans, C. L. Oxygen-Sensing Methods in Biomedicine from the Macroscale to the Microscale. *Angew. Chemie - Int. Ed.* **2015**, *54*, 8340–8362.

(49) Weiss, H. M. Appreciating Oxygen. *J. Chem. Educ.* **2008**, *85*, 1218–1219.

(50) Semenza, G. L. Life with Oxygen. *Science (80-.).* **2007**, *318*, 62–64.

(51) Rich, P. R. The Molecular Machinery of Keilin's Respiratory Chain. *Biochem. Soc. Trans.* **2003**, *31*, 1095–1105.

(52) Meier, R. J.; Fischer, L. H.; Wolfbeis, O. S.; Schäferling, M. Referenced Luminescent Sensing and Imaging with Digital Color Cameras: A Comparative Study. *Sensors Actuators B Chem.* **2013**, *177*, 500–506.

(53) Lemon, C. M.; Karnas, E.; Han, X.; Bruns, O. T.; Kempa, T. J.; Fukumura, D.; Bawendi, M. G.; Jain, R. K.; Duda, D. G.; Nocera, D. G. Micelle-Encapsulated Quantum Dot-Porphyrin Assemblies as *in Vivo* Two-Photon Oxygen Sensors. *J. Am. Chem. Soc.* **2015**, *137*, 9832–9842.

(54) Hirakawa, Y.; Yoshihara, T.; Kamiya, M.; Mimura, I.; Fujikura, D.; Masuda, T.; Kikuchi, R.; Takahashi, I.; Urano, Y.; Tobita, S.; et al. Quantitating Intracellular Oxygen Tension in Vivo by Phosphorescence Lifetime Measurement. *Sci. Rep.* **2015**, *5*, 1–10.

(55) Kurokawa, H.; Ito, H.; Inoue, M.; Tabata, K.; Sato, Y.; Yamagata, K.; Kizaka-Kondoh, S.; Kadonosono, T.; Yano, S.; Inoue, M.; et al. High Resolution Imaging of Intracellular Oxygen Concentration by Phosphorescence Lifetime. *Sci. Rep.* **2015**, *5*, 10657.

(56) Harris, A. L. Hypoxia — a Key Regulatory Factor in Tumour Growth. *Nat. Rev. Cancer* **2002**, *2*, 38–47.

(57) Bento, C. F.; Pereira, P. Regulation of Hypoxia-Inducible Factor 1 and the Loss of the Cellular Response to Hypoxia in Diabetes. *Diabetologia* **2011**, *54*, 1946–1956.

(58) Sen, C. K. Wound Healing Essentials: Let There Be Oxygen. *Wound Repair Regen.* **2009**, *17*, 1–18.

(59) Mink, J. W.; Blumenschine, R. J.; Adams, D. B. Ratio of Central Nervous System to Body Metabolism in Vertebrates: Its Constancy and Functional Basis. *Am. J. Physiol. - Regul. Integr. Comp. Physiol.* **1981**, *10*, 203–212.

(60) Harris, J. J.; Jolivet, R.; Attwell, D. Synaptic Energy Use and Supply. *Neuron* **2012**, *75*, 762–777.

(61) Devine, M. J.; Kittler, J. T. Mitochondria at the Neuronal Presynapse in Health and Disease. *Nat. Rev. Neurosci.* **2018**, *19*, 63–80.

(62) Neoptolemos, J. P.; Stocken, D. D.; Friess, H.; Bassi, C.; Dunn, J. A.; Hickey, H.; Beger, H.; Fernandez-Cruz, L.; Dervenis, C.; Falconi, M.; et al. Whole-Body Hypothermia for Neonates with Hypoxic–Ischemic Encephalopathy Seetha. *N Engl J Med* **2004**, *350*, 1200–1210.

(63) Tang, Y.; Lu, A.; Aronow, B. J.; Sharp, F. R. Blood Genomic Responses Differ after Stroke, Seizures, Hypoglycemia, and Hypoxia: Blood Genomic Fingerprints of Disease. *Ann. Neurol.* **2001**, *50*, 699–707.

(64) Prass, K.; Scharff, A.; Ruscher, K.; Löwl, D.; Muselmann, C.; Victorov, I.; Kapinya, K.; Dirnagl, U.; Meisel, A. Hypoxia-Induced Stroke Tolerance in the Mouse Is Mediated by Erythropoietin. *Stroke* **2003**, *34*, 1981–1986.

(65) Glass, H. C.; Glidden, D.; Jeremy, R. J.; Barkovich, A. J.; Ferriero, D. M.; Miller, S. P. Clinical Neonatal Seizures Are Independently Associated with Outcome in Infants at Risk for Hypoxic-Ischemic Brain Injury. *J. Pediatr.* **2009**, *155*, 318–323.

(66) Wirrell, E. C.; Armstrong, E. A.; Osman, L. D.; Yager, J. Y. Prolonged Seizures Exacerbate Perinatal Hypoxic-Ischemic Brain Damage. *Pediatr. Res.* **2001**, *50*, 445–454.

(67) Baud, O.; Daire, J.-L.; Dalmaz, Y.; Fontaine, R. H.; Krueger, R. C.; Sebag, G.; Evrard, P.; Gressens, P.; Verney, C. Gestational Hypoxia Induces White Matter Damage in Neonatal Rats: A New Model of Periventricular Leukomalacia. *Brain Pathol.* **2004**, *14*, 1–10.

(68) Ogunshola, O. O.; Antoniou, X. Contribution of Hypoxia to Alzheimer's Disease: Is HIF-1α a Mediator of Neurodegeneration? *Cell. Mol. Life Sci.* **2009**, *66*, 3555–3563.

(69) Zhang, X.; Le, W. Pathological Role of Hypoxia in Alzheimer's Disease. *Exp. Neurol.* **2010**, *223*, 299–303.

(70) Yoshihara, T.; Hosaka, M.; Terata, M.; Ichikawa, K.; Murayama, S.; Tanaka, A.; Mori, M.; Itabashi, H.; Takeuchi, T.; Tobita, S. Intracellular and in Vivo Oxygen Sensing Using Phosphorescent IR(III) Complexes with a Modified Acetylacetonato Ligand. *Anal. Chem.* **2015**, *87*, 2710–2717.

(71) Li, Z.; Navarro-Alvarez, N.; Keeley, E. J.; Nowell, N. H.; Goncalves, B. M. M.; Huang, C. A.; Evans, C. L. Non-Invasive Monitoring of Skin Inflammation Using an Oxygen-Sensing Paint-on Bandage. *Biomed. Opt. Express* **2017**, *8*, 4640–4651.

(72) Matsumoto, T.; Tanaka, K.; Chujo, Y. Synthesis and Characterization of Gallafluorene-Containing Conjugated Polymers: Control of Emission Colors and Electronic Effects of Gallafluorene Units on π-Conjugation System. *Macromolecules* **2015**, *48*, 1343–1351.

(73) Bates, C. M.; Bates, F. S. *50th Anniversary Perspective* : Block Polymers—Pure Potential. *Macromolecules* **2017**, *50*, 3–22.

(74) Hanlon, A. M.; Lyon, C. K.; Berda, E. B. What Is Next in Single-Chain Nanoparticles? *Macromolecules* **2016**, *49*, 2–14.

(75) Schneiderman, D. K.; Hillmyer, M. A. Aliphatic Polyester Block Polymer Design. *Macromolecules* **2016**, *49*, 2419–2428.

(76) Carlini, A. S.; Adamiak, L.; Gianneschi, N. C. Biosynthetic Polymers as Functional Materials. *Macromolecules* **2016**, *49*, 4379–4394.

(77) Liu, J.; Liu, B. Red and near Infrared Fluorescent Conjugated Polyelectrolytes for Biomedical Applications. *J. Polym. Sci. Part A Polym. Chem.* **2017**, *55*, 519–532.

(78) Jenkins, R.; Burdette, M. K.; Foulger, S. H. Mini-Review: Fluorescence Imaging in Cancer Cells Using Dye-Doped Nanoparticles. *RSC Adv.* **2016**, *6*, 65459–65474.

(79) Tanaka, K.; Chujo, Y. Advanced Luminescent Materials Based on Organoboron Polymers. *Macromol. Rapid Commun.* **2012**, *33*, 1235–1255.

(80) Nagai, A.; Chujo, Y. Luminescent Organoboron Conjugated Polymers. *Chem. Lett.* **2010**, *39*, 430–435.

(81) Hillmyer, M. A.; Tolman, W. B. Aliphatic Polyester Block Polymers: Renewable, Degradable, and Sustainable. *Acc. Chem. Res.* **2014**, *47*, 2390–2396.

(82) Albertsson, A.-C.; Varma, I. K. Recent Developments in Ring Opening Polymerization of Lactones for Biomedical Applications. *Biomacromolecules* **2003**, *4*, 1466–1486.

(83) Olsén, P.; Undin, J.; Odelius, K.; Keul, H.; Albertsson, A.-C. Switching from Controlled Ring-Opening Polymerization (CROP) to Controlled Ring-Closing Depolymerization (CRCDP) by Adjusting the Reaction Parameters That Determine the Ceiling Temperature. *Biomacromolecules* **2016**, *17*, 3995–4002.

(84) Madhavan Nampoothiri, K.; Nair, N. R.; John, R. P. An Overview of the Recent Developments in Polylactide (PLA) Research. *Bioresour. Technol.* **2010**, *101*, 8493–8501.

(85) Sitia, L.; Ferrari, R.; Violatto, M. B.; Talamini, L.; Dragoni, L.; Colombo, C.; Colombo, L.; Lupi, M.; Ubezio, P.; D'Incalci, M.; et al. Fate of PLA and PCL-Based Polymeric Nanocarriers in Cellular and Animal Models of Triple-Negative Breast Cancer. *Biomacromolecules* **2016**, *17*, 744–755.

(86) Farah, S.; Anderson, D. G. Physical and Mechanical Properties of PLA, and Their Functions in Widespread Applications — A Comprehensive Review. *Adv. Drug Deliv. Rev.* **2016**, *107*, 367–392.

(87) Elsabahy, M.; Wooley, K. L. Design of Polymeric Nanoparticles for Biomedical Delivery Applications. *Chem. Soc. Rev.* **2012**, *41*, 2545–2561.

(88) Brannon-Peppas, L.; Blanchette, J. O. Nanoparticle and Targeted Systems for Cancer Therapy. *Adv. Drug Deliv. Rev.* **2012**, *64*, 206–212.

(89) Alexis, F.; Pridgen, E.; Molnar, L. K.; Farokhzad, O. C. Factors Affecting the Clearance and Biodistribution of Polymeric Nanoparticles. *Mol. Pharm.* **2008**, *5*, 505–515.

(90) Fox, M. E.; Szoka, F. C.; Fréchet, J. M. J. Soluble Polymer Carriers for the Treatment of Cancer: The Importance of Molecular Architecture. *Acc. Chem. Res.* **2009**, *42*, 1141–1151.

(91) Wang, Z.; Chen, S.; Lam, J. W. Y.; Qin, W.; Kwok, R. T. K.; Xie, N.; Hu, Q.; Tang, B. Z. Long-Term Fluorescent Cellular Tracing by the Aggregates of AIE Bioconjugates. *J. Am. Chem. Soc.* **2013**, *135*, 8238–8245.

(92) Marusyk, A.; Almendro, V.; Polyak, K. Intra-Tumour Heterogeneity: A Looking Glass for Cancer? *Nat. Rev. Cancer* **2012**, *12*, 323–334.

(93) Junttila, M. R.; de Sauvage, F. J. Influence of Tumour Micro-Environment Heterogeneity on Therapeutic Response. *Nature* **2013**, *501*, 346–354.

(94) Egusquiaguirre, S. P.; Igartua, M.; Hernández, R. M.; Pedraz, J. L. Nanoparticle Delivery Systems for Cancer Therapy: Advances in Clinical and Preclinical Research. *Clin. Transl. Oncol.* **2012**, *14*, 83–93.

(95) Upreti, M.; Jyoti, A.; Sethi, P. Tumor Microenvironment and Nanotherapeutics. *Transl. Cancer Res.* **2013**, *2*, 309–319.

(96) Maruyama, K. Intracellular Targeting Delivery of Liposomal Drugs to Solid Tumors Based on EPR Effects. *Adv. Drug Deliv. Rev.* **2011**, *63*, 161–169.

(97) Tanaka, K.; Chujo, Y. Recent Progress of Optical Functional Nanomaterials Based on Organoboron Complexes with β-Diketonate, Ketoiminate and Diiminate. *NPG Asia Mater.* **2015**, *7*, e223.

(98) Karpenko, I. A.; Niko, Y.; Yakubovskyi, V. P.; Gerasov, A. O.; Bonnet, D.; Kovtun, Y. P.; Klymchenko, A. S. Push–Pull Dioxaborine as Fluorescent Molecular Rotor: Far-Red Fluorogenic Probe for Ligand–Receptor Interactions. *J. Mater. Chem. C* **2016**, *4*, 3002–3009.

(99) Mathew, A. S.; DeRosa, C. A.; Demas, J. N.; Fraser, C. L. Difluoroboron β-Diketonate Materials with Long-Lived Phosphorescence Enable Lifetime Based Oxygen Imaging with a Portable Cost Effective Camera. *Anal. Methods* **2016**, *8*, 3109–3114.

(100) Cogné-Laage, E.; Allemand, J. F.; Ruel, O.; Baudin, J. B.; Croquette, V.; Blanchard-Desce, M.; Jullien, L. Diaroyl(Methanato)Boron Difluoride Compounds as Medium-Sensitive Two-Photon Fluorescent Probes. *Chem. - A Eur. J.* **2004**, *10*, 1445–1455.

(101) Zhang, G.; Kooi, S. E.; Demas, J. N.; Fraser, C. L. Emission Color Tuning with Polymer Molecular Weight for Difluoroboron Dibenzoylmethane-Polylactide. *Adv. Mater.* **2008**, *20*, 2099–2104.

(102) Suwa, Y.; Yamaji, M.; Okamoto, H. Synthesis and Photophysical Properties of Difluoroboronated β-Diketones with the Fluorene Moiety That Have High Fluorescence Quantum Yields. *Tetrahedron Lett.* **2016**, *57*, 1695–1698.

(103) DeRosa, C. A.; Kerr, C.; Fan, Z.; Kolpaczynska, M.; Mathew, A. S.; Evans, R. E.; Zhang, G.; Fraser, C. L. Tailoring Oxygen Sensitivity with Halide Substitution in Difluoroboron Dibenzoylmethane Polylactide Materials. *ACS Appl. Mater. Interfaces* **2015**, *7*, 23633–23643.

(104) Zhang, G.; Chen, J.; Payne, S. J.; Kooi, S. E.; Demas, J. N.; Fraser, C. L. Multi-Emissive Difluoroboron Dibenzoylmethane Polylactide Exhibiting Intense Fluorescence and Oxygen-Sensitive Room-Temperature Phosphorescence. *J. Am. Chem. Soc.* **2007**, *129*, 8942–8943.

(105) Fraser, C. L.; Zhang, G. Luminescent Diketonate Polymers. WO 2011011646, 2011.

(106) Belanger, M. C.; Zhuang, M.; Ball, A. G.; Richey, K. H.; DeRosa, C. A.; Fraser, C. L.; Pompano, R. R. Labelling Primary Immune Cells Using Bright Blue Fluorescent Nanoparticles. *Biomater. Sci.* **2020**, *8*, 1897–1909.

(107) Zhang, G.; Clair, T. L. S.; Fraser, C. L. Synthesis and Fluorescent Properties of Difluoroboron Dibenzoylmethane Polycaprolactone Synthesis and Fluorescent Properties of Difluoroboron Dibenzoylmethane Polycaprolactone. *Macromolecules* **2009**, *42*, 3092–3097.

(108) Zhang, G.; Fiore, G. L.; St. Clair, T. L.; Fraser, C. L. Difluoroboron Dibenzoylmethane PCL-PLA Block Copolymers: Matrix Effects on Room Temperature Phosphorescence. *Macromolecules* **2009**, *42*, 3162–3169.

(109) Zhang, G.; Evans, R. E.; Campbell, K. a.; Fraser, C. L. Role of Boron in the Polymer Chemistry and Photophysical Properties of Difluoroboron-Dibenzoylmethane Polylactide. *Macromolecules* **2009**, *42*, 8627–8633.

(110) DeRosa, C. A.; Kerr, C.; Fan, Z.; Kolpaczynska, M.; Mathew, A. S.; Evans, R. E.; Zhang, G.; Fraser, C. L. Tailoring Oxygen Sensitivity with Halide Substitution in Difluoroboron Dibenzoylmethane Polylactide Materials. *ACS Appl. Mater. Interfaces* **2015**, *7*, 23633–23643.

(111) DeRosa, C. A.; Seaman, S. A.; Mathew, A. S.; Gorick, C. M.; Fan, Z.; Demas, J. N.; Peirce, S. M.; Fraser, C. L. Oxygen Sensing Difluoroboron β-Diketonate Polylactide Materials with Tunable Dynamic Ranges for Wound Imaging. *ACS Sensors* **2016**, *1*, 1366–1373.

(112) Zhang, G.; Palmer, G. M.; Dewhirst, M. W.; Fraser, C. L. A Dual-Emissive-Materials Design Concept Enables Tumour Hypoxia Imaging. *Nat. Mater.* **2009**, *8*, 747–751.

(113) DeRosa, C. A.; Samonina-Kosicka, J.; Fan, Z.; Hendargo, H. C.; Weitzel, D. H.; Palmer, G. M.; Fraser, C. L. Oxygen Sensing Difluoroboron Dinaphthoylmethane Polylactide. *Macromolecules* **2015**, *48*, 2967–2977.

(114) DeRosa, C. A.; Kolpaczynska, M.; Kerr, C.; Daly, M. L.; Morris, W. A.; Fraser, C. L. Oxygen-Sensing Difluoroboron Thienyl Phenyl β-Diketonate Polylactides. *Chempluschem* **2017**, *82*, 399–406.

Chapter 2: Labelling Primary Immune Cells Using Bright Blue Fluorescent Nanoparticles

2.1 Introduction

Well-controlled labelling of immune cells is of particular interest, as these highly motile cells are frequently tracked in vitro and in vivo, or labelled for flow cytometric analysis. Many fluorescent dyes provide intracellular labelling by binding in the cytoplasm or to DNA, but labelling reagents continue to be an area of active research, particularly to take advantage of the further ends of the UV-visible spectrum.[1] Cytoplasmic labelling reagents are preferred for live cell imaging over time, as DNA-binding dyes can interrupt transcription and cell replication.[1,2]

Common cytoplasmic dyes align well with standard green (Ex 470/40, Em 525/50) and red (Ex 550/25, Em 605/70) filter sets for widefield microscopy, including carboxyfluorescein succinimidyl ester (CSFE), calcein-AM, tetramethylrhodamine isothiocyanate (TRITC), and similar newer commercial fluorophores. However, the UV-excitable blue filter (Ex 365/50, Em 445/50) set is often underutilized for cell tracking. Many traditional blue fluorophores, such as DAPI and Hoechst, bind directly to DNA, while others suffer from low intensities, such as derivatives of pyrene or coumarin.[3] Dim fluorescence signal under the classic UV-excited blue filter makes it difficult to distinguish labelled cells from tissue autofluorescence. Newer, brighter blue and violet fluorophores are available, but are primarily designed for multiplexed flow cytometry and laser-based microscopy, with a maximum excitation at either 405 or 395 nm and narrow excitation peaks. This makes translating the same dyes from one excitation source to another difficult; concentration, time of labelling, and detector sensitivity must be optimized for each read-out. A bright blue reagent that can be used across multiple platforms such as flow cytometry, confocal microscopy, and widefield fluorescent microscopy would enable a single optimized labelling procedure to be used with flexible choice of read-out.

One of the brightest of boron dyes developed in Fraser Lab, methoxy substituted difluoroboron dibenzoymethane (BF_2dbmOMe), emits intense blue fluorescence with a quantum yield approaching unity ($\Phi_F = 0.99$)[4]. This is significantly larger than most commercially available blue fluorophores (e.g., DAPI: $\Phi_F = 0.58$; pyrene: $\Phi_F = 0.75$; 7-hydroxy-4-methylcoumarin: $\Phi_F = 0.63$). Therefore, we sought to harness this bright blue dye emission for *in vitro* and *ex vivo* imaging. In this collaborative work with the Pompano lab, we optimized this blue dyes for cytoplasmic labelling reagents in immune cells by conjugating the dyes with polymers.[5] Fabricating dye-polymer conjugates into nanoparticles offers the opportunity to tune uptake by immune cells.[6] Lymphocytes (T cells and B cells), dendritic cells, and macrophages each have been targeted for delivery of drugs or probes using nanoparticles.[7–9] Particles similar in size to viruses (20 – 200 nm) are readily internalized via endocytosis, particularly by phagocytic cells such as B cells or professional antigen presentation cells such as dendritic cells after adsorption of serum proteins.[10] Dyes were engineered with PLA, PCL, block co-polymers of PLA-PCL, and PEGylation. The purpose of choosing different polymers is first, altering the hydrophobicity of the nanoparticle can significantly affect internalization.[10] Second, the hydrophobicity and degree of crystallinity are associated with nanoparticle stability in aqueous environments.[12]

The utility of labelling and tracking primary immune cells (murine splenocytes) with boron dye-based nanoparticles containing different polymer chains was tested. After confirming the stability of the dyes and nanoparticles in solution, internalization and suitability for cellular staining as a function of polymer chemistry were assessed. The fluorescence intensity of cells labelled with these reagents was detectable by fluorescent microscopy under standard blue fluorescence filter sets and was compared to a commercial reagent, and finally was utilized in four-color fluorescent labelling and cell tracking in live tissue.

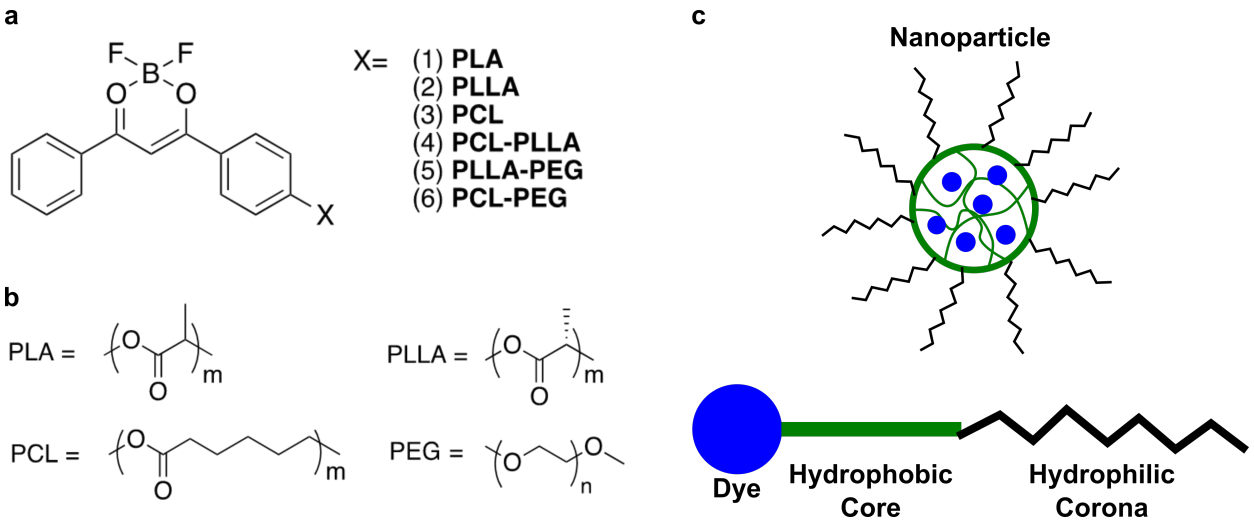

Figure 2. 1. Nanoparticle Design and Compositions. (a) Chemical structures of boron-based dye-polymer conjugates. (b) Chemical structures of each polymer tested. (c) Schematic of polymeric nanoparticles, which adopt a micellar structure with the boron-based dye in the core and the polymer in the outer shell.

2.2 Results and Discussion

2.2.1 Synthesis

In order to generate polymeric nanoparticles with different surface chemistries, we synthesized an array of polymers based on the blue-emitting boron-based dye BF_2dbm (**1**-**5** in Table 2.1, Figure 2.1a, and Scheme S2.1). We have previously shown that for BF_2dbmPLA, a molecular weight of ~10 kDa for the PLA corresponded to blue fluorescence,[13] so polymers in this size regime were targeted. The dye was prepared as either a primary alcohol (BF_2dbmOCH$_2$CH$_2$OH)[14] or a phenol (BF_2dbmOH)[15], to act as an initiator or a coupler respectively (Figure S2.1). The initiator BF_2dbmOCH$_2$CH$_2$OH was used to grow BF_2dbmPLA (**1**), BF_2dbmPLLA (**2**), and BF_2dbmPCL (**3**) by a solvent-free, tin-catalyzed ring-opening polymerization.31 The BF_2dbmPCL product was further used as a macroinitiator for the ring-opening polymerization of lactide to prepare a block copolymer, BF_2dbmPCL-PLLA (**4**).[16] Finally,

to generate the PEGylated material (**5**), BF_2dbmOH was coupled to PEG-PLLA via a Mitsunobu reaction.[17] The polymer molecular weights and polydispersities were determined by GPC and ^{1}H NMR spectroscopy (Table 3.1). The polydispersities were relatively low (Đ < 1.3) for all five samples, indicating the polymer chains were relatively uniform in chain length.

Table 2. 1. Polymer Synthesis Data

Polymer	#	Loading[a]	M_n[b] (GPC)	M_w[b] (GPC)	M_n[c] (NMR)	Đ[b]
BF_2dbmPLA	**1**	1/100	12 300	13 000	15 200	1.06
BF_2dbmPLLA	**2**	1/100	12 200	14 800	13 200	1.24
BF_2dbmPCL	**3**	1/130	6 900	7 300	10 400	1.06
BF_2dbmPCL-PLLA	**4**	1/100	7 700	9 000	14 100	1.17
BF_2dbmPLLA-PEG	**5**	1/130	10 500	11 000	14 400	1.05

[a]Initiator to lactide loading in the ring opening polymerization. For **1**-**3**, BF_2dbmOCH_2CH_2OH was used as the initiator. For BF_2dbmPCL-PLLA (**4**), BF_2dbmPCL (**3**) was used as the initiator. For **5**, PEG-OH (2 kDa) was used as the initiator and the dye (BF_2dbmOH) was added post polymerization. See **Schemes S3.1** and **S3.2** for reference. [b]Average molecular weight (M_n, Da) and weighted molecular weight (M_w, Da) of dye-polymer conjugates determined by gel permeation chromatography (GPC) in THF. Đ = polydispersity index (M_w/M_n). [c]Molecular weight determined by ^{1}H NMR (PLA-*H* or PCL-CH_2 vs 4-Ar-*H* of the dye).

2.2.2 Nanoparticles

Boron nanoparticles were fabricated by nanoprecipitation. The polymer was dissolved in a water miscible solvent (DMF), which was added dropwise to DI water. Dialysis against water removed the organic solvent to yield the nanoparticles. Nanoparticle sizes (hydrodynamic radius; R_H) ranged from 37-61 nm (Table 3.2), in the range suitable for cellular uptake.[18,19] All of the nanoparticles have narrow size distributions with low polydispersity values (0.1 ~ 0.3) and negative zeta potentials.[20] As expected, all five fluorescence spectra were similar with only subtle differences in spectral features, with excitation in the UV range (366-397 nm) and blue emission (438-447 nm) (Figure 2.2, Table 2.2). For convenience, here and throughout this paper we refer to the nanoparticles formed from the dye-polymer conjugates simply by the name of the polymer. The second, low energy feature observed in the total emission spectra for PCL and PCL-PLLA is

commonly observed for PCL-containing samples. This may be due to non-linear, long-range, dye-dye interactions, related to molar mass and matrix effects on the BF_2dbm-fluorophore, as previously described.[16] These spectra make the dyes well suited for use on traditional DAPI filter sets, as well as for excitation via a UV or 405 nm laser by flow cytometry or confocal microscopy.

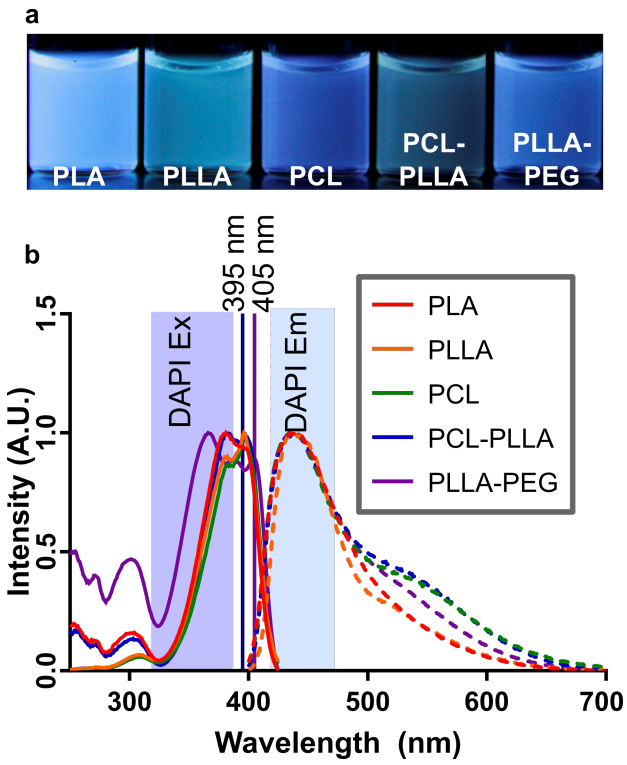

Figure 2. 2. Optical Properties of Boron Dye Nanoparticles. a) Images of freshly prepared nanoparticles suspended in water under UV illumination (λ_{ex} = 369 nm). b) Total excitation (solid lines) and emission spectra (dashed lines) of nanoparticle suspensions (λ_{ex} = 369 nm). Popular excitation sources including a DAPI filter set, 395 nm LED, and 405 nm laser all demonstrate good overlap with the spectra of the nanoparticles.

Table 2. 2. Nanoparticle Characterization Data

Nanoparticles	Radius[a] (nm)	PD[a]	ζ[b] (mV)	λ_{max}[c] (nm)	ε_λ[c] ($M^{-1}cm^{-1}$)	λ_{Ex}[d] (nm)	λ_F[d] (nm)
PLA	61	0.13	- 28.0[62]	398	32 100	381	439
PLLA	31	0.13	- 23.6	382	25 600	396	437
PCL	56	0.26	- 22.6	400	25 200	397	440
PCL-PLLA	51	0.12	- 36.9	399	21 100	381	438
PLLA-PEG	37	0.23	- 16.0[18]	396	29 800	366	439

[a]Determined by dynamic light scattering, for nanoparticles at 200 µg/mL in water. Polydispersity (PD) is the standard deviation of the distribution. PD = (peak width/peak height)^2.[b]Zeta potentials measured by Zetasizer. [c]Absorption maximum, λ_{max}, and corresponding extinction coefficient at

λ_{max}, ε_{λ}, for aqueous nanoparticle suspension (~ 50 μg/mL). [d]Fluorescence excitation and emission maximum for aqueous nanoparticle suspension.

2.2.3 Stability of Nanoparticles

We assessed the physical and optical stability of the nanoparticles in aqueous environments suitable for bioimaging, at the physiological temperature of 37 °C (Figure 2.3, Figures S2.2-S2.6). PLA nanoparticles show good shelf life with respect to molecular weight, size, absorption, and emission for months when stored at 4 °C in water.[20] At elevated temperature, all nanoparticles showed constant size in DI water over one week (Figure 2.3a). In PBS, however, nanoparticles containing PLA or PLLA polymers aggregated immediately, and the block copolymer PCL-PLLA aggregated after two days of incubation (Figure 2.3b). As an alternative to saline, we tested a solution of 5 % glucose in water, intended to match the osmotic pressure of the cells; 2 % serum was added to improve cell handling (water/glucose/serum solution). Compared with PBS, this solution greatly increased the stability of nanoparticles: PLA and PCL were stable for two days, and the other three particles maintained their sizes for over one week (Figure 2.3c). Surprisingly, complete cell culture media, RPMI supplemented with 10% serum and nutrients (see Methods), better maintained nanoparticle sizes despite its high ionic strength, perhaps because of spontaneous protein coating that protected the nanoparticles against aggregation (Figure 2.3d). The minor fluctuation in radii observed in complete media, known as swelling and deswelling, could be caused by a concentration gradient of ions (e.g., Na^+, Cl^-, amino acids) between the nanoparticle matrix and the surroundings, leading to ion diffusion and osmosis.[21,22] Regardless, nanoparticle radii were maintained consistently.

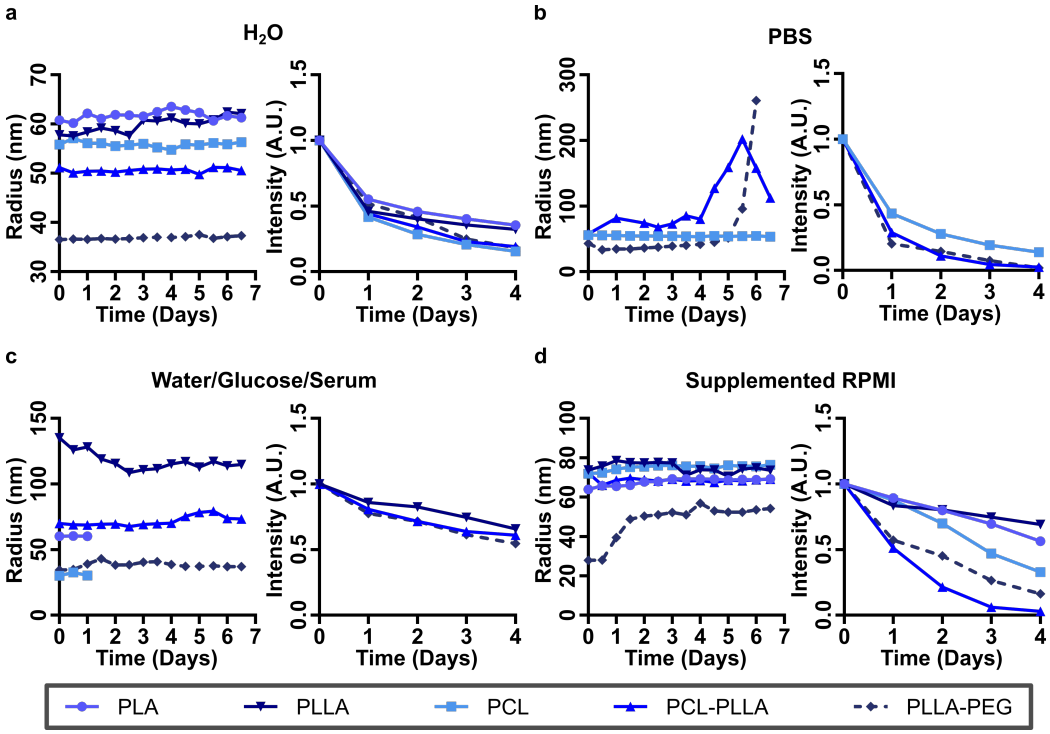

Figure 2. 3. Nanoparticle (200 µg/mL) stability at 37 °C in various media. Nanoparticle size was monitored by DLS (left), and emission monitored by fluorimeter (right). For samples with extensive aggregation, particle size exceeds the DLS detection limit of 2000 nm and associated precipitation leads to a weak fluorescence signal that cannot be accurately detected, thus, data are not shown.

Despite their relative stability in terms of size, the fluorescence intensity of all particle types decreased significantly over time in all solvents at 37 °C, and the rate of decay was sensitive to the choice of solvent (Figure 2.3). Compared to other particles, PLA and PLLA particles retained the most fluorescence intensity over time, and compared to other buffers, they were the most stable in glucose/serum solution and in complete RMPI culture media. In terms of "color," the peak emission wavelength was stable for PLA and PLLA particles (Figures S2.2-S2.3), and was blue-shifted by no more than 15 nm for PCL and PCL-PLLA nanoparticles (Figures S2.4-S2.5).

We hypothesized that the observed decay in fluorescence intensity was due to either hydrolysis of the polyester or degradation of the boron dye. Therefore, we tested polymer and fluorophore stability of the PLA and PCL nanoparticles after storage in water for 5 days at 37 °C.

GPC elution peaks for PLA and PCL nanoparticles were nearly identical before and after incubation (Figure S2.7), and polydispersity index remained low (1.10), indicating little fluctuation in polymer molecular weight and therefore no evidence of polymer hydrolysis. Based on ^{1}H NMR spectra, the fluorophore in the PLA particle remained unchanged. In the PCL sample, resonances appeared at 6.76 ppm and 16.94 ppm after incubation, which are characteristic of the ArC(O)C***H***=C(OH)Ar proton and associated enol proton ArC(O)CH=C(O***H***) in boron-free dbmPCL, respectively. These results indicate chemical and optical stability for BF_2dbmPLA, but hydrolysis of BF_2 from the dbm binding site of PCL. In the latter case, dye hydrolysis and the resulting reduction in dye concentration is expected to result in a blue-shifted emission, consistent with our experimental results for the PCL nanoparticle.[13,23] In summary, the physical and optical data suggested that nanoparticle stability in solution varies with the polymer chain and surrounding media. While it is not clear to what extent these results will predict the stability once internalized by a cell, we note that for short-term (hours) cellular imaging, boron nanoparticles have been widely and successfully used in many contexts. Longer-term stability in solution may be possible with additional polymer engineering.

2.2.4 Nanoparticle Labelling of Primary Immune Cells

With a good understanding of the particle chemistry and stability in solution, we next quantified the uptake of the nanoparticles by live cells. Biological testing was conducted by Maura Belanger in the Pompano Lab. We excluded the racemic PLA particles from these studies, as they offered surface chemistry similar to PLLA but were less physically stable in solution. Primary murine splenocytes were incubated with each remaining type of nanoparticle, washed, and analyzed by flow cytometry (405 nm laser) immediately (day 0) or after 24 hours of culture (day 1). For comparison, cells were labelled with Cell Tracker Blue (CTB), a commercially available,

coumarin-derived, small molecule reagent that diffuses passively into the cell and binds covalently with thiol groups in the cytoplasm. Mixed splenocytes incubated with CTB were labelled with high efficiency, while a lower percentage of cells incubated with nanoparticles were labelled, indicating a more selective labelling mechanism (Figure 2.4a). PCL and PCL-PLLA nanoparticles each labelled ~ 50% of the mixed splenocyte culture, while PLLA nanoparticles labelled only 25% on average. Cellular phenotyping showed that the nanoparticles labelled CD11c-positive and B220-positive cells more efficiently than CD3-positive T cells (Figure 2.4b, Figure S2.8). This result suggests that the nanoparticles may label the cells through an active uptake mechanism, as both B cells and CD11c+ cells can act as antigen presenting cells and are more endocytic than T cells.[24] Indeed, the increased uptake of the hydrophobic PCL-containing particles compared to PLLA particles is consistent with improved internalization of more hydrophobic polymers.[25] PEGylated nanoparticles (PLLA-PEG) labelled very few cells, consistent with PEG preventing binding and cellular internalization of nanoparticles.[26] Future work will explore the active uptake mechanism as a possible point of control; enabling the targeting of nanoparticles to different cellular subsets.

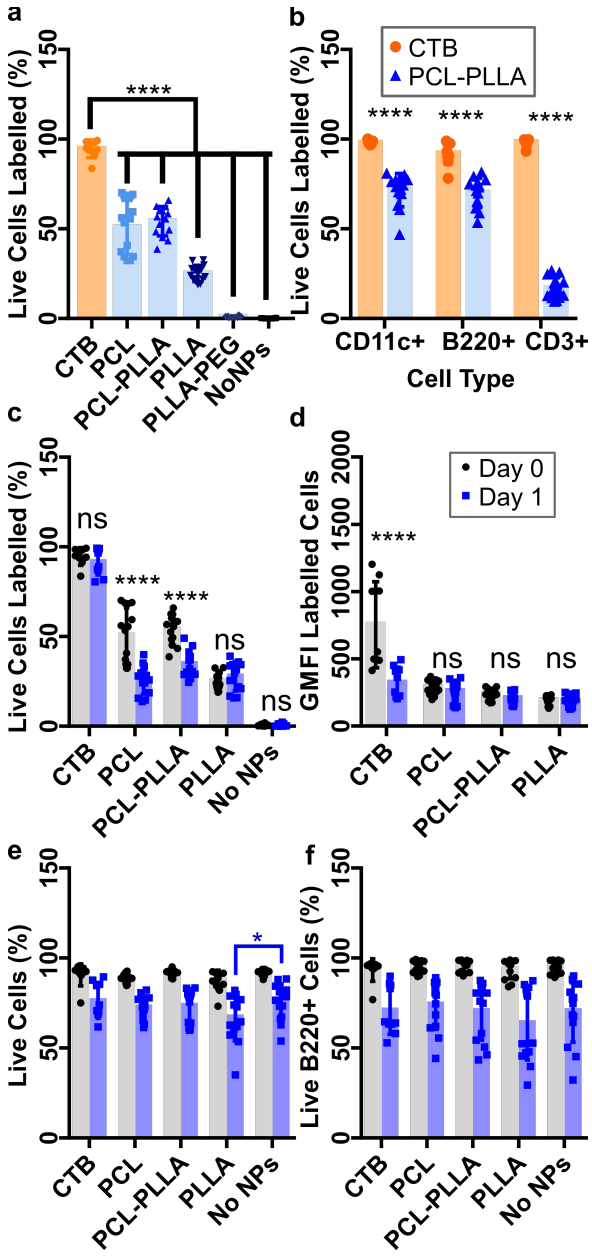

Figure 2. 4. Choosing a polymer formula for labelling primary immune cells. (a) Mixed primary splenocytes were labelled with Cell Tracker Blue (CTB), boron-based polymer nanoparticles, or no label. Uptake was measured immediately by flow cytometry. One-way ANOVA with comparisons of each group to CTB control. (b) Uptake of PCL-PLLA by cell type as determined by flow cytometry. More phagocytic cell types were more readily labelled by nanoparticles. (c,d) Stability of cellular labelling in mixed splenocytes after overnight culture as measured by flow cytometry both in terms of fraction of cells labelled (c) and intensity (d). (e,f) Viability of labelled and unlabeled cells in mixed splenocytes (e) and isolated B cells (f) as determined by flow cytometry after overnight culture. Viability is defined as 7-AAD negative. Two-way ANOVA with multiple comparisons. Each dot indicates one biological replicate. **** $p<0.0001$, *$p=0.0148$, ns denotes $p > 0.05$

Next, we tested the stability of cellular labelling. The fluorescence excitation and emission spectra immediately after cellular uptake (i.e. after 30 min incubation) were comparable to nanoparticles in solution (Figure S2.9). Labelled cells were also monitored after 24 hours. Cell Tracker Blue, like other cytoplasmic dyes, often suffers from a significant decrease in fluorescence intensity after the first 24 hours as unbound dye diffuses out of the cell. Indeed, we observed that the average CTB intensity per cell dropped by two-fold overnight, while there was no decrease in the percentage of CTB-labelled cells (Figure 2.4c/d). Interestingly the nanoparticle labelled cells showed an opposite effect. The percentage of cells that were labelled with nanoparticles decreased to 75%, on average, of its initial value after overnight culture, while the mean intensity per labelled cell did not drop significantly. These data suggest that the nanoparticles may be exported by a fraction of the cells. The relative stability of nanoparticle intensity per cell during this time frame compared to CTB labelled populations may be a point of control when transitioning this technology for long-term tracking.

Finally, we addressed whether labelling with nanoparticles affected cellular viability. Average viability in mixed splenocytes was unchanged by labelling with nanoparticles or CTB, except for a 20% reduction in viability of PLLA-labelled splenocytes after 24 hours of culture (Figure 2.4e). Thus, the nanoparticle-labelling process is compatible with maintaining high viability in primary splenocyte cultures. Based on these data, we selected the PCL-PLLA co-block polymer nanoparticles for further testing, based on its stability in solution, high initial labelling efficiency of the cell types of interest, and cytocompatibility.

2.2.5 Nanoparticle Labelling Does Not Affect Immune Cell Function

Having demonstrated that splenocyte viability was not affected by nanoparticle labelling, it was essential to determine whether labelling affected relevant cellular functions. Given their

prominent role in adaptive immunity, high frequency in the splenocyte culture, and high rate of staining, we focused on the effect of labelling on B cells in particular. B cells act as "antibody factories," and upon stimulation proliferate to begin the process of producing the most effective antibody against the pathogen, generating a strong adaptive response. We have shown that labelling with nanoparticles did not affect the viability of B cells in a mixed splenocyte culture (Figure 2.4f) and so to test the response to stimulation, we used the small molecule R848, which acts through Toll-like receptor 7 (TLR7) and results in proliferation, antibody production, and up-regulation of surface activation markers such as CD40 and CD80.66 In preliminary tests, R848 elicited a stronger response in unlabeled B cells than other common stimuli at matched doses (Figure S2.10).

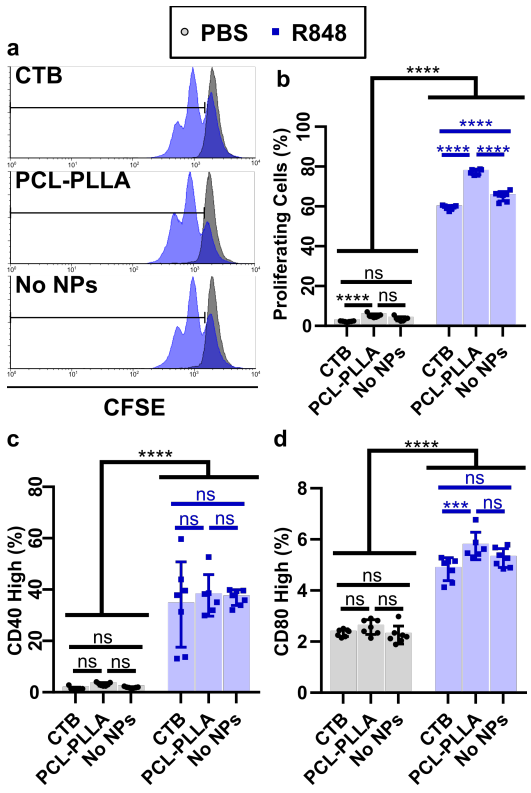

Figure 2. 5. Labelling of primary splenocyte B cells did not affect response to activation. (a) Representative histograms of CFSE intensity as measured by flow cytometry. Proliferation was measured as the percentage of cells with reduced CFSE intensity compared to unstimulated cells. (b) Quantification of proliferated cells. Stimulation with R848 resulted in increased proliferation

in all labelling schemes. (c) Percentage of live CD40 high cells. (d) Percentage of live CD80 high cells. Stimulation with R848 resulted in higher activation marker percentages in both cases. Two-way ANOVA with multiple comparisons. **** $p<0.0001$, *** $p=0.0003$, ns denotes $p>0.05$.

Purified B cell populations were labelled with either CTB or the PCL-PLLA nanoparticle and stimulated with R848. Proliferation was tracked by CFSE staining, the brightness of which is reduced with each cycle of cellular proliferation. In the absence of R848 stimulation, nanoparticle labelling did not induce B cell proliferation (Figure 2.5a-b) or activation marker expression (Figure 2.5c-d, Figure S2.11), indicating that the particles did not activate the cells on their own. After 48-hr R848 treatment, neither the Cell Tracker Blue nor the nanoparticles suppressed the proliferation and upregulation of activation markers on purified B cells (Figure 2.5). B cells labelled with PCL-PLLA nanoparticles did proliferate at a higher frequency than the unlabeled cells, but did not exhibit an increase in activation marker expression, indicating that any synergy of the nanoparticle loading with R848 stimulation was modest. In separate experiments, the ability of CD3+ T cells to respond to a non-antigen-specific stimulation was also uncompromised by nanoparticle labelling (Figure S2.12). Overall these data show that the labelling of primary splenocytes with PCL-PLLA nanoparticles does not compromise immune function.

2.2.6 Nanoparticle Labelling is Intracellular and Bright

For cell tracking applications, labelling with the nanoparticles must be intracellular, as any extracellular particles or aggregates could easily be washed away during handling. Therefore, we determined the distribution of PCL-PLLA nanoparticles in or on labelled splenocytes via confocal microscopy (400 nm laser excitation). Cell membranes were marked with anti-CD45, a surface-bound pan-lymphocyte marker, to visually determine whether each cell was unlabeled, labelled in the cytoplasm, labelled extracellularly (outer surface of membrane), or labelled on the membrane itself (Figure 2.6a/b). This method of data collection leaves some ambiguity as to whether the

“membrane”-associated nanoparticles are in contact with the inner or outer leaflet of the cell membrane or penetrate entirely. As expected for a cytoplasmic dye, all CTB signal was detected within the bounds of the cell membrane. Nanoparticle labelling was either cytoplasmic or associated with the membrane, and none of the latter cells had signal from the nanoparticles protruding out into the surrounding media. Thus, the majority of the signal from the PCL-PLLA nanoparticles is cytoplasmic and is useful for potentially tracking cells. We noted in this experiment that the CTB-labelled cells appeared dimmer than the nanoparticle labelled cells. This difference in brightness is consistent with the poor overlap between CTB and the 400 nm excitation source (Figure S2.13), though it does contrast with results seen earlier by flow cytometry, likely due to the difference in sensitivity between detectors on the two instruments.

The original goal was to develop a very bright blue labelling system for fluorescence microscopy, as many blue dyes suffer from low quantum yields. Thus, we measured the fluorescence intensity of labelled cells when imaged by widefield microscopy under standard UV excitation (360/60 nm filter). The intensity of cells labelled with PCL-PLLA nanoparticles was 1.43-fold brighter than cells labelled with CTB. In fact, CTB-labelled cells were not significantly brighter than unlabeled cells under these imaging conditions (Figure 2.6c). In this experiment, we did note large aggregates of nanoparticles (arrow head in Figure 2.6d) outside of the cells, which were difficult to remove. We speculate that this aggregation arose from the experimental procedure, in which cells were resuspended in 1x PBS for dual-labelling with Cell Trace Far Red after labelling with the blue reagent; 1x PBS causes free nanoparticles to aggregate quickly. Further experimentation is needed to determine the best approach to minimize extracellular aggregate formation during cellular manipulation, for example by keeping cells in protein-rich media.

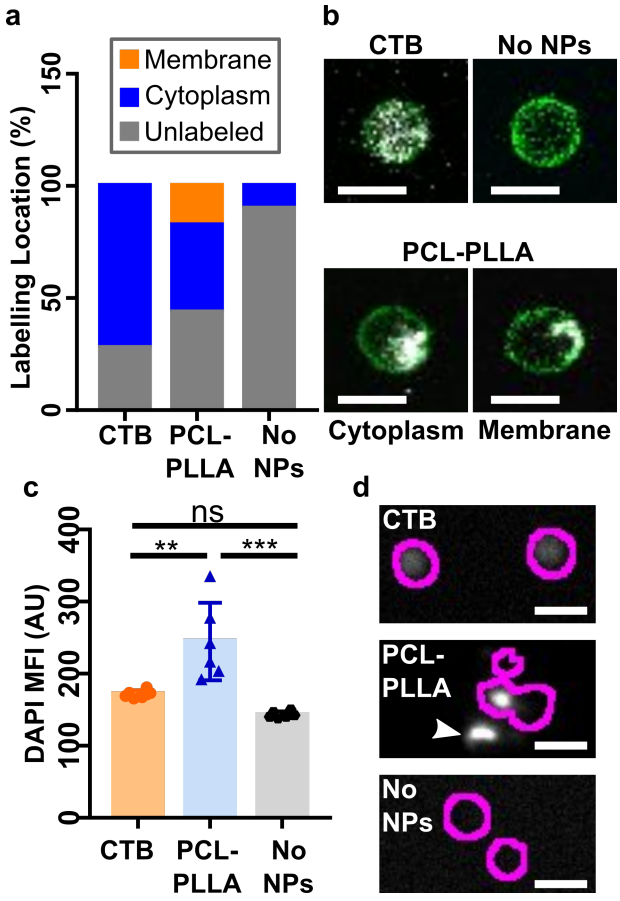

Figure 2. 6. Imaging PCL-PLLA labelled splenocytes. (a) Quantification of staining location as determined by confocal microscopy (400 nm excitation). (b) Representative images of labelling location. Cells were co-labelled with AF488 anti-CD45 antibody (green) to determine membrane location. Brightness and contrast differs between images to account for different excitation efficiencies. Scale bar is 10 µm. (c) Quantification of intensity using widefield microscopy (360 nm excitation) of labelled and unlabeled cells. PCL-PLLA labelled cells were on average 1.43 times brighter than CTB labelled cells. Each dot represents one sample averaged over 200+ cells. Ordinary one-way ANOVA with multiple comparisons. ** p=0.0029, *** p=0.0001, n.s. denotes p>0.05 (d) Representative images of cells labelled with CTB and PCL-PLLA nanoparticles with identical brightness and contrast settings. Cells were co-labelled with Cell Trace Far Red to locate cells efficiently (purple outlines). Large aggregates of PCL-PLLA particles were detected in this labelling scheme (arrowhead). Scale bar is 10 µm.

2.2.7 Nanoparticle Labelled Cells are Brightly Visible Against Tissue Autofluorescence

When working with typical blue fluorophores, their low fluorescence intensity is especially challenging to detect against tissue, a complex matrix that exhibits high background autofluorescence We hypothesized that the bright-blue fluorescent nanoparticles would not suffer

from this limitation. We tested the ability to detect nanoparticle-labelled cells embedded in living tissue with widefield microscopy, by labelling purified B cells and overlaying them onto live slices of murine lymph node as a model system.[27] As in the in vitro imaging above, the PCL-PLLA nanoparticle labelled cells were significantly brighter than both unlabeled and CTB labelled cells (Figure 2.7a) and easily detectable against the autofluorescence of the tissue.

The nanoparticles allowed us to capture bright signal within the blue channel of the widefield fluorescence microscope (360/60 nm excitation), freeing the remaining three channels for additional fluorophores to monitor multiple cell populations and tissue structures. As a proof-of-principle, we labelled purified B cells with the PCL-PLLA nanoparticles, labelled purified T cells with a rhodamine-based cytoplasmic dye (NHS-rhodamine), and overlaid these cells on a slice of lymph node tissue that was live immunostained for B220 (B cell zones) and Lyve-1 (lymphatic vessels) (Figure 2.7b-d). With this multi-color staining approach, we could visualize individual B cell follicles and the mixture of B cells (green) and T cells (blue) on the tissue. The fluorescent puncta from nanoparticle-labelled cells were smaller than the diameter of the cytoplasmic-labelled cells, since the particles do not fill the entire cytoplasm. Interestingly we also observed a collection of small signals in the nanoparticle channel that aligned with the lymphatic staining (Figure 2.7d, dashed oval). We speculate that this signal comes from free nanoparticles or aggregates coming into contact with the endocytic cells that line the lymphatic vessels in the lymph node.[28] This limitation should be taken into consideration when translating this technology in the future; it could also be taken advantage of to label endocytic cells in live tissue slices. Overall, we are able to easily visualize all four fluorophores simultaneously by widefield microscopy, using a set of four standard fluorescence filter sets.

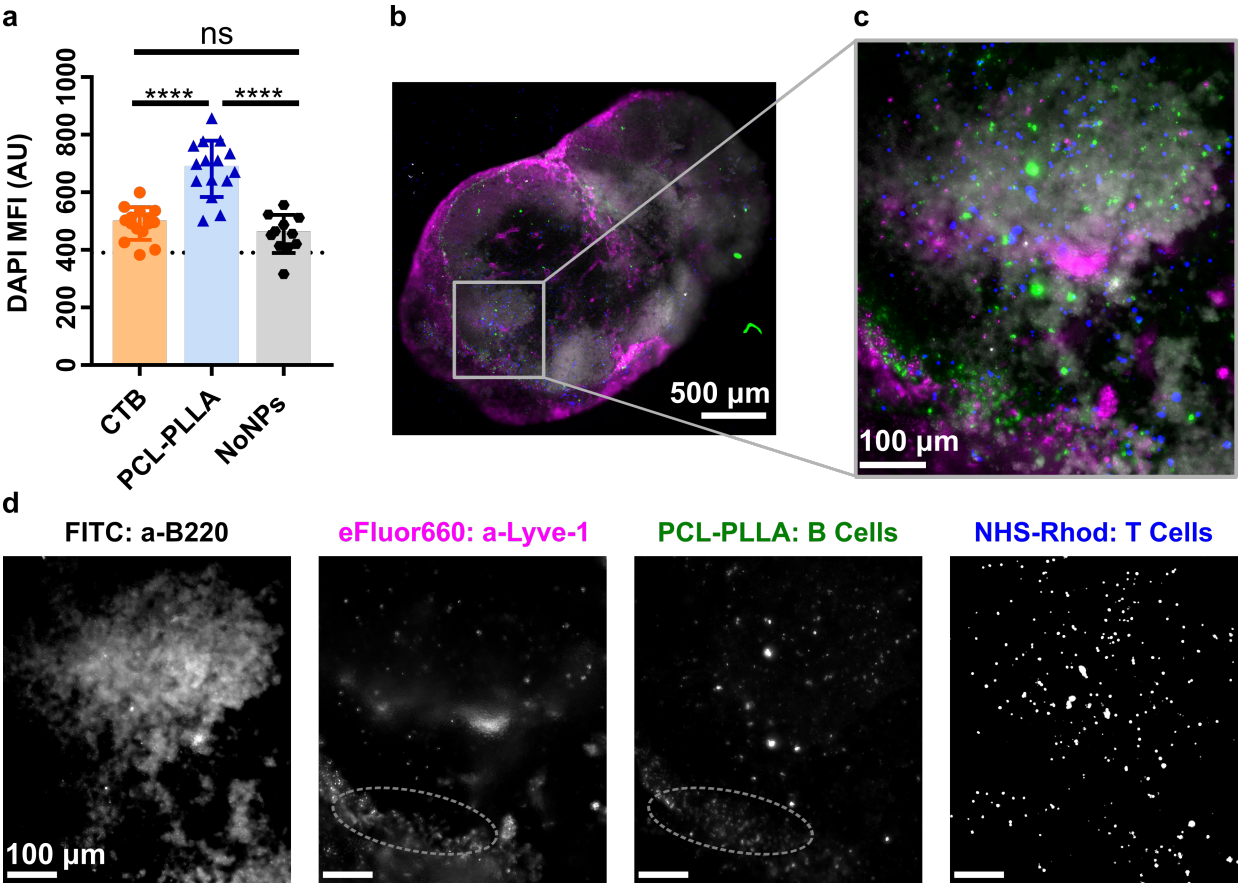

Figure 2. 7. Imaging PCL-PLLA labelled cells in tissue. (a) Quantification of labelled cells against tissue background. Nanoparticle labelled cells were significantly brighter after background subtraction compared to both CTB and unlabeled cells. Dotted line represents the average intensity of tissue autofluorescence in the DAPI filter. Two-way ANOVA with multiple comparisons. **** $p<0.0001$, ns $p>0.05$. (b) Image of representative stained tissue slice (3x mag). The live tissue was immunostained with FITC anti-B220 (white), and eFluor660 anti-Lyve-1 (false-colored pink) to show B cell follicles and lymphatics. (c) View of a single B cell follicle within the tissue slice (10x mag). Here we can visualize overlaid B cells labelled with PCL-PLLA nanoparticles (false-colored green) and T cells labelled with NHS-Rhodamine (false-colored blue). (d) Individual channel data from (c). Some nanoparticle aggregates align well with the Lyve-1 signal (dashed ovals).

2.2.8 Conclusion

This work described the fabrication and the characterization of a family of five bright-blue fluorescent boron-based polymeric nanoparticles. The nanoparticles exhibited high excitation and emission efficiency at wavelengths that match well with a variety of traditional sources for microscopy and flow cytometry, including a 405 nm laser, 395 nm LED and 360/60 nm excitation

filter. Nanoparticle stability at 37 °C was best maintained in supplemented RPMI media and an isotonic glucose solution without saline. Primary splenocytes, particularly the phagocytic cell types, were well labelled by these particles and remained brightly fluorescent overnight with no detectable impact on viability or ability to respond to stimulation. PCL-PLLA co-block polymer-based nanoparticles had the highest labelling efficiency and cellular retention over time. Nanoparticle labelling was cytoplasmic and is significantly brighter than cells labelled with Cell Tracker Blue, a commercially available cytoplasmic blue dye, when imaged by both confocal and widefield microscopy. Cells labelled with PCL-PLLA were easily distinguished against tissue autofluorescence, which enabled straightforward four-color imaging. This is the first demonstration of a materials-based blue fluorescent labelling reagent for cell tracking in the context of tissue autofluorescence. In the future, we will use this approach to image B and T cell interactions within ex vivo lymph node samples and map where these interactions occur. Broadly, these bright blue fluorescent nanoparticles expand the toolbox for cellular labelling and tracking in multi-color imaging experiments and may find many applications in a variety of tissues. Potential future improvements include varying the surface chemistry of the nanoparticles to enhance uptake by non-phagocytic cells, and adding functional groups such as succinimidyl esters or maleimides to increase dye retention within the cells.

2.3 Experimental Sections

2.3.1 Materials

3,6-Dimethyl-1,4-dioxane-2,5-dione ($_{D,L}$-lactide, Aldrich) was recrystallized twice from ethyl acetate and stored under nitrogen. Polyethylene glycol (PEG, Sigma Aldrich, MW = 2000 Da) was dried via azeotropic distillation from toluene according to a reported protocol.[29] The lactone, ε-caprolactone, was dried over CaH_2 and distilled under reduced pressure.[30] THF used for

Mitsunobu coupling reactions was dried (2 ×) over 3 Å molecular sieves activated at 300 °C.[31] All other chemicals were reagent grade from Sigma Aldrich and were used without further purification.

2.3.2 Methods

^{1}H NMR spectra were recorded on a Varian VMRS/600 (600 MHz) instrument in $CDCl_3$ unless otherwise indicated. ^{1}H NMR resonance was referenced to the residual protiochloroform signal at 7.260 ppm. Coupling constants are given in hertz. Polymer molecular weights (MW) and polydispersity indices (Đ) were determined by gel permeation chromatography (GPC) (THF, 25 °C, 1.0 mL / min) using multi-angle laser light scattering (MALLS) (λ = 658 nm, 25 °C) and refractive index (RI) (λ = 658 nm, 25 °C) detection. Polymer Laboratories 5 μm mixed-C columns (guard column plus two columns) along with Wyatt Technology (Optilab T-rEX interferometric refractometer, miniDAWN TREOS multi-angle static light scattering (MALS) detector, ASTRA 6.0 software) and Agilent Technologies instrumentation (series 1260 HPLC with diode array (DAD) detector, ChemStation) were used in GPC analysis. The incremental refractive index (*dn*/*dc*) was calculated by a single-injection method assuming 100% mass recovery from the columns. UV-vis spectra were recorded on a Hewlett-Packard 8452A diode-array spectrophotometer.

2.3.3 Synthesis

BF_2dbmPLA (**1**). The polymer was synthesized as previously described.[13] A representative procedure and characterization data are provided. A dry Kontes flask was charged with BF_2dbmOCH_2CH_2OH (28.4 mg, 0.085 mmol) and $_{D, L}$-lactide (1.25 g, 8.6 mmol) under nitrogen. The flask was sealed and entirely submerged into an oil bath at 130 °C to create a homogeneous melt. Under a positive flow of nitrogen, a stock solution of $Sn(Oct)_2$ (0.69 mg, 0.0017 mmol) in hexanes was added into the reaction mixture via syringe. The reaction was heated until a viscous mixture resulted (5 h). The reaction mixture was cooled to room temperature, dissolved in a

minimal amount of CH_2Cl_2, and precipitated by dropwise addition into cold MeOH (-20 °C, 50 mL). The polymer was collected by centrifuge, the supernatant was discarded, and the solid residue was reprecipitated from CH_2Cl_2/MeOH (-20 °C, 50 mL). The resulting solid was then precipitated from CH_2Cl_2/hexanes, and the residue was dried in vacuo to yield a yellow semicrystalline solid: 810 mg (76 %, corrected for monomer conversion). M_n (GPC/MALS) = 12 300 Da, Đ = 1.06. M_n (^{1}H NMR) = 15 200Da. ^{1}H NMR: (600 MHz, $CDCl_3$) δ 8.14 (q, J = 6, 4H, 2′, 6′-Ph-*H*, 2″, 6″-Ph-*H*), 7.67 (t, J = 6, 1H, 4′-Ph-*H*), 7.55 (t, J = 6, 2H, 3′, 5′-Ph-*H*), 7.07 (s, 1H, COC*H*CO), 7.02 (d, J = 6, 2H, 3″, 5″-Ph-*H*), 5.12-5.22 (m, broad, 206H, PLA-C*H*), 4.52 (d, J = 12, 2H, CH_2CH$_2$OAr), 4.33 (t, J = 6, 2H, CH$_2$CH_2OAr), 1.52-1.58 (m, broad, 655H, PLA-CH_3).

BF_2dbmPLLA (**2**). The polymer was synthesized as previously described for **1**, but $_L$-lactide was used as the monomer in place of $_{D, L}$-lactide to yield an off-white semicrystalline solid: 460 mg (65 %). M_n (GPC/MALS) = 12 200 Da, Đ = 1.24. ^{1}H NMR: (600 MHz, $CDCl_3$) δ 8.14 (q, J = 6, 4H, 2′, 6′-Ph-*H*, 2″, 6″-Ph-*H*), 7.67 (t, J = 6, 1H, 4′-Ph-*H*), 7.55 (t, J = 6, 2H, 3′, 5′-Ph-*H*), 7.10 (s, 1H, COC*H*CO), 7.02 (d, J = 12, 2H, 3″, 5″-Ph-*H*), 5.15 (q, J = 6, 132H, PLLA-C*H*), 4.53 (t, J = 6, 2H, CH_2CH$_2$OAr), 4.34 (t, J = 6, 2H, CH$_2$CH_2OAr), 1.45-1.68 (m, broad, 467H, PLLA-CH_3).

BF_2dbmPCL (**3**). The polymer was synthesized as previously described for **1**,[32] but ε-caprolactone was used as monomer in place of $_{D, L}$-lactide to yield a yellow solid: 512 mg (83 %). M_n (GPC/MALS) = 6 900 Da, Đ = 1.06. ^{1}H NMR: (600 MHz, $CDCl_3$) δ 8.14 (q, J = 6, 4H, 2′, 6′-Ph-*H*, 2″, 6″-Ph-*H*), 7.67 (t, J = 6, 1H, 4′-Ph-*H*), 7.54 (t, J = 6, 2H, 3′, 5′-Ph-*H*), 7.11 (s, 1H, COC*H*CO), 7.04 (d, J = 6, 2H, 3″, 5″-Ph-*H*), 4.47 (t, J = 6, 2H, CH_2CH$_2$OAr), 4.29 (t, J = 6, 2H, CH$_2$CH_2OAr), 4.04 (t, J = 6, 178H, RCOOCH_2), 3.66 (s, 1H, RO*H*), 2.29 (t, J = 6, 177H, CH_2COOR), 1.60-1.66 (m, broad, 360H, CH_2), 1.34-1.39 (m, broad, 186H, CH_2).

BF_2dbmPCL-PLLA (**4**). The PCL-PLLA copolymer was synthesized as previously described to yield a yellow solid: 344 mg (73 %).[16] M_n (GPC/MALS) = 7 700, Đ = 1.17. ^{1}H NMR: (600 MHz, $CDCl_3$) δ 8.14 (q, J = 6, 4H, 2′, 6′-Ph-*H*, 2″, 6″-Ph-*H*), 7.65 (t, J = 6, 1H, 4′-Ph-*H*), 7.53 (t, J = 6, 2H, 3′, 5′-Ph-*H*), 7.10 (s, 1H, COC*H*CO), 7.00 (d, J = 12, 2H, 3″, 5″-Ph-*H*), 5.16 (q, J = 6, 88H, PLLA-C*H*), 4.47 (t, J = 6, 2H, CH_2CH$_2$OAr), 4.29 (t, J = 6, 2H, CH$_2$CH_2OAr), 4.04 (t, J = 6, 169H, RCOOCH_2), 2.29 (t, J = 6, 168H, CH_2COOR), 1.60-1.67 (m, broad, 347H, CH_2), 1.35-1.38 (m, broad, 177H, CH_2).

BF_2dbmPLLA-PEG (**5**). The BF_2dbmOH dye was coupled to the PLLA-PEG block copolymer via a Mitsunobu reaction with diisopropyl azodicarboxylate (DIAD) as the activating reagent.[17] In a dry round bottom flask, PEG-PLLA-OH (M_n = 10 200 Da, 455 mg, 0.0445 mmol), BF_2dbmOH (26 mg, 0.089 mmol) and triphenyl phosphine (PPh_3, 54 mg, 0.178 mmol) were dissolved in anhydrous THF (60 mL) under nitrogen. The reaction mixture was chilled to -10 °C (acetone/ice bath) for 30 min before the DIAD reagent was added via syringe (40 μL, 0.178 mmol). The flask was removed from the chilled bath, and allowed to warm to room temperature. After stirring for 3 d, the THF was concentrated via rotary evaporation. Crude polymer was dissolved in a minimal amount of CH_2Cl_2, precipitated into cold MeOH (-20 °C, 2 × 30 mL), filtered, and washed with cold MeOH (-20 °C). The resulting residue was dried *in vacuo* to yield a yellow fluffy solid: 336 mg (73 %). M_n (GPC/MALS) = 10 500, Đ = 1.05. ^{1}H NMR: (600 MHz, $CDCl_3$) δ 8.13 (t, J = 6, 4H, 2′, 6′-Ph-*H*, 2″, 6″-Ph-*H*), 7.66 (t, J = 6, 1H, 4′-Ph-*H*), 7.54 (t, J = 6, 2H, 3′, 5′-Ph-*H*), 7.10 (s, 1H, COC*H*CO), 7.04 (d, J = 12, 2H, 3″, 5″-Ph-*H*), 5.15 (q, J = 6, 178H, PLLA-*H*), 3.63 (s, broad, 178H, PEG-OC$_2H_4$-O), 3.36 (s, 3H, PEG-OCH_3), 1.57 (m, broad, 541H, PLLA-CH_3).

2.3.4 Luminescence Measurements

Steady-state fluorescence spectra for the boron dye initiator, polymer and nanoparticle suspensions were recorded on a Horiba Fluorolog-3 Model FL3-22 spectrofluorometer (double-grating excitation and double-grating emission monochromator) after excitation. Optically dilute aqueous solutions of the nanoparticles, with absorbance <0.1 au, were prepared in 1 cm path length quartz cuvettes. Fluorescence spectra were obtained under ambient conditions (i.e., air, ~21% oxygen in volume).

2.3.5 Nanoparticle Fabrication and Characterization

Nanoparticles were fabricated as previously reported.[33] The polymer (~3.0 mg) was dissolved in DMF (3 mL), then the dye solution was added dropwise to rapidly stirred DI water (27 mL). The homogeneous mixture was stirred for 30 min, then the nanoparticle suspension was transferred into dialysis tubing (Specra/Pro, 12-14 kDa MWCO, Fisher Scientific) followed by dialysis against water for 24 hours. Nanoparticle size and polydispersity were analyzed by dynamic light scattering (DLS, Wyatt, DynaPro). Zeta potentials were determined by Zetasizer Nano Z (Malvern instruments, UK) and data were analyzed using DTS Nano software. UV-Vis absorbance was recorded by diluting ~1 mg/mL stock nanoparticle suspensions to 50 μg/mL in DI water. The extinction coefficient was estimated based on the Beer-Lambert law.

2.3.6 Nanoparticle Stability

The stock suspensions of nanoparticles (1 mg/mL) were serially diluted (200, 100, 50, 20, 10 μg/mL) with DI water, PBS, water/glucose/serum, and supplemented RPMI. Each sample (100 μL) was injected into a 96-well microtiter plate. Mineral oil was added on the top of each well via syringe to form a thin layer to prevent evaporation. The plate was put into the DLS instrument, protected from light, set to 37 °C and the sizes and polydispersities of the nanoparticles were recorded every 12 h for one week. Nanoparticle aggregates larger than 2000 nm exceed the DLS

detection limit. Separately, samples were incubated at 37 °C for five days to obtain daily photographs, as well as the emission spectra, to capture evidence of aggregation and fluorescence changes. GPC was used to monitor the polymer molecular weights (i.e. polymer stability) before and after incubation for specified times. To prepare samples for GPC analysis, nanoparticle aliquots in water were freeze-dried then dissolved in THF for injection into the GPC instrument. The degradation of boron dyes and hydrolysis of polyester were also analyzed by ^{1}H NMR spectroscopy in $CDCl_3$.

2.3.7 Cell Culture

All animal work was approved by the Animal Care and Use Committee of the University of Virginia under protocol #4042, and was conducted in compliance with guidelines from the University of Virginia Animal Care and Use Committee and the Office of Laboratory Animal Welfare at the National Institutes of Health (United States). Mice were housed in a vivarium and given food and water *ab libitium*. Spleens, and lymph nodes where appropriate, were collected from male and female C57Bl/6 mice aged 6-10 weeks (Jackson Laboratories, USA) after isoflurane anesthesia and cervical dislocation. To isolate splenocytes, the spleen was processed through a 70-µm pore size nylon filter (Fisher Scientific, USA) and rinsed with sterile 1x phosphate buffer saline (PBS) supplemented with 2% v/v fetal bovine serum (FBS, VWR, USA). Red blood cells were lysed and the cell suspension was filtered through a fresh 70-µm filter. Cell density was determined through trypan blue exclusion. Where noted, B cells were isolated from bulk splenocytes by using a B cell enrichment kit (StemCell Technologies, USA) based on negative magnetic selection, according to manufacturer instructions. For all overnight cultures, cells were cultured at a concentration of $1x10^6$ cells/mL in "complete RPMI;" RPMI (Lonza, 16-167F) supplemented with 10 % FBS (VWR, Seradigm USDA approved, 89510-186) 1x L-

glutamine (Gibco Life Technologies, 25030-081), 50 U/mL Pen/Strep (Gibco), 50 μM beta-mercaptoethanol (Gibco, 21985-023), 1 mM sodium pyruvate (Hyclone, GE USA), 1x non-essential amino acids (Hyclone, SH30598.01), and 20 mM HEPES (VWR, 97064-362) with 120 ng/mL IL-2 (Peprotech, USA).

2.3.8 Cell Labelling

To minimize nanoparticle aggregation, cellular labelling with nanoparticles was performed in an isotonic glucose solution without saline. Splenocytes were resuspended at $10x10^6$ cells/mL in a solution of 5% w/v D-glucose and 2% v/v FBS in ultra-pure water (water-glucose-serum solution, or 1x WGS; components from Thermo Fisher). A staining solution was prepared by mixing 3 parts nanoparticle stock solution (1 mg/mL in water), 2 parts 10x WGS, and 5 parts water. The staining solution was mixed in equal volumes with the cell suspension. This resulted in a 1x WGS solution that contained cells at $5x10^6$ cells/mL with nanoparticles at 0.15 mg/mL. Cells were incubated, protected from light, at room temperature for 30 min, then washed and resuspended at $1x10^6$ cells/mL in supplemented RPMI.

To label with Cell Tracker™ Blue CMF_2HC (4-chloromethyl-6,8-difluoro-7-hydroxycoumarin, Invitrogen), cells were resuspended at $1x10^6$ cells/mL in 1x PBS in the presence of 10 μM Cell Tracker™ Blue (CTB). Cells were incubated, protected from light, at 37 °C for 30 min, then washed and resuspended at $1x10^6$ cells/mL in supplemented RPMI.

2.3.9 Flow Cytometry

Cells were resuspended at 0.5 $x10^6$ cells/mL in 10 μg/mL anti-CD16/32 blocking antibody and incubated at 4 °C for 20 minutes. Antibody cocktail was added, and the cells were incubated for a further 30 minutes at 4 °C. Cells were then washed and resuspended at 0.5 $x10^6$ cells/mL and mixed with 5 μg/mL 7-AAD (AAT Bioquest). To stain bulk splenocytes, the antibody cocktail

was comprised of antibodies for CD3, CD4, CD11c, and B220 in 1x PBS with 2% v/v FBS. Details on antibody reagents are provided in the Supplementary Methods. All flow cytometry data was collected on a Guava 12HT EasyCyte Cytometer (EMD Millipore, USA) using a 405 nm laser and 450/45 nm emission filter and analyzed using FCS Express 6.

2.3.10 B Cell Activation In Vitro

Isolated B cells were labeled with 5 μM CFSE (carboxyfluorescein diacetate succinimidyl ester, BD Biosciences) for 30 minutes at 37 °C, rinsed, and resuspended in supplemented RPMI media. B cells were phenotyped by flow cytometry as above, using anti-B220 (FITC). The cells were cultured at $1x10^6$ cells/mL for 48 hours with 0.2 μg/mL of IL-4 (Pepro Tech) and 10 μg/mL R848 (Invivogen) or with PBS control. Afterwards, the cells were removed from the plate and stained for flow cytometry as described above, using CD40 and CD80.

2.3.11 Ex Vivo Overlays

Murine lymph nodes were collected and sliced as previously reported.[34–36] Briefly, inguinal, axial and brachial lymph nodes were collected from male and female C57Bl/6 mice, embedded in 6% low melting point agarose (Lonza) and sliced 300-μm thick on a vibratome (Leica VT1000s, USA). Lymph node slices were immunostained with FITC anti-mouse B220 and Lyve-1 as previously reported.[27] CD3+ T cells were isolated by using a CD3 negative selection kit according to manufacturer instructions (StemCell Technologies, USA) from splenocytes sex-matched to the lymph node slices. T cells ($1x10^6$ cells/mL) in 1x PBS were labelled by incubating with NHS-Rhodamine (1 μg/mL, Thermo Fisher) for 30 minutes at 37 °C. B cells were isolated and labeled with CFSE as above, mixed with labelled T cells and concentrated to $10x10^6$ cells/mL. The cell mixture was then overlaid onto immunostained lymph node slices for 1 hour at 37 °C. To remove

excess cells, slices were incubated for at least 30 minutes in 1x PBS with gentle agitation at regular intervals.

2.3.12 Imaging

Confocal microscopy was performed on a Nikon A1Rsi confocal upright microscope, using a 400 nm laser and 450/50 nm GaAsP detector. Images were captured with a 40x/0.45NA Plan Apo NIR WD objective. Widefield microscopy was performed on a Zeiss AxioZoom upright macroscope, using a Zeiss PlanNeoFluar Z 1x / 0.25 NA FWD 56mm objective, Zeiss Axiocam 506 mono camera, and HXP 200 C illuminator with metal halide lamp (Zeiss Microscopy, Germany). Images were collected with Zeiss filter sets 49 (Ex: 365, Em: 445/50), 38 HE (Ex: 470/40, Em: 525/50), 43 HE (Ex: 550/25, Em: 605/70), and 50 (Ex: 640/30, Em: 690/50). Image analysis was completed using ImageJ software 1.48v.[37]

2.4 Acknowledgements

This work was published in *Biomaterials*.[5] I would like to thank Maura Belanger, Alexandra Ball, and Kristen Richey for performing biology experiments, Christopher DeRosa for his help in the synthesis, Prof. Pompano and Prof. Fraser for their guidance and assistance in manuscript preparation. I'm also gratefully acknowledge the generous donation of $_{D-}$ and $_{L-}$lactide monomers from Purac Corbion©, funding source from Society for Analytical Chemists of Pittsburgh (SACP) and the NanoSTAR Institute at the University of Virginia, National Institute of Allergy and Infectious Diseases under Award Number R01AI131723 and the National Cancer Institute under Award Number R01CA167250, and UVA Cancer Center (P30 CA44579), all through the National Institutes of Health.

2.5 References

(1) Parish, C. R. Fluorescent Dyes for Lymphocyte Migration and Proliferation Studies. *Immunol. Cell Biol.* **1999**, *77*, 499–508.

(2) Atale, N.; Gupta, S.; Yadav, U. C. S.; Rani, V. Cell-death assessment by fluorescent and nonfluorescent cytosolic and nuclear staining techniques. *J. Microsc.* **2014**, *255*, 7–19.

(3) Gonçalves, M. S. T. Optimized UV/Visible Fluorescent Markers. In *Advanced Fluorescence Reporters in Chemistry and Biology I: Fundamentals and Molecular Design*; Demchenko, A. P., Ed.; Springer Series on Fluorescence; Springer Berlin Heidelberg: Berlin, Heidelberg, 2010; pp 27–64.

(4) Xu, S.; Evans, R. E.; Liu, T.; Zhang, G.; Demas, J. N.; Trindle, C. O.; Fraser, C. L. Aromatic Difluoroboron β-Diketonate Complexes: Effects of π-Conjugation and Media on Optical Properties. *Inorg. Chem.* **2013**, *52*, 3597–3610.

(5) Belanger, M. C.; Zhuang, M.; Ball, A. G.; Richey, K. H.; DeRosa, C. A.; Fraser, C. L.; Pompano, R. R. Labelling Primary Immune Cells Using Bright Blue Fluorescent Nanoparticles. *Biomater. Sci.* **2020**, *8*, 1897–1909.

(6) Du, J.; Zhang, Y. S.; Hobson, D.; Hydbring, P. Nanoparticles for Immune System Targeting. *Drug Discov. Today* **2017**, *22*, 1295–1301.

(7) Zolnik, B. S.; González-Fernández, Á.; Sadrieh, N.; Dobrovolskaia, M. A. Nanoparticles and the Immune System. *Endocrinology* **2010**, *151*, 458–465.

(8) Jiang, W.; Kim, B. Y. S.; Rutka, J. T.; Chan, W. C. W. Nanoparticle-Mediated Cellular Response Is Size-Dependent. *Nat. Nanotechnol.* **2008**, *3*, 145–150.

(9) Reddy, S. T.; Rehor, A.; Schmoekel, H. G.; Hubbell, J. A.; Swartz, M. A. In Vivo Targeting of Dendritic Cells in Lymph Nodes with Poly(Propylene Sulfide) Nanoparticles. *J. Control. Release* **2006**, *112*, 26–34.

(10) Scholzen, A.; Minigo, G.; David, C.; Apostolopoulos, V.; Mottram, P. L. Pathogen Recognition and Development of Particulate Vaccines: Does Size Matter? *Methods* **2006**, *40*, 1–9.

(11) Foged, C.; Brodin, B.; Frokjaer, S.; Sundblad, A. Particle Size and Surface Charge Affect Particle Uptake by Human Dendritic Cells in an in Vitro Model. *Int. J. Pharm.* **2005**, *298*, 315–322.

(12) Woodard, L. N.; Grunlan, M. A. Hydrolytic Degradation and Erosion of Polyester Biomaterials. *ACS Macro Lett.* **2018**, *7*, 976–982.

(13) Zhang, G.; Kooi, S. E.; Demas, J. N.; Fraser, C. L. Emission Color Tuning with Polymer Molecular Weight for Difluoroboron Dibenzoylmethane-Polylactide. *Adv. Mater.* **2008**, *20*, 2099–2104.

(14) Zhang, G.; Chen, J.; Payne, S. J.; Kooi, S. E.; Demas, J. N.; Fraser, C. L. Multi-Emissive Difluoroboron Dibenzoylmethane Polylactide Exhibiting Intense Fluorescence and Oxygen-Sensitive Room-Temperature Phosphorescence. *J. Am. Chem. Soc.* **2007**, *129*, 8942–8943.

(15) Cammack, J. K.; Marder, S. R.; Kippelen, B. No Title. US patent/2005 0209478 A1, 2015.

(16) Zhang, G.; Fiore, G. L.; St. Clair, T. L.; Fraser, C. L. Difluoroboron Dibenzoylmethane PCL-PLA Block Copolymers: Matrix Effects on Room Temperature Phosphorescence. *Macromolecules* **2009**, *42*, 3162–3169.

(17) Thévenaz, D. C.; Monnier, C. A.; Balog, S.; Fiore, G. L. Luminescent Nanoparticles with Lanthanide-Containing Poly(Ethylene Glycol)–Poly(ε-Caprolactone) Block Copolymers. *Biomacromolecules* **2014**, *15*, 3994–4001.

(18) Petros, R. A.; DeSimone, J. M. Strategies in the Design of Nanoparticles for Therapeutic Applications. *Nat. Rev. Drug Discov.* **2010**, *9*, 615–627.

(19) Panyam, J.; Sahoo, S. K.; Prabha, S.; Bargar, T.; Labhasetwar, V. Fluorescence and Electron Microscopy Probes for Cellular and Tissue Uptake of Poly(d,l-Lactide-Co-Glycolide) Nanoparticles. *Int. J. Pharm.* **2003**, *262*, 1–11.

(20) Pfister, A.; Zhang, G.; Zareno, J.; Horwitz, A. F.; Fraser, C. L. Boron Polylactide Nanoparticles Exhibiting Fluorescence and Phosphorescence in Aqueous Medium. *ACS Nano* **2008**, *2*, 1252–1258.

(21) Proikakis, C. S.; Mamouzelos, N. J.; Tarantili, P. A.; Andreopoulos, A. G. Swelling and Hydrolytic Degradation of Poly(d,l-Lactic Acid) in Aqueous Solutions. *Polym. Degrad. Stab.* **2006**, *91*, 614–619.

(22) Horkay, F.; Tasaki, I.; Basser, P. J. Osmotic Swelling of Polyacrylate Hydrogels in Physiological Salt Solutions. *Biomacromolecules* **2000**, *1*, 84–90.

(23) Contreras, J.; Xie, J.; Chen, Y. J.; Pei, H.; Zhang, G.; Fraser, C. L.; Hamm-Alvarez, S. F. Intracellular Uptake and Trafficking of Difluoroboron Dibenzoylmethane-Polylactide Nanoparticles in HeLa Cells. *ACS Nano* **2010**, *4*, 2735–2747.

(24) Antigen-Presenting Cells. In *Immunology for Pharmacy*; Elsevier, 2012; pp 37–44.

(25) Sitia, L.; Ferrari, R.; Violatto, M. B.; Talamini, L.; Dragoni, L.; Colombo, C.; Colombo, L.; Lupi, M.; Ubezio, P.; D'Incalci, M.; et al. Fate of PLA and PCL-Based Polymeric Nanocarriers

in Cellular and Animal Models of Triple-Negative Breast Cancer. *Biomacromolecules* **2016**, *17*, 744–755.

(26) Jokerst, J. V; Lobovkina, T.; Zare, R. N.; Gambhir, S. S. Nanoparticle PEGylation for Imaging and Therapy. *Nanomedicine (Lond).* **2011**, *6*, 715–728.

(27) Groff, B. D.; Kinman, A. W. L.; Woodroof, J. F.; Pompano, R. R. Immunofluorescence Staining of Live Lymph Node Tissue Slices. *J. Immunol. Methods* **2019**, *464*, 119–125.

(28) Bellomo, A.; Gentek, R.; Bajénoff, M.; Baratin, M. Lymph Node Macrophages: Scavengers, Immune Sentinels and Trophic Effectors. *Cell. Immunol.* **2018**, *330*, 168–174.

(29) Kinard, L. A.; Kasper, F. K.; Mikos, A. G. Drying Poly(Ethylene Glycol) : Protocol Exchange. *Nat. Protoc.* **2012**, *7*, 1219–1227.

(30) Grijpma, D. W.; Pennings, A. J. Polymerization Temperature Effects on the Properties of L-Lactide and e-Caprolactone Copolymers. *Polym. Bull.* **1991**, *25*, 335–341.

(31) Williams, D. B. G.; Lawton, M. Drying of Organic Solvents: Quantitative Evaluation of the Efficiency of Several Desiccants. *J. Org. Chem.* **2010**, *75*, 8351–8354.

(32) Zhang, G.; St. Clair, T. L.; Fraser, C. L. Synthesis and Fluorescent Properties of Difluoroboron Dibenzoylmethane Polycaprolactone. *Macromolecules* **2009**, *42*, 3092–3097.

(33) Fessi, H.; Puisieux, F.; Devissaguet, J. P.; Ammoury, N.; Benita, S. Nanocapsule Formation by Interfacial Polymer Deposition Following Solvent Displacement. *Int. J. Pharm.* **1989**, *55*, R1–R4.

(34) Ross, A. E.; Pompano, R. R. Diffusion of Cytokines in Live Lymph Node Tissue Using Microfluidic Integrated Optical Imaging. *Anal. Chim. Acta* **2018**, *1000*, 205–213.

(35) Ross, A. E.; Belanger, M. C.; Woodroof, J. F.; Pompano, R. R. Spatially Resolved Microfluidic Stimulation of Lymphoid Tissue: Ex Vivo. *Analyst* **2017**, *142*, 649–659.

(36) Catterton, M. A.; Dunn, A. F.; Pompano, R. R. User-Defined Local Stimulation of Live Tissue through a Movable Microfluidic Port. *Lab Chip* **2018**, *18*, 2003–2012.

(37) Schneider, C. A.; Rasband, W. S.; Eliceiri, K. W. NIH Image to ImageJ: 25 Years of Image Analysis. *Nat. Methods* **2012**, *9*, 671–675.

Chapter 3: Multi-Color Difluoroboron β-Diketonate Dyes for Camera-Based Wound Oxygen Imaging

3.1 Introduction

In biological oxygen imaging, the development of portable, cost effective, and simple imaging instrumentation has always been an important goal. Traditionally, ratiometric oxygen sensing is conducted by measuring separate images of fluorescence and phosphorescence with appropriate emission filters. For resolved spatiotemporal ratiometry, capturing multiple images is not desired to produce reliable and fast readout. Simpler systems have been developed, using a red/green/blue (RGB) color camera to minimize data demands and offer fast acquisition and processing. Each color channel in an RGB camera holds information as light intensity. In ratiometric imaging, emission from the fluorescence standard and the phosphorescence sensor can be captured simultaneously in separate color channels.

Ratiometric oxygen sensors employing RGB imaging have been realized in many biomedicine contexts. For example, Moßhammer and coworkers prepared sensor films to image pH and O_2 simultaneously with minimal signal crosstalk using an RGB and near-infrared camera for soil/water applications.[1] This was achieved by combining a green fluorescent reference (Bu_3Coum) and an O_2-sensitive phosphor (Eu(HPhN)$_3$dpp) in a polystyrene (PS) film on a poly(ethylene terephthalate) (PET) support. Then, another pH-sensitive hydrogel layer consisting of OHButoxy-aza-BODIPY in polyurethane was deposited on top. The power of the RGB technique is the ability to match luminophore reference and sensor emissions with the channel quantum efficiencies of the camera. Moreover, it can be easily adapted to other imaging systems such as widefield and confocal microscopy with CCD or CMOS cameras, and accelerates the imaging acquisition time.

For efficient and accurate RGB ratiometric imaging, the standard and the sensor should have emissions well separated without overlap, and the emissions should be aligned with

corresponding camera channels. In addition, it is ideal for the standard and the sensor to be excited by the same excitation source. The ratio of fluorescence to phosphorescence should also be optimized. Ideally, phosphorescence is strong enough to detect oxygen level variations, and fluorescence is bright enough to be visualized over tissue background or autofluorescence. In our initial report of RGB camera imaging, a series of difluoroboron naphthyl phenyl β-diketonate-PLA materials (BF_2nbm(X)PLA; where X = H, Br, or I) were used to achieve ratiometric oxygen sensing in a murine wound model.[2] These dyes showed excellent control of oxygen sensitivity, large singlet-triplet energy gaps between the F and P emissions,[3] and tunable F/P intensity ratios *via* heavy-atom substitution.

To expand the BF_2bdks luminophore toolbox, investigation into new dye scaffolds is needed. Having a range of dyes will increase the versatility and capabilities of BF_2bdk oxygen sensors. In this report, we prepare a range of new BF_2bdk oxygen sensors for RGB-imaging applications. We designed six new dyes by substituting aromatic groups (phenyl, naphthyl, and thienyl) and methoxy donors (numbers and positions) to optimize the luminescence for peak separation and RGB channel alignment (Figure 3.1).[4–6] These derivatives were also equipped with an iodide to enhance intersystem crossing, and a C_{12} carbon chain to improve solubility in common organic solvents (e.g. EtOAc) for synthesis and processing. The optical properties of new dyes were studied in solution and in solid state. For demonstrating the oxygen capabilities, simple dye/polymer blends were applied on murine wound model, in combination with an RGB-camera imaging system. To optimize oxygen calibration, we established a MATLAB software to resolve fluorescence and phosphorescence emissions, and to evaluate the oxygen sensing ability of each dye/polymer blend. Previously, we used polylactide-based nanoparticles for wound imaging.[2] PLA nanoparticles can be readily up taken by cells, and it is possible that cellular uptake and NP

penetration into the wound bed protects the nanoparticles from ambient conditions.[7] Another possibility is that the hydrophobic nanoparticles precipitate when they come in contact by the wound media (a.k.a. blood), thus coating the wound surface. To better understand the mechanism of cover-free oxygen-sensing, we propose changing the nanoparticle formulation and testing both PLA and PLA-PEG nanoparticles. Having the PEGylated surface on the nanoparticles will hinder cellular uptake and possibly stabilize the nanoparticle suspension in the wound bed.[7,8] Changes in ratios and images will provide more information on the importance of the sensor formulation.

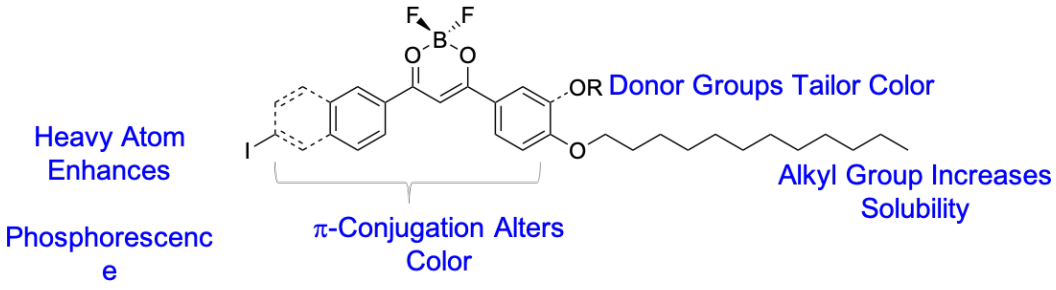

Figure 3. 1. Boron dye design for dual-emissive materials in PLA.

3.2 Results and Discussions

3.2.1 Synthesis

Dyes were prepared with various arenes (phenyl, naphthyl or thienyl) and alkoxy groups and positions as illustrated in Figure 3.2. The chemical structures are designed with several goals in mind: 1) to have the F and P align with the blue, green or red camera channels, 2) to spectrally isolate F and P emission, and 3) to optimize F and P as well-balanced, comparable intensities (not overly strong fluorescence or phosphorescence). We hypothesized that only subtle changes in the electronic structure of the dyes are necessary to optimize the emission colors for the RGB camera.[2] In previous reports, dramatic changes in structure resulted in extremely weak or undetectable P emission (e.g. anthracyl and dialkylamino substitution).[3,4] Also, the dinaphthoylmethane ligands

(dnm) were excluded because previous reports showed that the increased π–conjugation resulted in significant F and P overlap,[9] which is undesirable for RGB camera imaging.[10]

Though the exact method for achieving desirable optical properties is not yet known, some general principles may be applied. Compared to BF_2nbm(Br)PLA, P only needs to be blue-shifted ~20 nm into the green channel, or ~20 nm into the red channel. We hypothesize that an alkoxy donor can achieve this, without diminishing P. Phenyl units were selected to blue-shift the emission properties,[4] and thienyl units, for red-shifting emission.[6,11] Also, alkoxy substituents can play many roles in tuning emission color and intensity, such as larger Stokes shift and higher quantum yield.[12,13] Therefore, we focused on *meta-* and *para-* monosubstituted *and meta-* dialkoxy substituted derivatives. Compound **1** was included for comparison, because it has been studied previously by our group.[14–19]

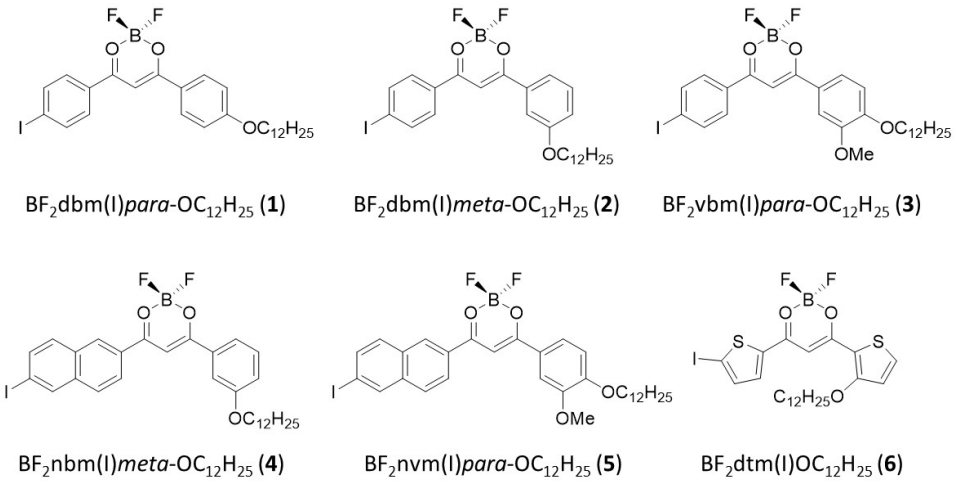

Figure 3. 2. Chemical structures of difluoroboron β-diketonate dyes.

All the derivatives in this study have iodide included on the ligand to enhance the rate of intersystem crossing (ISC). This serves two purposes for the oxygen sensing materials. First, the heavy atom increases the intensity of the P relative to the F for ratiometric imaging.[18] Second, it decreases the P lifetime, which in turn decreases the oxygen sensitivity of the dyes.[20] The longer

P lifetimes of dyes are quenched rapidly by oxygen and respond within a much narrower oxygen sensing range, often outside reasonable ranges for biological sensing. Previously we reported an iodide version of BF_2nbm(X)PLA (X = iodide) that can sense oxygen from 0-100%.[2] Although certain iodide-substituted materials suffer from poor solubility in common organic solvents (*e.g.* acetone), here this challenge is addressed by adding a dodecyloxy (-$OC_{12}H_{25}$) chain to facilitate the purification process and making dye/polymer blends rather than dye-polymer conjugates.

Scheme 3.1. Synthesis of BF_2dtm(I)$OC_{12}H_{25}$ (**6**).

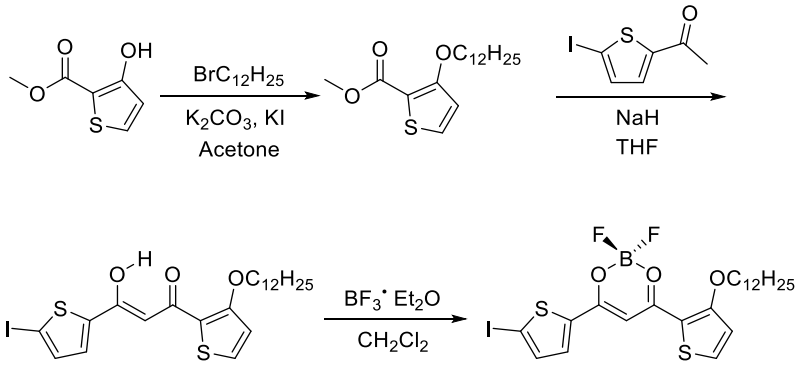

The BF_2bdk dyes **1-6** were prepared as previously described[15,21] Phenolic ketones and esters were alkylated via Williamson ether synthesis to generate dyes precursors with a hydrophobic solubilizing C12 unit. Alkylated ketones and esters were subjected to Claisen condensation with an iodide-substituted ketone or ester to form the diketonate ligand. Ligands were then coordinated to boron difluoride in the presence of boron trifluoride diethyl etherate to produce the boron dye products. Dyes **1-5** were prepared in moderate yields (20-80%). For the thienyl-substituted dye, BF_2dtm(I)$OC_{12}H_{25}$ (**6**) (Scheme 3.1) the ligand was purified via column chromatography to yield a brown oil, which showed poor stability in air. Thus, the crude ligand was carried on directly to boronation. The boron complex was purified via column chromatography (4:1 hexanes/EtOAc), followed by recrystallization in ethyl acetate/hexanes to yield a stable orange crystalline solid. Generally, these dual-emitting dyes are easy to prepare in

a few steps. Compared to iodinated boron dye initiators for lactide polymerizations,[2,9] these derivative are more soluble in common organic solvents (e.g. CH_2Cl_2, acetone, EtOAc).

3.2.2 Optical Properties in Solution

The dyes were first characterized in dilute CH_2Cl_2 solution (1.0×10^{-5} M) to evaluate differences based on molecular structure, without aggregation or matrix effects that occur in the solid-state (Table 3.1).[3,4,12,22,23] The influence of alkoxy substitution can be observed with the difluoroboron dibenzoylmethane (BF_2dbm) derivatives, **1**-**3**. The dye with C12 at the *para*-position (**1**) showed the highest extinction coefficient and the smallest Stokes shift of the series (ε = 63 000 M^{-1} cm^{-1}, $\Delta_{abs\text{-}F}$ = 28 600 cm^{-1}). When the alkoxy group is present at the *meta*-position (**2**), the extinction coefficient decreased and the fluorescence redshifted considerably, resulting in a larger Stokes shift (ε = 31 000 M^{-1} cm^{-1}, $\Delta_{abs\text{-}F}$ = 92 600 cm^{-1}). When both the *meta*- and *para*-positions are alkoxy substituted, the extinction coefficient increased slightly, and the absorption and fluorescence maxima red-shifted by about 20 nm compared to compound **2** (ε = 44 900 M^{-1} cm^{-1}, $\Delta_{abs\text{-}F}$ = 97 100 cm^{-1}). The para-substituted dyes showed shorter fluorescence lifetimes compared to the derivative with only a *meta*-substituted alkoxy (τ_F; **1** = 1.50 ns and **3** = 1.23 ns vs. **2** = 7.65 ns). For compound **2**, the low extinction coefficient, large Stokes shift and long fluorescence lifetime suggest greater intramolecular charge transfer (ICT) character.[4,24,25] A similar trend can be observed for the naphthyl-phenyl derivatives (nbm; **4** and **5**), however, the effects are less dramatic (**4**; ε = 46 300 M^{-1} cm^{-1}, $\Delta_{abs\text{-}F}$ = 60 nm, **5**; ε = 49 600 M^{-1} cm^{-1}, $\Delta_{abs\text{-}F}$ = 86 nm). It is likely that the naphthalene aromatic unit contributes more to the electronic properties compared to the phenyl, even if the alkoxy donors are present on the phenyl ring.[25] Nevertheless, dialkoxy substitution (**5**) red-shifted both absorption and emission compared to the single *meta*-alkoxy substituted derivative (**4**). Impressively, the dithienyl dye (**6)** showed strong 446 nm absorption (ε

= 69 600 M^{-1} cm^{-1}) in CH_2Cl_2, absorbing blue light, which is important for reducing the phototoxicity associated with UV excitation.[26,27]

Table 3. 1. Optical Properties of Boron Dyes in CH_2Cl_2

Sample	λ_{abs} [a] (nm)	ε [b] (M^{-1} cm^{-1})	λ_{em} [c] (nm)	τ_F [d] (ns)	Φ_F [e]
1[f]	409	63 000	444	1.50	0.67
2[g]	394	31 000	502	7.65	0.22
3	420	44 900	523	1.23	0.18
4	413	46 300	473	0.78	0.03
5	432	49 600	518	0.81	0.12
6	446	69 600	470	1.01	0.05

[a]Absorption maxima. [b]Extinction coefficients calculated at the absorption maxima. [c]Fluorescence emission maxima excited at 369 nm. [d]Fluorescence lifetime excited with a 369 nm light-emitting diode (LED) monitored at the emission maximum. All fluorescence lifetimes are fitted with single-exponential decay. [e]Relative quantum yield, versus anthracene in EtOH as a standard.[28] [f] Values reproduced from Morris et al.[15] [g] Values reproduced from Daly et al.[13]

3.2.3 Computational Study

The optical properties in solution were supplemented by DFT calculations of the dye molecules in the singlet ground state in CH_2Cl_2 solvent (B3LYP and 6-31+G(d)). According to previous reports involving BF_2bdks, two main features in the calculations can be indicative of strong P emission in the solid state. First, for strong P, the halide heavy atom (Br or I) must have sufficient electron density in participating orbitals to promote intersystem crossing.[3,25] Second, P is further enhanced via intramolecular charge transfer (ICT).[13,29] Balancing these electronic properties can facilitate the design of dual-emitting fluorophores.

Evaluation of the frontier molecular orbital diagrams of **1**-**6** provides important insights into material design. First, the molecular geometries were optimized to the lowest energy in the ground state, shown in Figure 3.3 and Tables S3.1-S3.6. All dyes showed planar geometries, typical for π–conjugated dyes. Then, the singlet absorption energy in the ground state geometry (S_0) was calculated. This is the transition from the highest occupied molecular orbitals (HOMO)

to the lowest unoccupied molecular orbitals (LUMO) to general the frontier molecular orbital diagrams (FMO), as shown in Figure 3.3.[4]

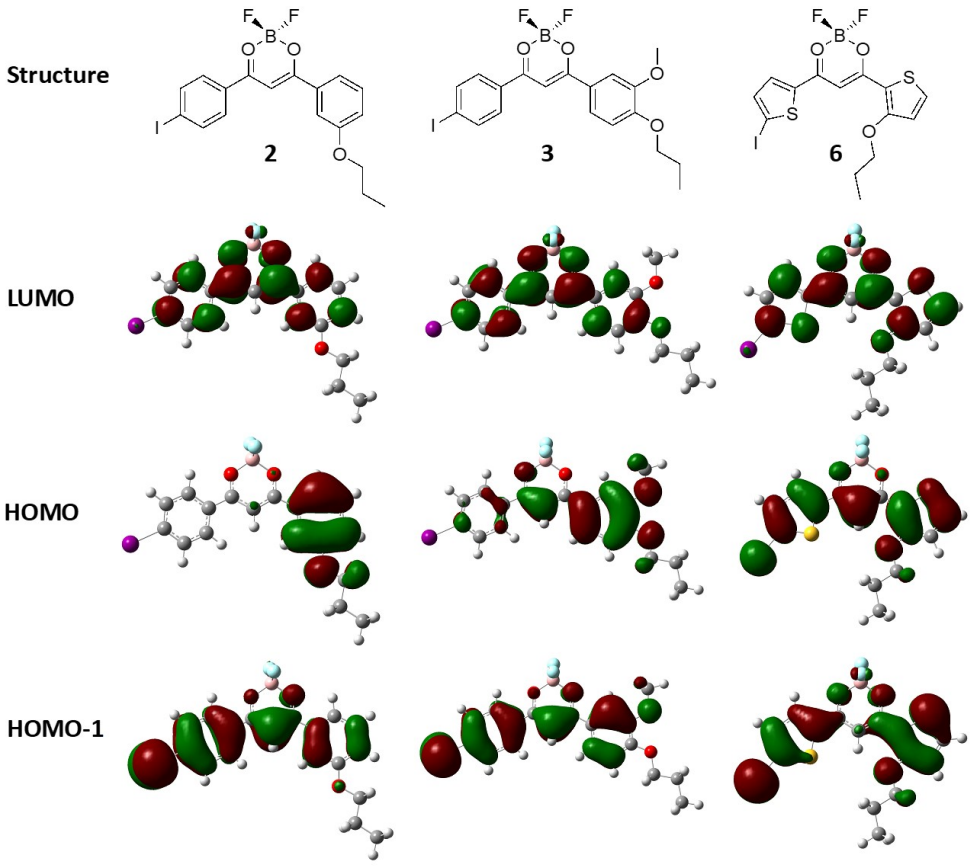

Figure 3. 3. Calculated Frontier Molecular Orbitals for Compounds **2**, **3**, and **6**. Note: For compound **6**, the geometry optimization shown was the only rotamer tested. Images for **2** were reproduced with permission from Daly et al.[13]

Two main types of absorption features can be qualitatively observed in the molecular orbital diagrams for compounds **1-6**, namely, a π–π* transition and a intramolecular charge transfer transition (ICT).[30] The π–π* transition is indicated by a delocalization of electrons in both the HOMO and the LUMO diagrams. In contrast, ICT-transitions typically have an electron-localized HOMO, where the molecule is electronically rich, and a π–delocalized LUMO. ICT and π–π* transitions in the molecules can be indicative of fluorescence and phosphorescence

properties in the solid state. Structural changes in the dyes, such as alkoxy number and placement, altered the localization of electrons in the dyes. However, the LUMO FMOs of all six compounds are similar, where electrons are evenly distributed along the ligand and the dioxaborine (OBO) (e.g. Figure 3.3: LUMO row). Therefore, it can be speculated that variations in the β-diketonate structure influenced the HOMO energy more than the LUMO, as the HOMO FMOs vary dramatically.

Analysis of BF_2dbm dyes (**1**-**3**) reveals the role of alkoxy-substitution in the dyes. Compound **1**, with a *para*-substituted -OC12 chain, showed a small charge-transfer effect but retained the distinct π–π∗ transition; that is, electron density is delocalized across the aromatic π–system similar to previous reports (Table S3.1).[14] When the alkoxy-substituent is solely at the *meta*-position (**2**), the electron density became localized and the transition from the HOMO to the LUMO is more ICT in character(Figure 3.3). This is also the case for the dialkoxy-substituted dye (**3**), where the main absorption is ICT in character as well (Figure 3.3; Table S3.3). The alkoxy influences on the electron density in the HOMO are less pronounced in the naphthyl-phenyl variations (**4** and **5**; Tables S3.4-S3.5). Increased π–conjugation in fluorophores (e.g. phenyl vs. naphthyl) simultaneously raises the HOMO energy and lowers the LUMO energy.[31–33] The result is lower energy absorption and emission from the dyes.[9] Because the naphthalene is higher in energy compared to the phenyl ring, substitution on the phenyl ring in naphthyl-phenyl dyes will have less influence compared to the phenyl-phenyl dyes.[3] As a result, the FMOs of compounds **4** and **5** are very similar, having a mix of both ICT and π–π∗ transitions.

Compound **6** showed the most promising results of the set given the HOMO and LUMO FMOs are delocalized along the entire molecule, showing good π-conjugation important for red-shifting the absorption and emission. Abundant electron density is localized on the iodo-heavy

atom in all the molecular orbitals. This should produce intense, red-shifted RTP, ideal for oxygen sensing.

3.2.4 Model Studies in Poly (lactic acid) Films

For BF_2bdks, RTP is only observed when the dyes are embedded in amorphous matrices.[34] Compounds **1**-**6** were combined with poly(lactic acid) (PLA) and the dye-polymer blends were used to cast films on the inside of vials to analyze their phosphorescence properties. The vial provides a convenient chamber for controlling the environmental oxygen level exposed to the dye/PLA films. Dyes were loaded at 2.5% (w/w) in PLA to mimic the dye loading of a 25-30 kDa PLA polymer conjugate,[35] which showed larger F to RTP wavelength gaps compared to higher dye loadings in previous reports.[19] Important oxygen sensing features, such as fluorescence wavelength (λ_F), phosphorescence wavelength (λ_P), the F/P gap, the F/P ratio, the phosphorescence lifetime (τ_{RTP}) and the oxygen sensitivity in the hypoxic range (0-1%) were evaluated (Table 3.2).

Table 3. 2. Optical Properties of Boron Dyes in PLA Films[a]

Sample	λ_{Ex}[b] (nm)	λ_F[c] (nm)	τ_F[d] (ns)	λ_{RTP}[e] (nm)	τ_{RTP}[f] (ms)	S[g] ($\tau_0/\tau_{1\%}$)
1[h]	405	438	1.19	522	5.03	2.81
2[h]	398	472	1.99	536	11.06	3.45
3	420	493	2.41	576	15.00	4.13
4	408	459	0.81	558	1.70	1.44
5	434	492	0.80	574	6.17	3.13
6	433	464	0.65	585	2.09	1.70

[a]2.5% weight percent dye (mass of dye/mass of PLA). [b] Maxima of the excitation spectrum monitored at the fluorescence maxima. [c] Fluorescence emission maxima excited at 369 nm. [d]Fluorescence lifetime excited with a 369 nm light-emitting diode (LED) monitored at the emission maximum. All fluorescence lifetimes are fitted to a double-exponential decay. [e]Phosphorescence maxima in the delayed emission spectrum (λ_{ex} = 369 nm from a Xenon flash lamp and with a 0.5 ms delay). [f]Phosphorescence lifetime monitored at the phosphorescence maximum (λ_{Ex} = 369 nm from a Xenon flash lamp). [g]Sensitivity parameter ($S = \tau_0/\tau_{1\%}$ to indicate the amount quenched in the most sensitive range).[36] [h] Values reproduced from Daly et al.[13]

The fluorescence of the dyes in PLA matched expectations based on the fluorescence in CH_2Cl_2 solution. For the fluorescence maxima, the *para*-substituted dibenzoylmethane dye (**1**)

showed the bluest emission (438 nm) and the *meta-para*-dialkoxy derivatives (**3** and **5**) showed the reddest emission (~490 nm). The fluorescence lifetimes (τ_F) in PLA showed multi-exponential decays, typical for dyes embedded in PLA.[9] On average, the lifetimes of dbm dyes **1**-**3** (1-3 ns) were generally longer than the nbm dyes **4** (0.81 ns) and **5** (0.80 ns) and the dithienyl derivative (**6;** 0.65 ns) (Table 3.2). Given the greatest difference in the scaffolds is the heavy-atom substituted aromatic (*e.g.* phenyl, naphthyl or thienyl), the decrease in fluorescence lifetime could be a result of the depopulation of the singlet state to the triplet state via intersystem crossing.[15,19] This is supported qualitatively with the electron densities on the iodide atom in the DFT calculations.

An important parameter of dual-emissive materials for RGB oxygen-sensing applications is the phosphorescence lifetime (τ_P), which is directly correlated to the oxygen sensitivity (S) of the material. For the material to provide a good response, the sensitivity must be well-matched to expected oxygen levels. For example, in tumors, the oxygen level varies in the hypoxic range (0-5% O2),18,37 whereas diabetic tests utilizing Clark electrodes measure oxygen levels higher than ambient levels (>21% O2).38,39 The Stern-Volmer quenching constant (K_{SV}) in Eq. 1 and Eq. 2 is a combination of the unquenched lifetime ($\tau 0$) and the rate of oxygen diffusion through the matrix (k_q), and the intensity ratio of the unquenched reference (I_0) to the sensor response (I) can be used to monitor the concentration of the quencher (Q), or oxygen.

$$\frac{I_0}{I} = \frac{\tau_0}{\tau} = 1 + K_{SV}[Q] \qquad \textbf{Equation 3.1}$$

$$K_{SV} = k_q \tau_0 \qquad \textbf{Equation 3.2}$$

As a result, long lifetimes result in highly sensitive oxygen sensors.[40,41] Since PLA is used as the matrix for all these dye sensors, it can be inferred that all the changes in oxygen sensitivity are most directly linked to the RTP lifetime (τ_0) and not the diffusion of oxygen through the matrix (k_q). Sensitivity is represented as the ratio of the unquenched phosphorescence lifetime (τ_0) to the

phosphorescence lifetime at 1% oxygen ($\tau_{1\%}$).[36] In this report, the dbm dyes (**1**-**3**) had the longest phosphorescence lifetimes (5-15 ms), and therefore, the highest sensitivity values (*S*; Table 3.2) between 0-1% oxygen. It has been shown in previous reports that this range of oxygen concentration has the most linear relationship between phosphorescence quenching and oxygen concentration.[42] The nbm derivatives (**4** and **5**) on average showed decreased lifetimes (2-6 ms) and are less sensitive to oxygen. Finally, with similar properties to the naphthyl dyes, compound **6**, showed a phosphorescence lifetime of 2.09 ms and reduced sensitivity. With a wide range of oxygen sensitivities at multiple wavelengths across the visible spectrum, simultaneous oxygen sensing could be achieved using a combination of dyes.

3.2.5 Oxygen-Sensing Nanoparticles

For oxygen calibration and RGB camera imaging, the dyes were embedded in PLA-PEG nanoparticles. The nanoparticles can be used in an array of applications, such as tumor or wound hypoxia imaging.[43] Nanoparticles were fabricated by co-dissolution of a PLA-PEG block copolymer (PLA= 10K, PEG = 2K; PDI = 1.05)[8] and a boron dye (**1**-**6**; 2.5 weight percent) in dimethylformamide (DMF), followed by precipitation into stirred distilled water.[7] The formation of the nanoparticles was confirmed by DLS. For nanoparticles fabricated from dye **6**, the particle radii (R_H) is 60 nm with polydispersity of 23.5%, which is typical for boron dye-polymer nanoparticles (Figure S3.1).[7,8] Oxygen calibrations were performed as previously described by recording the total emission spectra at different oxygen levels.[18] As expected, the fluorescence intensity remained unchanged, while the phosphorescence intensity decreased with increasing oxygen concentration.

When the oxygen was purged from the aqueous nanoparticle environment, phosphorescence is greatly enhanced. Because phosphorescence is only observed in an amorphous

matrix, such as PLA, it can be assumed that the dyes assembled into the hydrophobic core of the nanoparticles, and are not present in the aqueous media or associated with the PEG.[34] The optical properties were comparable in the two media (i.e. PLA blends and PLA-PEG nanoparticles). Figure 3.4 shows the nanoparticles responding to ambient (air; 21% O_2) and hypoxic conditions (N_2; 0% O_2). Distinct color changes can be observed for all the derivatives.

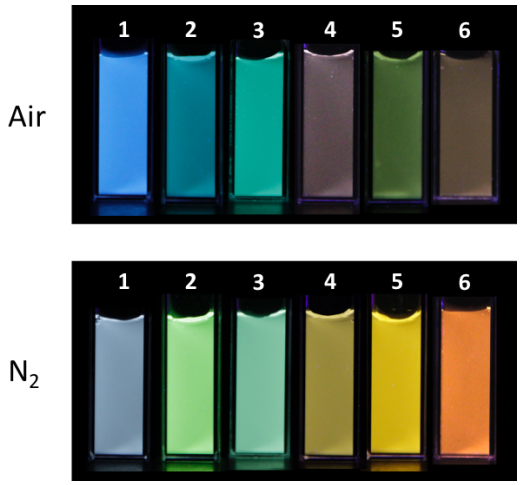

Figure 3. 4. Visualization of Dye Embedded in PLA-PEG Nanoparticles in Air and N_2 (λ_{Ex} = 369 nm). Images of compound **1** and **2** were reproduced with permission from Daly et al.[13]

3.2.6 MATLAB Calibration Optimization

To facilitate analysis of the nanoparticles, matrix laboratory (MATLAB) programs were designed and developed for the oxygen calibration and RGB camera data (https://github.com/uva-peirce-cottler-lab/nanoxim). Three programs were designed; a calibration optimization, an RGB camera channel analysis, and a program for video processing. The first is for general use when analyzing the emission of the dyes, such as deconvolution of the F and P, picking optimal F and P wavelengths for ratiometry, and incorporation of scalar values to linearize the calibration data if needed. For boron dyes, this program greatly facilitates oxygen-quenching analysis. For most dual-emissive boron dyes, the F and P partially overlap to greater or lesser extents in total emission spectra, and deconvolution allows for better calibration analysis. This is demonstrated in Figure

3.5 with two extreme cases where first, the phosphorescence is very weak (BF_2vbm(I)*para*-$OC_{12}H_{25}$, **3**), and second, where the fluorescence is very weak (BF_2dtm$OC_{12}H_{25}$, **6**). The calibration data namely, the total emission spectra at various oxygen levels, is inputted *via* an excel spreadsheet and the program finds and isolates the fluorescence and phosphorescence wavelengths and plots the F/P. With the isolated phosphorescence, the Stern-Volmer oxygen quenching constants (K_{sv}) can be estimated (Figure 3.6). The oxygen quenching K_{sv} values are in good agreement with the phosphorescence lifetimes of the dyes in PLA, where dyes with longer phosphorescence lifetimes show a greater sensitivity to oxygen quenching.

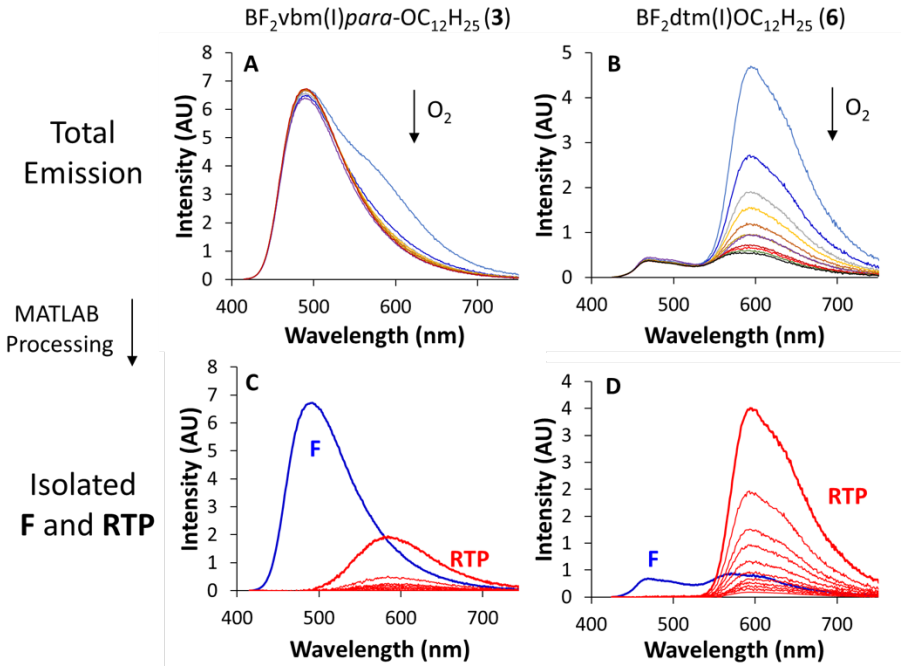

Figure 3. 5. MATLAB Processing of Oxygen Calibration Data from Boron Dyes in PLA-PEG Nanoparticles (2.5%). A) Total emission spectra of **3** at various O_2 levels (λ_{ex} = 385 nm). B) Total emission spectra of **6** at various O_2 levels (λ_{Ex} = 385 nm). C) Isolated F and P of **3** after MATLAB processing. D) Isolated F and P of **6** after MATLAB processing.

The second program enables calibration-free imaging by generating an RGB camera calibration curve (Figures S3.2-S3.18). The quantum efficiencies of the camera are uploaded and over-lain with the emission profiles of the dye. Also, filters can be added to tailor the ratios and

output emission from the dyes. This program allows for fluorescence calibrations to be estimated for channels and cameras without tediously conducting O_2-calibrations for every camera/filter combination for imaging applications.

Table 3. 3. Stern-Volmer Quenching Constants of BF_2bdks in PLA-PEG Nanoparticles

Sample	K_{sv}[a] $(\%\ O_2)^{-1}$	τ_{RTP}[b] (ms)
1	0.57	5.03
2	0.94	11.06
3	1.78	15.00
4	0.33	1.70
5	0.79	6.17
6	0.36	2.09

[a]Stern-Volmer slope from isolated phosphorescence intensity (I_0/I; Figure 3.6). [b]Phosphorescence lifetime of dye polylactide film monitored at the phosphorescence maximum (λ_{Ex} = 369 nm from a Xenon flash lamp).

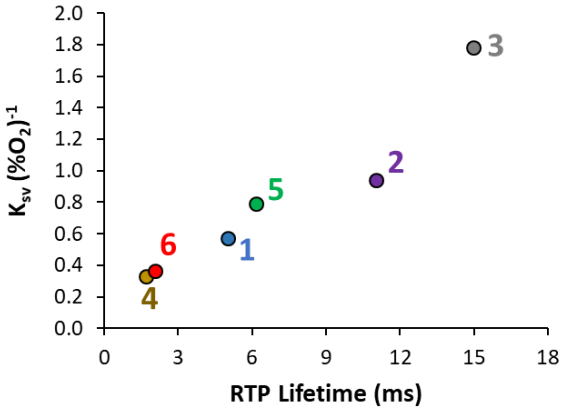

Figure 3. 6. Plot comparing the unquenched phosphorescence (RTP Lifetime) of dyes **1-6** and their corresponding Stern-Volmer quenching constants (K_{sv}) of in PLA-PEG Nanoparticles (Values from **Table 3.3**).

3.2.7 Oxygen Sensing with RBG Imaging

Select dyes showed promising features for RGB camera imaging applications. Important features include the wavelength gap between the fluorescence and phosphorescence, RGB channel alignment, and fluorescence to phosphorescence intensity ratio balance, that is, the fluorescence is bright enough to be visualized over autofluorescence from tissues and cells, and the

phosphorescence can respond in a physiologically relevant range. NPs containing compound **2** exhibit some of these ideal properties, where the fluorescence aligns well in the blue channel, and the phosphorescence aligns in the green channel. Furthermore, the O_2-sensing range of the dye is ideal for hypoxia imaging (0-5% O_2). NPs containing the dithienyl dye **6** have impressive red phosphorescence, ideal for reduced interference from autofluorescence and light scattering in biological imaging.[27] The fluorescence in the blue channel is quite weak but may be sufficient for RGB imaging techniques. Also, there is minimal overlap between the fluorescence and phosphorescence, therefore, both signals can be effectively and independently captured for quantitative ratiometric analysis. NPs containing compound **5** were also analyzed. Compound **5** has a good O_2-sensing range and reasonable emission intensities for F and P, but the channel separation is poor; the F and P span essentially all the channels indiscriminately. Comparing these three dyes clarifies the importance of channel alignment for RGB O_2 sensing.

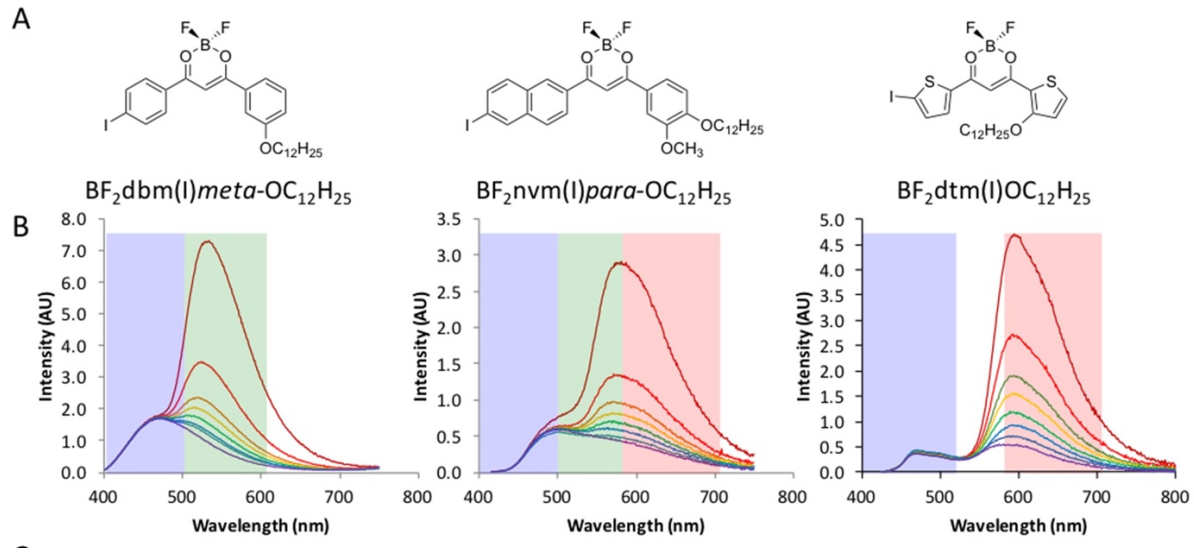

Figure 3. 7. Comparison of Boron Dyes for RGB Camera Imaging. A) Chemical structures of dyes **2**, **5** and **6**. B) Oxygen calibration data; total emission spectra of the PLA-PEG nanoparticles at various oxygen levels (λ_{ex} = 385 nm). Shaded regions correspond to the respective channels of the blue, green and red channels of the camera.

Videos of nanoparticle suspensions while being purged with nitrogen were recorded using a RGB camera mounted on a microscope as previously reported.[2] The videos were processed by the MATLAB video analysis (https://github.com/uva-peirce-cottler-lab/nanoxim). Over the course of 350 seconds, emission colors changed from blue to green for the BF_2dbm dye (**2**), and from blue to orange-red for BF_2dtm dye (**6**). Ratiometric images revealed that the F/P ratio decreases as nitrogen concentration increases (decreasing oxygen concentration). The raw channel intensity changes were plotted in respective channels (Figure 3.8). For the *meta*-alkoxy dye (**2**), the green channel increases intensity with decreasing oxygen concentration, as expected for increasing phosphorescence intensity, with minimal change in the blue channel. This is due to the channel overlap in the camera (Figure S3.12), therefore, there will always be change in adjacent channels (e.g. blue/green or green/red). The important thing is that the phosphorescence is predominantly influencing the green channel for ratiometry, and other factors can be accounted for in the sensor calibration. Nanoparticles containing compound **5** showed emission intensity changes in all the channels at all oxygen levels. This is a result of the broad emission of the dye. In contrast, the dithienyl dye (**6**), showed a consistent blue channel intensity with changing oxygen concentration, and a very responsive red channel. This is ideal for ratiometric oxygen sensing, as one of the channels should be entirely insensitive to the oxygen level to serve as a reliable standard to account for the signal heterogeneity, and could be potentially used in multiplexing applications, such as adding a fluorescence pH sensor. All dyes could be potentially used for biological O_2 sensing with an RGB camera.

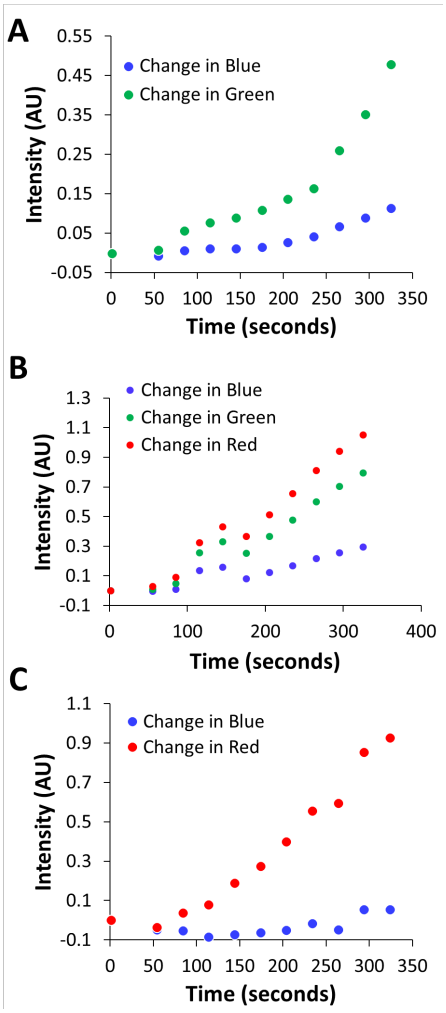

Figure 3. 8. Fluorescence and Phosphorescence Channel Assessment for Nanoparticles from Compound **2** (A), **5** (B), and **6** (C).

The MATLAB processed video screenshots are shown in Figure 3.9 for the blue-to-green dye, BF_2dbm(I)*meta*-$OC_{12}H_{25}$ (**2**), and the blue-to-red dye BF_2dtm(I)$O_{12}H_{25}$ (**6**). The F/P ratios match the expected values from the calibrations. Compound **6** showed a greater change in ratio (F/P changes more dynamically with O_2 level) and the O_2 range surpasses ambient conditions (>21% [O_2]). As a result, nanoparticles with compound **6** were used for biological oxygen sensing in wounds. Having the greater range of oxygen-sensitivity enables wound hypoxia imaging without the need for covering the wound from ambient conditions.[2] Compound **6** also has bright red phosphorescence, which will be less sensitive to the autofluorescence.[44]

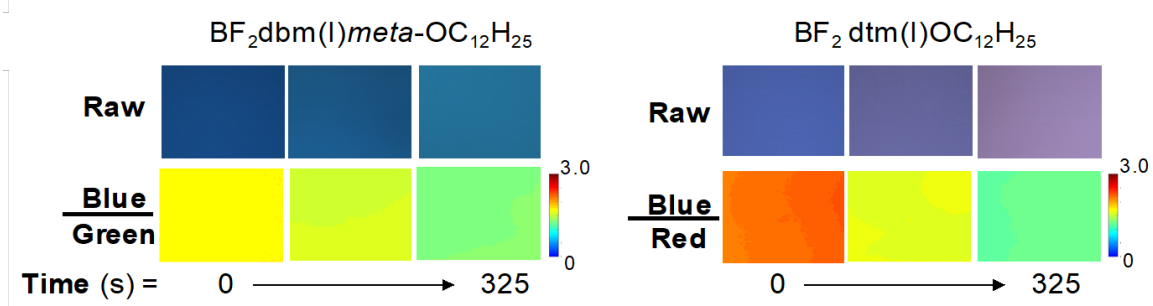

Figure 3. 9. Video processing of nanoparticle solutions in a cuvette overtime during nitrogen purging (top row) and the corresponding ratiometric images processed by MATLAB (bottom row).

3.2.8 Wound Hypoxia Imaging

Wounds are of particular interest for oxygen sensing, as tissue oxygenation is a critical indicator in wound healing, for example, in burn and diabetes cases.[45,46] In previous reports, we found that by using a dye with full-range sensitivity, it was possible to sense oxygenation in a wound bed without covering the wound and isolating the material from ambient conditions (air).[2,47] This minimizes perturbation of the wound bed, which can sometimes correspond to longer healing times. To demonstrate the oxygen sensing ability of the newly designed boron dyes in RGB camera imaging, the best candidate, the dithienyl dye (**6**), was chosen for monitoring wound healing in a murine model. The dithienyl dye possesses full range O_2 sensing capabilities, as well as separated fluorescence and phosphorescence peaks.

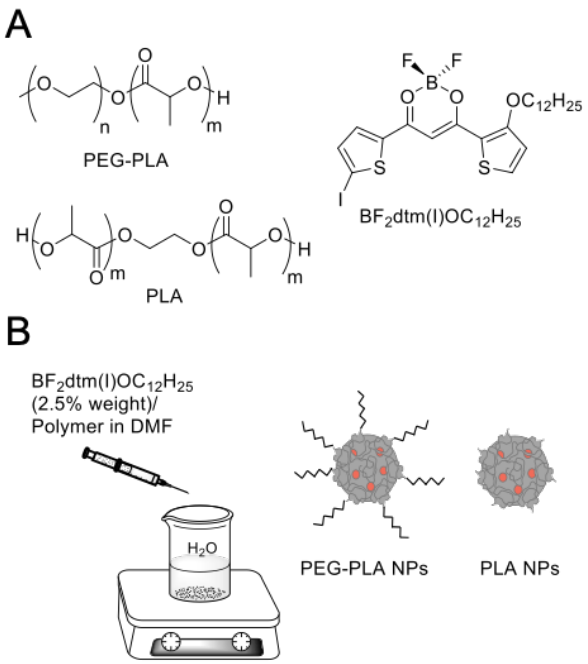

Figure 3. 10. Oxygen Sensing with $BF_2dtm(I)OC_{12}H_{25}$. A) Chemical structures and polymers used in nanoparticle fabrication. B) Fabrication of $BF_2dtm(I)OC_{12}H_{25}$ oxygen sensing nanoparticles with PLA or PLA-PEG.

As shown in Figure 3.10, the dithienyl dye (**6**) was co-precipitated with PLA (M_n = 9,700 g/mol) or PLA-PEG (M_n = 12,000 g/mol) to form PLA nanoparticles (PLA NPs) and PLA-PEG nanoparticles (PLA-PEG NPs), respectively. Two dorsal wound beds were treated with PLA NPs and PLA-PEG NPs. Upon application, the nanoparticles emit the characteristic red luminescence, indicating strong phosphorescence and the oxygen level is very low (Figure 3.11). The wounds were then monitored every two days over the time course of seven days, and images were taken and analyzed. At day 0, luminescence in the red channel from the PLA-NPs was much brighter compared to the PLA-PEG-NPs luminescence (Figure 3.11; Red Channel Images). This suggests the phosphorescence, or hypoxia, response from the nanoparticles is much more dramatic in the PLA-NPs. The PLA-NPs may be readily untaken by cells in the wound bed, triggering the phosphorescence, whereas the PLA-PEG NPs reside on the surface or outside the cells in the

media.[48] However, the ratiometric response is quite similar, showing an expected hypoxia environment.[2] Interestingly, the vasculature in the wound bed was more clearly visualized by PLA-PEG NPs compared to PLA NPs.

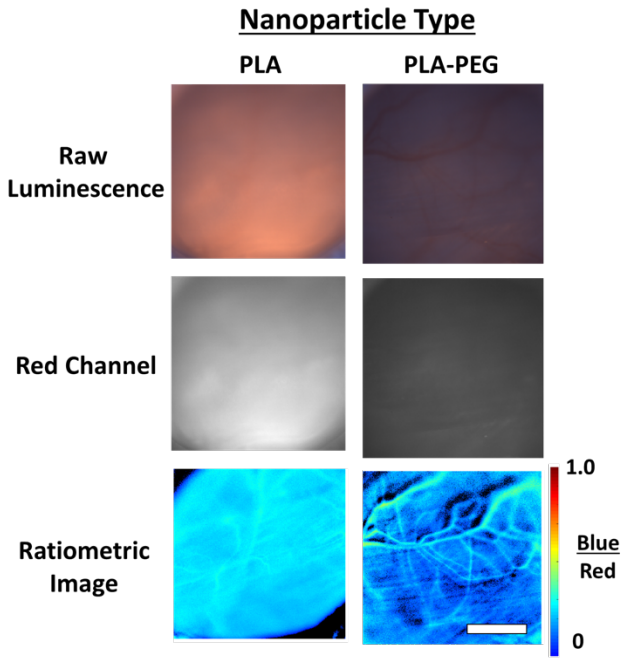

Figure 3. 11. Oxygen Sensing with $BF_2dtm(I)OC_{12}H_{25}$ PLA and PLA-PEG Nanoparticles (NPs). NPs were applied to a fresh murine wound (Day 0) and imaged. The "raw luminescence" is wound + NPs under UV light illumination. The "red channel" is the raw intensity in the red channel of the RGB camera showing the hypoxia response; the brighter the image, the greater the phosphorescence. The ratiometric image is the blue channel intensity divided by the red channel intensity (Scale bar = 1 mm).

During the week-long time course, fresh NPs were applied. From day 2 on, the ratios remained low, or varied very little, indicating the oxygen level, or nanoparticle response was not changing, as shown in Figure 3.12. It is possible that the weak fluorescence of the dithienyl dye could be responsible for the ratios remaining unchanged throughout the wound healing timecourse, and the reason the response from the PLA and PEG-PLA nanoparticles appear similar in the ratiometric images. If the fluorescence from the dye is barely above the background fluorescence, the blue fluorescence from the dye may be insufficient to give a reliable ratio, as all ratiometric

values would be near-zero (low blue channel intensity). This is contrary to our test in a cuvette (Figure 3.9), but it shows the complexity of biological imaging. As the wound bed heals and new skin develops, the background fluorescence may increase (e. g., tissue autofluorescence). Ratiometric images were analyzed without background subtraction as well. Both PLA and PLA-PEG NPs were able to response according to local oxygen level variations within the wound beds during healing (Figure S3.19), but the O_2-level does not appear to change, therefore, more strategies may need to be undertaken to use dye **6** in ratiometric O_2-sensing, such as ratio optimization though varying the dye loading or dye mixing.[49]

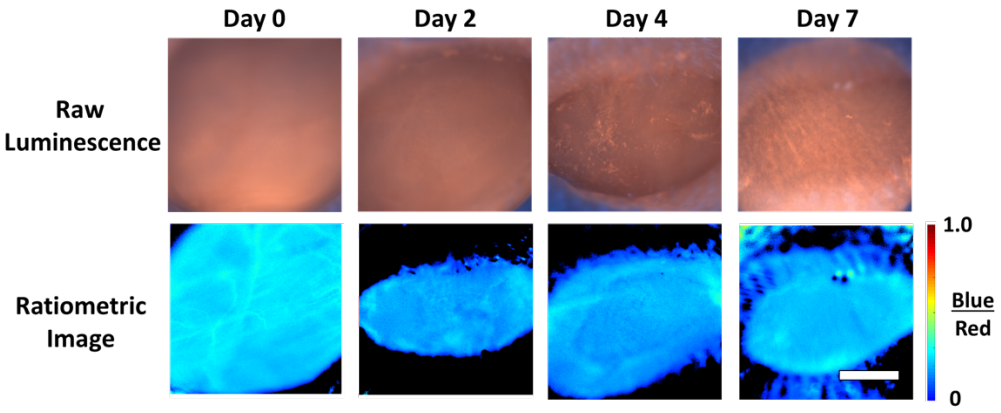

Figure 3. 12. Wound Healing Monitored Over Seven Days with PLA NPs and PLA-PEG NPs. Images were analyzed in MATLAB with a background subtraction. Scale bar = 1 mm.

For both PLA and PLA-PEG NP treatments, it was also observed that the wound area decreased by measuring wound size lacking epidermis (Figure S3.20), and the healing process was not significantly affected. This data suggested that the newly designed dye could serve as non-invasive oxygen sensing reagent in monitoring wound oxygenation with a cost-effective RGB camera system, especially at the early stage of wound healing. In the future, dyes with a more intense blue reference will be explored to increase the imaging time frame of these nanoparticles.

However, the O_2-sensing range and phosphorescence color of BF_2dtm(I)$C_{12}H_{25}$ shows an improvement in RGB imaging capabilities.

3.2.9 Conclusion

Advancement in biological oxygen sensing relies on improved design of sensing materials, instrumentation, and software adapted for compatibility with specific models and medical needs. This study optimized all these parameters for improved understanding of tissue oxygenation during wound healing. Synthetic strategies were investigated to optimize BF_2bdk dyes for non-invasive color camera-based ratiometric oxygen imaging. By modifying the chemical structure of six boron dyes with respect to π-conjugation and alkoxy chains, the optical properties, including emission alignment with RGB channels, F/P ratio, and oxygen sensitivity, were tuned. Wound imaging experiments demonstrated the oxygen sensing capability of nanoparticles fabricated from compound **6** in combination with an RGB color camera system and the computer software. This simple setup, with a portable imaging camera and user-friendly software, provides a cost-effective technique to perform ratiometry efficiently and quickly for oxygen sensing, including for future clinical application. While there are limitations in the weak blue fluorescence of dye **6**, facile synthesis, advances in color, wound clearance and oxygen-sensing range were achieved. Future efforts will focus on boosting the reference intensity for longer imaging, while maintaining the good color and oxygen-sensing capabilities.

3.3 Experimental Section

3.3.1 Materials

Solvents CH_2Cl_2 and THF were dried over 3 Å molecular sieves activated at 300 °C, transferred via cannula, and dried a second time over 3 Å molecular sieves activated at 300 °C.[50] The solvents were stored in a dry pot under nitrogen until use. The *para*-alkoxy iodide substituted

dye (**1**) and the *meta*-alkoxy iodine substituted dye (**2**) were prepared as previously described.[13,17] The ester, 6-iodo-2-methyl naphthoate was prepared as previously described.[51] 3,6-Dimethyl-1,4-dioxane-2,5-dione (D,L-lactide, Sigma Aldrich) was recrystallized twice from ethyl acetate and stored under nitrogen. Polylactide was prepared as previously described by Xu et al. using ethylene glycol as an initiator (M_n = 9,700 g/mol).[52] The poly(ethylene glycol) (PEG; 2,000 g/mol; Sigma) was dried via azeotropic distillation in toluene[53] prior to be used as the initiator for lactide polymerization to yield poly(ethylene glycol)-poly(lactic acid) block polymer (PLA-PEG; PLA= 10K, PEG = 2K; PDI = 1.05), as previously descibed.[8] All other chemicals were reagent grade from Sigma-Aldrich or TCI America and were used without further purification.

3.3.2 Methods

^{1}H NMR spectra (600 MHz) were recorded on a Varian VMRS 600/51 instrument in $CDCl_3$ or d_6-DMSO. ^{1}H NMR spectra were referenced to the residual signals for protiochloroform (7.26 ppm), protioDMSO (2.50 ppm), and protioacetone (2.09 ppm). In the ^{1}H NMR assignments, aromatic positions are defined for phenyl (Ar), naphthyl, (Np), and thienyl (Th). Coupling constants are given in hertz. UV−vis spectra were recorded on a Hewlett-Packard 8452A diode-array spectrophotometer. The synthesis procedures are shown in Scheme 3.1 and Schemes S3.1-S3.2. The compound yields, annotated ^{1}H NMR spectra data, and mass spectroscopy results for new compounds are provided. Nanoparticle size and polydispersity were analyzed by dynamic light scattering (DLS, Wyatt, DynaPro).

3.3.3 Luminescence Measurements

Steady-state fluorescence emission spectra were recorded on a Horiba Fluorolog-3 Model FL3-22 spectrofluorometer (double-grating excitation and double-grating emission monochromator). A 1 ms delay was used when recording the delayed emission spectra. Time-

correlated single-photon counting (TCSPC) fluorescence lifetime measurements were performed with a NanoLED-370 (λ_{ex} = 369 nm) excitation source and a DataStation Hub as the SPC controller. Phosphorescence lifetimes were measured with a 1 ms multichannel scalar (MCS) excited with a flash xenon lamp (λ_{ex} = 369 nm; duration <1 ms). Lifetime data were analyzed with DataStation v2.4 software from Horiba Jobin Yvon. Fluorescence quantum yields (Φ_F) of boron dyes in CH_2Cl_2 were calculated against anthracene as a standard as previously described, using the following values: Φ_F (anthracene) = 0.27,[28] (EtOH) = 1.360, n_D^{20} (CH_2Cl_2) = 1.424. Optically dilute CH_2Cl_2 solutions of the dyes, with absorbances <0.1 au, were prepared in 1 cm path length quartz cuvettes. Thin films were prepared on the inner wall of vials by dissolving polymers in CH_2Cl_2 (2 mg/mL) and evaporating the solvent by slowly rotating the vial under a low stream of nitrogen. The solution-cast films were then dried in vacuo overnight before measurements. Fluorescence spectra and lifetimes were obtained under ambient conditions (e.g., air, ~21% oxygen). For phosphorescence measurements, vials were capped with a 12 mm PTFE/silicone/PTFE seal (Chromatography Research Supplies) and were continuously purged with analytical grade N_2 (Praxair) for five minutes before measurements. For 21% O_2 (i.e. air), measurements were taken under ambient conditions (open vial, no cap). Oxygen calibration was performed as previously described with Cole-Palmer flow gauges and mixtures of analytical grade O_2, N_2 and 1% O_2 (in N_2) gases (Praxair).[18] For nanoparticles, fluorescence and phosphorescence lifetimes were fit to double exponential decays . Fluorescence lifetimes of dyes in CH_2Cl_2 were fit to single exponential decays.

3.3.4 Computation Modeling

The boron initiator was modeled with the Gaussian 09 suite of programs[54] using density functional theory (DFT) with the hybrid functional B3LYP and 6-31+G(d) basis sets to simulate the B, O, and C atoms. All vibrational frequencies were positive to make sure that the geometries

are at least a local minimum. Single-point energy calculations were used to generate the molecular orbital diagrams utilizing B3LYP/6-31+G(d) for B, O, and C atoms. Time-dependent DFT, TD-B3LYP/6-311+G(d) for B, O, and C atoms, was employed for an estimate of the absorption spectrum at the optimized ground-state geometry. A Tomasi polarized continuum for dichloromethane solvent was used in each calculation.[55] Molecular orbital diagrams were depicted using GaussView 5 software.

3.3.5 Synthesis

1-(3-(Dodecyloxy)phenyl)ethan-1-one. The *meta*-$OC_{12}H_{25}$ ketone was prepared as previously described[13], but 3-hydroxyacteophene was used in place of 4-hydroxyacetophenone to yield a white crystalline powder: 1.56 g (35%). ^{1}H NMR (600 MHz, $CDCl_3$): δ 7.50 (d, J = 12, 1H, 6-Ph-*H*), 7.46 (s, 1H, 2-Ph-*H*), 7.34 (t, J = 12, 1G, 5-Ph-*H*), 7.08 (d, J = 6, 1H, 4-Ph-*H*), 3.98 (t, J = 12, 2H, Ar-OC*H*$_2$$CH_2CH_2C_8H_{16}CH_3$), 2.58 (s, 3H, OC-C*H*$_3$), 1.79 (p, J = 6, 2H, Ar-OCH_2C*H*$_2$$CH_2C_8H_{16}CH_3$) 1.47 (p, J = 6, 2H, Ar-OCH_2CH_2C*H*$_2$$C_8H_{16}CH_3$) 1.28 (m, broad, 16H, Ar-$OCH_2CH_2CH_2C_8$*H*$_{16}$$CH_3$), 0.86 (t, J = 6, 3H, Ar-$OCH_2CH_2CH_2C_8H_{16}$C*H*$_3$).

1-(4-(Dodecyloxy)-3-methoxyphenyl)ethan-1-one. The *para*-methoxy-$OC_{12}H_{25}$ ketone was prepared by a previously described method for the meta-$OC_{12}H_{25}$, but 1-(4-hydroxy-3-methoxyphenyl)ethan-1-one was used in place of 4-hydroxyacetophenone to yield a white crystalline powder: 1.83 g (24%). H^1 NMR (600 MHz, $CDCl_3$): δ 7.54 (d, J = 6, 1H, 6-Ph-*H*), 7.50 (s, J = 6, 1H, 2-Ph-*H*), 6.86 (d, J = 6, 1H, 5-Ph-*H*), 4.06 (t, J = 6, 2H, Ar-OC*H*$_2$$CH_2CH_2C_8H_{16}CH_3$), 3.90 (s, 3H, Ar-OC*H*$_3$), 2.54 (s, 3H, Ar-COC*H*$_3$), 1.81 (p, J = 6, 2H, Ar-OCH_2C*H*$_2$$CH_2C_8H_{16}CH_3$), 1.47 (p, J = 6, 2H, Ar-OCH_2CH_2C*H*$_2$$C_8H_{16}CH_3$) 1.28 (m, broad, 16H, Ar-$OCH_2CH_2CH_2C_8$*H*$_{16}$$CH_3$), 0.86 (t, J = 6, 3H, Ar-$OCH_2CH_2CH_2C_8H_{16}$C*H*$_3$).

Methyl 3-(dodecyloxy)thiophene-2-carboxylate. The $C_{12}H_{25}$ thienyl ester was prepared by a previously described method,[21] but methyl 3-hydroxythiophene-2-carboxylate was used in place of 4-hydroxyacetophenone to yield a white crystalline powder: 1.92 g (30%). ^{1}H NMR (600 MHz, $CDCl_3$): δ 7.38 (d, J = 6, 1H, 5-Th*H*), 6.89 (d, J = 6, 1H, 5-Th*H*), 4.11 (t, J = 6, 2H, Ar-OC*H*$_2$CH$_2$CH$_2$C$_8$H$_{16}$CH$_3$), 3.85 (s, 3H, 2-ThCOOC*H*$_3$), 1.81 (p, J = 6, 2H, Ar-OCH$_2$C*H*$_2$CH$_2$C$_8$H$_{16}$CH$_3$), 1.47 (p, J = 6, 2H, Ar-OCH$_2$CH$_2$C*H*$_2$C$_8$H$_{16}$CH$_3$) 1.28 (m, broad, 16H, Ar-OCH$_2$CH$_2$CH$_2$C$_8$*H*$_{16}$CH$_3$), 0.87 (t, J = 6, 3H, Ar-OCH$_2$CH$_2$CH$_2$C$_8$H$_{16}$C*H*$_3$). HRMS (ESI, TOF) m/z calcd for $C_{18}H_{31}O_3S$: 327.1994 $[M + H]^+$; found 327.1993.

1-(4-(Dodecyloxy)-3-methoxyphenyl)-3-(4-iodophenyl)propane-1,3-dione (**L3**). The *meta-, para*-dialkoxy substituted ligand was prepared by a previously described method,[21] but the ketone 1-(3-(dodecyloxy)phenyl)ethan-1-one was used in place of 1-(4-(dodecyloxy)phenyl)ethan-1-one to yield a faint yellow powder after recrystallization from hexanes/acetone: 1.03 g (58%). ^{1}H NMR (600 MHz, DMSO): 7.91 (d, J = 12, 2H, 2, 6-i-Ph-*H*), 7.89 (d, J = 12, 2H, 3, 5-i-Ph-*H*), 7.81 (d, J = 6, 1H, 6-o-Ph-*H*), 7.59 (s, 1H, 2-o-Ph-*H*), 7.25 (s, 1H, COC*H*CO), 7.08 (d, J = 6, 1H, 5-o-Ph-*H*), 4.04 (t, J = 6, 2H, Ar-OC*H*$_2$CH$_2$CH$_2$C$_8$H$_{16}$CH$_3$), 3.83 (s, 3H, Ar-OC*H*$_3$), 1.71 (p, J = 6, 2H, Ar-OCH$_2$C*H*$_2$CH$_2$C$_8$H$_{16}$CH$_3$), 1.38 (p, J = 6, 2H, Ar-OCH$_2$CH$_2$C*H*$_2$C$_8$H$_{16}$CH$_3$), 1.21 (m, broad, 16H, Ar-OCH$_2$CH$_2$CH$_2$C$_8$*H*$_{16}$CH$_3$), 0.81 (t, J = 6, 3H, Ar-OCH$_2$CH$_2$CH$_2$C$_8$H$_{16}$C*H*$_3$). HRMS (ESI, TOF) m/z calcd for $C_{28}H_{38}O_4I$: 565.1815 $[M + H]^+$; found 565.1816.

1-(3-(Dodecyloxy)phenyl)-3-(6-iodonaphthalen-2-yl)propane-1,3-dione (nbm(I)*meta*-$OC_{12}H_{25}$, **L4**). The *ortho*-substituted ligand was prepared by a previously described method,[21] but the ketone 1-(3-(dodecyloxy)phenyl)ethan-1-one was used in place of 1-(4-(dodecyloxy)phenyl)ethan-1-one, and the ester methyl 6-iodo-2-naphthoate[51] was used in place of methyl 4-iodobenzoate to yield a tan powder after recrystallization from hexanes/EtOAc: 522 mg

(57%). ^{1}H NMR (600 MHz, $CDCl_3$): δ 16.86 (s, 1H, -O*H*), 8.47 (s, 1H, 1-Np-*H*), 8.30 (s, 1H, 5-Np-*H*), 8.01 (d, J = 6, 1H, 8-Np-*H*), 7.80 (m, 2H, 3-Np-*H*, 6-Ph-*H*), 7.69 (d, J = 12, 1H, 7-Np-*H*), 7.58 (d, J = 6, 1H, 4-Ph-*H*), 7.53 (s, 1H, 2-Ph-*H*), 7.39 (t, J = 6, 1H, 5-Ph-*H*), 7.10 (d, J = 6, 1H, 4-Np-*H*), 6.94 (s, 1H, COC*H*CO), 4.03 (t, J = 6, 2H, Ar-OC*H*$_2$CH$_2$CH$_2$C$_8$H$_{16}$CH$_3$), 1.81 (p, J = 6, 2H, Ar-OCH$_2$C*H*$_2$CH$_2$C$_8$H$_{16}$CH$_3$) 1.47 (p, J = 6, 2H, Ar-OCH$_2$CH$_2$C*H*$_2$C$_8$H$_{16}$CH$_3$) 1.28 (m, broad, 16H, Ar-OCH$_2$CH$_2$CH$_2$C$_8$*H*$_{16}$CH$_3$), 0.86 (t, J = 6, 3H, Ar-OCH$_2$CH$_2$CH$_2$C$_8$H$_{16}$C*H*$_3$). HRMS (ESI, TOF) m/z calcd for $C_{31}H_{36}O_3I$: 583.1709 $[M - H]^+$; found 583.1715.

1-(4-(Dodecyloxy)-3-methoxyphenyl)-3-(6-iodonaphthalen-2-yl)propane-1,3-dione (nvm(I)*para*-$OC_{12}H_{25}$, **L5**). The *ortho*-substituted ligand was prepared by a previously describe method,[21] but the ketone 1-(4-(dodecyloxy)-3-methoxyphenyl)ethan-1-one, was used in place of 1-(4-(dodecyloxy)phenyl)ethan-1-one, and the ester methyl 6-iodo-2-naphthoate,[51] was used in place of methyl 4-iodobenzoate to yield a tan powder after recrystallization from hexanes/EtOAc: 90 mg (20%). ^{1}H NMR (600 MHz, $CDCl_3$): δ 17.01 (s, 1H, -O*H*), 8.46 (s, 1H, 1-Np-*H*), 8.29 (d, 1H, 5-Np-*H*), 7.99 (t, J = 6, 1H, 8-Np-*H*), 7.79 (d, J=12, 2H, 3-Np-*H*, 6-Ph-*H*), 7.69 (d, J = 6, 1H, 7-Np-*H*), 7.64 (d, J = 6, 1H, 4-Np-*H*), 7.58 (s, 1H, 2-Ph-*H*), 6.93 (d, J = 12, 1H, 5-Ph-*H*), 6.90 (s, 1H, COC*H*CO), 4.09 (t, J = 6, 2H, Ar-OC*H*$_2$CH$_2$CH$_2$C$_8$H$_{16}$CH$_3$), 3.96 (s, 3H, Ar-OCH$_3$), 1.87 (p, J = 6, 2H, Ar-OCH$_2$C*H*$_2$CH$_2$C$_8$H$_{16}$CH$_3$), 1.47 (p, J = 6, 2H, Ar-OCH$_2$CH$_2$C*H*$_2$C$_8$H$_{16}$CH$_3$) 1.28 (m, broad, 16H, Ar-OCH$_2$CH$_2$CH$_2$C$_8$*H*$_{16}$CH$_3$), 0.86 (t, J = 6, 3H, Ar-OCH$_2$CH$_2$CH$_2$C$_8$H$_{16}$C*H*$_3$). HRMS (ESI, TOF) m/z calcd for $C_{32}H_{38}O_4I$: 613.1815 $[M - H]^+$; found 613.1821.

1-(3-(Dodecyloxy)thiophen-2-yl)-3-(5-iodothiophen-2-yl)propane-1,3-dione (dtm(I)$OC_{12}H_{25}$, **L6**). The dithienyl ligand was prepared by a previously described method,[21] but the ketone 2-acetyl, 5-iodothiophene, was used in place of 1-(4-(dodecyloxy)phenyl)ethan-1-one, and the ester, methyl 3-(dodecyloxy)thiophene-2-carboxylate, was used in place of methyl 4-

iodobenzoate. The crude ligand was passed through a silica column (hexanes/ethyl acetate 3:1) and obtained as a brown oil: 431 mg (23%). Given the crude ligand darkened and decomposed in air, it was carried on quickly to the next step without further purification.

Difluoroboron-1-(4-(dodecyloxy)-3-methoxyphenyl)-3-(4-iodophenyl)propane-1,3-dione (BF_2vbm(I)*para*-$OC_{12}H_{25}$, **3**) The iodo-phenyl C12 dye was prepared as previously described.[13] Briefly, the ligand, **L3** (513 mg; 0.9 mmol), was added to an oven-dried 100 mL round bottom flask. Under an $N_{2(g)}$ atmosphere, the ligand was dissolved in $CH_2Cl_{2(anhy.)}$ (35 mL) then $BF_3 \cdot OEt_2$ (170 µl; 1.4 mmol) was added. The reaction was stirred overnight then the solvent was removed via rotary evaporation. The product was purified by recrystallization from hexanes/acetone to yield a yellow solid: 117 mg (21%). ^{1}H NMR (600 MHz, $CDCl_3$): δ 7.90 (d, J = 12, 2H, 2, 6-i-Ph-*H*), 7.80 (d, J = 12, 2H, 3, 5-i-Ph-*H*), 7.77 (d, J = 6, 1H, 6-o-Ph-*H*), 7.66 (s, 1H, 2-o-Ph-*H*), 7.04 (s, 1H, COC*H*CO), 6.95 (d, J = 6, 1H, 5-o-Ph-*H*), 4.12 (t, J = 6, 2H, Ar-OC*H*$_2$$CH_2CH_2C_8H_{16}CH_3$), 3.96 (s, 3H, Ar-OC*H*$_3$), 1.88 (p, J = 6, 2H, Ar-OCH_2C*H*$_2$$CH_2C_8H_{16}CH_3$), 1.46 (p, J = 6, 2H, Ar-OCH_2CH_2C*H*$_2$$C_8H_{16}CH_3$), 1.25 (m, broad, 16H, Ar-$OCH_2CH_2CH_2C_8$*H*$_{16}$$CH_3$), 0.87 (t, J = 6, 3H, Ar-$OCH_2CH_2CH_2C_8H_{16}$C*H*$_3$). HRMS (ESI, TOF) m/z calcd for $C_{28}H_{37}BO_4F_2I$: 613.1798 $[M + H]^+$; found 613.1802.

Difluoroboron-1-(3-(dodecyloxy)phenyl)-3-(6-iodonaphthalen-2-yl)propane-1,3-dione (BF_2nbm(I)*meta*-$OC_{12}H_{25}$, **4**). The iodo-naphthyl C12 dye was prepared as previously described for **3**, but the ligand, **L4**, was used in place of **L3** to yield a yellow powder: 214 mg (78%). ^{1}H NMR (600 MHz, $CDCl_3$): δ 8.71 (s, 1H, 1-Np-*H*), 8.33 (s, 1H, 5-Np-*H*), 8.10 (d, J = 6, 1H, 8-Np-*H*), 7.86 (m, 2H, 3-Np-*H*, 6-Ph-*H*), 7.73 (m, 2H, 7-Np-*H*, 4-Ph-*H*), 7.67 (s, 1H, 2-Ph-*H*), 7.45 (t, J = 6, 1H, 5-Ph-*H*), 7.28 (s, 1H, COC*H*CO), 7.24 (d, J = 6, 4-Np-*H*), 4.04 (t, J = 6, 2H, Ar-OC*H*$_2$$CH_2CH_2C_8H_{16}CH_3$), 1.82 (p, J = 6, 2H, Ar-OCH_2C*H*$_2$$CH_2C_8H_{16}CH_3$) 1.47 (p, J = 6, 2H, Ar-

$OCH_2CH_2CH_2C_8H_{16}CH_3$) 1.28 (m, broad, 16H, Ar-$OCH_2CH_2CH_2C_8H_{16}CH_3$), 0.87 (t, J = 6, 3H, Ar-$OCH_2CH_2CH_2C_8H_{16}CH_3$). HRMS (ESI, TOF) m/z calcd for $C_{31}H_{37}BO_3F_2I$: 633.1848 $[M + H]^+$; found 633.1852.

Difluoroboron-1-(4-(dodecyloxy)-3-methoxyphenyl)-3-(6-iodonaphthalen-2-yl)propane-1,3-dione (BF_2nvm(I)*para*-$OC_{12}H_{25}$, **5**). The iodo-naphthyl C12 dye was prepared as previously described for **1**, but the ligand, **L5**, was used in place of **L1** to yield a yellow powder: 28 mg (35%). ^{1}H NMR (600 MHz, DMSO): δ 8.99 (s, 1H, 1-Np-*H*), 8.55 (s, 1H, 5-Np-*H*), 8.36 (d, J = 6, 1H, 8-Np-*H*), 8.15 (d, J=12, 1H, 4-Np-*H*), 8.08 (d, J = 6, 1H, 3-Np-*H*), 7.98 (d, J = 6, 1H, 7-Np-*H*), 7.93 (q, J = 6, 2H, 2-Ph-*H*, 6-Ph-*H*), 7.75 (s, 1H, COC*H*CO), 7.24 (d, J = 6, 1H, 5-Ph-*H*), 4.14 (t, J = 6, 2H, Ar-O$CH_2$$CH_2CH_2C_8H_{16}CH_3$), 3.90 (s, 3H, Ar-$OCH_3$), 1.74 (t, J = 6, 2H, Ar-$OCH_2CH_2$$CH_2C_8H_{16}CH_3$), 1.47 (p, J = 6, 2H, Ar-$OCH_2CH_2CH_2$$C_8H_{16}CH_3$) 1.22 (m, broad, 16H, Ar-$OCH_2CH_2CH_2C_8H_{16}CH_3$), 0.81 (t, J = 6, 3H, Ar-$OCH_2CH_2CH_2C_8H_{16}CH_3$). HRMS (ESI, TOF) m/z calcd for $C_{32}H_{39}BO_4F_2I$: 663.1954 $[M + H]^+$; found 663.1947.

Difluoroboron-1-(3-(dodecyloxy)thiophen-2-yl)-3-(5-iodothiophen-2-yl)propane-1,3-dione (BF_2dtm(I)$OC_{12}H_{25}$, **6**). The iodo-thienyl C12 dye was prepared as previously described for **1**, but the crude ligand, **L6**, was used in place of **L1**. The product was purified by column chromatography (hexanes/ethyl acetate 4:1), followed by recrystallization (ethyl acetate/hexanes) to yield an orange solid: 250 mg (50%). ^{1}H NMR (600 MHz, $CDCl_3$): δ 7.78 (d, J = 6, 1H, 3-iodoTh*H*), 7.53 (d, J = 6, 1H, 5-C12Th*H*), 7.36 (d, J = 6, 1H, 4-iodoTh*H*), 7.20 (s, 1H, COC*H*CO), 6.88 (d, J = 6, 1H, 4-C12Th*H*), 4.27 (t, J = 6, 2H, Ar-O$CH_2$$CH_2CH_2C_8H_{16}CH_3$), 1.74 (t, J = 6, 2H, Ar-$OCH_2CH_2$$CH_2C_8H_{16}CH_3$), 1.50 (p, J = 6, 2H, Ar-$OCH_2CH_2CH_2$$C_8H_{16}CH_3$) 1.25 (m, broad, 16H, Ar-$OCH_2CH_2CH_2C_8H_{16}CH_3$), 0.85 (t, J = 6, 3H, Ar-$OCH_2CH_2CH_2C_8H_{16}CH_3$). HRMS (ESI, TOF) m/z calcd for $C_{23}H_{30}BO_3F_2S_2I$: 594.0742 $[M]^+$; found 594.0751.

3.3.6 Nanoparticle Imaging

A Grasshopper 3 camera (FLIR) was mounted to a Nikon Eclipse 80i microscope equipped with a UV excitation filter cube and 4X dry objective. An X-Cite 120 fluorescence illuminator (Lumen Dynamics) was used for nanoparticle excitation. A 415 nm longpass filter was placed in the light path immediately before the camera. Nanoparticle suspensions were placed in a cuvette connecting to a nitrogen tank. As nitrogen started to bubble, videos of nanoparticle fluorescence and phosphorescence were recorded in a dark room using FlyCap2 software (FLIR) over a time course of 350 seconds. Data were analyzed by Two-Way Repeated Measures ANOVA with SigmaPlot 13.0 software. Ratiometric images at time 0, 175, and 350 seconds were generated in MATLAB as previously described with modifications in code to adjust color scale.

3.3.7 Animal Model

All procedures were performed in accordance with the University of Virginia Institutional Animal Care and Use Committee (ACUC). Male 9-week-old C57BL/6J mice (Jackson Laboratories) were anesthetized by inhalation of 1.5% isoflurane/98.5% medical air mixture. Dorsa were shaved and depilated before being sterilized with three alternating scrubs of povidone-iodine and 70% isopropanol. Full-thickness circular cutaneous wounds 4 mm in diameter, were surgically made on the dorsum of each mouse. An analgesic (buprenorphine, 0.1 mg/kg) was administered following the surgery and the wounds were covered with a Tegaderm (3M) dressing. Mice were singly housed with food and water available *ad libitum*. A heated pad was placed on the microscope stage to maintain mouse body temperature during imaging. A Canon EOS Rebel T6 camera equipped with a Canon 100 mm macro lens was used to document open wound sizes. Wounds were imaged immediately after being made, and then again on days 2, 4, and 7 post-surgery.

Tegaderm bandages were removed prior to wound imaging. Exposed wounds were kept moist with sterile 0.9% saline injection, USP. Imaging was performed on one wound at a time. To document background emissions, 20 video frames were recorded over 20 seconds on saline-moistened wounds. Saline was wicked from wounds using sterile cotton-tipped applicators immediately prior to nanoparticle addition. 40 mL of nanoparticle solution was added to the wound. After three minutes, 20 video frames of nanoparticle fluorescence and phosphorescence were captured over 20 seconds. UV excitation was blocked using the shutter during the three-minute normalization period in between video recordings. Nanoparticles were then flushed from the wound using 2 ml sterile 0.9% saline injection, USP. Tegaderm bandages were reapplied upon completion of imaging each day. Wound sizes were measured using ImageJ software to trace the regions lacking epidermis. ImageJ software was used to measure background-thresholded red channel emissions in wounds on days 2, 4, and 7, prior to nanoparticle additions on those days, to quantify nanoparticle adhesion to wound bed tissue. Data were analyzed by Two-Way Repeated Measures ANOVA in SigmaPlot 13.0 software. Raw images were analyzed in MATLAB to generate ratiometric oxygen map.

3.4 Acknowledgements

I would like to thank Christopher DeRosa for initiating the project, Fang Wang for helping in the synthesis, Richard Doty, Prof. Demas, and Bruce Corliss for developing the MATLAB software, Anthony Bruce for performing surgery and wound imaging. I also want to acknowledge Prof. Fraser for her guidance and assistantance in preparing manuscripts and the National Institutes of Health (R01 CA167250) and the UVA Cancer Center (P30 CA44579) for financial support.

3.5 References

(1) Moßhammer, M.; Strobl, M.; Kühl, M.; Klimant, I.; Borisov, S. M.; Koren, K. Design and Application of an Optical Sensor for Simultaneous Imaging of PH and Dissolved O2 with Low Cross-Talk. *ACS Sensors* **2016**, *1*, 681−687.

(2) DeRosa, C. A.; Seaman, S. A.; Mathew, A. S.; Gorick, C. M.; Fan, Z.; Demas, J. N.; Peirce, S. M.; Fraser, C. L. Oxygen Sensing Difluoroboron β-Diketonate Polylactide Materials with Tunable Dynamic Ranges for Wound Imaging. *ACS Sensors* **2016**, *1*, 1366–1373.

(3) Liu, T.; Zhang, G.; Evans, R. E.; Trindle, C. O.; Altun, Z.; DeRosa, C. A.; Wang, F.; Zhuang, M.; Fraser, C. L. Phosphorescence Tuning through Heavy Atom Placement in Unsymmetrical Difluoroboron β-Diketonate Materials. *Chem. Eur. J.* **2018**, *24*, 1859–1869.

(4) Xu, S.; Evans, R. E.; Liu, T.; Zhang, G.; Demas, J. N.; Trindle, C. O.; Fraser, C. L. Aromatic Difluoroboron β-Diketonate Complexes: Effects of π-Conjugation and Media on Optical Properties. *Inorg. Chem.* **2013**, *52*, 3597–3610.

(5) Daly, M. L.; DeRosa, C. A.; Kerr, C.; Morris, W. A.; Fraser, C. L. Blue Thermally Activated Delayed Fluorescence from a Biphenyl Difluoroboron β-Diketonate. *RSC Adv.* **2016**, *6*, 81631–81635.

(6) Kolpaczynska, M.; DeRosa, C. A.; Morris, W. A.; Fraser, C. L. Thienyl Difluoroboron β-Diketonates in Solution and Polylactide Media. *Aust. J. Chem.* **2016**, *69*, 537–545.

(7) Pfister, A.; Zhang, G.; Zareno, J.; Horwitz, A. F.; Fraser, C. L. Boron Polylactide Nanoparticles Exhibiting Fluorescence and Phosphorescence in Aqueous Medium. *ACS Nano* **2008**, *2*, 1252–1258.

(8) Kersey, F. R.; Zhang, G.; Palmer, G. M.; Dewhirst, M. W.; Fraser, C. L. Stereocomplexed Poly(Lactic Acid)−Poly(Ethylene Glycol) Nanoparticles with Dual-Emissive Boron Dyes for Tumor Accumulation. *ACS Nano* **2010**, *4*, 4989–4996.

(9) DeRosa, C. A.; Samonina-Kosicka, J.; Fan, Z.; Hendargo, H. C.; Weitzel, D. H.; Palmer, G. M.; Fraser, C. L. Oxygen Sensing Difluoroboron Dinaphthoylmethane Polylactide. *Macromolecules* **2015**, *48*, 2967–2977.

(10) Meier, R. J.; Fischer, L. H.; Wolfbeis, O. S.; Schäferling, M. Referenced Luminescent Sensing and Imaging with Digital Color Cameras: A Comparative Study. *Sensors Actuators B Chem.* **2013**, *177*, 500–506.

(11) DeRosa, C. A.; Kolpaczynska, M.; Kerr, C.; Daly, M. L.; Morris, W. A.; Fraser, C. L. Oxygen-Sensing Difluoroboron Thienyl Phenyl β-Diketonate Polylactides. *Chempluschem* **2017**, *82*, 399–406.

(12) DeRosa, C. A.; Daly, M. L.; Kerr, C.; Fraser, C. L. Methoxy-Substituted Difluoroboron Benzoylacetonate Complexes with Color-Tunable Phosphorescence. *ChemPhotoChem* **2019**, *3*, 31–36.

(13) Daly, M. L.; Kerr, C.; Derosa, C. A.; Fraser, C. L. Meta-Alkoxy-Substituted Difluoroboron Dibenzoylmethane Complexes as Environment-Sensitive Materials. *ACS Appl. Mater. Interfaces* **2017**, *9*, 32008–32017.

(14) Morris, W. A.; Sabat, M.; Butler, T.; DeRosa, C. A.; Fraser, C. L. Modulating Mechanochromic Luminescence Quenching of Alkylated Iodo Difluoroboron Dibenzoylmethane Materials. *J. Phys. Chem. C* **2016**, *120*, 14289–14300.

(15) Morris, W. A.; Liu, T.; Fraser, C. L. Mechanochromic Luminescence of Halide-Substituted Difluoroboron β-Diketonate Dyes. *J. Mater. Chem. C* **2015**, *3*, 352–363.

(16) Samonina-Kosicka, J.; Weitzel, D. H.; Hofmann, C. L.; Hendargo, H.; Hanna, G.; Dewhirst, M. W.; Palmer, G. M.; Fraser, C. L. Luminescent Difluoroboron β-Diketonate PEG-PLA Oxygen Nanosensors for Tumor Imaging. *Macromol. Rapid Commun.* **2015**, *36*, 694–699.

(17) Zhang, G.; Lu, J.; Fraser, C. L. Mechanochromic Luminescence Quenching: Force-Enhanced Singlet-to-Triplet Intersystem Crossing for Iodide-Substituted Difluoroboron−Dibenzoylmethane−Dodecane in the Solid State. *Inorg. Chem.* **2010**, *49*, 10747–10749.

(18) Zhang, G.; Palmer, G. M.; Dewhirst, M. W.; Fraser, C. L. A Dual-Emissive-Materials Design Concept Enables Tumour Hypoxia Imaging. *Nat. Mater.* **2009**, *8*, 747–751.

(19) DeRosa, C. A.; Kerr, C.; Fan, Z.; Kolpaczynska, M.; Mathew, A. S.; Evans, R. E.; Zhang, G.; Fraser, C. L. Tailoring Oxygen Sensitivity with Halide Substitution in Difluoroboron Dibenzoylmethane Polylactide Materials. *ACS Appl. Mater. Interfaces* **2015**, *7*, 23633–23643.

(20) DeRosa, C. A.; Kerr, C.; Fan, Z.; Kolpaczynska, M.; Mathew, A. S.; Evans, R. E.; Zhang, G.; Fraser, C. L. Tailoring Oxygen Sensitivity with Halide Substitution in Difluoroboron Dibenzoylmethane Polylactide Materials. *ACS Appl. Mater. Interfaces* **2015**, *7*, 23633–23643.

(21) Nguyen, N. D.; Zhang, G.; Lu, J.; Sherman, A. E.; Fraser, C. L. Alkyl Chain Length Effects on Solid-State Difluoroboron β-Diketonate Mechanochromic Luminescence. *J. Mater. Chem.* **2011**, *21*, 8409–8415.

(22) Wang, F.; DeRosa, C. A.; Song, D.; Dickie, D. A.; Fraser, C. L. Environment-Sensitive Azepane-Substituted β-Diketones and Difluoroboron Complexes with Restricted C–C Bond Rotation. *J. Phys. Chem. C* **2019**, *123*, 23124–23130.

(23) Derosa, C. A.; Hiroto, S.; Fraser, C. L. Amplified Heavy-Atom Free Phosphorescence from Meta-Dimethoxy Difluoroboron β-Diketonate Charge-Transfer Materials. *J. Phys. Chem. C* **2019**, *123*, 20488–20496.

(24) Grabowski, Z. R.; Rotkiewicz, K.; Rettig, W. Structural Changes Accompanying Intramolecular Electron Transfer: Focus on Twisted Intramolecular Charge-Transfer States and Structures. *Chem. Rev.* **2003**, *103*, 3899–4032.

(25) Samonina-Kosicka, J.; DeRosa, C. A.; Morris, W. A.; Fan, Z.; Fraser, C. L. Dual-Emissive Difluoroboron Naphthyl-Phenyl β-Diketonate Polylactide Materials: Effects of Heavy Atom Placement and Polymer Molecular Weight. *Macromolecules* **2014**, *47*, 3736–3746.

(26) Borisov, S. M.; Fischer, R.; Saf, R.; Klimant, I. Exceptional Oxygen Sensing Properties of New Blue Light-Excitable Highly Luminescent Europium(III) and Gadolinium(III) Complexes. *Adv. Funct. Mater.* **2014**, *24*, 6548–6560.

(27) Weissleder, R. A Clearer Vision for in Vivo Imaging. *Nat. Biotechnol.* **2001**, *19*, 316–317.

(28) Demas, J. N.; Crosby, G. A. The Measurement of Photoluminescence Quantum Yields. A Review. *J. Phys. Chem.* **1971**, *75*, 991–1024.

(29) DeRosa, C. A.; Hiroto, S.; Fraser, C. L. Amplified Heavy-Atom Free Phosphorescence from Meta -Dimethoxy Difluoroboron β-Diketonate Charge-Transfer Materials . *J. Phys. Chem. C* **2019**, *123*, 20488–20496.

(30) Butler, T.; Morris, W. A.; Samonina-Kosicka, J.; Fraser, C. L. Mechanochromic Luminescence and Aggregation Induced Emission of Dinaphthoylmethane β-Diketones and Their Boronated Counterparts. *ACS Appl. Mater. Interfaces* **2016**, *8*, 1242–1251.

(31) Liu, T.; Chien, A. D.; Lu, J.; Zhang, G.; Fraser, C. L. Arene Effects on Difluoroboron β-Diketonate Mechanochromic Luminescence. *J. Mater. Chem.* **2011**, *21*, 8401–8408.

(32) Yin, X.; Guo, F.; Lalancette, R. A.; Jäkle, F. Luminescent Main-Chain Organoborane Polymers: Highly Robust, Electron-Deficient Poly(Oligothiophene Borane)s via Stille Coupling Polymerization. *Macromolecules* **2016**, *49*, 537–546.

(33) Lee, D.; Ma, X.; Jung, J.; Jeong, E. J.; Hashemi, H.; Bregman, A.; Kieffer, J.; Kim, J. The Effects of Extended Conjugation Length of Purely Organic Phosphors on Their Phosphorescence Emission Properties. *Phys. Chem. Chem. Phys.* **2015**, *17*, 19096–19103.

(34) Zhang, G.; Fiore, G. L.; St. Clair, T. L.; Fraser, C. L. Difluoroboron Dibenzoylmethane PCL-PLA Block Copolymers: Matrix Effects on Room Temperature Phosphorescence. *Macromolecules* **2009**, *42*, 3162–3169.

(35) Zhang, G.; Kooi, S. E.; Demas, J. N.; Fraser, C. L. Emission Color Tuning with Polymer Molecular Weight for Difluoroboron Dibenzoylmethane-Polylactide. *Adv. Mater.* **2008**, *20*, 2099–2104.

(36) Wang, X. D.; Wolfbeis, O. S. Optical Methods for Sensing and Imaging Oxygen: Materials, Spectroscopies and Applications. *Chem. Soc. Rev.* **2014**, *43*, 3666–3761.

(37) Höckel, M.; Vaupel, P. Tumor Hypoxia: Definitions and Current Clinical, Biologic, and Molecular Aspects. *J. Natl. Cancer Inst.* **2001**, *93*, 266–276.

(38) Yudovsky, D.; Nouvong, A.; Pilon, L. Hyperspectral Imaging in Diabetic Foot Wound Care. *J. diabetes Sci. Technol.* **2010**, *4*, 1099–1113.

(39) Kalani, M.; Brismar, K.; Fagrell, B.; Ostergren, J.; Jorneskog, G. Transcutaneous Oxygen Tension and Toe Blood Pressure as Predictors for Outcome of Diabetic Foot Ulcers. *Diabetes Care* **1999**, *22*, 147–151.

(40) Lehner, P.; Staudinger, C.; Borisov, S. M.; Klimant, I. Ultra-Sensitive Optical Oxygen Sensors for Characterization of Nearly Anoxic Systems. *Nat. Commun.* **2014**, *5*, 4460–4474.

(41) Mathew, A. S.; DeRosa, C. A.; Demas, J. N.; Fraser, C. L. Difluoroboron β-Diketonate Materials with Long-Lived Phosphorescence Enable Lifetime Based Oxygen Imaging with a Portable Cost Effective Camera. *Anal. Methods* **2016**, *8*, 3109–3114.

(42) Felouat, A.; D'Aléo, A.; Charaf-Eddin, A.; Jacquemin, D.; Le Guennic, B.; Kim, E.; Lee, K. J.; Woo, J. H.; Ribierre, J.-C.; Wu, J. W.; et al. Tuning the Direction of Intramolecular Charge Transfer and the Nature of the Fluorescent State in a T-Shaped Molecular Dyad. *J. Phys. Chem. A* **2015**, *119*, 6283–6295.

(43) Kerr, C.; DeRosa, C. A.; Daly, M. L.; Zhang, H.; Palmer, G. M.; Fraser, C. L. Luminescent Difluoroboron β-Diketonate PLA–PEG Nanoparticles. *Biomacromolecules* **2017**, *18*, 551–561.

(44) Monici, M. Cell and Tissue Autofluorescence Research and Diagnostic Applications. *Biotechnol. Annu. Rev.* **2005**, *11*, 227–256.

(45) Bento, C. F.; Pereira, P. Regulation of Hypoxia-Inducible Factor 1 and the Loss of the Cellular Response to Hypoxia in Diabetes. *Diabetologia* **2011**, *54*, 1946–1956.

(46) Sen, C. K. Wound Healing Essentials: Let There Be Oxygen. *Wound Repair Regen.* **2009**, *17*, 1–18.

(47) Sun, N.; Ning, B.; Hansson, K. M.; Bruce, A. C.; Seaman, S. A.; Zhang, C.; Rikard, M.; DeRosa, C. A.; Fraser, C. L.; Wågberg, M.; et al. Modified VEGF-A MRNA Induces Sustained Multifaceted Microvascular Response and Accelerates Diabetic Wound Healing. *Sci. Rep.* **2018**, *8*, 17509–17520.

(48) Belanger, M. C.; Zhuang, M.; Ball, A. G.; Richey, K. H.; DeRosa, C. A.; Fraser, C. L.; Pompano, R. R. Labelling Primary Immune Cells Using Bright Blue Fluorescent Nanoparticles. *Biomater. Sci.* **2020**, *8*, 1897–1909.

(49) Li, X.; Liu, H.; Sun, X.; Bi, G.; Zhang, G. Highly Fluorescent Dye-Aggregate-Enhanced Energy-Transfer Nanoparticles for Neuronal Cell Imaging. *Adv. Opt. Mater.* **2013**, *1*, 549–553.

(50) Williams, D. B. G.; Lawton, M. Drying of Organic Solvents: Quantitative Evaluation of the Efficiency of Several Desiccants. *J. Org. Chem.* **2010**, *75*, 8351–8354.

(51) Irvine, M. W.; Costa, B. M.; Dlaboga, D.; Culley, G. R.; Hulse, R.; Scholefield, C. L.; Atlason, P.; Fang, G.; Eaves, R.; Morley, R.; et al. Piperazine-2,3-Dicarboxylic Acid Derivatives as Dual Antagonists of NMDA and GluK1-Containing Kainate Receptors. *J. Med. Chem.* **2012**, *55*, 327–341.

(52) Zhang, G.; Xu, S.; Zestos, A. G.; Evans, R. E.; Lu, J.; Fraser, C. L. An Easy Method to Monitor Lactide Polymerization with a Boron Fluorescent Probe. *ACS Appl. Mater. Interfaces* **2010**, *2*, 3069–3074.

(53) Thévenaz, D. C.; Monnier, C. A.; Balog, S.; Fiore, G. L. Luminescent Nanoparticles with Lanthanide-Containing Poly(Ethylene Glycol) − Poly(ε -Caprolactone) Block Copolymers. *Biomacromolecules* **2014**, *15*, 3994–4001.

(54) Frisch, M. J.; Trucks, G. W.; Schlegel, H. B.; Scuseria, G. E.; Robb, M. A.; Cheeseman, J. R.; Scalmani, G.; Barone, V.; Mennucci, B.; Petersson, G. A. Gaussian 09 Suite. *Gaussian 09 Revision A.1; Gaussian, Inc.: Wallingford, CT*. 2009.

(55) Tomasi, J.; Mennucci, B.; Cammi, R. Quantum Mechanical Continuum Solvation Models. *Chem. Rev.* **2005**, *105*, 2999–3093.

Chapter 4: Optimization of Fluorescence to Phosphorescence Ratio of Difluoroboron β-Diketonate Dyes for Wound Oxygen Imaging

4.1 Introduction

For ratiometric oxygen sensing reagents, the fluorescence to phosphorescence (F/P) ratio is critical for imaging. Ideally, phosphorescence should be strong enough so that the response to oxygen variation can be easily detected. For fluorescence, an optimized intensity is desired as it serves as an internal standard to indicate the sensor concentration. For sensors having blue fluorescence, it is also essential for generating effective colormetrics, especially in tissue imaging where the autofluorescence often interferes with the sensor signal. In Chapter 3, a series of new oxygen sensing dyes were developed for RGB imaging. Among those dyes, the iodide and C12 substituted difluoroboron dithienylmethane ($BF_2dtm(I)OC_{12}H_{25,}$ referred as BF_2dtm), exhibited excellent RGB alignment and effective imaging in wound beds. The red phosphorescence is valuable in diminishing light scattering and increasing tissue penetration. The preparation is facile with few steps. However, low intensity blue fluorescence is limitation, leading to low ratio of F/P during the imaging process. The ratio of F/P is directly related to sensing ability, and ratiometric sensors that have larger F/P are able to distinguish oxygen changes more easily and therefore, with greater resolution and accuracy of imaging results.

In this work, we explore a simple strategy for enhancing signal in the blue channel and optimizing F/P ratio by introducing an additional blue fluorescent dye, difluoroboron dibenzoymethane with fluorine and C12 substitution, $BF_2dbm(F)OC_{12}H_{25}$ (referred as BF_2dbm). As a commonly used carrier for encapsulating imaging agents or drugs, PLA nanoparticles can be readily taken up by cells.[1] However, the hydrophobicity of PLA might lead to nanoparticle aggregates as the wound bed dries out, because imaging with boron dye materials does not require covering. Though prior BNP studies showed that samples are non-toxic, still, residual material might be left in the wound beds and be more difficult to wash out between multiple imaging

sessions.[2] For certain dye formulations and biomedical uses, this is not desired. To address this issue, and broaden the range of NPs materials and scope of applications, BNPs with PEG blocks were also prepared. PEG can potentially stabilize the nanoparticles, prevent cellular uptake, and may affect wound imaging.[3] The two dyes were blended with PLA and PLA-PEG for nanoparticle fabrication, characterization and wound imaging. Oxygen sensing nanoparticles were applied on a murine wound model to monitor healing process.

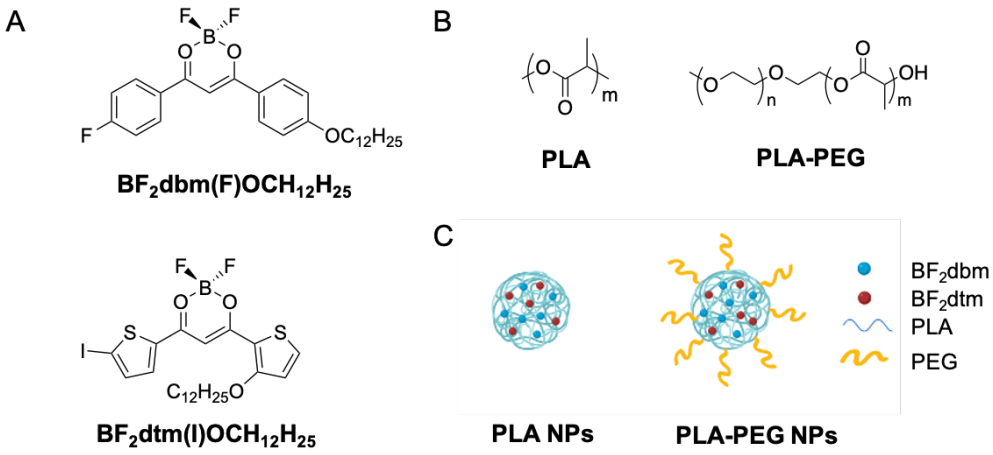

Figure 4. 1. Nanoparticle Design and Composition. A) Chemical Structures of boron dyes BF_2dbm (reference) and BF_2dtm (sensor). B) Chemical structures of polymer PLA and PLA-PEG used in nanoparticle fabrication. C) Schematic illustration of PLA nanoparticles (PLA NPs) and PLA-PEG nanoparticles (PLA-PEG NPs).

4.2 Results and Discussion

4.2.1 Optical Properties

In previous reports, optical properties of boron dyes BF_2dtm (in Chapter 3) and BF_2dbm[4] have been studied both in solution (Table 4.1) and in the solid state (Table S4.1). In CH_2Cl_2, the BF_2dtm dye showed strong absorption at 446 nm (ε = 69 600 M^{-1} cm^{-1}). This is important to avoid sample damage by photobleaching because the dye can be excited by blue light instead of a higher energy UV excitation source.[5] When the dye is confined to a PLA matrix, room temperature

phosphorescence is activated at 585 nm. The oxygen insensitive fluorescence and oxygen sensitive phosphorescence are well aligned with blue and red camera channels, respectively, making effective for ratiometric oxygen sensing via RGB imaging. As shown in Table 4.1, however, the BF_2dtm dye has a very low fluorescence quantum yield ($\Phi_F = 0.05$), providing little signal to indicate the dye concentration. In contrast, difluoroboron dibenzoymethane dyes are known for their high quantum yields ($\Phi_F = 0.99$) and have been utilized as bright cell labelling reagents in HeLa and immune cells.[1,3] The aromatic fluorine derivative was chosen in our design because it has blue-shifted fluorescence compared to the unsubstituted BF_2dbm dye, which can potentially increase the gap between fluorescence and phosphorescence in blue and red channels.

Table 4. 1. Optical Properties of Dyes dtm and dbm in CH_2Cl_2

Sample	λ_{abs} [a] (nm)	ε [b] (M^{-1} cm^{-1})	λ_{em} [c] (nm)	τ_F [d] (ns)	Φ_F [e]
BF_2dtm[f]	446	69 600	470	1.01	0.05
BF_2dbm[g]	400	55 000	435	1.77	0.99

[a]Absorption maxima. [b]Extinction coefficients calculated at the absorption maxima. [c]Fluorescence emission maxima excited at 369 nm. [d]Fluorescence lifetime excited with a 369 nm light-emitting diode (LED) monitored at the emission maximum. All fluorescence lifetimes are fitted with single-exponential decay. [e]Relative quantum yield, versus anthracene in EtOH as a standard.[6]

4.2.2 Oxygen Sensing Nanoparticles

The boron dyes were blended with polymers to form nanoparticles in aqueous suspension, suitable for application in a variety of biological contexts. Dyes and PLA or PLA-PEG were dissolved in DMF, precipitated into water, followed by dialysis against water to prepare PLA NPs and PLA-PEG NPs, respectively.[7] For optimal RGB imaging, it is best if the F and P intensities are well balanced and readily detectable. First, the fluorescence alone should be bright enough to be visualized over the background in tissue imaging. Second, the phosphorescence response from air to nitrogen is related to oxygen sensitivity K_{SV}. Therefore, the ratio of dyes BF_2dbm and BF_2dtm (i.e. relative dye loadings) were optimized before wound imaging. The overall dye loading

(BF_2dbm + BF_2dtm) was kept to 2.5% to parallel 25-30 kDa dye-PLA conjugates, for which a large fluorescence to phosphorescence gap is observed.[8] Relative masses of 1:9, 1:1, and 9:1 BF_2dbm to BF_2dtm were screened. As expected, the fluorescence signal increased relative to phosphorescence as the percentage of BF_2dbm dye increased. As illustrated in Figure 4.3, when the ratio of BF_2dbm to BF_2dtm is 1:9, the phosphorescence intensity is nearly 9 times the fluorescence intensity in nitrogen. However, the fluorescence is still too weak as shown in images taken under UV light (Figure 4.2A). For a ratio of 9:1, the phosphorescence is dimmer than fluorescence when under nitrogen, which would lead to very low oxygen sensitivity and is not optimal. When the ratio of BF_2dbm to BF_2dtm is 1:1, the fluorescence is visually brighter than that of 1:9 ratio, and the value of phosphorescence relative to fluorescence is 6. This value is in a comparable range to our previously reported boron dye polymer oxygen sensors.[2,9,10] Based on these results, NPs with 1:1 BF_2dbm to BF_2dtm loading was chosen for further characterization and wound imaging analysis.

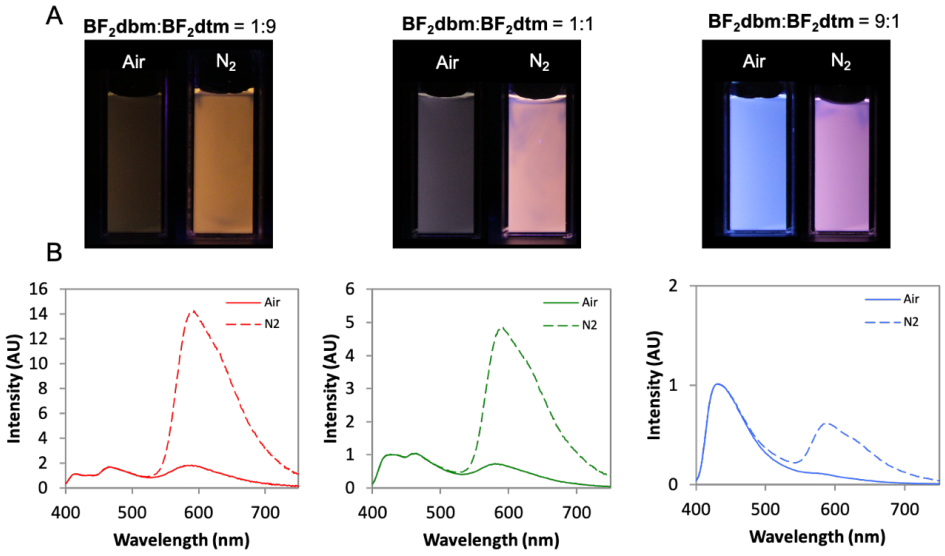

Figure 4. 2. Ratio Screening of Mixed Nanoparticles. A) Images taken under UV excitation (λ_{ex} = 369 nm) under air and nitrogen. B) Total emission of mixed nanoparticles under air and nitrogen.

Nanoparticles were characterized by DLS (Figure 4.3), where the PLA NPs hydrodynamic radii (R_H) are 57 nm with a polydispersity (PD) of 14%, and PLA-PEG NPs are 25 nm in radii with PD of 21%. These values are in the typical range for this class of boron dye PLA NPs.[1,11] The 1:1 PLA NPs were calibrated as previously described by purging with different oxygen percentages and recording the total emission.[9] As shown in Figure 4.4, the fluorescence intensity was steady, while the phosphorescence was gradually quenched with increasing oxygen levels from 0 to 100%. Since room temperature phosphorescence for boron dyes is usually activated when the dye is confined in a rigid matrix (e.g., PLA), the presence of phosphorescence suggests that dyes are encapsulated within PLA in the nanoparticles. At each oxygen level, an image of PLA NPs was captured in a dark room with the UV lamp on, for excitation (Figure 4.4C). The blue to pink response is clearly observed when the atmosphere changes from 100% O_2 to nitrogen (0% O_2).

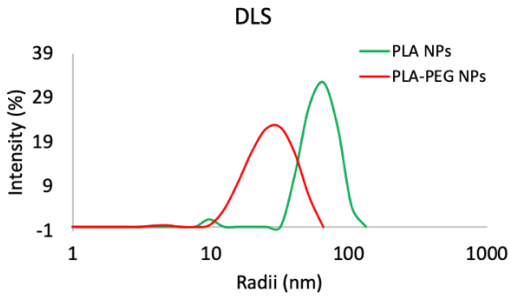

Figure 4. 3. Dynamic light scattering traces of PLA NPs and PLA-PEG NPs.

To compare the oxygen sensitivity of 1:1 PLA NPs with dtm NPs (i.e. no blue emitting dbm reference dye), the F/P ratio versus oxygen concentration plots for both kinds of NPs are shown in Figure 4.4B. As expected, the F/P ratio increased with more signal in fluorescence for the mixed dye NPs. This is not only important for tracking the oxygen-insensitive fluorescence reference, but also provides greater resolution and accuracy in imaging as the mixed dye NPs is

more capable of distinguishing changes in oxygen concentration. The oxygen calibration experiment suggests that the mixed dye NP material design might lead to improvements over the single dtm NPs in RGB wound imaging.

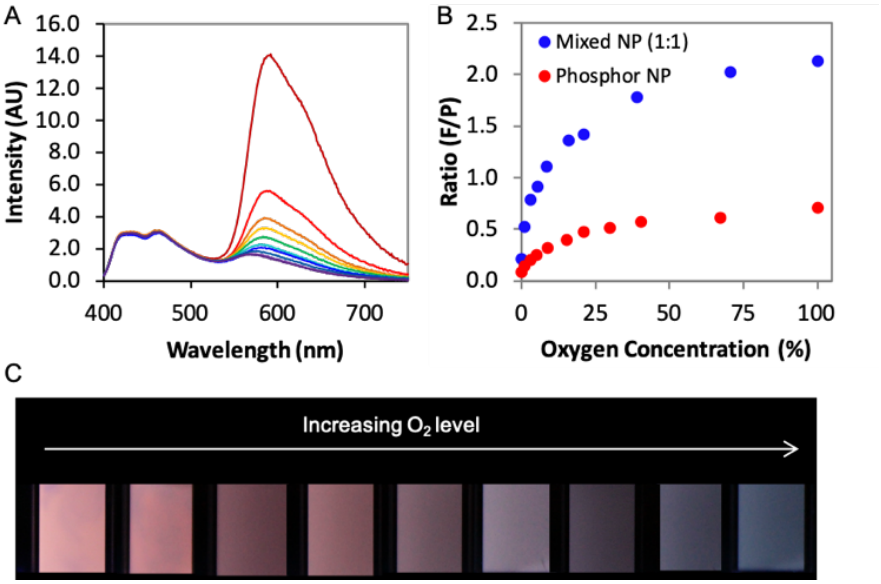

Figure 4. 4. Oxygen Calibration of 1:1 PLA NPs. A) Total emission of nanoparticles under varied oxygen concentration from 0-100 %. B) F/P ratio of 1:1 PLA NPs and pure dtm NPs, data taken from ref. CameraOpt. C) Visualization of 1:1 PLA NPs under UV excitation with varied oxygen concentration.

4.2.3 Wound Imaging

Oxygen level is an essential profile in evaluating wound healing. To demonstrate the wound oxygen imaging ability of the PEGylated nanoparticles, both PLA NPs and PLA-PEG NPs (Figure 4.1C) were fabricated and applied to dorsal wound beds. Wounds were monitored and imaging data were recorded every two days over the course of a week. The ratiometric images were analyzed in MATLAB. As shown in Figure 4.5, upon application, the nanoparticles emit mostly phosphorescence, indicative of low oxygen levels in early stage wounds. When the wounds start to heal, they consume less oxygen and return to normoxic conditions after one week. While both PLA NPs and PLA-PEG NPs enabled oxygenation maps over the time course, PLA NPs were

more sensitive to the local oxygen level changes. This is likely because PLA NPs are more readily adhere to and are taken up by the tissue.

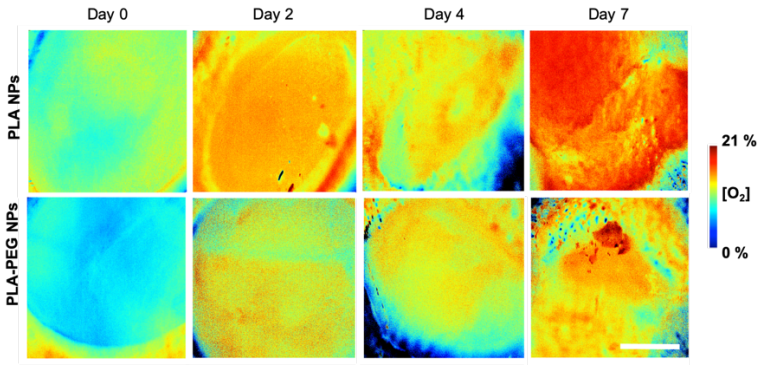

Figure 4. 5. Wound Oxygenation Monitored by PLA-NPs (top row) and PLA-PEG NPs (bottom row). Scale bar = 1 mm.

In order to compare the oxygen sensing performance of the mixed NP system with our previous dyes, the wound beds were also treated with single dye BF_2dtm PLA and BF_2dtm PLA-PEG nanoparticles, as well as BF_2nbm(I)PLA NPs. As shown in Figure 4.6, BF_2nbm(I)PLA responded to oxygen level changes within the wounds during healing. Single dye BF_2dtm NPs (BF_2dtm PLA and BF_2dtm PLA-PEG) were unable to offer effective colormetrics over time. The images were mostly dark and blue, likely due to weak fluorescence of the dtm dye and very low F/P values. The newly designed two-dye system significantly improved the imaging accuracy with both an enhanced blue reference signal. The two-dye nanoparticles have F/P ratios that are comparable to BF_2nbm(I)PLA (Figure S4.2), but they benefit from more convenient dye synthesis. In addition, the healing process was tracked by measuring the wound size, which showed the application of two-dye nanoparticles did not significantly affect or delay the wound closure (Figure S4.1). These results demonstrated an advancement in material design over chapter 4, where the mixed nanoparticle system exhibited improved resolution and accuracy as non-invasive oxygen sensing reagents wound healing evaluation by an RGB camera.

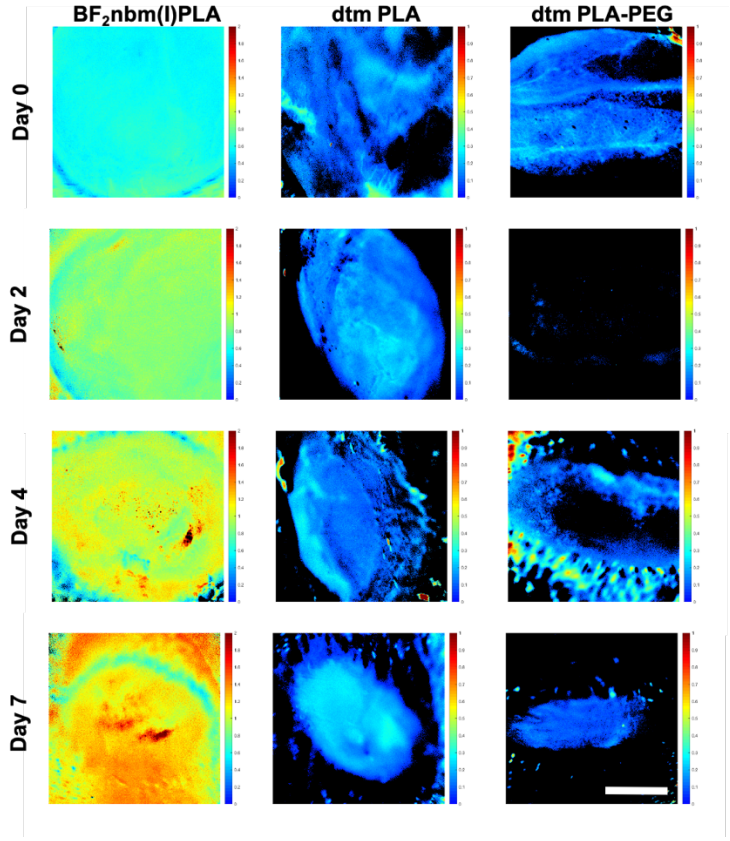

Figure 4. 6. Wound Oxygenation Monitored by Oxygen Sensing Nanoparticles from BF_2nbm(I)PLA, dtm PLA, and dtm PLA-PEG NPs. Scale bar = 1 mm.

4.2.4 Conclusion

Ratiometric oxygen sensing combined with RGB camera imaging provided an effective way to measure tissue oxygenation. This work demonstrated a simple two dye strategy to generate materials with an improved fluorescence to phosphorescence ratio by adding an oxygen-insensitive fluorescence compound BF_2dbm as a standard. Boron dyes BF_2dbm and BF_2dtm were embedded in PLA and PLA-PEG to form nanoparticle suspensions. A 1:1 ratio of BF_2dbm to BF_2dtm was determined to be optimal for oxygen calibration and imaging. Murine wound RGB imaging suggested that both PLA and PLA-PEG two dye nanoparticles serve as viable oxygen sensing reagents in monitoring the wound healing process. This work is a further advancement over the BF_2dtm oxygen sensing dye, described in Chapter 4, for RGB ratiometric imaging. The mixed dye

nanoparticle system is facile and could more precisely control the fluorescence and phosphorescence intensity compared with single dye nanoparticle, offering a general way to fabricate ratiometric oxygen sensors in other sensing applications with desired purpose. In the future, the particle stability will be investigated and optimized as the dyes are non-covalently linked to the polymer.

4.3 Experimental Section

4.3.1 Materials

The boron dyes $BF_2dtm(I)OC_{12}H_{25}$ and $BF_2dbm(F)OC_{12}H_{25}$ were prepared as previously described.[12] Polylactide (PLA) was prepared as previously described by Xu et al. using ethylene glycol as an initiator (M_n = 9,700 g/mol).[13] The poly(ethylene glycol) (PEG; 2,000 g/mol; Sigma) was dried via azeotropic distillation of toluene[14] prior to use as a macroinitiator for lactide polymerization to yield a poly(ethylene glycol)-poly(lactic acid) (PLA-PEG) block polymer (PLA= 10K, PEG = 2K; PDI = 1.05), as previously descibed.[11] All other chemicals were purchase from Sigma Aldrich and were used without further purification unless otherwise stated.

4.3.2 Luminescence Measurements

Steady-state fluorescence emission spectra were recorded on a Horiba Fluorolog-3 Model FL3-22 spectrofluorometer (double-grating excitation and double-grating emission monochromator). A 2 ms delay was used when recording the delayed emission spectra. Time-correlated single-photon counting (TCSPC) fluorescence lifetime measurements were performed with a NanoLED-370 (λ_{ex} = 369 nm) excitation source and a DataStation Hub as the SPC controller. Phosphorescence lifetimes were measured with a 1 ms multichannel scalar (MCS) excited with a flash xenon lamp (λ_{ex} = 369 nm; duration <1 ms). Lifetime data were analyzed with DataStation v2.4 software from Horiba Jobin Yvon. Fluorescence quantum yields (Φ_F) of initiator and polymer

samples in CH_2Cl_2 were calculated against anthracene as a standard as previously described, using the following values: Φ_F (anthracene) = 0.27,[6] (EtOH) = 1.360, n_D^{20} (CH_2Cl_2) = 1.424, Optically dilute CH_2Cl_2 solutions of the dyes, with absorbances <0.1 au, were prepared in 1 cm path length quartz cuvettes. Fluorescence spectra and lifetimes were obtained under ambient conditions (e.g., air, ~21% oxygen). Phosphorescence measurements were performed under a N_2 atmosphere. Vials were continuously purged in the headspace between the solution and the vial cap with analytical grade N_2 (Praxair) during measurements with a 12 mm PTFE/silicone/PTFE seal (Chromatography Research Supplies), connected by a screw cap. For 21% O_2 (i.e. air), measurements were taken under ambient conditions (open vial, no cap). Oxygen calibration was performed as previously described with Cole-Palmer flow gauges with mixtures of analytical grade O_2, N_2 and 1% O_2 (in N_2) gases (Praxair).[9] Fluorescence and phosphorescence lifetimes were fit to double exponential decays in nanoparticles. Fluorescence lifetimes in CH_2Cl_2 were fit to single exponential decays.

4.3.3 Nanoparticle Fabrication

Nanoparticles were fabricated as previously reported.[7] Materials (BF_2dbm, BF_2dtm, and polymers ~3 mg total; 2.5 % w/w dye loading) were dissolved in DMF (3 mL). The mass ratio of BF_2dbm to BF_2dtm dyes were 9:1, 1:1, and 1:9, to prepare three PLA nanoparticles in ratio screening experiment. The dye polymer solution was added dropwise to rapidly stirred DI water (27 mL). The homogeneous mixture was stirred for 30 min, and the nanoparticle suspensions were transferred into dialysis tubing (Specra/Pro, 12-14 kDa MWCO, Fisher Scientific) followed by dialysis against water for 24 h. Nanoparticle size and polydispersity were analyzed by dynamic light scattering (DLS, Wyatt, DynaPro). Nanoparticles were stored under 4 °C prior to use or further characterization.

4.3.4 Animal Preparation

All procedures were performed in accordance with the University of Virginia Institutional Animal Care and Use Committee. Male 9-week-old C57BL/6J mice (Jackson Laboratories) were anesthetized by inhalation of 1.5% isoflurane/98.5% medical air mixture. Dorsa were shaved and depilated before being sterilized with three alternating scrubs of povidone-iodine and 70% isopropanol. Full-thickness circular cutaneous wounds, which were 4 mm in diameter, were surgically made on the dorsum of each mouse. An analgesic (buprenorphine, 0.1 mg/kg) was administered following the surgery and the wounds were covered with a Tegaderm (3M) dressing. Mice were singly housed with food and water available *ad libitum*.

4.3.5 Imaging

A Grasshopper 3 camera (FLIR) was mounted to a Nikon Eclipse 80i microscope equipped with a UV excitation filter cube and 4X dry objective. An X-Cite 120 fluorescence illuminator (Lumen Dynamics) was used for nanoparticle excitation. A 415 nm longpass filter was placed in the light path immediately before the camera. A Canon EOS Rebel T6 camera equipped with a Canon 100 mm macro lens was used to document open wound sizes. A heated pad was placed on the microscope stage to maintain mouse body temperature during imaging. Wounds were imaged immediately after being made, and then again on days 2, 4, and 7 post-surgery. Tegaderm bandages were removed prior to wound imaging. Exposed wounds were kept moist with sterile 0.9% saline injection, USP. Nanoparticle imaging was performed on one wound at a time. To document background emissions, 20 video frames were recorded over 20 seconds on saline-moistened wounds. Saline was wicked from wounds using sterile cotton-tipped applicators immediately prior to nanoparticle addition. 40 uL of nanoparticle solution was added to the wound. After three minutes, 20 video frames of nanoparticle fluorescence and phosphorescence were captured over

20 seconds. UV excitation was blocked using the shutter during the three-minute normalization period in between video recordings. Nanoparticles were then flushed from the wound using 2 ml sterile 0.9% saline injection, USP. Tegaderm bandages were reapplied upon completion of imaging each day. Wound sizes were measured using ImageJ software to trace the regions lacking epidermis. ImageJ software was used to measure background-thresholded red channel emissions in wounds on days 2, 4, and 7, prior to nanoparticle additions on those days, to quantify nanoparticle adhesion to wound bed tissue. Data were analyzed by Two-Way Repeated Measures ANOVA in SigmaPlot 13.0 software. Raw images were analyzed in MATLAB to generate ratiometric oxygen map.

4.4 Acknowledgements

I thank Christopher DeRosa for initiating this project and for his ongoing assistance and collaboration. I acknowledge Fang Wang who helped with the synthesis, Richard Doty, Prof. Demas, and Bruce Corliss for developing the MATLAB software, and Anthony Bruce who performed the surgery and wound imaging. I thank Prof. Fraser for her guidance and assistance in preparing manuscripts and the National Institutes of Health (R01 CA167250) and the UVA Cancer Center (P30 CA44579) for financial support.

4.5 References

(1) Pfister, A.; Zhang, G.; Zareno, J.; Horwitz, A. F.; Fraser, C. L. Boron Polylactide Nanoparticles Exhibiting Fluorescence and Phosphorescence in Aqueous Medium. *ACS Nano* **2008**, *2*, 1252–1258.

(2) DeRosa, C. A.; Seaman, S. A.; Mathew, A. S.; Gorick, C. M.; Fan, Z.; Demas, J. N.; Peirce, S. M.; Fraser, C. L. Oxygen Sensing Difluoroboron β-Diketonate Polylactide Materials with Tunable Dynamic Ranges for Wound Imaging. *ACS Sensors* **2016**, *1*, 1366–1373.

(3) Belanger, M. C.; Zhuang, M.; Ball, A. G.; Richey, K. H.; DeRosa, C. A.; Fraser, C. L.; Pompano, R. R. Labelling Primary Immune Cells Using Bright Blue Fluorescent Nanoparticles. *Biomater. Sci.* **2020**, *8*, 1897–1909.

(4) Morris, W. A.; Sabat, M.; Butler, T.; DeRosa, C. A.; Fraser, C. L. Modulating Mechanochromic Luminescence Quenching of Alkylated Iodo Difluoroboron Dibenzoylmethane Materials. *J. Phys. Chem. C* **2016**, *120*, 14289–14300.

(5) Borisov, S. M.; Fischer, R.; Saf, R.; Klimant, I. Exceptional Oxygen Sensing Properties of New Blue Light-Excitable Highly Luminescent Europium(III) and Gadolinium(III) Complexes. *Adv. Funct. Mater.* **2014**, *24*, 6548–6560.

(6) Demas, J. N.; Crosby, G. A. The Measurement of Photoluminescence Quantum Yields. A Review. *J. Phys. Chem.* **1971**, *75*, 991–1024.

(7) Zhuang, M.; Perkins, A.; DeRosa, C. A.; Butler, T.; Demas, J. N.; Fraser, C. L. Meta-Dimethoxy-Substituted Difluoroboron Dibenzoylmethane Poly(Lactic Acid) Nanoparticles for Luminescence Anisotropy. *Macromol. Chem. Phys.* **2018**, *219*, 1800240–1800249.

(8) Zhang, G.; Kooi, S. E.; Demas, J. N.; Fraser, C. L. Emission Color Tuning with Polymer Molecular Weight for Difluoroboron Dibenzoylmethane-Polylactide. *Adv. Mater.* **2008**, *20*, 2099–2104.

(9) Zhang, G.; Palmer, G. M.; Dewhirst, M. W.; Fraser, C. L. A Dual-Emissive-Materials Design Concept Enables Tumour Hypoxia Imaging. *Nat. Mater.* **2009**, *8*, 747–751.

(10) DeRosa, C. A.; Kolpaczynska, M.; Kerr, C.; Daly, M. L.; Morris, W. A.; Fraser, C. L. Oxygen-Sensing Difluoroboron Thienyl Phenyl β-Diketonate Polylactides. *Chempluschem* **2017**, *82*, 399–406.

(11) Kersey, F. R.; Zhang, G.; Palmer, G. M.; Dewhirst, M. W.; Fraser, C. L. Stereocomplexed

Poly(Lactic Acid)−Poly(Ethylene Glycol) Nanoparticles with Dual-Emissive Boron Dyes for Tumor Accumulation. *ACS Nano* **2010**, *4*, 4989–4996.

(12) Morris, W. A.; Liu, T.; Fraser, C. L. Mechanochromic Luminescence of Halide-Substituted Difluoroboron β-Diketonate Dyes. *J. Mater. Chem. C* **2015**, *3*, 352–363.

(13) Zhang, G.; Xu, S.; Zestos, A. G.; Evans, R. E.; Lu, J.; Fraser, C. L. An Easy Method to Monitor Lactide Polymerization with a Boron Fluorescent Probe. *ACS Appl. Mater. Interfaces* **2010**, *2*, 3069–3074.

(14) Thévenaz, D. C.; Monnier, C. A.; Balog, S.; Fiore, G. L. Luminescent Nanoparticles with Lanthanide-Containing Poly(Ethylene Glycol) − Poly(ε -Caprolactone) Block Copolymers. *Biomacromolecules* **2014**, *15*, 3994–4001.

Chapter 5: Folic Acid Conjugated Difluoroboron β-Diketonate PLA-PEG Nanoparticles for Tumor Hypoxia Imaging

5.1 Introduction

In cancer biology, oxygen is a critical factor in investigating rumor metabolism.[1,2] Hypoxia occurs in primary solid tumor regions when tumor cells grow beyond the diffusion distance of oxygen supplied by vasculature. The presence of hypoxia triggers growth factors such as vascular endothelial growth factor (VEGF) which in turn lead to cancer angiogenesis and tumor microenvironment region being very chaotic and hetereogeneous. Clinically, tumor hypoxia is associated with resistance to therapy. In radiotherapy, hypoxic regions (defined as pO_2 less than 10mmHg) are three times more radioresistant than well-oxygenated areas. Because of chaotic vasculature, hypoxic regions also exhibit poor drug delivery.[3–5] As hypoxia remains a major hinderance in therapeutic outcomes for most cancers, preclinical techniques for quantifying hypoxia are significant. Understanding tumor oxygenation has great importance to address preclinical problems. Among oxygen sensing techniques, oxygen imaging based on phosphorescence quenching provides an effective way to study tumor hypoxia, with temporal and spatial resolution.[6,7]

Previsouly, our lab has demonstrated that stereocomplex nanoparticles fabricated from dye-PLLA-PEG and PDLA-PEG exhibited improved aqueous stability and good accumulation in the tumor tissue.[8] The nanoparticle design strategy holds several merits. First, PEGylation is known for increased stability and stealth properties for prolonged circulating. Second, the formation of stereocomplex nanoparticles yielded smaller particle size, which is beneficial for uptake. Compared with non-stereocomplexation, it also even has greater aqueous stability. The *in vivo* biodistribution study indicated successful delivery of the stereocomplex nanoparticles to tumors and strong targeting efficiency as passive targeting agents achieved by enhanced permeation and retention (EPR) effect. Although stereocomplex PEGylated nanoparticles found

applications in short-term imaging, these materials displayed non-specific binding, modest cell accumulatio, and slow cellular internalization.[10–12] To address these issues, active targeting has been developed providing improved delivery and accumulation in tumor microenvironments, with spatial specificity.[13] Active targeting of drug-loaded nanoparticles has been extensily utilized in cancer therapeutics. Depending on ligand-receptor interactions, drugs with targeting group can selectively bind to regions of interest due to higher affinity in diseased tissues than healthy tissues. It can effeciently increase the quantity of drug delivered to the desired location compared to passive targeting. Active targeting is usually achieved by surface functionalization with receptors that could bind to ligands overexpressed on the tumor cells, such as peptides, proteins, nuclei acids, and aptamers.[14–16] A vast number of receptors have been realized and synthesized for *in vitro* and *in vivo* study. For example, RGD peptide binds to $\alpha_v\beta_3$ integrin, which are found to present on glioma cells and tumor microenvironment vasculature.[17]

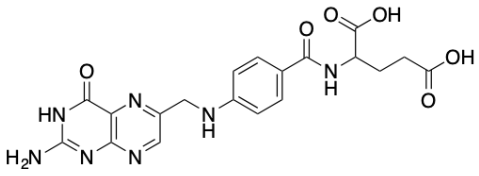

Folic acid (FA)

In this work, we strived to achieve active targeting for multicolor imaging and oxygen sensing. One advantage of PEGylation is that the end group of PEG can be easily functionalized to allow modification with targeting groups. We started with a commonly used biomolecule, folic acid (FA). Folic acid is known to selectively binds to folate receptors that are overexpressed on many tumor types.[12,18–20] It exhibits greater affinity to cancer cells than healthy cells, and could be internalized by cells through receptor mediated endocytosis. The stereocomplex nanoparticle strategy was adapted as shown in Figure 5.1A. Five previously developed fluorophores were

chosen to design FA conjugated nanoparticles for multicolor probes and oxygen imaging. The boron dyes with phenolics were coupled with PLLA-PEG to form dye polymer conjugates (**P1**-**P5**), which were coprecipitated with FA conjugated polymers PDLA-PEG-FA to yield stereocomplex nanoparticles. The functionality of FA conjugation was determined and calibrated by UV absorbtion. The optical properties of these FA conjugated nanoparticles were studied. To evaluate the uptake ability, the FA conjugated blue nanoparticles were tested in tumor cells.

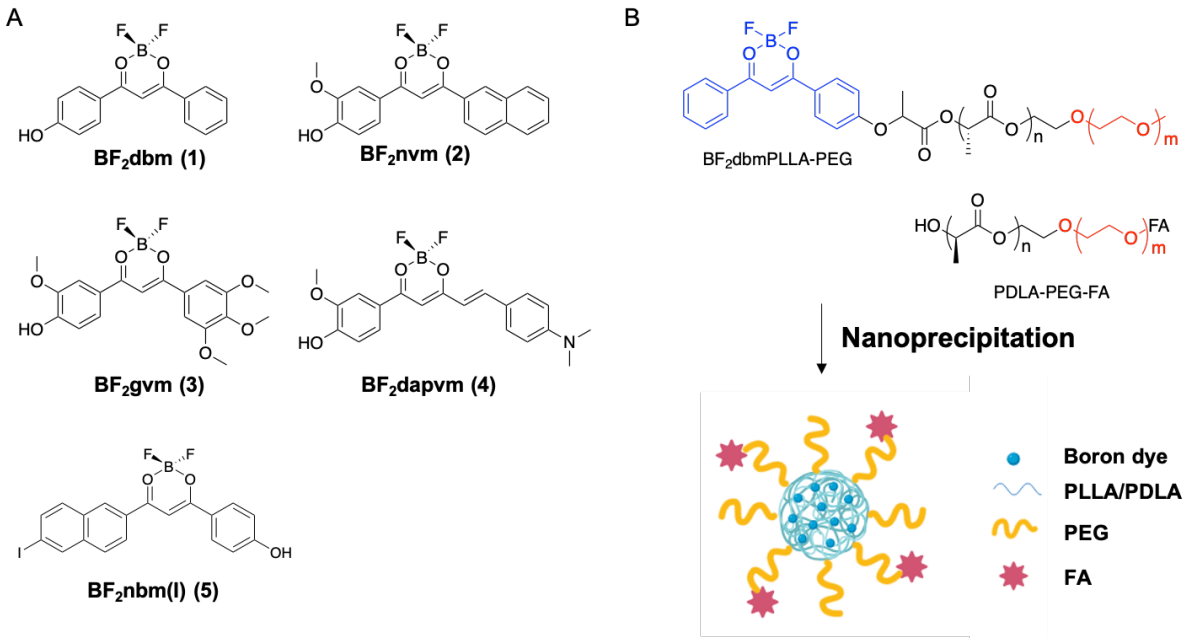

Figure 5. 1. FA Nanoparticle Composition and Design. A) Chemical structures of boron dyes. B) Chemical structures of polymers (using dye 1 as an example) and schematic illustration of folic acid (FA) conjugated nanoparticles.

5.2 Results and Discussion

5.2.1 Synthesis

Dye-polymer conjugates (**P1**-**P5**) were prepared as previously described via Mitsunobu reaction conditions.[8] To synthesize full-range oxygen sensing, BF_2nbm(I)PLLA-PEG (**P5**), the β-diketones was first generated via commercially available ketone and ester reagents (Scheme 6.1). The β-diketone coordinates to difluoroboron to form a phenol-functionalized dye, which allowed

for Mitsunobu post-polymerization modification. The coupling reaction was monitored by color changes. When DIAD was added, the yellow boron dye solution turned red, possibly due to deprotonation of the phenol dye. As an ether group was formed during the reaction, the solution gradually became to yellow again. The reaction was allowed to run for three days for optimal coupling. The dye precursor was characterized by ^{1}H NMR spectroscopy, and the dye polymer conjugates was analyzed by GPC, as shown in Figure S5.1-S5.4. The successful coupling of the boron dye to the PLLA-PEG was confirmed via GPC; the UV absorbance was present and in accordance with polymer elution verified by the RI trace. The polymers were characterized with GPC, and the optical properties of **P1**-**P5** were studied in CH_2Cl_2 (Table S6.1). Those data were all in accordance with the literature.[8]

Scheme 5.1. Synthesis of BF_2nbm(I)PLLA-PEG.

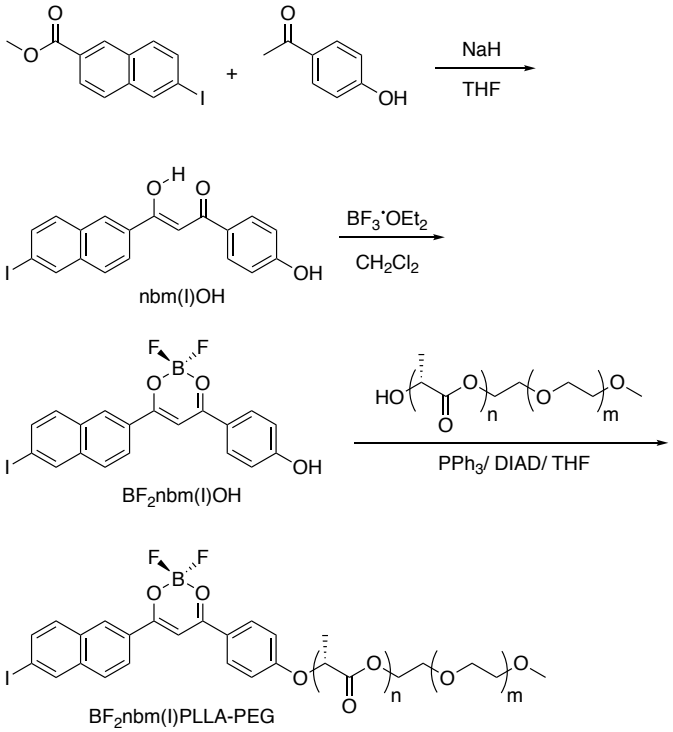

To synthesize FA conjugated polymers, solvent-free ring-opening polymerization with commercially available Boc-NH-PEG-OH as the initiator and D-lactide the monomer was employed (Scheme 6.2). Boc protection prevents interaction between the active amine group and lactide. After deprotection, a method reported by Xiong et al.[21] was used to crosslink the primary amine to the carboxylic acid. The coupling reaction involving NHS and DCC created activated acid intermediates for conjugation with the amine to form amides at physiological pH values.[22] The reaction was allowed to run for 24 hours, followed by dialysis against DMSO to remove small molecules and DI water to remove DMSO. The successful conjugation of folic acid was confirmed by UV absorption, as characteristic peaks around 289 nm and 364 nm were observed (Figure S5.5). According to a standard calibration curve, this approach generated 78% functionality of folic acid in the FA-PEG-PDLA, which is sufficient for targeting and cellular uptake (Figure S5.6). In summary, the synthesis of folate conjugated polymer and preparation of nanoparticles were conducted under mild conditions in controllable ways. This is important given surface density of the targeting group is known to be a significant factor in delivery efficiency.[23] Also, the primary amine end group on NH_2-PEG-PDLA allows coupling with many other biomolecules and proteins for active targeting.

Scheme 5.2. Synthetic pathway of FA-PEG-PDLA

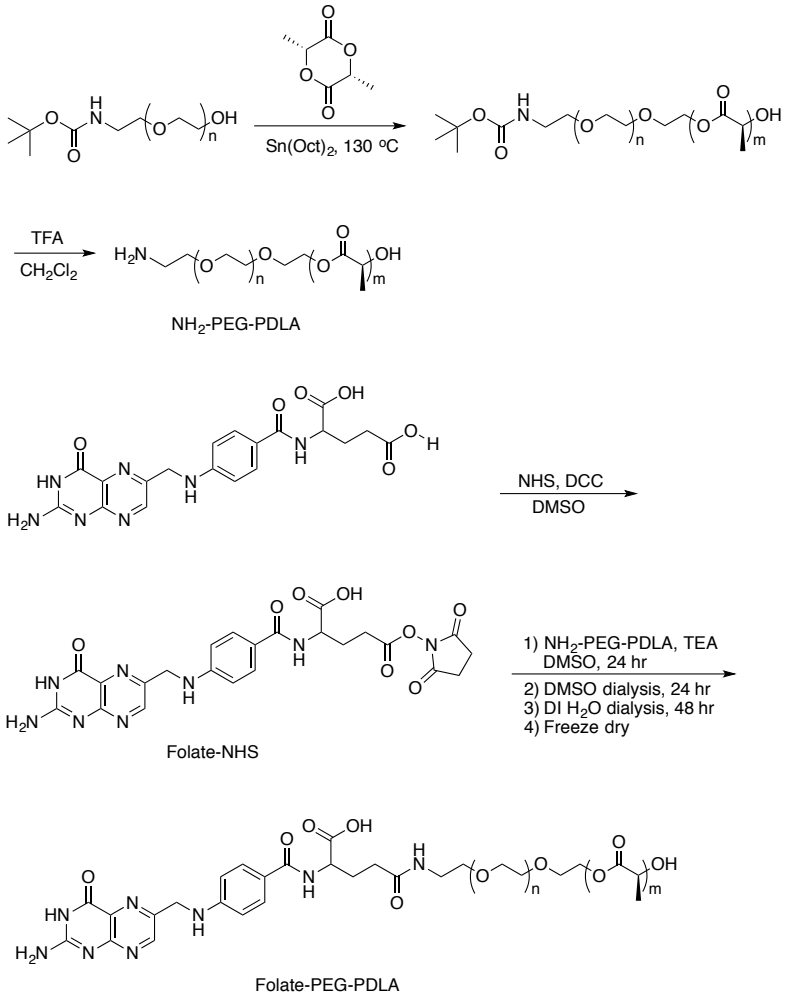

5.2.2 Nanoparticles

Stereocomplex nanoparticles (**NP1**-**NP5**) were fabricated as previously described.[8] In briefly, equal mass of PDLA-PEG-FA and dye-PLLA-PEG were dissolved in DMF. Because PDLA-PEG-FA showed limited soluility in common organic solvents, the mixture was sonicated to facilitate dissolution and yield a homogeneous solution before adding to water. The molecular weight of Boc-NH-PEG-OH is 5 kDa, longer than mPEG-OH (2 kDa) used to produce dye-PLLA-PEG. This is to avoid folic acid crowding with neighboring PEG antenna and to fully expose targeting groupsa on the nanoparticle surface. Based on a previous report, the stererocomplexation is expected to offer less nanoparticle aggregation and more stable nanoparticles in aqueous

environments, especially for long-term circulation. In addition, it offered smaller nanoparticle sizes, which is also beneficial for stealth properties.[8] Nanoparticles were characterized by DLS (Table 6.1). It was observed that for **NP1**-**NP5** the hydrodynamic radius was around 50 nm (ranging from 44 nm to 63 nm), and the polydispersities were low (< 25 %). These are typical values for particles made from BF_2bdkPLA materials and further support the formation of nanoparticle suspensions.[8] This mix-and-match strategy for fabricating stereocomplex nanoparticles can be easily adapted with different boron dye polymer conjugates and bioconjugates to generate active targeting materials for specific biological purposes.

Table 5. 1. Nanoparticle Characterization Data.

Boron Dye	#	R_H[a] (nm)	PD[a] (%)	λ_{abs}[b] (nm)	λ_{em}[c] (nm)	τ_F[d] (ns)	λ_{RTP}[e] (nm)	τ_{RTP}[f] (ms)
BF_2dbm	**NP1**	63	19	379	425	11.4	518	151
BF_2nvm	**NP2**	44	20	420	487	31.5	555	95.1
BF_2gvm	**NP3**	45	20	415	545	29.8	565	53.0
BF_2dapvm	**NP4**	57	23	530	613	6.30	N.A.[g]	N.A.[g]
BF_2nbm(I)	**NP5**	50	22	375	468	1.54	567	2.79

[a]Dynamic light scattering (DLS) of **NP1-NP5**; hydrodynamic radius (R_H) radii and polydispersity (PD) determined by DLS. [b]Absorption maxima. [c]Fluorescence emission maxima excited at 369 nm, except sample **4** and **5** (λ_{ex} = 485 nm). [d]Fluorescence lifetime excited with a 369 nm light-emitting diode (LED) monitored at the emission maximum. All fluorescence lifetimes are fitted with multiexponential decays. [e]Delayed emission spectra maxima under N_2 at 298 K. Excitation source: xenon flash lamp. [f]Pre-exponential weighted RTP lifetime. Excitation source: xenon flash lamp; RTP lifetime fit to double-exponential decay. [g]No phosphorescence was observed.

Because oxygen sensing and imaging requires long-term circulation, it is necessary to evaluate the nanoparticle stability in biologically relevant buffer over the time course at elevated temperature (i.e., body temperature). Factors including hydrophobicity of the nanoparticle core, surface charge of the polymer, and composition and properties (e.g., pH) of the buffer, could all affect the nanoparticle stability. Two types of cell culture medium, MCF7 and MDA-MB-231, were used to dilute the nanoparticles. At 37 °C, the radii of nanoparticles were recorded every three hours during the time course (Figure 5.2). It was found for **NP1** and **NP2**, the nanoparticle size remained relatively constant over 40 hours, although the size of **NP2** increased slightly after

about one day (i.e., 20 hours). This phenomenon known as swelling is due to an ion gradient between the nanoparticle matrix and surroundings, leading to ion diffusion and osmosis. Swelling (increase in size) or deswelling (decrease in size) is commonly observed for polymeric nanoparticles when they are exposed into aqueous environments. The stability of **NP3** was optimized only in MDA-MB-231 cell culture medium, as aggregation occurred rapidly in the other medium after several hours, while **NP4** showed stable size in MCF cell culture medium over the time course. For **NP5**, it remained stable for one day in MCF cell culture medium and two days in MDA-MB-231 cell culture medium. The differences in stability might due to dye aggregation or degradation given dye is the only variable among these nanoparticles. Optical measurements should be involved to fully understand how they interact with the medium in future studies. Nevertheless, the stability of **NP1** and **NP5** over the short term is sufficient for a proof of concept in oxygen sensing and imaging.

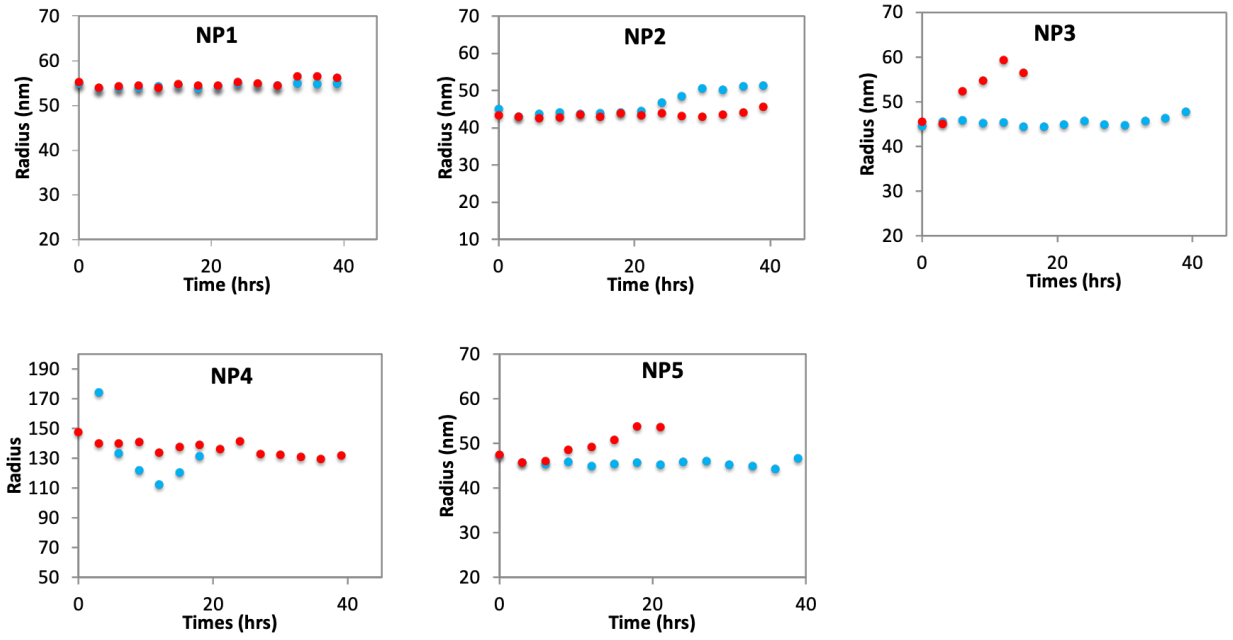

Figure 5. 2. Stability of Nanoparticles. The radius of nanoparticles was monitored by DLS in cell culture medium, respectively. Red dots: MCF cell culture medium; blue dots: MDA-MB-231 cell culture medium. The lack of data points is due to aggregation that exceeds the instrument limitation.

5.2.3 Optical Properties

The optical properties of nanoparticles are listed in Table 6.1. As expected, with increased π-conjugation and electron-donating groups (-OMe and -$N(CH_3)_2$) from **NP1**-**NP4**, the fluorescence emission is red-shifted (λ = 188 nm). The emission of these four types of nanoparticles spans the visible range, making them useful in multicolor imaging (Figure 5.3). In particular, the red fluorescence (λ_{em} = 613 nm) of **NP4** can be potentially be used in deeper tissue imaging to minimize light scattering and for improved tissue penetration of light. In UV absorption, the characteristic peak of FA was observed, indicating the presence of FA within the nanoparticles (Figure 5.3). The maximum absorption of **NP1**-**NP3** ranges from 379 nm to 420 nm, can be effectively excited with a 405 laser in fluorescence imaging. In comparison with previously reported non-FA conjugated nanoparticles, the absorption and emission are similar, though the lifetime increased slightly.

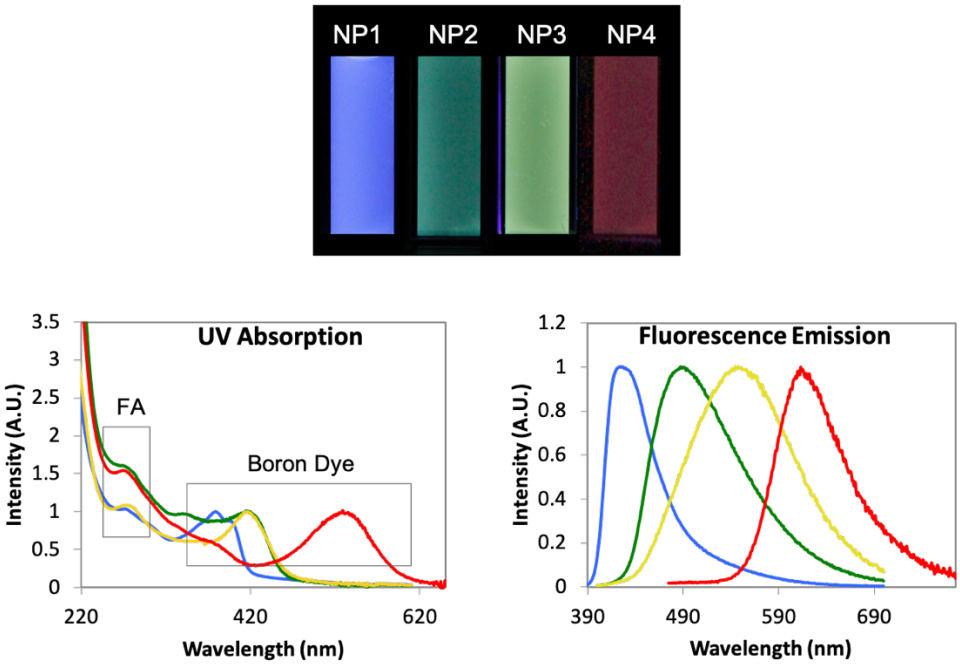

Figure 5. 3. Fluorescence Absorption and Emission of **NP1**-**NP4**. Images of folic acid targeted multicolor nanoparticles under UV excitation (top), and corresponding UV absorption (bottom left)

with FA peak and aromatics peak outlined, and the total emission spectra (bottom right). Fluorescence emission maxima were excited at 369 nm except **NP4** (λ_{ex} = 485 nm).

Room temperature phosphorescence (RTP) was observed for **NP1**-**NP3** when under nitrogen. With extended conjugation and donating groups, the RTP redshifted. Since room temperature phosphorescence for boron dyes is usually activated when the dye is confined in a rigid matrix (e.g., PLA), the presence of phosphorescence further supports that dyes were encapsulated within polymers in the nanoparticles. However, phosphorescence was not detected for **NP4**, which is probably due to twisting and nonradiative decay caused by the presence of the vinyl group. Nevertheless, the optical properties of FA conjugated nanoparticles **NP1**-**NP4** followed the same trend with the non-FA conjugated nanoparticles, suggesting that FA did not significantly affect the optical properties of boron dye polymers.

The nanoparticles based on the full range oxygen sensing dye-polymer, **NP5**, were studied under varying atmospheres. When in oxygen where the phosphorescence is quenched, the total emission was mostly blue fluorescence. When in nitrogen and the phosphorescence is no longer quenched, the nanoparticles exhibited strong yellow emission. Oxygen calibration was conducted when purging nanoparticles with varying percentages of oxygen (i.e., 0-100 %). As expected, phosphorescence intensity decreases with increasing oxygen concentration. The oxygen sensing capability of **NP5** was in accordance with non-FA conjugated stereocomplexed nanoparticles (Figure S5.7), enabling it to serve as ratiometric oxygen sensor for tumor hypoxia.

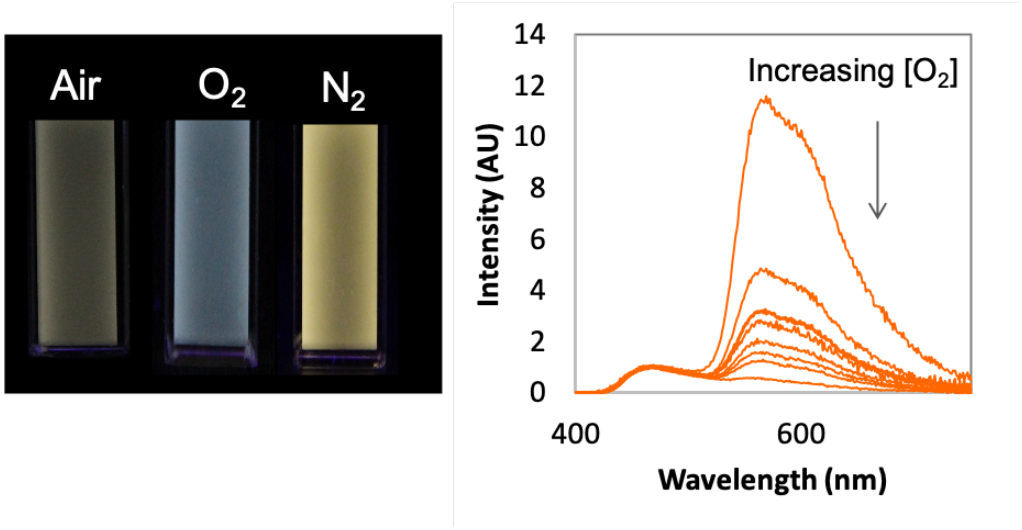

Figure 5. 4. Oxygen Sensing **NP5**. Images of nanoparticles under air, oxygen, and nitrogen (left) and the total emission at varying oxygen levels (right).

5.2.4 Cellular Uptake

To evaluate tumor accumulation and whether these newly prepared nanoparticles will be localized, **NP1** was chosen for preliminary cellular uptake studies. These nanoparticles contain a blue dye with high quantum yield and bright fluorescence, ideal for labelling cells and tracking localization. As a control, analogous nanoparticles without FA conjugation were also fabricated, both of which exhibited intense blue emission (Figure 5.5A). The cellular uptake experiments were conducted by Ashlyn Rickard in Palmer Lab at Duke University. For boron nanoparticles with and without FA conjugation, referred as BNP+FA and BNP-FA, respectively, the concentrations and incubation times were studied in tumor cells. As shown in Figures 5.5, BNP+FA and BNP-FA were diluted to achieve a series of concentrations (1 mg/mL, 500 μg/mL, 200 μg/mL, 100 μg/mL). When the concentration is 1 mg/mL, the uptake of BNP-FA was greater than that of BNP+FA. This is unexpected; maybe FA is not fully exposed on the surface in a concentrated suspension, resulting in less interaction between FA and the FA receptor. However, in diluted nanoparticles, the presence of FA significantly improved the uptake, especially when the concentration was 500

μg/mL. Using 500 μg/mL as an optimal concentration, the incubation time was also screened (0.5, 1, 2, 4, 6 hours). It was observed that generally, more cells take up BNP+FA than BNP-FA. When the incubation time was 4 hours, the uptake of BNP+FA was most effective.

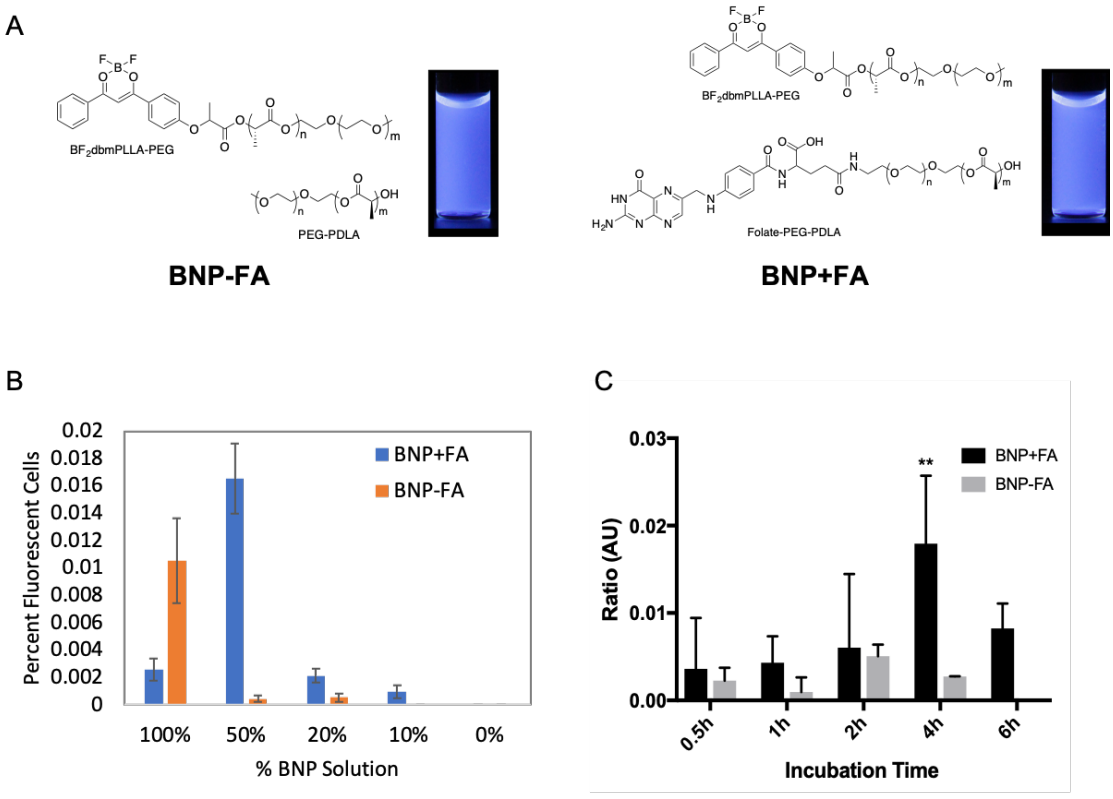

Figure 5. 5. Cellular Uptake Study. A) Chemical structures of BNP-FA and BNP+FA. B) Percentage of cells labelled at varying nanoparticle concentration. C) Percentage of cells labelled at varying incubation times.

5.2.5 Conclusion

Materials prepared in this chapter are designed to further improve delivery and accumulation in the tumor microenvironment. An active mechanism is targeted by conjugating FA, a biomolecule that has greater affinity to tumor cells than healthy cells, to PDLA-PEG block copolymer. The FA decorated polymer was coprecipitated with dye-PLLA-PEG to form stereocomplexed nanoparticles with greater aqueous stability. Multicolored (**NP1**-**NP4**) and

oxygen sensing **NP5** nanoparticles were fabricated, all of which maintained their optical properties as promising fluorescence probes and oxygen sensors, respectively. The synthetic strategy provided a decent FA functionality, sufficient for cellular uptake. Preliminary cellular uptake experiments revealed that the FA conjugation significantly improved the delivery to tumor sites. Future work will involve developing **NP5** as oxygen sensing tools for tumor hypoxia imaging. This is a novel material strategy developed for active targeting. It can be readily modified with other active groups and fluorohpores, opening many more possibilities in oxygen sensing applications using the family of our boron dye-polymer.

5.3 Experimental Section

5.3.1 Materials

Tert-butyloxycarbonyl protected polyethylene glycol (Boc-NH-PEG, Sigma Aldrich, MW = 5000 Da) was dried over azeotropic distillation in toluene according to a previous protocol.[24] The Boc-NH-PEG was stored under nitrogen prior to use. The lactide monomer ($_L$-lactide and $_D$-lactide) were generous gifts from Corbion Purac. Lactide was purified by recrystallization twice from diethyl ether and was dried under vacuo overnight. The polymer, HO-PLLA-PEG (M_n = 9 300 Da, Đ = 1.08) difluoroboron β–diketonate dyes, and their corresponding PEG-PLLA conjugates involved in this study were all prepared as previously described.[8] All other chemicals were reagent grade from Sigma Aldrich and were used without further purification.

5.3.2 Methods

^{1}H NMR spectra (600 MHz) were recorded on a Varian VMRS 600/51 instrument in $CDCl_3$ or d_6-DMSO. ^{1}H NMR spectra were referenced to the residual signals for protiochloroform (7.26 ppm), protioDMSO (2.50 ppm), and protioacetone (2.09 ppm). In the ^{1}H NMR assignments, aromatic positions are defined for phenyl (Ph) and naphthyl (Np) positions. Coupling constants

are given in hertz. Number average molecular weights (M_n), weight average molecular weights (M_w) and polydispersity index (Đ) were determined by gel permeation chromatography (GPC) (THF, 25 °C, 1.0 mL/min) using multiangle laser light scattering (MALLS; λ = 658 nm, 25 °C) and refractive index (λ = 658 nm, 25 °C) detection. A Polymer Laboratories 5 μm mixed-C guard column and two GPC columns along with Wyatt Technology Corp. (Optilab REX interferometric refractometer, miniDawn TREOS laser photometer) and Agilent Technologies instrumentation (series 1260 HPLC) and Wyatt Technology software (ASTRA 6.0) were used for analysis. The incremental refractive index (*dn*/*dc*) was determined by a single-injection method assuming 100% mass recovery from the columns. UV−vis spectra were recorded on a Hewlett-Packard 8452A diode-array spectrophotometer.

5.3.3 Luminescence Measurements

Steady-state fluorescence emission spectra were recorded on a Horiba Fluorolog-3 Model FL3-22 spectrofluorometer (double-grating excitation and double-grating emission monochromator). A 2 ms delay was used when recording the delayed emission spectra. Time-correlated single-photon counting (TCSPC) fluorescence lifetime measurements were performed with a NanoLED-370 (λ_{ex} = 369 nm) excitation source and a DataStation Hub as the SPC controller. Phosphorescence lifetimes were measured with a 1 ms multichannel scalar (MCS) excited with a flash xenon lamp (λ_{ex} = 369 nm; duration <1 ms). Lifetime data were analyzed with DataStation v2.4 software from Horiba Jobin Yvon. Fluorescence quantum yields (Φ_F) of initiator and polymer samples in CH_2Cl_2 were calculated against anthracene or Rhodamine G6 (Exciton) as a standard as previously described, using the following values: Φ_F (anthracene) = 0.27,[25] Φ_F (Rhodamine G6) = 0.97, n_D^{20} (EtOH) = 1.360, n_D^{20} (CH_2Cl_2) = 1.424, Optically dilute CH_2Cl_2 solutions of the dyes, with absorbances <0.1 au, were prepared in 1 cm path length quartz cuvettes. Fluorescence spectra

and lifetimes were obtained under ambient conditions (e.g., air, ~21% oxygen). Phosphorescence measurements were performed under a N_2 atmosphere. Dilute nanoparticle solutions (absorbance = ~0.1) were purged with N_2 (Praxair) in a cuvette and sealed with a 12 mm PTFE/silicone/PTFE seal (Chromatography Research Supplies), connected by a screw cap. Vials were continuously purged in the headspace between the solution and the vial cap with analytical grade N_2 (Praxair) during measurements. For 21% O_2 (i.e. air), measurements were taken under ambient conditions (open vial, no cap). Fluorescence and phosphorescence lifetimes were fit to double or triple exponential decays in nanoparticles. Fluorescence lifetimes in CH_2Cl_2 were fit to single exponential decays.

5.3.4 Nanoparticles

Stereocomplex nanoparticles were fabricated as previously described.[8] In brief, the oxygen-sensing polymer BF_2nbm(I)PLLA-PEG (45 mg) and of mPEG-PDLA (45 mg) were dissolved in DMF (9 mL). The solution was briefly heated with a heat gun to facilitate polymer dissolution. With a syringe pump, the DMF solution was added to 81 mL of DI water at a constant rate (1mL/min). The solution was filtered (Whatman filter paper) and DMF was removed by dialysis (Select/Por; 12-14 kDa molecular weight cutoff) with frequent water changes overnight (24 h). The nanoparticle solution was filtered (Whatman 200 nm Anotop filter) and characterized by dynamic light scattering (DLS, Wyatt, DynaPro).

5.3.5 Synthesis

nbm(I)OH. The iodo-substituted, naphthyl-phenyl ligand was prepared as previously described by Jin et al for 3-hydroxy-1-(4-hydroxyphenyl)-3-phenylprop-2-en-1-one,[26] except the aromatic ester 6-iodo, 2-methylnaphthoate was used in place of methyl benzoate to yield a dark brown powder: 178 mg (13%). ^{1}H NMR: (600 MHz, D_6-DMSO) δ17.38 (s, 1H, enol-O*H*), 10.47

(s, broad, 1H, phenol-O*H*), 8.75 (s, 1H, 1-Np*H*), 8.48 (s, 1H, 8-Np*H*) 8.18 (d, J = 12, 3-Np*H*), 8.08 (d, J = 12, 2H, 2, 6-Ph*H*), 7.98 (d, J = 12, 1H, 4-Np*H*) 7.85 (s, broad, 2H, 5, 7-Np*H*), 7.34 (s, 1H, COC*H*CO), 6.90 (d, J = 12, 2H, 3, 5-Ph*H*). HRMS (ESI, TOF) m/z calcd for $C_{19}H_{12}O_3I$: 414.9831 $[M - H]^+$; found 414.9825.

BF_2nbm(I)OH. The boron dye coupler was prepared as previously described for previously described couplers, but the ligand, nbm(I)OH, was in place for the β-diketonate ligand to yield a yellow powder after recrystallization from acetone/hexanes; 45 mg (35%). ^{1}H NMR: (600 MHz, D_6-DMSO) δ11.22 (s, broad, 1H, phenol-O*H*), 8.99 (s, 1H, 1-Np*H*), 8.55 (s, 1H, 5-Np*H*), 8.33 (m, 3H, 2, 6-Ph*H*, 4-Np*H*), (d, J = 6, 1H, 3-Np*H*), 7.95 (m, 2H, 7, 8-Np*H*), 7.87 (s, 1H, COC*H*CO), 7.00 (d, J = 6, 2H, 3, 5-Ph*H*). HRMS (ESI, TOF) m/z calcd for $C_{19}H_{11}BO_3F_2I$: 462.9814 $[M - H]^+$; found 462.9814.

BF_2nbm(I)PLLA-PEG. The dye-coupled polymer was prepared as previously described by Kerr et al,[8] except the dye, BF_2nbm(I)OH, was used in placed of BF_2dbmOH. A lower MW block copolymer of mPEG-PLLA-OH (PEG= 2 000 g/mol and PLLA = 5 000 g/mol), was also used in this reaction, prepared as previously described.[27] The product was obtained as a yellow powder; 513 mg (76%). M_n (GPC/MALS) = 7 600 (d*n*/d*c* = 0.056), Đ = 1.05 (^{1}H NMR) = 7 300; ^{1}H NMR: (600 MHz, $CDCl_3$) δ8.69 (s, 1H, 1-Np*H*), 8.32 (s, 1H, 5-Np*H*), 8.17 (d, J = 6, 2H, 2, 6-Ph*H*), 8.09 (d, J =12, 1H, 3-Np*H*), 7.85 (m, H, 7, 8-Np*H*), 7.72 (d, J = 12, 1H, 4-Np*H*), 7.21 (s, 1H, COC*H*CO), 7.06 (d, J = 6, 2H, 3, 5-Ph*H*), 5.17 (q, J = 6, 66H, PLLA-*H*), 3.62 (s, broad, 179H, PEG-OCH_2CH_2-), 3.36 (s, 3H, PEG-OCH_3), 1.55 (m, broad, 217H, PLLA-CH_3).

NH_2-PEG-PDLA. The polymer was synthesized as previously described,[28] but $_D$-lactide was used as monomer in place of $_{D,\,L}$-lactide, and Boc-NH-PEG-OH (MW = 5,000) was used as initiator in place of boron dye to yield a white fibrous solid: 250 mg (78% yield, corrected for 44%

conversion). M_n (GPC/MALS) = 9 800 Da, PDI = 1.42. ^{1}H NMR: (600 MHz, $CDCl_3$) δ 5.15 (q, J = 6, 150H, PDLA-C*H*), 3.63 (s, broad, 454H, PEG-OC_2H_4-O), 1.56 (m, broad, 509H, PDLA-CH_3, Boc-CH_3). To deprotect Boc group, the above polymer (155 mg) was dissolved in a TFA/DCM mixture (1:1 v/v) and stirred at room temperature for 2 h.[29] The solvent was rotary evaporated, and the crude polymer the product was dissolved in a minimal amount of DCM and then precipitated into diethyl ether. The amino-terminated NH_2-PEG-PDLA was collected by centrifuge and dried under *vacuo* to yield a white powder: 100 mg (65% yield). M_n (GPC/MALS) = 9 000 Da, PDI = 1.49.

FA-PEG-PDLA. Folate conjugated polymer was synthesized by a previously reported method.[30] Folic acid (0.45 mmol), NHS (1.4 mmol), and DCC (0.45 mmol) were dissolved in DMSO in a round-bottom flask to yield a yellow homogenous solution. The carboxyl group of folic acid was activated in the dark at room temperature for 6 h, followed by filtering the byproduct 1,3-dicyclohexylurea (DCU). In another round-bottom flask, NH_2-PEG-PDLA (100 mg) and TEA (10 μL) were dissolved in DMSO (4 mL), and was treated with the filtered solution (6 mL). The reaction mixture was allowed to proceed in the dark at room temperature for 24 hours. The product was dialyzed against DMSO (pre-treated RC tubing, MWCO: 3.5 kDa) for 48 hours to remove small molecules that are uncoupled in the reaction, and against DI water (dialysis tubing, MWCO: 12-14 kDa) to remove DMSO for another 48 hours. A yellow powder was obtained by freeze-drying overnight: 168 mg (46%). The polymer was further characterized by UV to confirm the FA functionality.

5.4 Acknowledgements

I thank Christopher DeRosa for starting this project when he was in the Fraser group, Ashlyn Richard in the Palmer Lab at Duke University for conducting the biology experiments. I

also thank the National Institutes of Health (R01 CA167250) and UVA Cancer Center (P30 CA44579) for financial support, and Duke Optical Molecular Imaging and Analysis shared resources, which is supported by the Duke Cancer Institute and Duke School of Medicine.

5.5 References

(1) Rockwell, S.; Dobrucki, I.; Kim, E.; Marrison, S.; Vu, V. Hypoxia and Radiation Therapy: Past History, Ongoing Research, and Future Promise. *Curr. Mol. Med.* **2009**, *9*, 442–458.

(2) D., H. H.; L.M., M.; A., A.; T.H., L.; D., H. H.; L., M.; Hennessey, D.; Martin, L. M.; Atzberger, A.; Lynch, T. H.; et al. Exposure to Hypoxia Following Irradiation Increases Radioresistance in Prostate Cancer Cells. *Urol. Oncol. Semin. Orig. Investig.* **2013**, *31*, 1106–1116.

(3) Dewhirst, M. W.; Cao, Y.; Moeller, B. Cycling Hypoxia and Free Radicals Regulate Angiogenesis and Radiotherapy Response. *Nature Reviews Cancer*. June 2008, pp 425–437.

(4) Lee, C. T.; Boss, M. K.; Dewhirst, M. W. Imaging Tumor Hypoxia to Advance Radiation Oncology. *Antioxidants and Redox Signaling*. Mary Ann Liebert Inc. July 10, 2014, pp 313–337.

(5) Skala, M. C.; Fontanella, A.; Lan, L.; Izatt, J. A.; Dewhirst, M. W. Longitudinal Optical Imaging of Tumor Metabolism and Hemodynamics. *J. Biomed. Opt.* **2010**, *15*, 011112.

(6) Schreml, S.; Meier, R. J.; Kirschbaum, M.; Kong, S. C.; Gehmert, S.; Felthaus, O.; Küchler, S.; Sharpe, J. R.; Wöltje, K.; Weiß, K. T.; et al. Luminescent Dual Sensors Reveal Extracellular PH-Gradients and Hypoxia on Chronic Wounds That Disrupt Epidermal Repair. *Theranostics* **2014**, *4*, 721–735.

(7) Yoshihara, T.; Hosaka, M.; Terata, M.; Ichikawa, K.; Murayama, S.; Tanaka, A.; Mori, M.; Itabashi, H.; Takeuchi, T.; Tobita, S. Intracellular and in Vivo Oxygen Sensing Using

Phosphorescent IR(III) Complexes with a Modified Acetylacetonato Ligand. *Anal. Chem.* **2015**, *87*, 2710–2717.

(8) Kerr, C.; DeRosa, C. A.; Daly, M. L.; Zhang, H.; Palmer, G. M.; Fraser, C. L. Luminescent Difluoroboron β-Diketonate PLA–PEG Nanoparticles. *Biomacromolecules* **2017**, *18*, 551–561.

(9) Maruyama, K. Intracellular Targeting Delivery of Liposomal Drugs to Solid Tumors Based on EPR Effects. *Advanced Drug Delivery Reviews*. 2011.

(10) Egusquiaguirre, S. P.; Igartua, M.; Hernández, R. M.; Pedraz, J. L. Nanoparticle Delivery Systems for Cancer Therapy: Advances in Clinical and Preclinical Research. *Clinical and Translational Oncology*. 2012, pp 83–93.

(11) Jenkins, R.; Burdette, M. K.; Foulger, S. H. Mini-Review: Fluorescence Imaging in Cancer Cells Using Dye-Doped Nanoparticles. *RSC Adv.* **2016**, *6*, 65459–65474.

(12) El-Gogary, R. I.; Rubio, N.; Wang, J. T.-W.; Al-Jamal, W. T.; Bourgognon, M.; Kafa, H.; Naeem, M.; Klippstein, R.; Abbate, V.; Leroux, F.; et al. Polyethylene Glycol Conjugated Polymeric Nanocapsules for Targeted Delivery of Quercetin to Folate-Expressing Cancer Cells *in Vitro* and *in Vivo*. *ACS Nano* **2014**, *8*, 1384–1401.

(13) Attia, M. F.; Anton, N.; Wallyn, J.; Omran, Z.; Vandamme, T. F. An Overview of Active and Passive Targeting Strategies to Improve the Nanocarriers Efficiency to Tumour Sites. *Journal of Pharmacy and Pharmacology*. Blackwell Publishing Ltd August 1, 2019, pp 1185–1198.

(14) Kamaly, N.; Xiao, Z.; Valencia, P. M.; Radovic-Moreno, A. F.; Farokhzad, O. C. Targeted Polymeric Therapeutic Nanoparticles: Design, Development and Clinical Translation. *Chemical Society Reviews*. April 7, 2012, pp 2971–3010.

(15) Torchilin, V. P. Multifunctional, Stimuli-Sensitive Nanoparticulate Systems for Drug Delivery. *Nat. Rev. Drug Discov.* **2014**, *13*, 813–827.

(16) Wang, X.; Li, S.; Shi, Y.; Chuan, X.; Li, J.; Zhong, T.; Zhang, H.; Dai, W.; He, B.; Zhang, Q. The Development of Site-Specific Drug Delivery Nanocarriers Based on Receptor Mediation. *J. Control. Release* **2014**, *193*, 139–153.

(17) Bello, L.; Francolini, M.; Marthyn, P.; Zhang, J.; Carroll, R. S.; Nikas, D. C.; Strasser, J. F.; Villani, R.; Cheresh, D. A.; Black, P. M. Alpha(v)Beta3 and Alpha(v)Beta5 Integrin Expression in Glioma Periphery. *Neurosurgery* **2001**, *49*, 380–390.

(18) Van Dam, G. M.; Themelis, G.; Crane, L. M. A.; Harlaar, N. J.; Pleijhuis, R. G.; Kelder, W.; Sarantopoulos, A.; De Jong, J. S.; Arts, H. J. G.; Van Der Zee, A. G. J.; et al. Intraoperative Tumor-Specific Fluorescence Imaging in Ovarian Cancer by Folate Receptor-α Targeting: First in-Human Results. *Nat. Med.* **2011**, *17*, 1315–1319.

(19) Gabizon, A.; Horowitz, A. T.; Goren, D.; Tzemach, D.; Mandelbaum-Shavit, F.; Qazen, M. M.; Zalipsky, S. Targeting Folate Receptor with Folate Linked to Extremities of Poly(Ethylene Glycol)-Grafted Liposomes: In Vitro Studies. *Bioconjug. Chem.* **1999**, *10*, 289–298.

(20) Sunoqrot, S.; Bae, J. W.; Pearson, R. M.; Shyu, K.; Liu, Y.; Kim, D.-H.; Hong, S. Temporal Control over Cellular Targeting through Hybridization of Folate-Targeted Dendrimers and PEG-PLA Nanoparticles. *Biomacromolecules* **2012**, *13*, 1223–1230.

(21) Xiong, J.; Meng, F.; Wang, C.; Cheng, R.; Liu, Z.; Zhong, Z. Folate-Conjugated Crosslinked Biodegradable Micelles for Receptor-Mediated Delivery of Paclitaxel. *J. Mater. Chem.* **2011**, *21*, 5786–5794.

(22) Pasut, G.; Caboi, F.; Schrepfer, R.; Tonon, G.; Schiavon, O.; Veronese, F. M. New Active

Poly(Ethylene Glycol) Derivative for Amino Coupling. *React. Funct. Polym.* **2007**, *67*, 529–539.

(23) Gindy, M. E.; Ji, S.; Hoye, T. R.; Panagiotopoulos, A. Z.; Prud'Homme, R. K. Preparation of Poly(Ethylene Glycol) Protected Nanoparticles with Variable Bioconjugate Ligand Density. *Biomacromolecules* **2008**, *9*, 2705–2711.

(24) Kinard, L. A.; Kasper, F. K.; Mikos, A. G. Drying Poly(Ethylene Glycol) : Protocol Exchange. *Nat. Protoc.* **2012**, *7*, 1219–1227.

(25) Demas, J. N.; Crosby, G. A. The Measurement of Photoluminescence Quantum Yields. A Review. *J. Phys. Chem.* **1971**, *75*, 991–1024.

(26) Jin, H.; Zhang, W.; Wang, D.; Chu, Z.; Shen, Z.; Zou, D.; Fan, X.; Zhou, Q. Dendron-Jacketed Electrophosphorescent Copolymers: Improved Efficiency and Tunable Emission Color by Partial Energy Transfer. *Macromolecules* **2011**, *44*, 9556–9564.

(27) Kersey, F. R.; Zhang, G.; Palmer, G. M.; Dewhirst, M. W.; Fraser, C. L. Stereocomplexed Poly(Lactic Acid)−Poly(Ethylene Glycol) Nanoparticles with Dual-Emissive Boron Dyes for Tumor Accumulation. *ACS Nano* **2010**, *4*, 4989–4996.

(28) Zhang, G.; Chen, J.; Payne, S. J.; Kooi, S. E.; Demas, J. N.; Fraser, C. L. Multi-Emissive Difluoroboron Dibenzoylmethane Polylactide Exhibiting Intense Fluorescence and Oxygen-Sensitive Room-Temperature Phosphorescence. *J. Am. Chem. Soc.* **2007**, *129*, 8942–8943.

(29) Jia, Z.; Liu, J.; Boyer, C.; Davis, T. P.; Bulmus, V. Functional Disulfide-Stabilized Polymer−Protein Particles. *Biomacromolecules* **2009**, *10*, 3253–3258.

(30) Xiong, J.; Meng, F.; Wang, C.; Cheng, R.; Liu, Z.; Zhong, Z. Folate-Conjugated Crosslinked Biodegradable Micelles for Receptor-Mediated Delivery of Paclitaxel. *J. Mater.*

Chem. **2011**, *21*, 5786–5794.

Chapter 6: Difluoroboron β-Diketonate Polylactic Acid Nanoparticles as Intracellular Oxygen Sensors for Brain Imaging

6.1 Introduction

In neuroscience, O_2 regulates structural and functional integrity of the brain. Though brain is only 2% of the body's mass, it consumes nearly 20% of O_2 by the resting body.[1] Neuronal computation is energetically expensive which requires an adequate supply of ATP or O_2 for neuronal activities from maintaining electrochemical gradients to releasing and recycling synaptic vesicles.[2,3] Failure of the oxidative metabolism is proposed to occur in many neurological disorders. Hypoxia-ischemia is a major cause of brain injury in humans including conditions such as hypoxic-ischemic encephalopathy[4], stroke[5,6], seizures[5,7,8], periventricular leukomalacia[9], and even Alzheimer's disease[10,11]. Epilepsy is a common neuronal disease afflicting 1 in 26 Americans. Seizures are known to cause permanent brain damage. A leading hypothesis for brain damage due to seizures is that the metabolic demand imposed by repetitive firing of neurons exceeds the oxygen supply to the tissue rendering relative hypoxia.

Understanding hypoxia and brain oxygenation has significant importance to provide information on clinic treatment and early diagnosis. Oxygen sensing offers new fundamental insight into brain function. In particular, phosphorescence quenching is able to generate an oxygenation map with good spatial and temporal resolution. Efforts have been made during the past decades in applying phosphorescence probes as oxygen sensor in neuroscience.[12–14] For example, Ingram *et al*. developed platinum (II) octaethylporphine ketone (PtOEPK) and nanocystal quantum dot (NQD) blends to measure interstitial oxygen concentration of active brain slices through fluorescence resonance energy transfer (FRET).[15] The Papkovsky group designed cell-permeable probes based on the phosphorescent Pt(II)-tetrakis(pentafluorophenyl)porphyrin (PtPFPP) dye and a fluorescent poly(9,9-diheptylfluorene-alt-9,9-di-p-tolyl-9H-fluorene standard.[16] These methods rely on blending a phosphorescence probe, a fluorescence standard, and

a polymer matrix all together, rendering the final material quite complex. In addition, currently reported sensors that are able to measure intracellular oxygen level in living brain slices are rare. Due to the presence of the blood-brain barrier (BBB) that regulates and limits the exchange of certain type of chemicals between the bloodstream and the central nervous system, the delivery of imaging/therapeutic agents into the brain non-invasively is also challenging in vivo.[17]

Boron dye polymer nanoparticles were ultilized as oxygen nanosensors for brain imaging. Preliminary unpublished data from Haglund, Hochman, and Palmer at Duke University revealed that the oxygen level mapped by boron nanoparticles correlated with electroencephalogram (EEG) brain activity in a primate model when seizures were induced. This suggests many possibilities for follow up studies of brain activity. Dye-PLA nanoparticles are likely to respond to intraneuronal oxygen variation given in prior cell studies, they showed perinuclear localization.[18,19] Also, sterocomplex PEGylated nanoparticles with active targeting groups might provide a non-invasive approach for *in vivo* brain oxygen sensing without physical damage to the brain tissue. For example, transferrin receptors are expressed in the luminal membrane of BBB capillary endothelial cells. Transferrin conjugated nanoparticles made from PEG-PLA block copolymers were shown to across the BBB via receptor-mediated transport (RMP) and to efficiently deliver therapeutic agents.[20] In this chapter, we first established the labeling and sensing method by employing blue-fluorescent nanoparticles and oxygen sensing nanoparticles (shown in Figure 6.1) to study synaptic activity. The optical properties and stability were evaluated in the relevant biological environment. The primary neuronal cultures were used to study cellular uptake, and the brain slices were used to study oxygen ability of nanoparticles *ex vivo*.

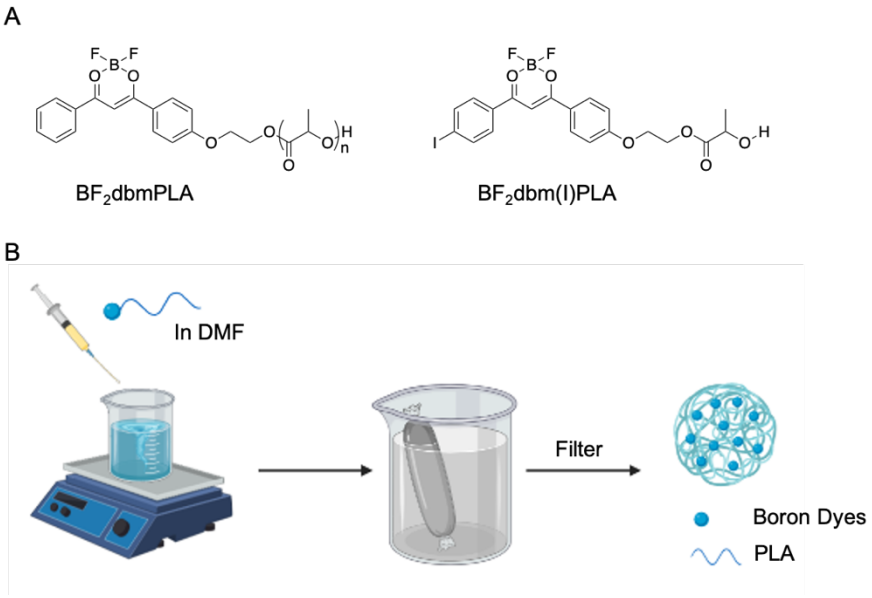

Figure 6. 1. Nanoparticle Composition and Fabrication. A) Chemical structures of BF_2dbmPLA and BF_2dbm(I)PLA. B) Nanoparticle fabricated by the nanoprecipitation method.

6.2 Results and Discussion

6.2.1 Nanoparticles

The boron dye polymers were synthesized as previously described.[21] In general, boron dyes with primary alcohol, served as initiator, was dissolved in melted lactide. The polymers were grown with the presence of tin catalyst via ring opening polymerization. The crude polymers were purified by dissolving with a minimal amount of CH_2Cl_2, followed by addition into cold methanol to remove small organic dyes and lactide. The polymers were characterized by NMR and GPC. The nanoparticles were fabricated by a method known as nanoprecipitation, which involves interfacial deposition due to displacement of solvent (i.e., DMF) with non-solvent (i.e., DI water). Nanoparticle characteristics have been extensively studied in the previous reports, as listed in Table 6.1. Blue nanoparticles BF_2dbmPLA (blue NPs) were chosen for labelling primary neuronal cells because their high quantum yield and bright fluorescence, easily to be detected and ideal for tracking cell.[18] Oxygen sensing nanoparticles BF_2dbmPLA (O_2 NPs) were to generate ratiometric

oxygenation where the fluorescence (λ_F = 450 nm) acts as an internal standard and the oxygen sensitive phosphorescence (λ_F = 535 nm) is the sensor. The maximum UV excitation for both nanoparticles (blue NPs: λ_{ex} = 396 nm; O_2 NPs: λ_{ex} = 405 nm) are compatible with a 405 nm laser excitation.

Table 6. 1. Nanoparticles Characteristics

	Optical Properties					Physical Properties		
Nanoparticles	λ_{ex}[a] (nm)	λ_F[b] (nm)	λ_P[c] (nm)	τ_F[d] (ns)	τ_P[e] (ms)	R_h[f] (nm)	PD[f] (%)	ζ[g] (mV)
BF_2dbmPLA	396	439	509	3.84	200	52	15	-28
BF_2dbm(I)PLA	405	450	535	0.54	4.37	71	24	-24

[a]Estimated extinction coefficient for aqueous nanoparticle suspension (~ 50 μg/mL). [b]Determined by dynamic light scattering, nanoparticles are 200 μg/mL in water. PD = polydispersity. [c]Fluorescence emission maximum for aqueous nanoparticle suspension.

The physical properties, including radius and zeta potential, were measured by DLS and ZetaSizer. It is believed that size and surface charge are critical factors affecting interaction between nanomaterials and biological components, consequently the efficiency of localization into cells and tissue. As listed in Table 6.1, the hydrodynamic radius for blue NPs was 52 nm with polydispersity of 15 %, and for O_2 NPs was 71 nm with polydispersity of 24 %, both of which are typical values for the family of BF_2bdkPLA and are in consistent with previous results.[19,22] The data suggested the polymers successfully self-assembly into nanoparticles. In addition, nanoparticles with radius ranging from 20 - 200 nm can be readily internalized via endocytosis; and they are large enough for renal clearance and small enough for clearance from spleen. Based on zeta potential, blue NPs and O_2 NPs were negatively charged, in accordance with commonly developed PLA nanoparticles. Early report from Dante et al. revealed that NPs with negative charge rapidly localize on neuronal membrane, while those with positive or neutral charge showed no or slow interaction with neurons.[23] With size and zeta potential suitable for endocytosis, we

hypothesized that the boron dye polymer NPs are able to internalized by neurons and exhibit response to intracellular oxygen variations.

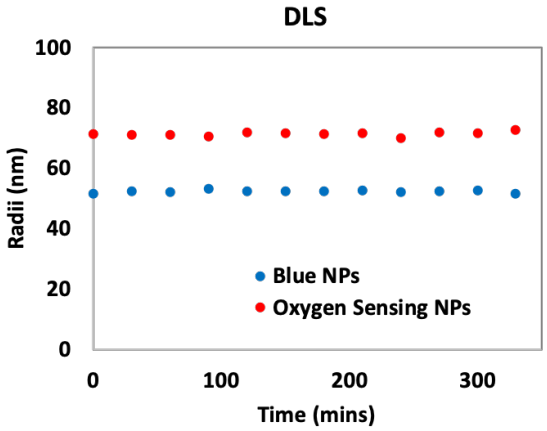

Figure 6. 2. DLS Traces for NPs.

6.2.2 Cellular Uptake

To confirm the intracellular uptake, the stability (i.e., no aggregation) of NPs was firstly evaluated in regular neuronal medium at elevated temperature (i.e., 37 °C) over time as nanoparticles fabricated from pure hydrophobic polyesters is prone to precipitate out from aqueous solution. The NPs were diluted with neuronal medium at a final concentration of 500 μg/mL, monitored by DLS every 30 mins over six hours, a period of time sufficient for incubation and imaging. It was observed that the NPs could maintain their size without no aggregation occurred (Figure 6.2). The blue NPs suspended in neuronal medium were then used to label primary neuronal cultures. The cultures were 14 DIV at the time of experiment, with well-formed neuronal structures including synapses. The mitochondria were labelled with MitoTracker Red FM, the maxima fluorescence of which (λ_F = 644 nm) is far away from the blue NPs emission. With confocal microscopy, we found that blue NPs showed non-specific interactions with living cells (e.g., neurons and glia cells), as well as debris from the cultures. However, neuronal cell bodies

(i.e., perinuclear region of cytoplasm), dendrites and synapses can be easily visualized with the bright blue fluorescence, which is supported by colocalization with MitoTracker Red FM because the blue and red emissions were perfectly matched as shown in Figure 6.3. By specifically binding to mitochondria membrane, the MitoTracker targets mitochondria where the oxygen is consumed to generate ATP and energy for a variety of neuronal activities. It is critical to ensure that the NPs have the same internalization pathway with MitoTracker Red FM, which would allow effective intracellular oxygenation detected from the oxygen sensing NPs.

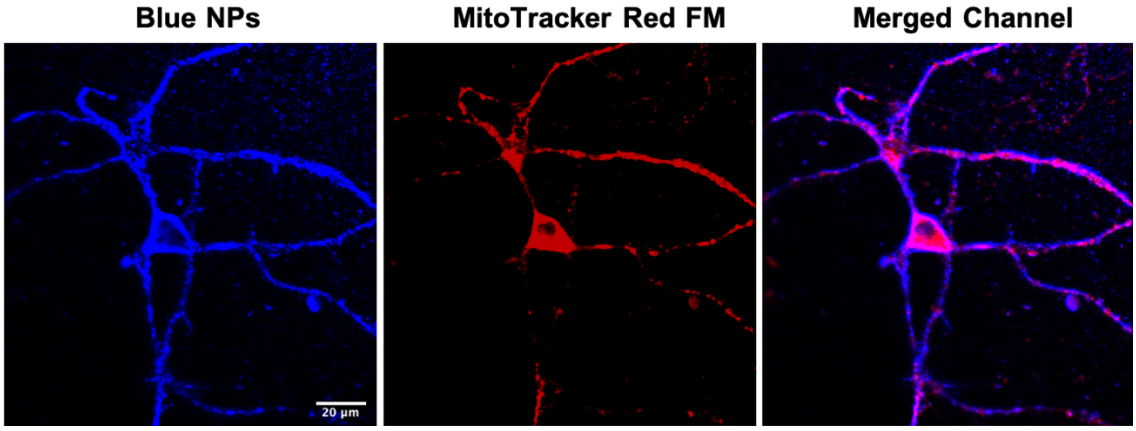

Figure 6. 3. Neuronal Imaging under Confocal Microscopy. The images showed labelling from blue NPs (left) and MitoTracker Red (middle), and merged channel from blue and red (right). Excitation wavelength is 405 and 595 nm.

6.2.3 Slice Imaging

Dual-emissive O_2 sensing NPs possess oxygen-insensitive fluorescence and room temperature oxygen-sensitive phosphorescence. As oxygen concentration increases, the phosphorescence intensity decreases, whereas the fluorescence remains unchanging (Figure S6.1), serving as promising reagents for ratiometric oxygen sensing. At a range of 0-21 % O_2, the O_2 NPs has a liner relationship between the ratio fluorescence to phosphorescence (F/P) and oxygen concentration. After intracellular uptake of NPs was confirmed, the capability of O_2 NPs was demonstrated using living brain slice. The brain slices were incubated with solution containing

500 µg/mL O_2 NPs, during which the 95% O_2 was supplied. The granular cell layers in hippocampus were imaged because the neuronal circuits activated during seizures spreads from hippocampus, in particular, the dentate granule cells (DGC) which regulate the flow of signal within neuronal network. It is thus of interest and importance to investigate how oxygen level varies in DGC layer. During imaging, the brain slice was sealed in a closed chamber with circulation solution containing 95% O_2. A shown in Figure 6.3A, the DGC layer is clearly visualized in brightfield, and the emission captured from fluorescence was indicative the slice stained by nanoparticles. It was observed that DGC layer has brighter fluorescence, which due to a great number of cells are tightly packed here and more nanoparticles get loaded.

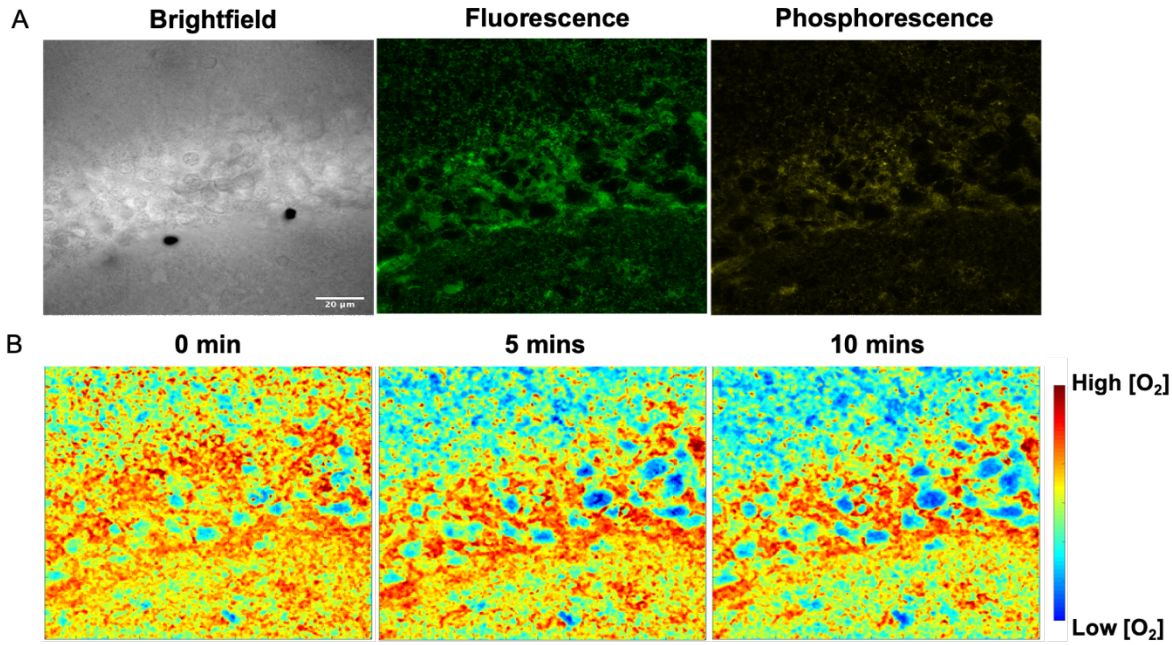

Figure 6. 4. Brain Slice Imaging with O_2 NPs. A) Brightfield, fluorescence and phosphorescence emission of hippocampus DGC layer. B) Ratiometric imaging when the oxygen supply is off over time.

The fluorescence and phosphorescence were analyzed to generate ratiometric images with F/P ratio correlates with oxygen levels. While the brain slice is supplied with oxygen, it was found that subtle contrast between dendrites and cell bodies where oxygen level is less in dendrites than

that in cell bodies of granule layers. To show how the NPs respond to oxygen changes in tissue, the oxygen supply was switched off and imaging was taken every 5 min. The F/P ratio decreased generally over time, and the contrast between dendrites and cell bodies is pronounced. Oxygen is consumed by mitochondria in neuronal cell bodies, at dendrites and at synapses. At dendrites where synapses are located there are many neuronal activities taking place, therefore mitochondria are more concentrated than that in cell bodies, which consumes more oxygen and consumes quickly, leading to lower oxygen level.

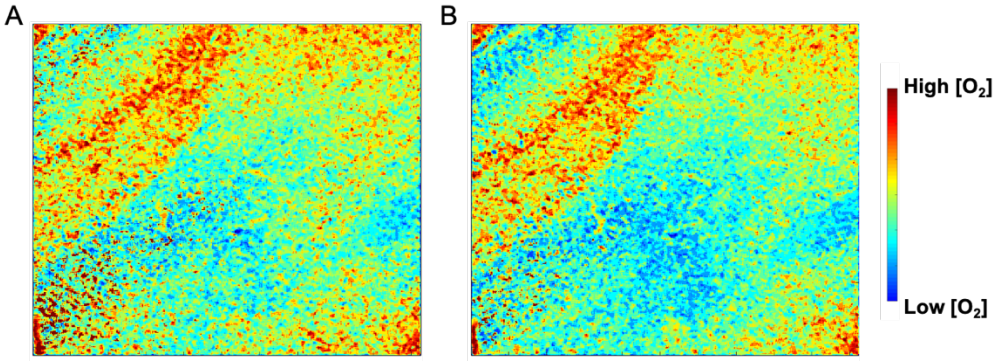

Figure 6. 5. Ratiomeric Images under Low K^+ (A) and High K^+ Concentration (B). The red-yellow triangle regions in the left corner represents more oxygenated DGC layer, and blue region in the middle is less-oxygenated dendrites.

To further support the statement that oxygen is expensively consumed due to synaptic activity, the potassium concentration in perfusion solution was increased from 2 mM to 5 mM. Potassium regulates neuronal activity, and elevated extracellular K^+ concentration is known to affect synaptic potentials and increase neuronal activities. We performed slice oxygen imaging under different potassium concentration and found when potassium concentration was increased, the regions away from molecular layer are more hypoxia as suggested by the F/P ratio in the ratiometric oxygen imaging shown in Figure 6.4. The results from brain slice imaging demonstrated the effectiveness of oxygen sensing nanoparticles, being able to study brain activity by measuring intracellular oxygen levels.

6.2.4 Conclusion

Oxygen nanosensors based on phosphorescence quenching can provide information in the brain with improved micron level spatial and sub-seconds temporal resolution. In this work, the boron nanoparticles were used to study brain activity. Particularly, primary neuronal cell cultures were labelled by blue nanoparticles from BF_2dbmPLA to confirm intracellular uptake. Electrophysiology experiments revealed that the application of nanoparticles did not have significant effect on electrophysiological properties of neurons. Oxygen sensing nanoparticles from BF_2dbm(I)PLA was able to generate ratiometric oxygenation for brain slices. In *ex vivo* brain slice, it was found that the neuronal cell bodies consume less oxygen than dendrites and synapses where mitochondria are more concentrated. The data was in accordance with the knowledge that oxygen is expensively consumed in synaptic activity, suggesting the capability of boron nanoparticles to serve as powerful and non-invasive sensing agents in the brain. Future work will involve the oxygen imaging in the living animal, and in combination with seizures induced via a cobalt model to study how oxygen levels are related to seizures.

6.3 Experimental Section

6.3.1 Polymer Synthesis and Characterization

The boron dye-polymer was prepared according to a previously reported method.[21] ^{1}H NMR spectra were recorded on a Varian VMRS/600 (600 MHz) instrument in $CDCl_3$ unless otherwise indicated. ^{1}H NMR resonance was referenced to the residual protiochloroform signal at 7.260 ppm. Coupling constants are given in hertz. Polymer molecular weights (MW) and polydispersity indices (Đ) were determined by gel permeation chromatography (GPC) (THF, 25 °C, 1.0 mL / min) using multi-angle laser light scattering (MALLS) (λ = 658 nm, 25 °C) and refractive index (RI) (λ = 658 nm, 25 °C) detection. Polymer Laboratories 5 μm mixed-C columns

(guard column plus two columns) along with Wyatt Technology (Optilab T-rEX interferometric refractometer, miniDAWN TREOS multi-angle static light scattering (MALS) detector, ASTRA 6.0 software) and Agilent Technologies instrumentation (series 1260 HPLC with diode array (DAD) detector, ChemStation) were used in GPC analysis. The incremental refractive index (*dn*/*dc*) was calculated by a single-injection method assuming 100% mass recovery from the columns. UV-vis spectra were recorded on a Hewlett-Packard 8452A diode-array spectrophotometer.

6.3.2 Luminescence Measurements

Steady-state fluorescence spectra for the nanoparticle suspensions were recorded on a Horiba Fluorolog-3 Model FL3-22 spectrofluorometer (double-grating excitation and double-grating emission monochromator) after excitation. Optically dilute aqueous solutions of the nanoparticles, with absorbance <0.1 au, were prepared in 1 cm path length quartz cuvettes. Fluorescence spectra were obtained under ambient conditions (i.e., air, ~21% oxygen in volume). For phosphorescence measurements, vials were capped with a 12 mm PTFE/silicone/PTFE seal (Chromatography Research Supplies) and were continuously purged with analytical grade N_2 (Praxair) for five minutes before measurements. For 21% O_2 (i.e. air), measurements were taken under ambient conditions (open vial, no cap). Oxygen calibration was performed as previously described with Cole-Palmer flow gauges with mixtures of analytical grade O_2, N_2 and 1% O_2 (in N_2) gases (Praxair).[22]

6.3.3 Nanoparticle Fabrication

Nanoparticles were fabricated as previously reported.[19] The polymer (~3.0 mg) was dissolved in DMF (3 mL) and was added dropwise to rapidly stirred DI water (27 mL). The homogeneous mixture was stirred for 30 min, and the nanoparticle suspensions were transferred into dialysis tubing (Specra/Pro, 12-14 kDa MWCO, Fisher Scientific) followed by dialysis against

DI water for 24 hours. Nanoparticle size and polydispersity were analyzed by dynamic light scattering (DLS, Wyatt, DynaPro). Zeta potentials were determined by Zetasizer Nano Z (Malvern instruments, UK) and data were analyzed using DTS Nano software.

6.3.4 Nanoparticle Fabrication

The stock suspensions of nanoparticles (1 mg/mL) were diluted (500 μg/mL) with neuronal regular medium (for cell labelling) and glucose (for slice labelling), respectively. Each sample (100 μL) was injected into a 96-well microtiter plate. Mineral oil was added on the top of each well via syringe to form a thin layer to prevent evaporation. The plate was put into the DLS instrument, protected from light, set to 37 °C and the sizes and polydispersities of the nanoparticles were recorded over the course of two hours.

6.3.5 Primary Neuronal Culture

Animals were treated according to a protocol approved by the University of Virginia Animal Care and Use Committee (ACUC), and efforts were made to minimize animal stress and discomfort. Cultures were prepared from postnatal day 0 to postnatal day 1 (P0 –P1) C57BL/65 mice using methods described previously.[24] The newborn pups were decapitated, and their brains removed and placed in cold HEPES-buffered Hanks' balanced salt solution (HEPES-HBSS). The hippocampi were removed under a dissecting microscope and collected in a small petri dish containing HEPES-HBSS. The hippocampi were transferred to 0.125 % trypsin HEPES-HBSS and were incubated for 15 min at 37°C. Trypsin solution was centrifuged for 7 min at 700 rpm, and the supernatant was replaced with 5 ml HEPES-HBSS. The cells were rinsed with warm surgical medium by centrifuging for 7 min at 700 rpm and discarding the supernatant. Hippocampi were triturated until no fragments of tissue remained. Cell density was determined by trypan blue exclusion. Culture dishes were coated with poly-lysine and filled with 2 ml of surgical medium,

which was prepared from Dulbecco's modified Eagles medium (DMEM) and F-12 supplement (1:1) (Invitrogen) with 10% fetal bovine serum (heat inactivated, Invitrogen), 2 mM L-glutamine (Invitrogen), and penicillin-streptomycin (100 U/ml). Cells were plated at a density of 50,000 per 35 mm^2 dish and kept in a 5% CO_2 incubator at 37 °C. After 24 h, the surgical medium was changed to serum-free neuronal regular medium containing DMEM and neurobasal (2.28:1) with 2% B27 and 2 mM glutamine. The medium was replaced with fresh regular medium every two days.

6.3.6 Cell Labelling

Primary neurons were 14 days *in vitro* (DIV) at the time of imaging for best observation of synapses. Blue NPs were diluted in regular medium to yield a final concentration of 500 μg/mL. Cells were incubated in the above solution at 37 °C in a 5% CO_2 incubator for one hour. After staining, the cells were washed twice with HEPES-ACSF (pH 7.4, osmolarity 314-316 mOsm) containing (in mM) 147 NaCl, 2.6 KCl, 2 $CaCl_2$, 3 $MgCl_2$, 10 glucose, 10 HEPES and were kept in such medium during imaging. To label mitochondria, cells were incubated with regular medium containing MitoTracker™ Red FM (250 nM) for an additional 30 minutes before washing with HEPES-ACSF.

6.3.7 Brain Slice

Acutely isolated brain slices were prepared as previously described.[25] The animals were sacrificed under anesthesia and the brains were removed and immersed immediately in ice-cold (4 °C) oxygenated (95 % O_2, 5 % CO_2) sucrose-ACSF (pH 7.4, osmolarity 300-310 mOsm) containing (in mM) 56.5 NaCl, 2 KCl, 5 $MgSO_4$, 25 $NaHCO_3$, 1 KH_2PO_4, 0.5 $CaCl_2$, 10 glucose, 113 sucrose. Coronal hippocampal slices (200μm) were prepared with a vibratome (VT1200S; Leica, Wetzlar, Germany) and were incubated in oxygenated sucrose-ACSF at 34 °C for 30 min prior to labelling or recording. To minimize NP aggregation, O_2 sensing NPs were suspended in 3

M glucose with NP final concentration at 500 μg/mL. Slices were labelled by incubating in the oxygenated NP glucose solution for two hours. Slices were washed and kept in oxygenated sucrose-ACSF prior to imaging.

6.3.8 Imaging

Imaging was performed using a Zeiss 780 confocal/multiphoton microscope system with Zeiss Zen software for image acquisition (Carl Zeiss, Oberkochen, Germany). For imaging cultured neurons, excitation wavelength used to visualize blue NPs and MitoTracker™ Red FM were 405 nm and 595 nm, respectively. Emission filter ranged from 410 nm to 500 nm for blue, and 600 nm to 700 nm for red. In regions of interest, 40× or higher magnification was used. For imaging live slices, the brain slices were anchored in a closed bath chamber and perfused with oxygenated sucrose-ACSF. Laser 405 nm was used as excitation source, and emission ranged from 410 nm to 500 nm to capture fluorescence and 500 nm to 650 nm to capture phosphorescence. For high K^+ measurement, K^+ concentration was increased from 2 mM to 5 mM in the perfusion solution (56.5 NaCl, 5 KCl, 5 $MgSO_4$, 25 $NaHCO_3$, 1 KH_2PO_4, 0.5 $CaCl_2$, 10 glucose, 107 sucrose). Ratiometric data was produced in MATLAB.

6.4 Acknowledgements

I thank Dr. Suchitra Joshi for her help on cultures, Dr. Tamal Batabyal for developing the MATLAB code, Dr. Huayu Sun for performing electrophysiology experiments, and Dr. Ruofan Cao for his training on Keck Center Zeiss 780 Confocal microscopy system (NIH OD016446; PI: AP). I'm also gratefully acknowledge Prof. Kapur and Prof. Fraser for their guidance and assistance, and UVA Brain Institute for financial support.

6.5 References

(1) Mink, J. W.; Blumenschine, R. J.; Adams, D. B. Ratio of Central Nervous System to Body

Metabolism in Vertebrates: Its Constancy and Functional Basis. *Am. J. Physiol. - Regul. Integr. Comp. Physiol.* **1981**, *10*, 203–212.

(2) Harris, J. J.; Jolivet, R.; Attwell, D. Synaptic Energy Use and Supply. *Neuron* **2012**, *75*, 762–777.

(3) Devine, M. J.; Kittler, J. T. Mitochondria at the Neuronal Presynapse in Health and Disease. *Nat. Rev. Neurosci.* **2018**, *19*, 63–80.

(4) Neoptolemos, J. P.; Stocken, D. D.; Friess, H.; Bassi, C.; Dunn, J. A.; Hickey, H.; Beger, H.; Fernandez-Cruz, L.; Dervenis, C.; Falconi, M.; et al. Whole-Body Hypothermia for Neonates with Hypoxic–Ischemic Encephalopathy Seetha. *N Engl J Med* **2004**, *350*, 1200–1210.

(5) Tang, Y.; Lu, A.; Aronow, B. J.; Sharp, F. R. Blood Genomic Responses Differ after Stroke, Seizures, Hypoglycemia, and Hypoxia: Blood Genomic Fingerprints of Disease. *Ann. Neurol.* **2001**, *50*, 699–707.

(6) Prass, K.; Scharff, A.; Ruscher, K.; Löwl, D.; Muselmann, C.; Victorov, I.; Kapinya, K.; Dirnagl, U.; Meisel, A. Hypoxia-Induced Stroke Tolerance in the Mouse Is Mediated by Erythropoietin. *Stroke* **2003**, *34*, 1981–1986.

(7) Glass, H. C.; Glidden, D.; Jeremy, R. J.; Barkovich, A. J.; Ferriero, D. M.; Miller, S. P. Clinical Neonatal Seizures Are Independently Associated with Outcome in Infants at Risk for Hypoxic-Ischemic Brain Injury. *J. Pediatr.* **2009**, *155*, 318–323.

(8) Wirrell, E. C.; Armstrong, E. A.; Osman, L. D.; Yager, J. Y. Prolonged Seizures Exacerbate Perinatal Hypoxic-Ischemic Brain Damage. *Pediatr. Res.* **2001**, *50*, 445–454.

(9) Baud, O.; Daire, J.-L.; Dalmaz, Y.; Fontaine, R. H.; Krueger, R. C.; Sebag, G.; Evrard, P.; Gressens, P.; Verney, C. Gestational Hypoxia Induces White Matter Damage in Neonatal

Rats: A New Model of Periventricular Leukomalacia. *Brain Pathol.* **2004**, *14*, 1–10.

(10) Ogunshola, O. O.; Antoniou, X. Contribution of Hypoxia to Alzheimer's Disease: Is HIF-1α a Mediator of Neurodegeneration? *Cell. Mol. Life Sci.* **2009**, *66*, 3555–3563.

(11) Zhang, X.; Le, W. Pathological Role of Hypoxia in Alzheimer's Disease. *Exp. Neurol.* **2010**, *223*, 299–303.

(12) Mauleon, G.; Fall, C. P.; Eddington, D. T. Precise Spatial and Temporal Control of Oxygen within in Vitro Brain Slices via Microfluidic Gas Channels. *PLoS One* **2012**, *7*, 43309.

(13) Zhang, C.; Bélanger, S.; Pouliot, P.; Lesage, F. Measurement of Local Partial Pressure of Oxygen in the Brain Tissue under Normoxia and Epilepsy with Phosphorescence Lifetime Microscopy. *PLoS One* **2015**, *10*, 0135536.

(14) Tsytsarev, V.; Arakawa, H.; Borisov, S.; Pumbo, E.; Erzurumlu, R. S.; Papkovsky, D. B. In Vivo Imaging of Brain Metabolism Activity Using a Phosphorescent Oxygen-Sensitive Probe. *J. Neurosci. Methods* **2013**, *216*, 146–151.

(15) Ingram, J. M.; Zhang, C.; Xu, J.; Schiff, S. J. FRET Excited Ratiometric Oxygen Sensing in Living Tissue. *J. Neurosci. Methods* **2013**, *214*, 45–51.

(16) Dmitriev, R. I.; Borisov, S. M.; Kondrashina, A. V; Pakan, J. M. P.; Anilkumar, U.; Prehn, J. H. M.; Zhdanov, A. V.; McDermott, K. W.; Klimant, I.; Papkovsky, D. B. Imaging Oxygen in Neural Cell and Tissue Models by Means of Anionic Cell-Permeable Phosphorescent Nanoparticles. *Cell. Mol. Life Sci.* **2015**, *72*, 367–381.

(17) Attia, M. F.; Anton, N.; Wallyn, J.; Omran, Z.; Vandamme, T. F. An Overview of Active and Passive Targeting Strategies to Improve the Nanocarriers Efficiency to Tumour Sites. *J. Pharm. Pharmacol.* **2019**, *71*, 1185–1198.

(18) Belanger, M. C.; Zhuang, M.; Ball, A. G.; Richey, K. H.; DeRosa, C. A.; Fraser, C. L.;

Pompano, R. R. Labelling Primary Immune Cells Using Bright Blue Fluorescent Nanoparticles. *Biomater. Sci.* **2020**, *8*, 1897–1909.

(19) Pfister, A.; Zhang, G.; Zareno, J.; Horwitz, A. F.; Fraser, C. L. Boron Polylactide Nanoparticles Exhibiting Fluorescence and Phosphorescence in Aqueous Medium. *ACS Nano* **2008**, *2*, 1252–1258.

(20) Lecoq, J.; Parpaleix, A.; Roussakis, E.; Ducros, M.; Houssen, Y. G.; Vinogradov, S. a; Charpak, S. Simultaneous Two-Photon Imaging of Oxygen and Blood Flow in Deep Cerebral Vessels. *Nat. Med.* **2011**, *17*, 893–898.

(21) Zhang, G.; Chen, J.; Payne, S. J.; Kooi, S. E.; Demas, J. N.; Fraser, C. L. Multi-Emissive Difluoroboron Dibenzoylmethane Polylactide Exhibiting Intense Fluorescence and Oxygen-Sensitive Room-Temperature Phosphorescence. *J. Am. Chem. Soc.* **2007**, *129*, 8942–8943.

(22) Zhang, G.; Palmer, G. M.; Dewhirst, M. W.; Fraser, C. L. A Dual-Emissive-Materials Design Concept Enables Tumour Hypoxia Imaging. *Nat. Mater.* **2009**, *8*, 747–751.

(23) Dante, S.; Petrelli, A.; Petrini, E. M.; Marotta, R.; Maccione, A.; Alabastri, A.; Quarta, A.; De Donato, F.; Ravasenga, T.; Sathya, A.; et al. Selective Targeting of Neurons with Inorganic Nanoparticles: Revealing the Crucial Role of Nanoparticle Surface Charge. *ACS Nano* **2017**, *11*, 6630–6640.

(24) Johnson, S. E.; Hudson, J. L.; Kapur, J. Synchronization of Action Potentials during Low-Magnesium-Induced Bursting. *J. Neurophysiol.* **2015**, *113*, 2461–2470.

(25) Joshi, S.; Sun, H.; Rajasekaran, K.; Williamson, J.; Perez-Reyes, E.; Kapur, J. A Novel Therapeutic Approach for Treatment of Catamenial Epilepsy. *Neurobiol. Dis.* **2018**, *111*, 127–137.

Chapter 7: Future Directions

7.1 Introduction

The research during the past five years has successfully extended the applications of boron dye polymers as oxygen sensing and imaging reagents. The work and achievements discussed in the previous chapters demonstrated the possibility and potential of boron dye materials to be used as oxygen sensors alternatives to commercially available phosphors. Further improvements include optimizing nanoparticles for long-term imaging and developing active targeting strategies for multiple biological models. Moreover, *in vivo* oxygen sensing must be optimized for use in clinical fields. This chapter will discuss important future directions.

7.2 Future Directions

7.2.1 Long-term Imaging

Long-term imaging is essential for tracking cell behaviors. Our optimization of blue nanoparticles for labelling primary immune cells worked for a short period of time (24 hours), but long-term imaging was not yet successful. Even though the blue snanoparticles have very high quantum yields (~ 99 %) and those with specific polymer composition (i.e., PCL-PLLA) are stable (e.g., radius and fluorescence intensity) in biological relevant media for days, the fluorescence intensity drops to nearly baseline after 24 hours once they are taken up by cells. This may be due to faster degradation by esterases in the endosomes. To circumvent this issue, further polymer engineering such as succinimidyl ester functionalization is needed. As a good leaving group, the succinimidyl group activates carboxylic acids and for amide formation with amine nucleophiles, especially lysine residues, and other amino acids and intracellular molecules.[1] Formation of this covalent bond between dyes and intracellular components may make it possible for dyes to be retained in the cells for a relatively long time.

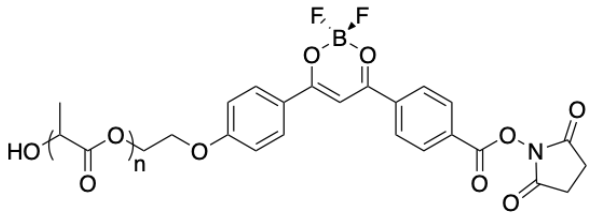

NHS-BF_2dbmPLA

The boron dye can be adapted with an N-hydroxysuccinimide (NHS) group via a synthetic routine illustrated in Scheme S7.1. Nanoparticles fabricated from NHS functionalized polymers may be evaluated in *in vitro* and *in vivo* imaging. This could also potentially improve long term tracking for tumor cells and hypoxia imaging.[2]

7.2.2 Active Targeting

Although we synthesized folic acid conjugated nanoparticles, our active targeting efforts are still in the early stages. The chemistry for developing folic acid targeting is fairly simple, however, the binding between the ligand and targets is not strong enough, which limits the application in therapeutics and diagnosis. There are types of macromolecular ligands, including proteins, antibodies, and aptamers. Many of these show high affinity and strong binding, and some are already in clinical trials. New nanoparticles with high affinity ligands must be prepared to improve spatial specificity of targeting in tumor microenvironments.

Possible next steps include bioconjugation of boron dye polymers with single chain VEGF (scVEGF) and antiHER2 affibody for oxygen quantification.[3,4] In breast cancer, scVEGF targets VEGF receptors overexpressed on tumor endothelial cells, which is related to angiogenesis and vascular permeability. With scVEGF targets, it is possible to spatially measure vascular oxygen levels in tumors. The antiHER2 affibody binds to HER2 receptor, which is also present in breast cancer cells and is known to regulate cell proliferation and oxygen consumption. Both scVEGF and antiHER2 affibody can be coupled to maleimide functionalized PEG-PDLA (MA-PEG-PLA)

via cysteine thiol bonding (Figure 7.1).[5] Oxygen sensing nanoconjugates with these active targeting groups can be incorporated into stereocomplex formation where target-MA-PEG-PDLA and dye-PLLA-PEG may be coprecipitated into nanoparticles.

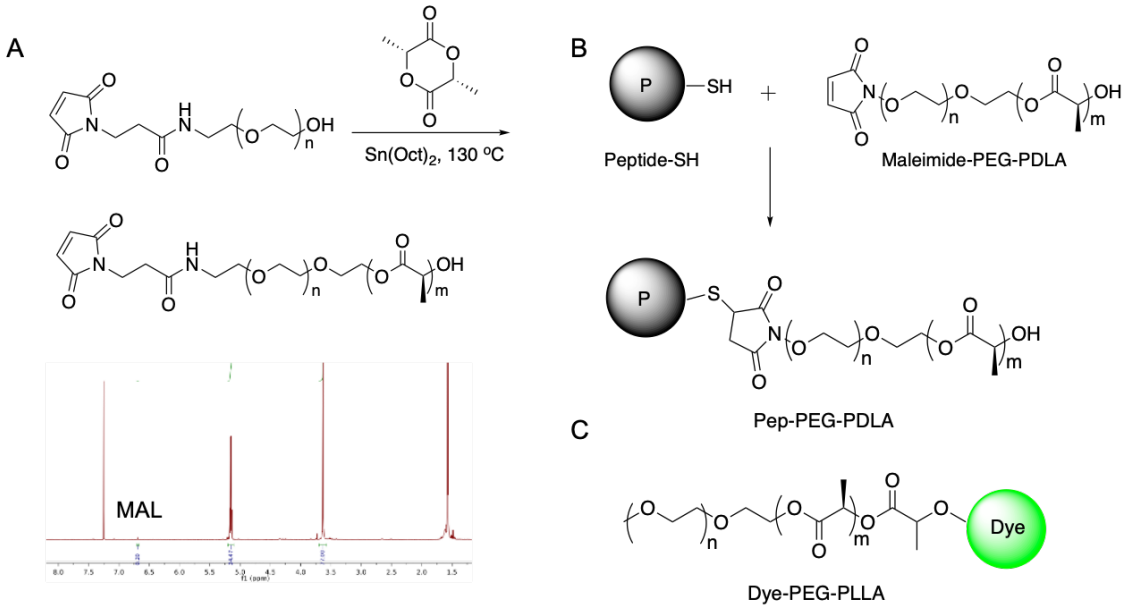

Figure 7. 1. Active Bioconjugates Composition. A) Polymerization of MA-PEG-PDLA and NMR characterization showing MAL peak. B) Formation of cysteine thiols. C) Chemical structure of dye-PEG-PLLA.

7.2.3 In Vivo Wound Oxygen Imaging

In the development and optimization of oxygen sensing nanoparticles for wound imaging, we were able to monitor wound healing using a full range dye (0 – 100 % O_2), which has significant phosphorescence intensity even under air. The strong phosphorescence makes it possible to generate oxygen maps without covering the wound beds. However, nanoparticles tend to be retained within wound tissue after multiple applications, which, even though degradable and non-toxic, may nonetheless, be a barrier to FDA approval for certain uses. The PEGylated nanoparticles did not entirely resolve this issue, therefore decreasing wound retention or even more definitively proving that nanoparticle retention is not a problem, are areas for further investigation.

One solution is to incorporate boron dye-polymers into gels or nanosheets that can be washed or peeled off after application. Unlike aqueous suspensions, the delivery of oxygen sensors via gels can address the issue of imaging agent runoff, while still retaining easy and conformal application benefits. For those purpose, we attempted to embed aqueous nanoparticles into Plurogel®, a commercially available wound dressing consisting of pluronic F68. The critical micelle temperature of pluronic F68 is concentration dependent; that is, at a certain concentration of the polymer, there is transition temperature above which the gel will be formed.[6] By taking this unique property into account, the nanoparticles were mixed thoroughly with liquid pluronic F68 at low temperature (e.g., 0 °C), and the mixture turned into a gel at high temperature (e.g., 37 °C). As proof of concept, the mixture was applied to a murine wound model to demonstrate utility in response to local oxygen variations. Future experiments will involve exploring other oxygen permeable and optically transparent polymers as carriers. The ultimate goal from here is to perform clinical trials and to test the oxygen sensors in humans.

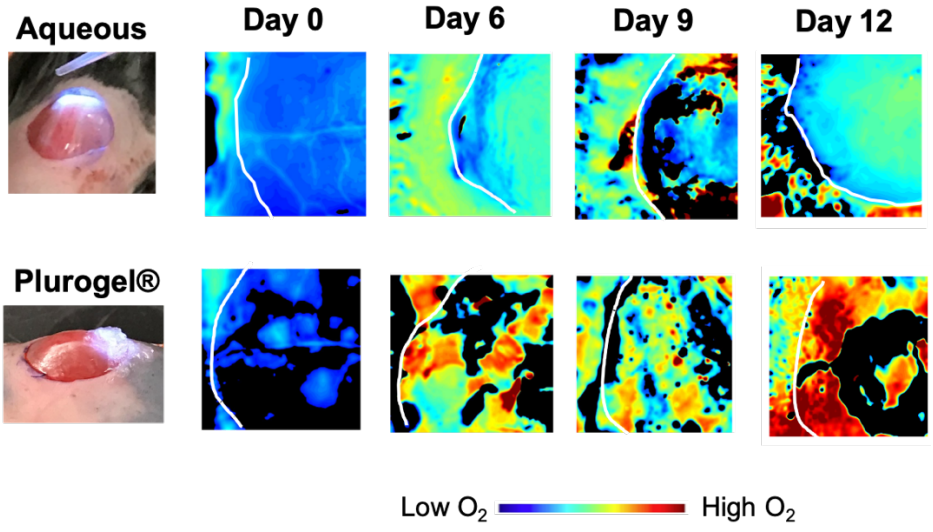

Figure 7. 2. Wound Imaging with Aqueous Nanoparticles (top) and Plurogel (bottom). The nanoparticles or gel was applied on the wound beds, the images were taken and were analyzed according to a previously established method.[7] Ratiometric images over time revealed the sensor response to local oxygen variations during healing process.

7.2.4 In Vivo Brain Oxygen Imaging

Oxygen sensing in the surface of the brain is important to study changes in oxygen during seizures. Besides *in vitro* and *ex vivo*, *in vivo* imaging also needs to be extended. A mouse model was selected as a good starting point for this work given its prevalence in brain and neuroscience research. For whole animal imaging, delivery methods usually include IV injection or direct application. Given the presence of the blood brain barrier (BBB) that might prevent the diffusion of boron nanoparticles, in preliminary collaborative studies with the Kapur Lab, we opened the mouse brain by creating a 3 x 3 mm cranial window, with the dura remaining intact.[8] The nanoparticles were then delivered underneath the dura with a micro-glass pipette. Preliminary results with an RGB color camera showed emission of the nanoparticles under UV excitation (Figure 7.3). The imaging can be extended to a higher resolution imaging setup, such as a two-photon microscope or mesoscale camera. The Kapur lab has developed a cobalt/homocysteine model of seizures. Cobalt implantation creates a seizure focus in the frontal lobe of the mouse brain and then systemic administration of homocysteine causes seizures to propagate along the cortical mantle, with activation of layer 2/3 neurons. This is the model we aim to use in this project, in conjunction with O_2 imaging, to analyze how the oxygen concentration is related to seizures, once imaging methods are developed and optimized. Once the imaging methods are optimized, nanoparticles with active conjugation may be developed to deliver the imaging and sensing agents, such as via transferrin and lactoferrin, both of which have receptors expressed in the BBB. This could avoid interfering with brain tissue, leaving the dura mater intact when the cranial window is opened for imaging.

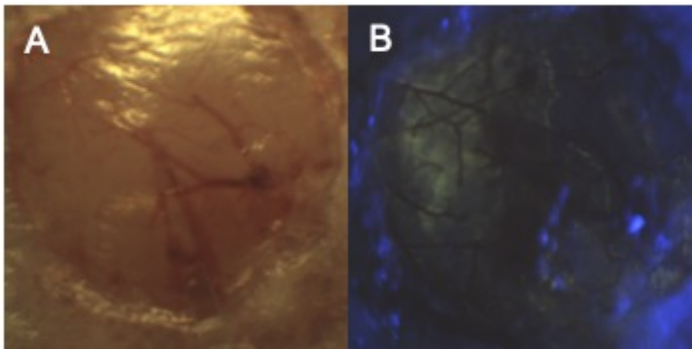

Figure 7. 3. Mouse Cranial Window Imaging. A) Picture of cranial window before nanoparticle application under ambient light. B) Image taken with hand held UV excitation (λ = 405 nm) after the nanoparticles are injected. Yellow emission around vasculature is indicative of nanoparticle localization.

7.3 Conclusion

The work from the past five years achieved the main goal of this research, that is, to optimize and engineer the boron dye polymers for broader applications in biological context. In particular, the blue nanoparticles were demonstrated to be used as bright blue cell labeling reagents in immunology and the oxygen sensing nanoparticles were optimized to study brain activity. A series of new oxygen sensing dyes were developed, in combination with a custom MATLAB software for calibration optimization and a RGB camera, offering a portable, cost-effective, and simple imaging setup. More importantly, the active targeting strategy was established to accommodate multi-colored dyes and biomolecules. Efforts have also been made to promote the regulation and approval of the BNPs in clinical trial including the ongoing project on human testing, which will be the ultimate goal of the research in Fraser Lab. In summary, the excellent properties of boron dye polymers will ensure that there are still lots of possibilities for them to serve as oxygen sensing and imaging agents in research and clinical fields.

7.4 References

(1) Parish, C. R. Fluorescent Dyes for Lymphocyte Migration and Proliferation Studies.

Immunol. Cell Biol. **1999**, *77*, 499–508.

(2) Wang, H.; Mao, D.; Wang, Y.; Wang, K.; Yi, X.; Kong, D.; Yang, Z.; Liu, Q.; Ding, D. Biocompatible Fluorescent Supramolecular Nanofibrous Hydrogel for Long-Term Cell Tracking and Tumor Imaging Applications. *Sci. Rep.* **2015**, *5*, 16680.

(3) Anderson, C. R.; Rychak, J. J.; Backer, M.; Backer, J.; Ley, K.; Klibanov, A. L. ScVEGF Microbubble Ultrasound Contrast Agents: A Novel Probe for Ultrasound Molecular Imaging of Tumor Angiogenesis. *Invest. Radiol.* **2010**, *45*, 579–585.

(4) Hardee, M. E.; Eapen, R. J.; Rabbani, Z. N.; Dreher, M. R.; Marks, J.; Blackwell, K. L.; Dewhirst, M. W. Her2/Neu Signaling Blockade Improves Tumor Oxygenation in a Multifactorial Fashion in Her2/Neu+ Tumors. *Cancer Chemother. Pharmacol.* **2009**, *63*, 219–228.

(5) Gindy, M. E.; Ji, S.; Hoye, T. R.; Panagiotopoulos, A. Z.; Prud'Homme, R. K. Preparation of Poly(Ethylene Glycol) Protected Nanoparticles with Variable Bioconjugate Ligand Density. *Biomacromolecules* **2008**, *9*, 2705–2711.

(6) Bahadur, P.; Li, P.; Almgren, M.; Brown, W. Effect of Potassium Fluoride on the Micellar Behavior of Pluronic F-68 in Aqueous Solution. *Langmuir* **1992**, *8*, 1903–1907.

(7) DeRosa, C. A.; Seaman, S. A.; Mathew, A. S.; Gorick, C. M.; Fan, Z.; Demas, J. N.; Peirce, S. M.; Fraser, C. L. Oxygen Sensing Difluoroboron β-Diketonate Polylactide Materials with Tunable Dynamic Ranges for Wound Imaging. *ACS Sensors* **2016**, *1*, 1366–1373.

(8) Holtmaat, A.; Bonhoeffer, T.; Chow, D. K.; Chuckowree, J.; De Paola, V.; Hofer, S. B.; Hübener, M.; Keck, T.; Knott, G.; Lee, W. C. A.; et al. Long-Term, High-Resolution Imaging in the Mouse Neocortex through a Chronic Cranial Window. *Nat. Protoc.* **2009**, *4*, 1128–1144.

Appendix A

Supporting Information for Chapter 2

Scheme S2.1. Synthetic Pathways for Boron Polymers.

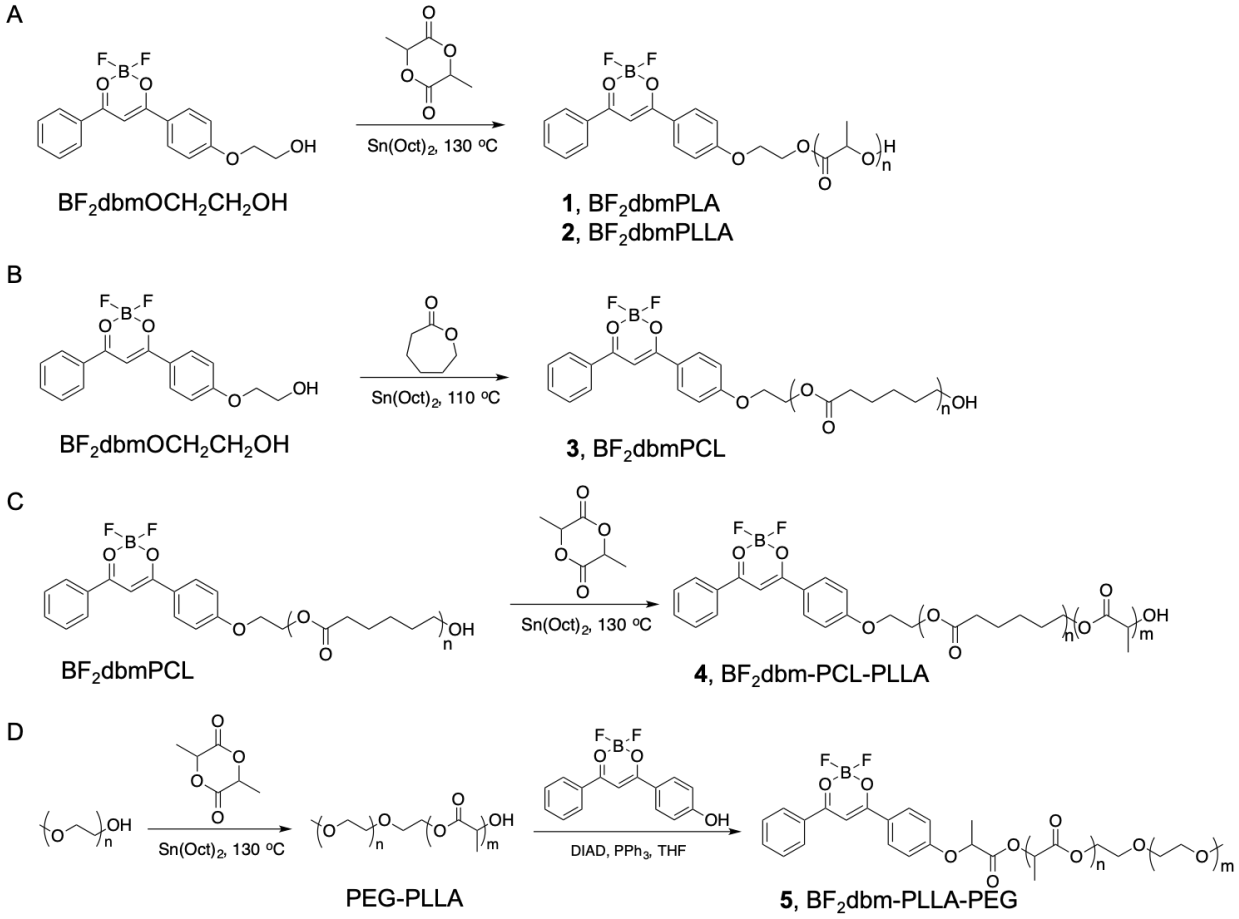

Table S2.1. Antibodies Used for Flow Cytometry and Imaging Experiments

Target	Fluorophore	Target Species	Clone	Vendor
CD3	AlexaFluor 488	Mouse	17A2	Biolegend
CD11c	Phycoerythrin (PE)	Mouse	N418	Biolegend
B220	AlexaFluor 647	Mouse	RA3-6B2	Biolegend
B220	FITC	Mouse	RA3-6B2	Biolegend
CD4	APC/Cy7	Mouse	GK1.5	Biolegend
CD80	PE	Mouse	16-10A1	Biolegend
CD40	AlexaFluor 647	Mouse	HM40-3	Biolegend
Lyve-1	eFluor 660	Mouse	ALY7	eBioscience

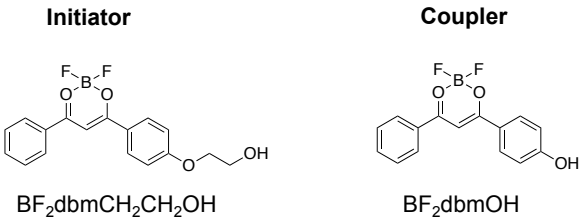

Figure S2.1. Boron dyes for polymer initiation (initiator) and post polymerization modification (coupler).

Note: As in the Chapter 2, in the figures below, the boron dye-polymers and nanoparticles are referred by their polymer compositions (e.g. PLA = BF_2dbmPLA).

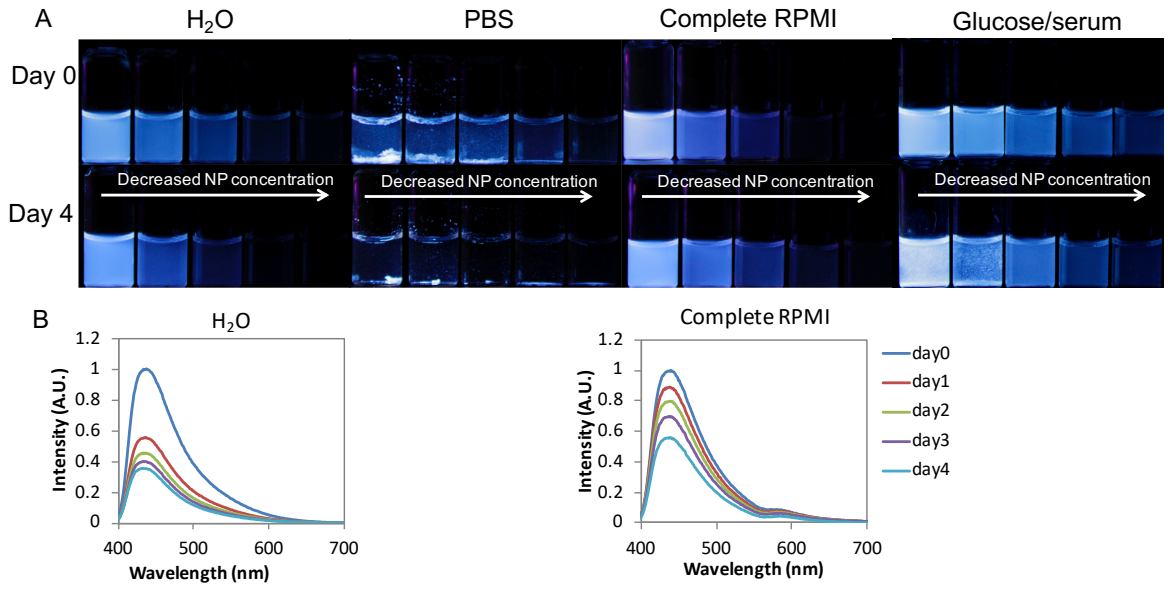

Figure S2.2. (A) Visual inspection of PLA in different media before and after incubation for 5 days (concentration from left to right: 200, 100, 50, 20, 10 μg/mL). (B) Fluorescence emission spectra of nanoparticles (200 μg/mL) recorded everyday over the time course. Spectra are not shown for nanoparticles that aggregated in PBS and glucose/serum during the time course.

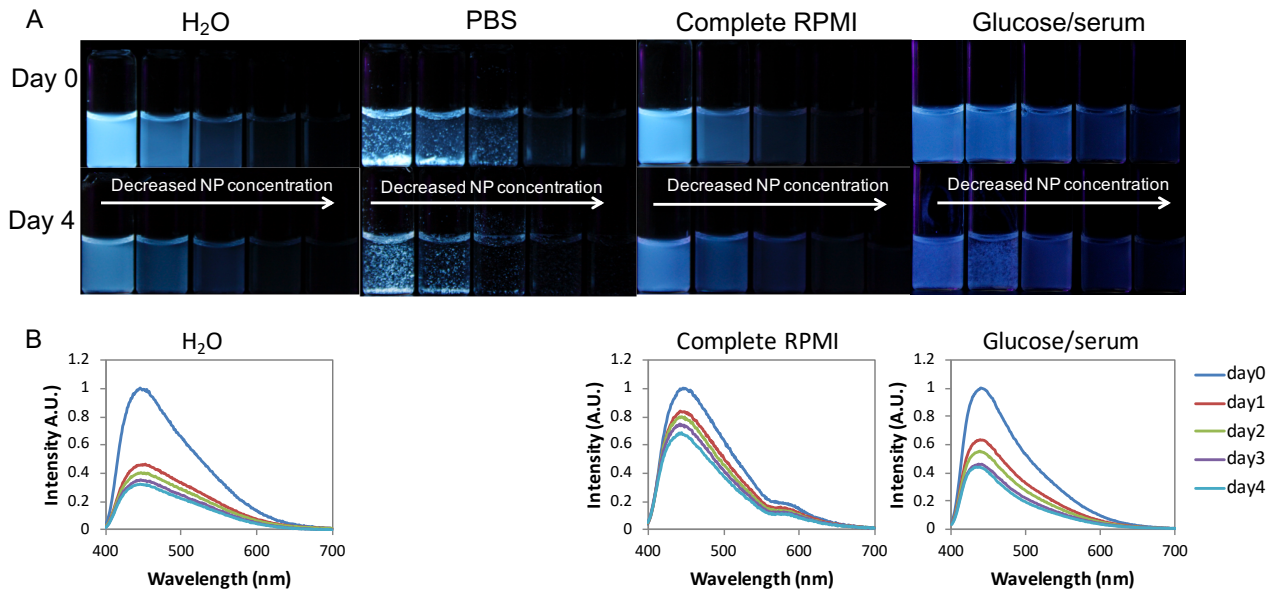

Figure S2.3. (A) Visual inspection of PLLA in different media before and after incubation for 5 days (concentration from left to right: 200, 100, 50, 20, 10 μg/mL). (B) Fluorescence emission spectra of nanoparticles (200 μg/mL) recorded everyday over the time course. Spectra are not shown for nanoparticles that aggregated in PBS during the time course.

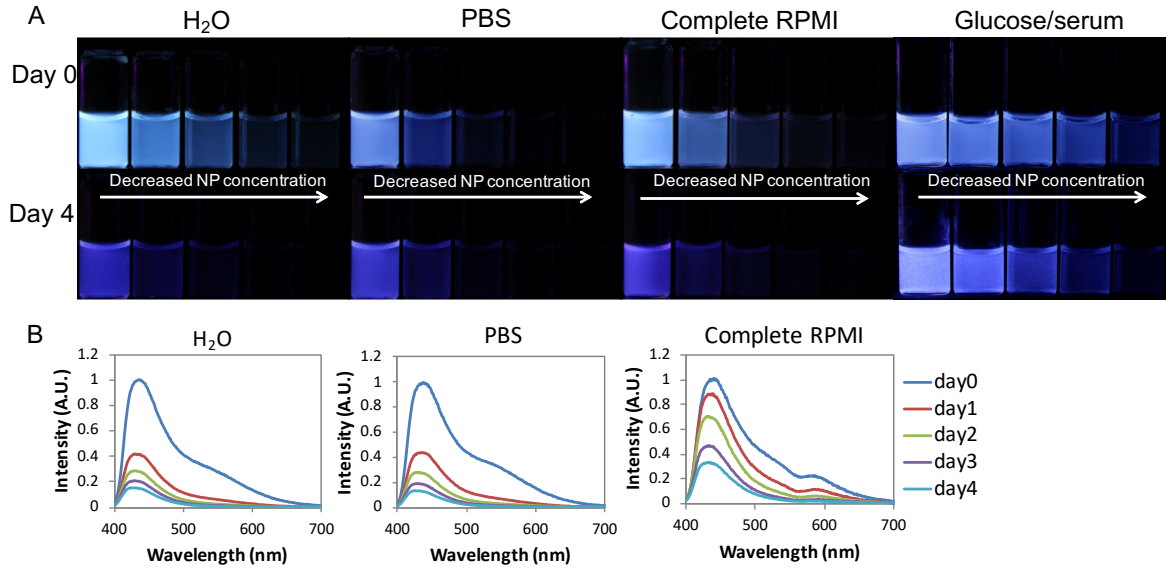

Figure S2.4. (A) Visual inspection of PCL in different media before and after incubation for 5 days (concentration from left to right: 200, 100, 50, 20, 10 μg/mL). (B) Fluorescence emission spectra of nanoparticles (200 μg/mL) recorded everyday over the time course. Spectra are not shown for nanoparticles that aggregated in glucose/serum during the time course.

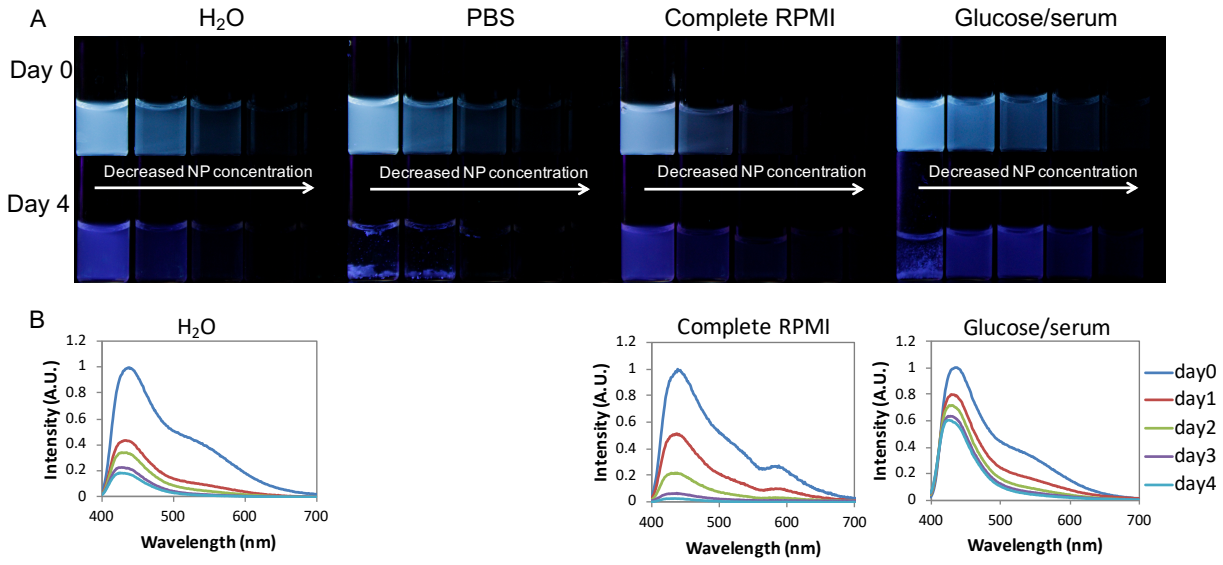

Figure S2.5. (A) Visual inspection of PCL-PLLA in different media before and after incubation for 5 days (concentration from left to right: 200, 100, 50, 20, 10 μg/mL). (B) Fluorescence emission spectra of nanoparticles (200 μg/mL) recorded everyday over the time course. Spectra are not shown for nanoparticles that aggregated in PBS during the time course.

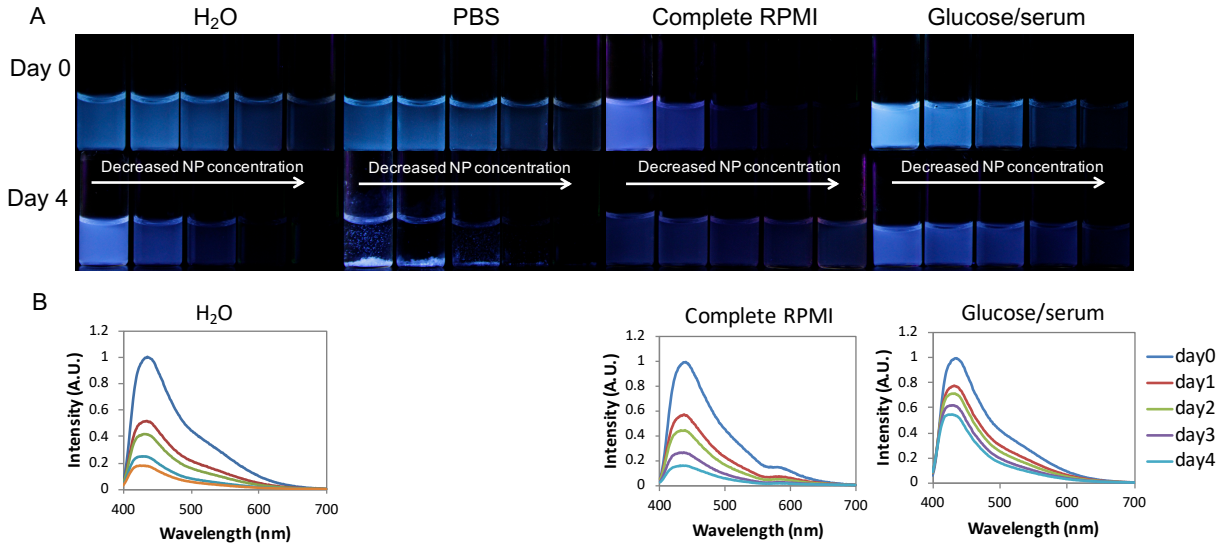

Figure S2.6. (A) Visual inspection of PLLA-PEG in different media before and after incubation for 5 days (concentration from left to right: 200, 100, 50, 20, 10 μg/mL). (B) Fluorescence emission spectra of nanoparticles (200 μg/mL) recorded everyday over the time course. Spectra are not shown for nanoparticles that were aggregated in PBS during the time course.

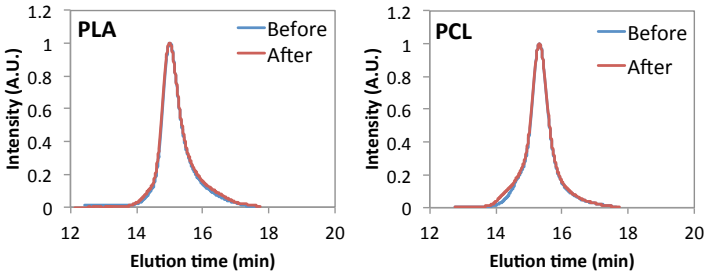

Figure S2.7. GPC traces boron PLA and PCL nanoparticle samples in water before and after incubation in the dark under 37 °C for five days.

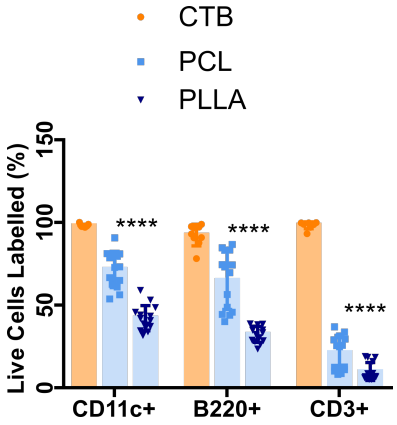

Figure S2.8. Labelling efficiency of PCL and PLLA nanoparticles compared to Cell Tracker Blue for each cell type in the mixed splenocyte population. CD11c+ and B220+ cells were labelled more efficiently than CD3+ cells, consistent with the results for PCL-PLLA nanoparticles. CTB labelled all cell types efficiently. Two-way ANOVA with comparisons to CTB column only. **** $p<0.0001$

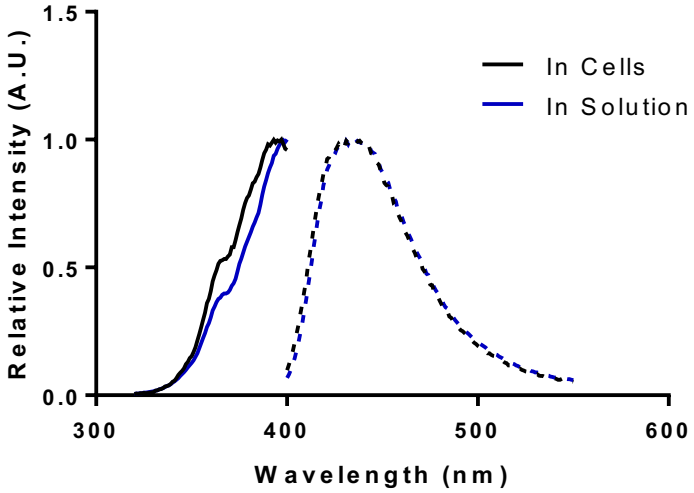

Figure 2.9. Excitation (solid) and emission (dashed) scans of PCL-PLLA nanoparticles immediately after labelling mixed splenocytes (black) and suspended in water (blue). Traces are averaged over three replicates and background subtracted.

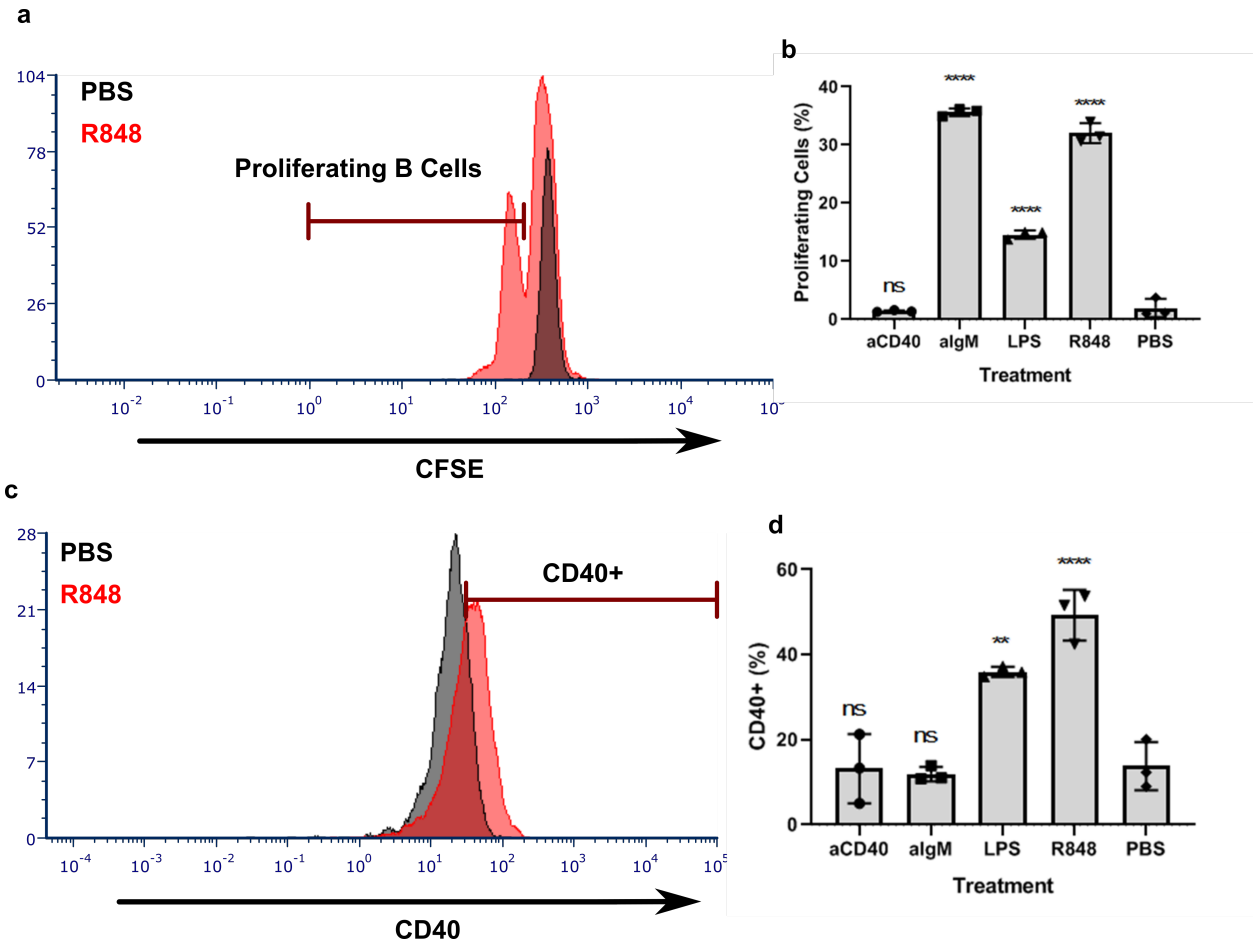

Figure S2.10. Unlabeled purified naïve B cells were treated with 10 µg/mL various stimuli for 48 hours. Activation was measured by proliferation (CFSE dilution) and CD40 upregulation. (a) Representative histograms of PBS (black) and R848 (red) stimulated population showing proliferation by CFSE dilution. (b) Quantification of proliferation of differentially treated cells. (c) Representative histograms of PBS and R848 treated cells showing CD40 upregulation. (d) Quantification of CD40 upregulation of differentially treated cells. R848 gave the highest CD40 upregulation and showed a high percentage of proliferating cells and was chosen for further stimulation studies. Ordinary one way ANOVA with multiple comparisons. Each dot represents a biological replicate. **** $p < 0.0001$, ** $p = 0.0014$, ns denotes $p > 0.05$.

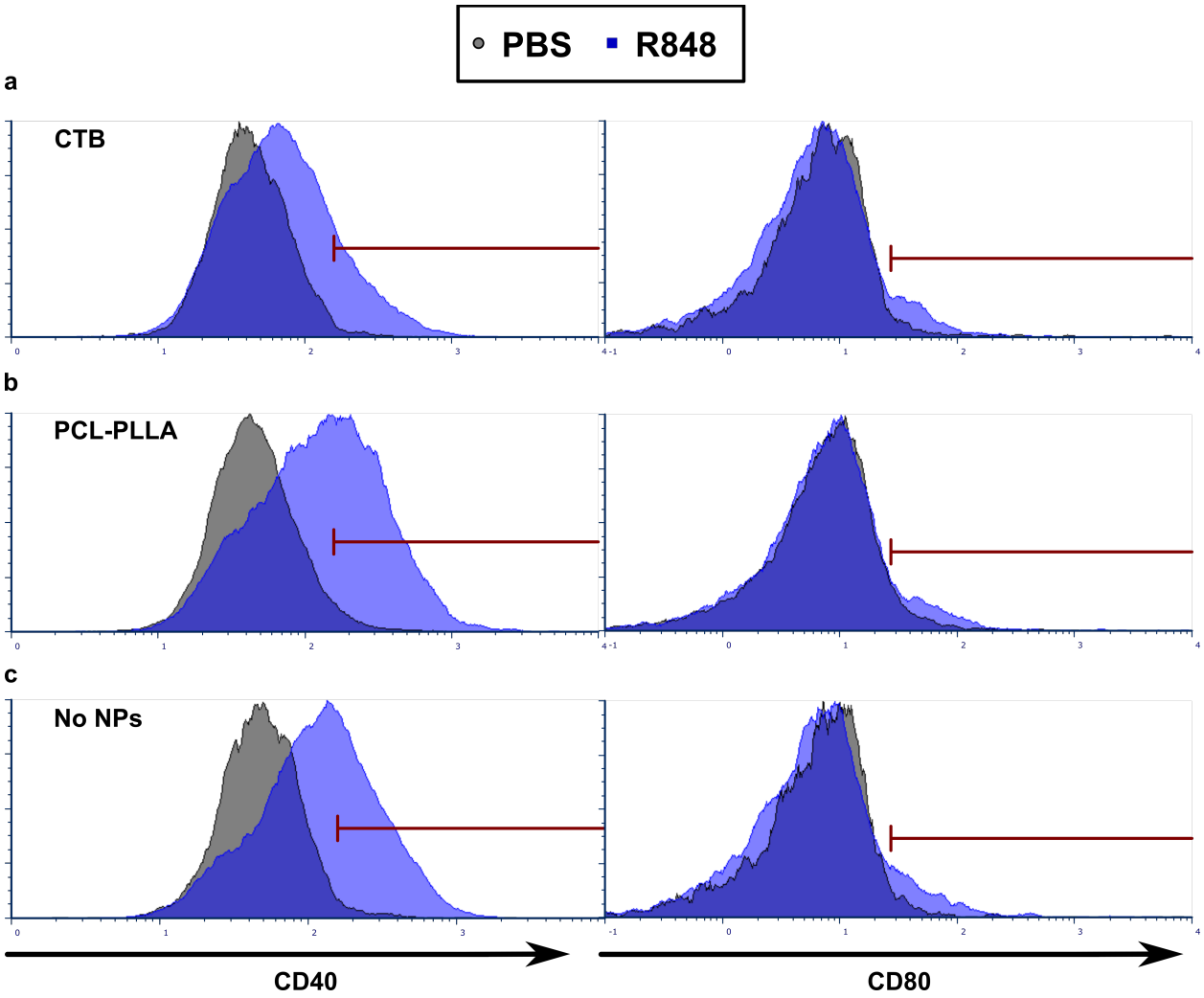

Figure S2.11. B cells stimulated with R848 express activation markers regardless of labelling scheme. Representative histograms showing activation markers CD40 and CD80. (a) CTB labelled, (b) PCL-PLLA labelled, and (c) unlabeled purified B cells. CD40 showed significant shifts in PBS (grey) vs R848 stimulated (blue) traces. CD80 is a much subtler shift.

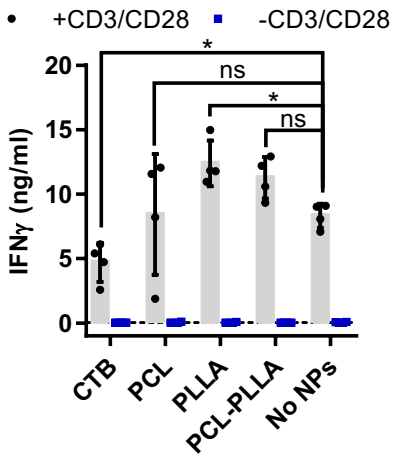

Figure S2.12. T cell activation in bulk splenocytes labelled with nanoparticles. Splenocytes were incubated with anti-CD3/CD28 to induce non-antigen-specific T cell activation. After 24 hours, IFN-γ secretion in the supernatant was analyzed by ELISA. There were significant differences between the stimulated and PBS conditions in all labelling schemes. CTB-labelled cells were significantly lower than the no nanoparticle control whereas the PCL-PLLA-labelled cells were not significant. Dashed line near zero depicts the ELISA limit of detection. Two-way ANOVA with multiple comparisons. * $p < 0.05$.

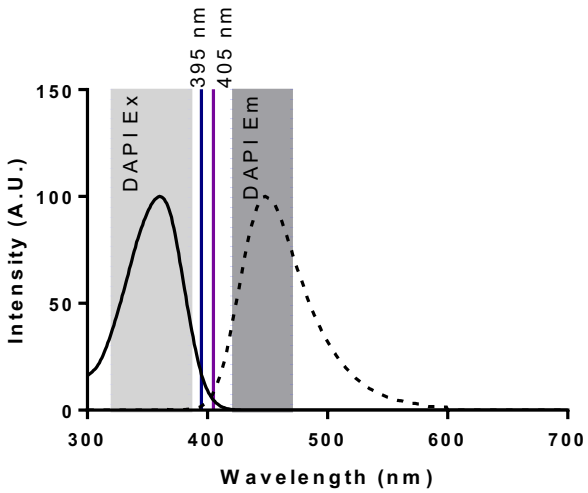

Figure S2.13. Excitation (solid) and emission (dashed) data for 7-hydroxy-4-methylcoumarin, overlaid with typical excitation sources and DAPI emission filter. This data is representative of the spectra for Cell Tracker Blue. The dye has very low overlap with 395 nm and 405 nm excitation sources. Spectral data from Thermo Fisher spectra viewer page for 7-hydroxy-4-methylcoumarin.

Appendix B

Supporting Information for Chapter 3

Scheme S3.1. Alkylation Reactions for Ligand Precursors

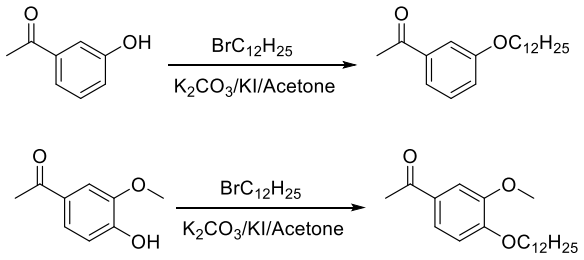

Scheme S3.2. Synthesis of Ligands and Dyes

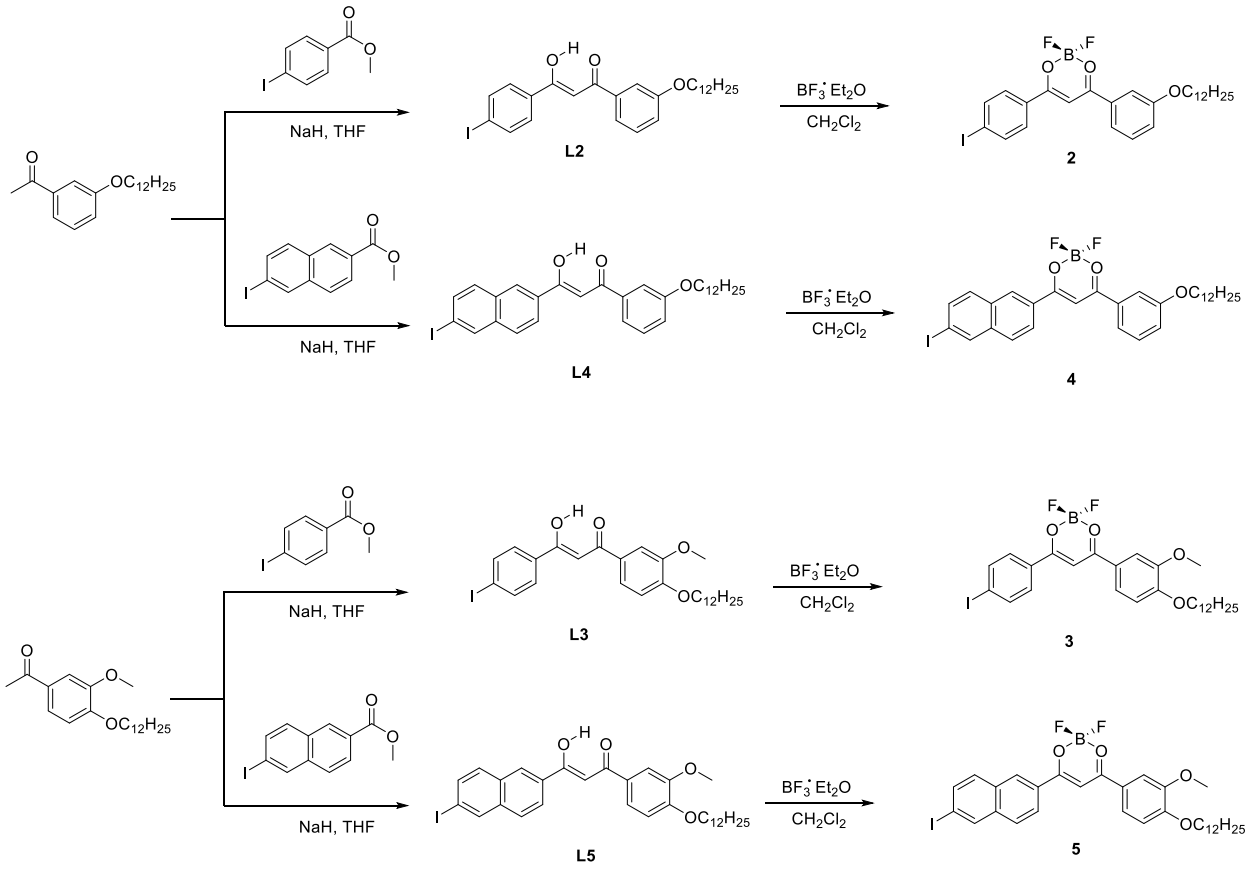

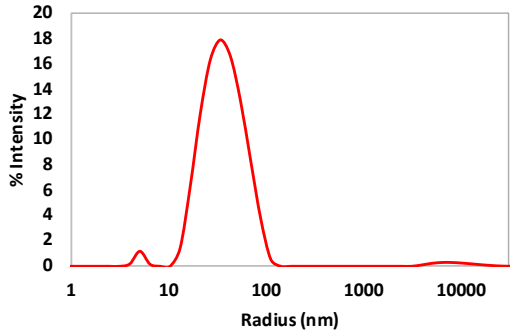

Figure S3.1. DLS Measurement of the Nanoparticles (R_H = 60 nm, % Pd = 23.5)

MATLAB Software

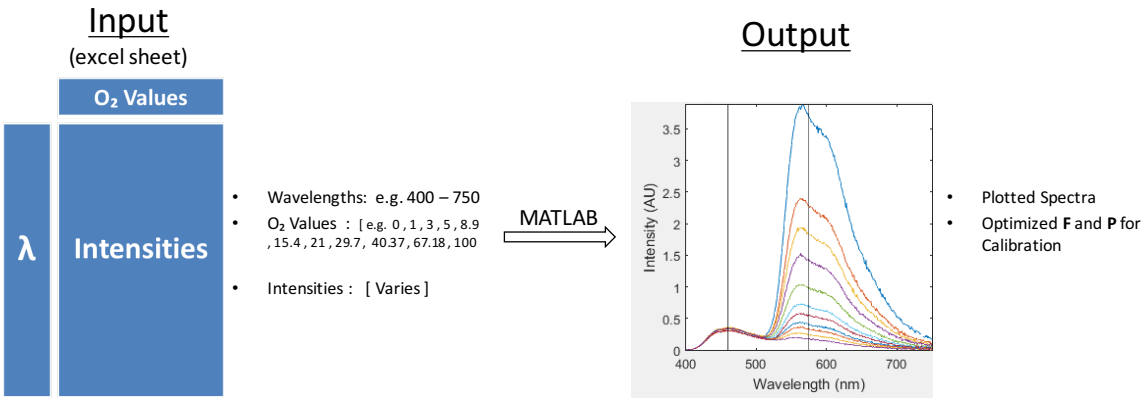

Figure S3.2. A Schematic Illustration of Input and Output for Calibration Optimization Software.

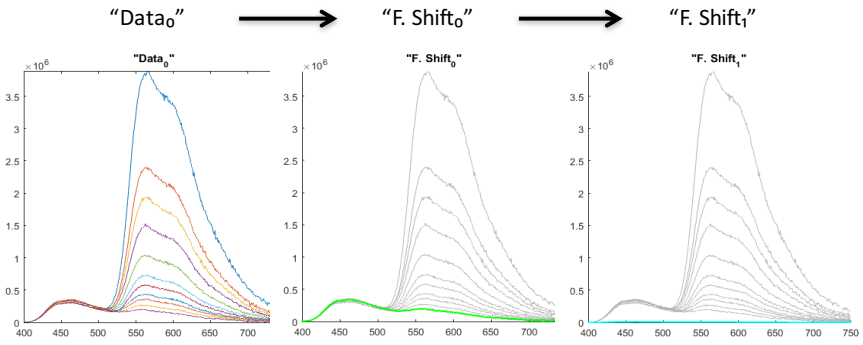

Figure S3.3. Step 1 of Data Processing. The most quenched sample (Green) from the original data (or "$Data_0$") and call it "F. $Shift_0$", then Scale "F. $Shift_0$" so it is ≤ all the other samples in "$Data_0$" at all wavelengths. This scaled version is called "F. $Shift_1$"

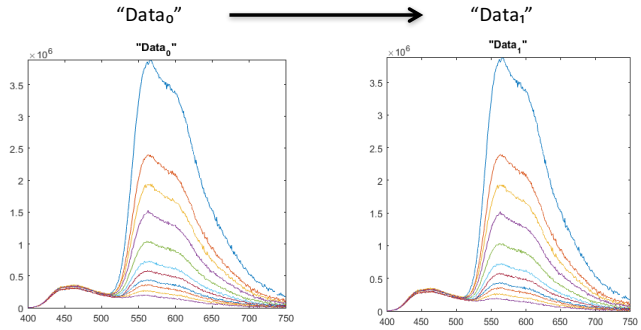

Figure S3.4. Step 2 of Data Processing. Subtract "F. $Shift_1$" from "$Data_0$" to create "$Data_1$"

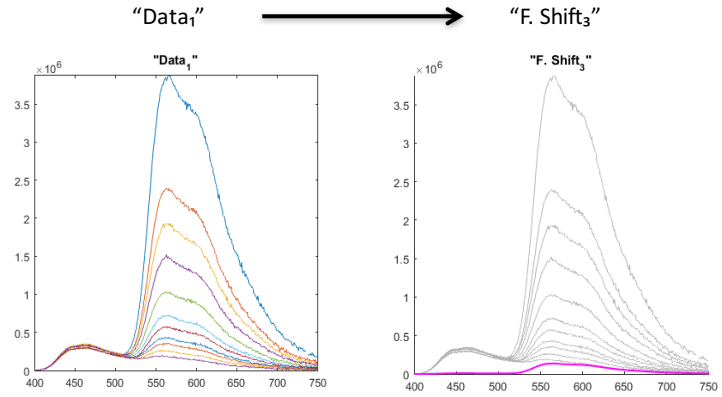

Figure S3.5. Step 3 of Data Processing. Take the **LEAST** quenched sample from "$Data_1$" and multiply it by **the scalar** and call this curve "F. $Shift_3$"

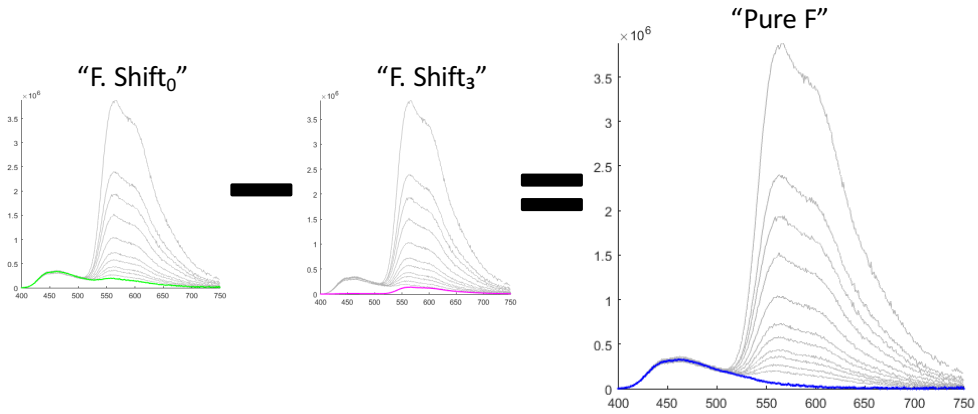

Figure S3.6. Step 4 of Data Processing. Subtract "F. Shift$_3$" from "F. Shift$_0$" and this is the isolated fluorescence or "PureF"

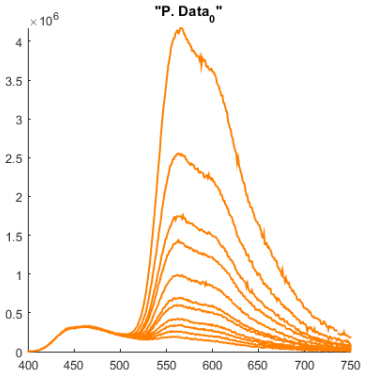

Figure S3.7. Step 5 of Data Processing. Scale "Data$_0$" so it is equal to "PureF" at the selected fluorescence wavelength and call this "PData$_0$"

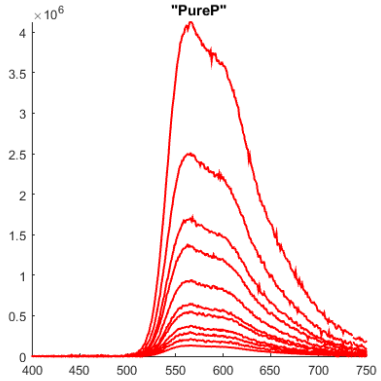

Figure S3.8. Step 6 of Data Processing. Subtract "PureF" from "PData$_0$" to get "PureP"

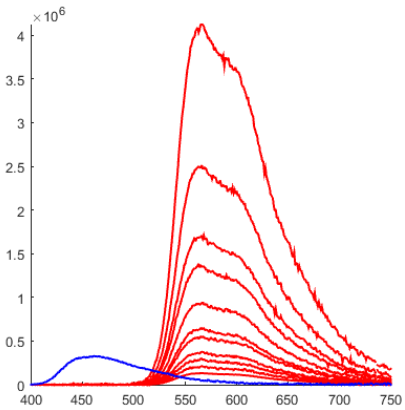

Figure S3.9. Final Product of Data Processing: Overlay of "PureF" and "PureP" spectra.

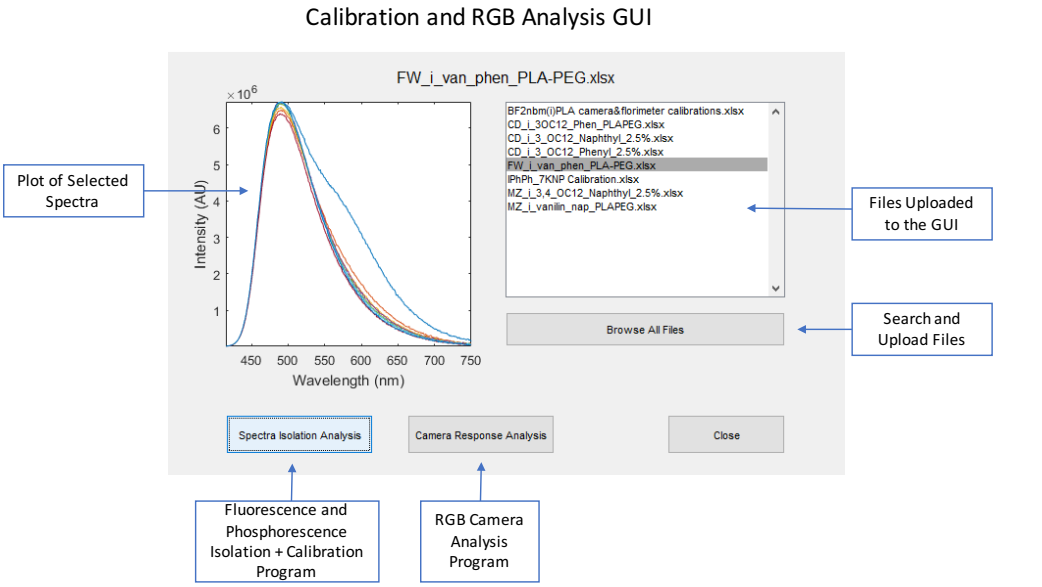

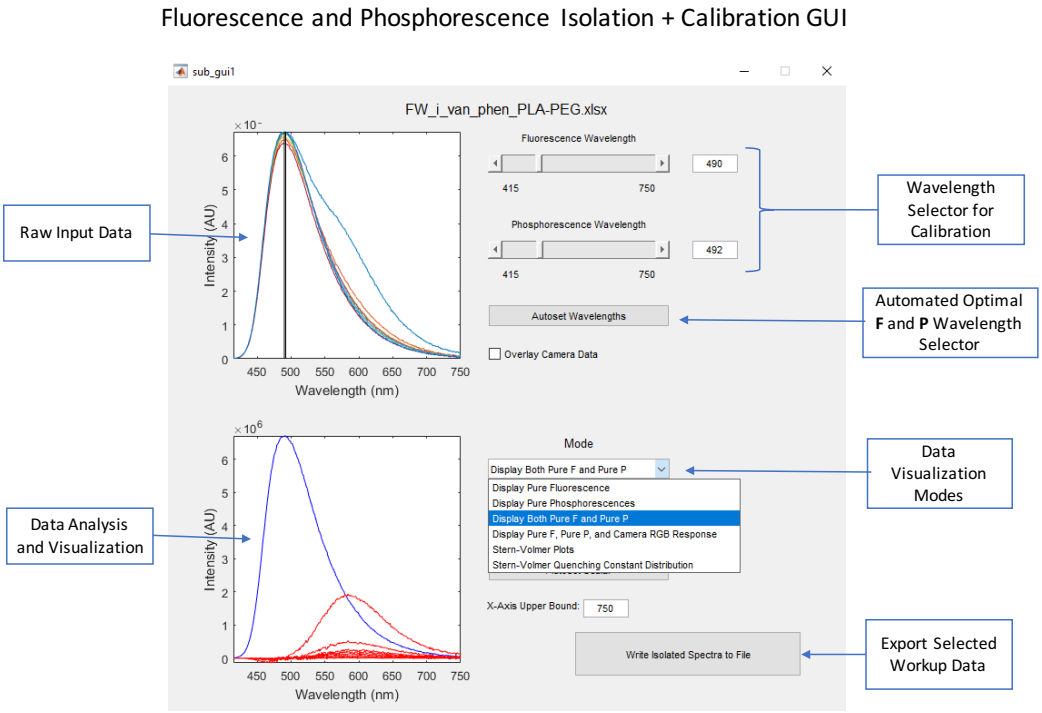

Figures S3.10. GUI of Calibration and RGB Analysis and Peak Isolation.

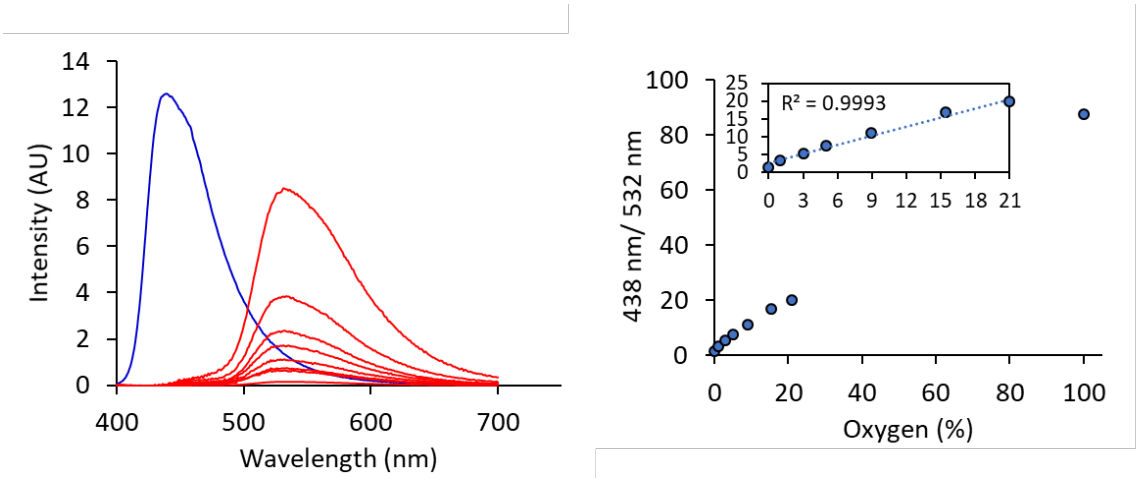

Figure S3.11. Isolated Fluorescence (Blue) and Phosphorescence (Red) of **1** in PLA-PEG NPs. Total emission and FP ratio plot.

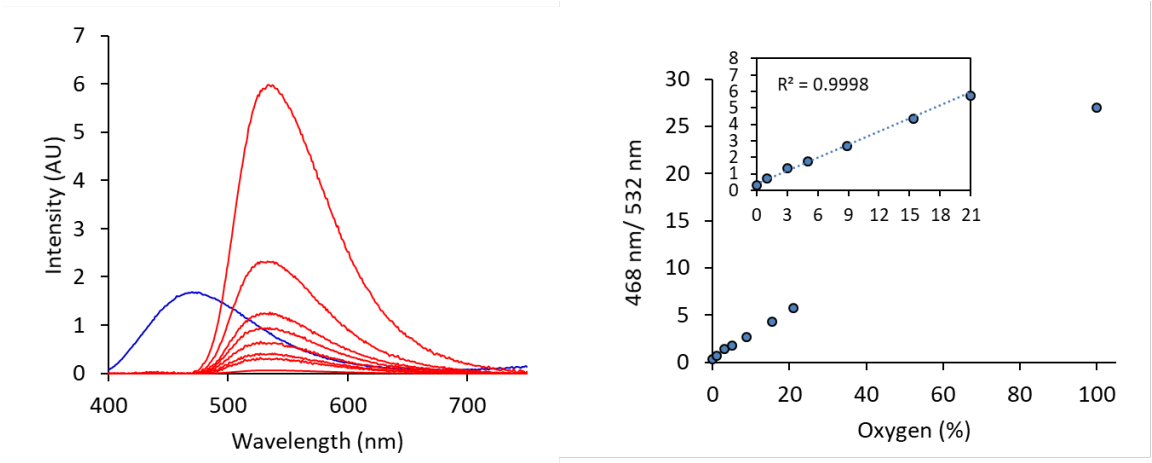

Figure S3.12. Isolated Fluorescence (Blue) and Phosphorescence (Red) of **2** in PLA-PEG NPs. Total emission and FP ratio plot.

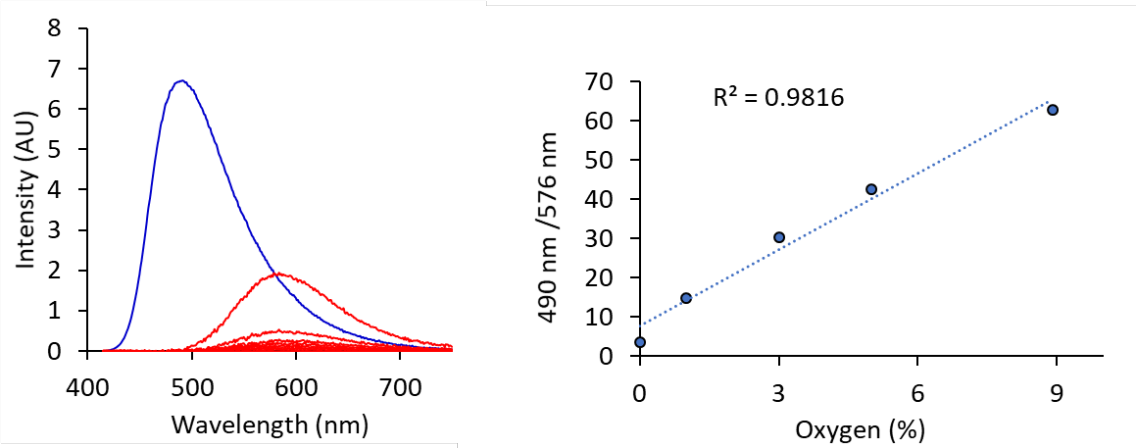

Figure S3.13. Isolated Fluorescence (Blue) and Phosphorescence (Red) of **3** in PLA-PEG NPs. Total emission and FP ratio plot.

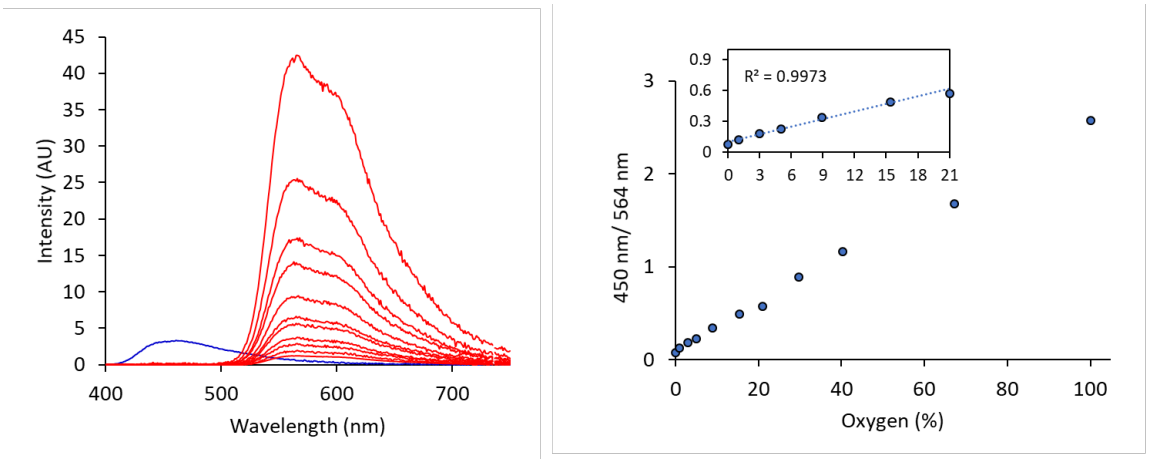

Figure S3.14. Isolated Fluorescence (Blue) and Phosphorescence (Red) of **4** in PLA-PEG NPs. Total emission and FP ratio plot.

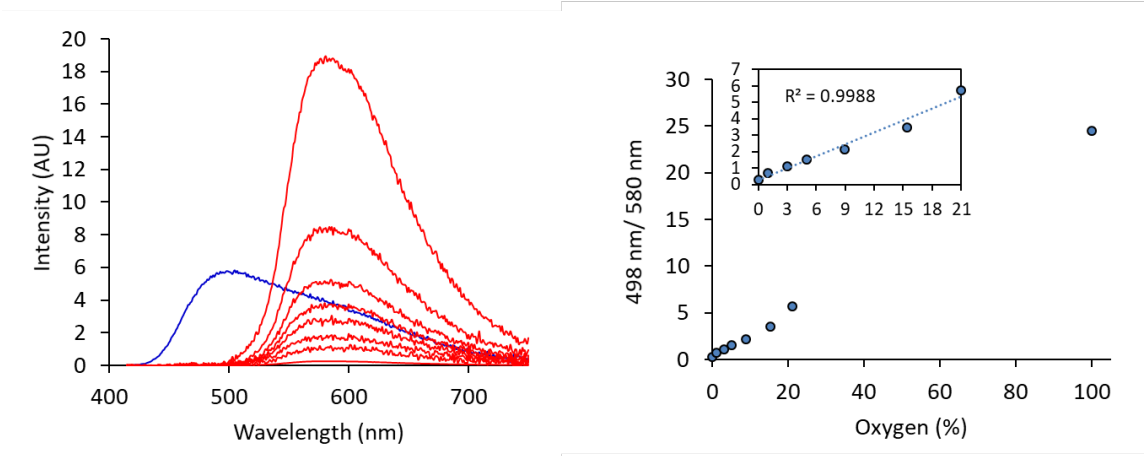

Figure S3.15. Isolated Fluorescence (Blue) and Phosphorescence (Red) of **5** in PLA-PEG NPs. Total emission and FP ratio plot.

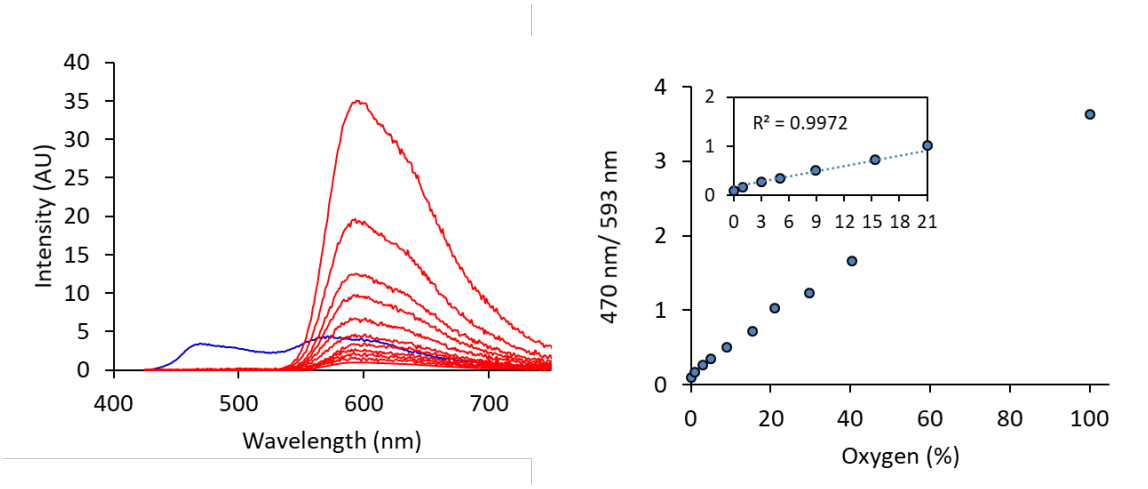

Figure S3.16. Isolated Fluorescence (Blue) and Phosphorescence (Red) of **6** in PLA-PEG NPs. Total emission and FP ratio plot.

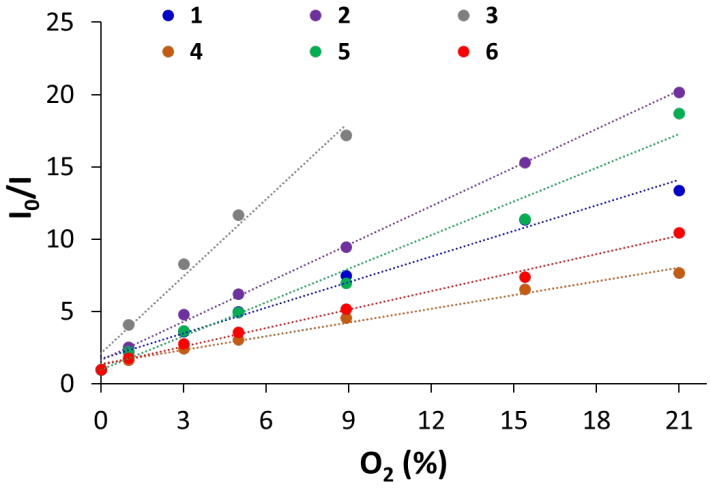

Figure S3.17. Stern-Volmer Oxygen Quenching Plots of Is Boron Dyes in PLA-PEG Nanoparticles (Values summarized on **Table 4.3**).

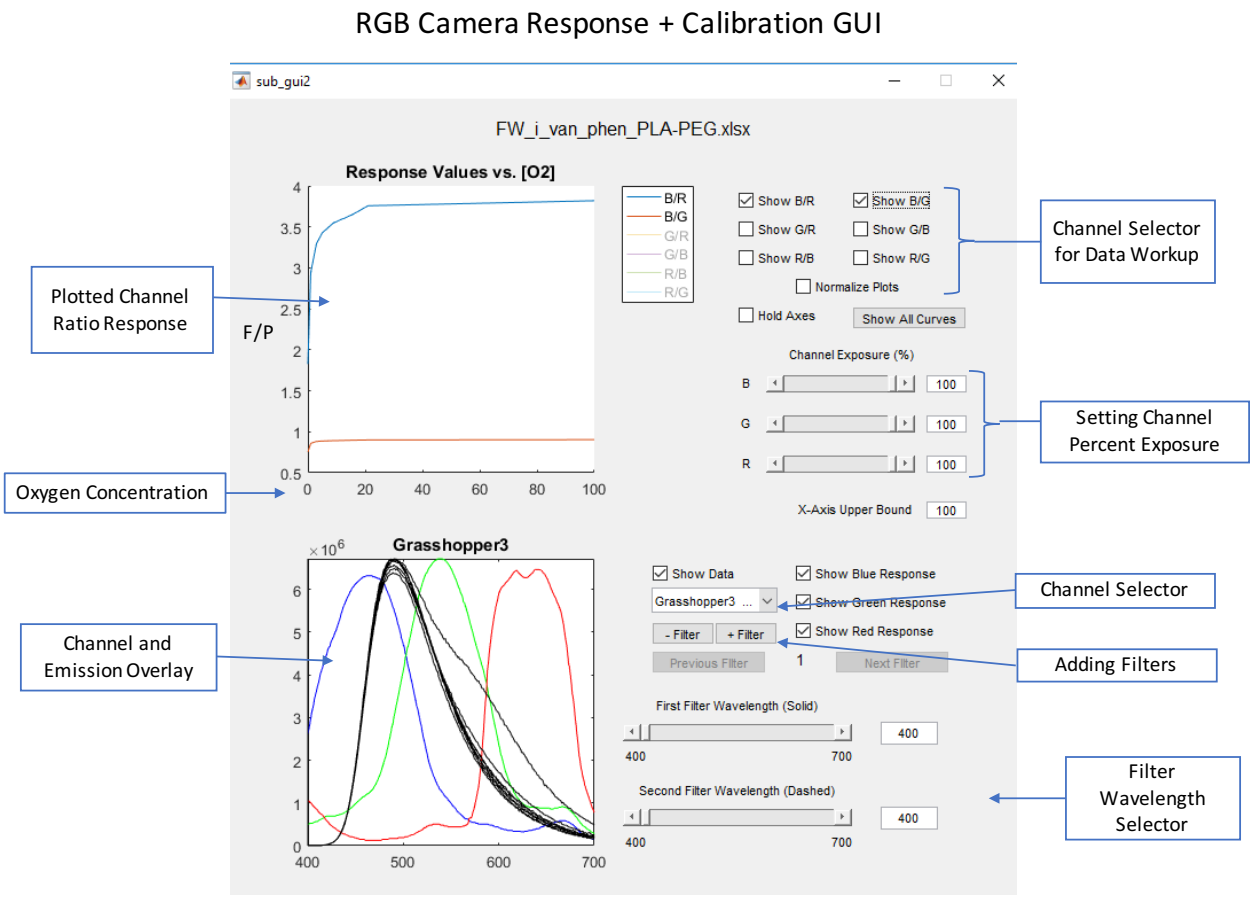

Figure S3.18. RGB Camera Response and Calibration GUI.

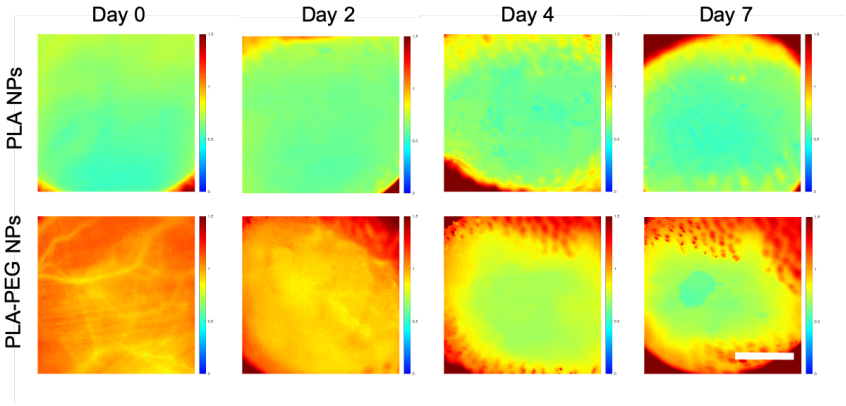

Figure S3.19. Wound Healing Monitored Over Seven Days. Top row and bottom row are PLA NPs and PLA-PEG NPs respectively. Images were analyzed in MATLAB without background subtraction. Scale bar = 1 mm.

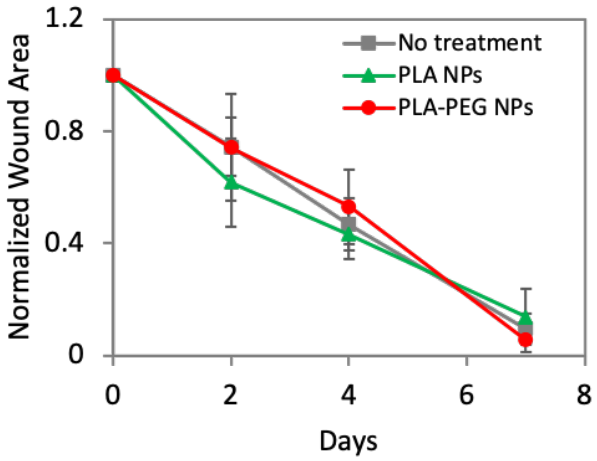

Figure S3.20. Wound Area Monitored by Tracking the Regions Lacking Epidermis.

Computational Details

Tables S3.1. Computational Details for Compound **1**

Sample	Occupied Orbitals	Unoccupied Orbitals
Calculated Structure 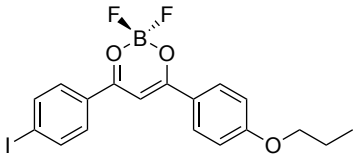	HOMO 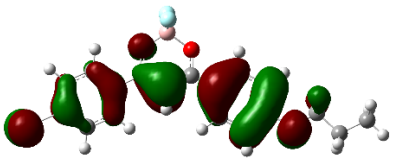	LUMO 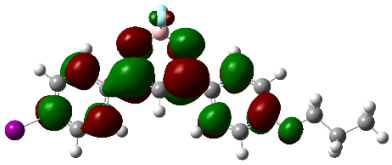
Geometry 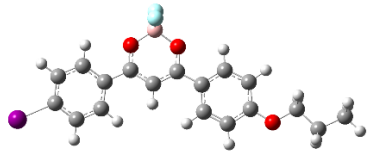	HOMO-1 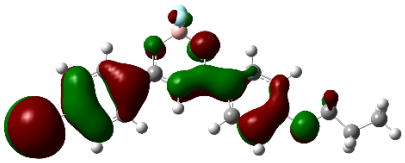	

C	1.72287	0.98543	-0.01934
C	0.46643	0.36975	0.11379
H	0.39968	-0.69076	0.29557
O	1.80007	2.28286	-0.18947
C	-0.69485	1.1239	-0.03664
O	-0.63856	2.42363	-0.20381
B	0.62751	3.18332	-0.01811
F	0.69234	4.18432	-0.97697
F	0.65075	3.71416	1.27528
C	-2.05166	0.54746	-0.03566
C	-3.1642	1.39951	0.09214
C	-2.26919	-0.83693	-0.16241
H	-3.01093	2.46856	0.18861
C	-3.56069	-1.36016	-0.15283
H	-1.43792	-1.52179	-0.29047
C	-4.46048	0.88594	0.10723
C	-4.64782	-0.49316	-0.01382
C	2.99223	0.26549	-0.00751
C	4.20312	0.98638	-0.03755
C	3.05882	-1.14775	0.03249
C	5.43436	0.34044	-0.02435
H	4.17343	2.06986	-0.06582
C	4.2773	-1.80156	0.04485
H	2.1549	-1.7467	0.04415
C	5.48037	-1.0656	0.01745
H	4.32851	-2.88551	0.07151
H	-3.70856	-2.42915	-0.25818
H	6.34314	0.92992	-0.04408
H	-5.30554	1.55752	0.21428
C	7.89562	-1.12989	-0.00209
H	7.95995	-0.52584	-0.9161
H	7.97683	-0.46445	0.8668

```
 O                     6.61568  -1.79553   0.03287
 C                     8.97833  -2.19858   0.02473
 H                     8.85578  -2.80558   0.93054
 H                     8.83794  -2.86808  -0.83325
 C                    10.38301  -1.5834   -0.01143
 H                    10.55583  -0.92825   0.8514
 H                    11.14685  -2.36824   0.00772
 H                    10.53699  -0.98986  -0.92114
 I                    -6.63229  -1.29841   0.01081

Excitation energies and oscillator strengths:

 Excited State   1:      Singlet-A      3.0442 eV  407.28 nm  f=1.3041
<S**2>=0.000
      89 -> 90         0.70110
 This state for optimization and/or second-order correction.
 Total Energy, E(TD-HF/TD-KS) =  -1157.29229214
 Copying the excited state density for this state as the 1-particle RhoCI
density.

 Excited State   2:      Singlet-A      3.5889 eV  345.47 nm  f=0.0807
<S**2>=0.000
      88 -> 90         0.69511

 Excited State   3:      Singlet-A      3.9035 eV  317.62 nm  f=0.0138
<S**2>=0.000
      84 -> 90        -0.15077
      86 -> 90         0.67278

 Excited State   4:      Singlet-A      3.9293 eV  315.54 nm  f=0.0001
<S**2>=0.000
      87 -> 90         0.70106

 Excited State   5:      Singlet-A      3.9976 eV  310.15 nm  f=0.0217
<S**2>=0.000
      85 -> 90         0.68207

 Excited State   6:      Singlet-A      4.2993 eV  288.38 nm  f=0.0791
<S**2>=0.000
      84 -> 90         0.66224
      86 -> 90         0.16984

 Excited State   7:      Singlet-A      4.5128 eV  274.74 nm  f=0.0004
<S**2>=0.000
      88 -> 91        -0.17047
      88 -> 92        -0.42508
      89 -> 91         0.21495
      89 -> 92         0.48670

 Excited State   8:      Singlet-A      4.7935 eV  258.65 nm  f=0.0722
<S**2>=0.000
      83 -> 90         0.12325
      89 -> 91         0.62023
      89 -> 92        -0.23232
```

```
 Excited State   9:      Singlet-A      4.8438 eV  255.96 nm  f=0.0012
<S**2>=0.000
      80 -> 90         0.34501
      81 -> 90        -0.20998
      82 -> 90         0.54524
      83 -> 90         0.16506

 Excited State  10:      Singlet-A      5.0024 eV  247.85 nm  f=0.0469
<S**2>=0.000
      82 -> 90        -0.13026
      83 -> 90         0.61069
      88 -> 91        -0.22625
      89 -> 91        -0.12965
      89 -> 94        -0.12856
```

Tables S3.2. Computational Details for Compound **2**

Sample	Occupied Orbitals	Unoccupied Orbitals
Calculated Structure 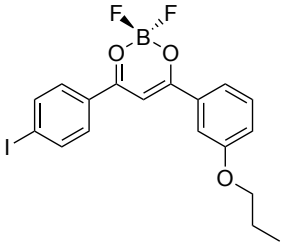	HOMO 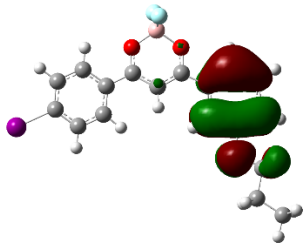	LUMO 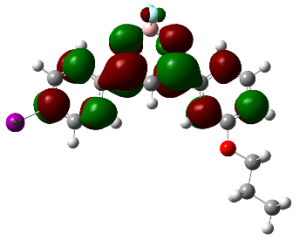
Geometry 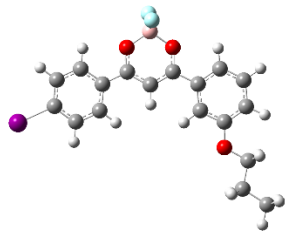	HOMO-1 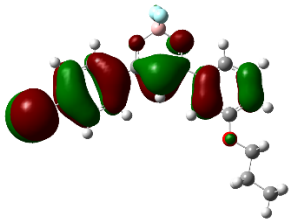	

C	1.97693	1.71141	-0.00672
C	0.82394	0.93097	0.14062
H	0.90827	-0.11988	0.36707
O	1.885	2.99846	-0.21816
C	-0.43298	1.51348	-0.0436
O	-0.54814	2.79925	-0.25776
B	0.59733	3.73822	-0.09652
F	0.53513	4.69266	-1.09926
F	0.52962	4.31851	1.17132
C	-1.69926	0.76192	-0.03061
C	-2.91595	1.46844	0.01196
C	-1.73191	-0.64487	-0.06329
H	-2.90491	2.55218	0.03821
C	-2.94533	-1.3303	-0.04837
H	-0.81613	-1.2231	-0.11924
C	-4.13415	0.79243	0.03074
C	-4.13882	-0.60437	0.00075
C	3.34734	1.17411	0.04539
C	4.43274	2.06818	0.15538
C	3.58848	-0.20661	-0.01462
C	5.72847	1.56616	0.21181
H	4.24991	3.13493	0.20366
C	4.89759	-0.70301	0.0382
H	2.78258	-0.92335	-0.1251
C	5.97541	0.18868	0.15433
H	-2.95134	-2.41432	-0.0797
H	6.56788	2.24952	0.30366
H	-5.0612	1.35359	0.07006

```
 I                    -6.00723  -1.64914   0.02623
 H                     6.99628  -0.17231   0.19766
 C                     6.32875  -2.64837  -0.00854
 H                     6.83379  -2.37231   0.92705
 H                     6.91817  -2.26117  -0.85074
 C                     6.16438  -4.15809  -0.11102
 H                     5.62082  -4.39338  -1.03492
 H                     5.54329  -4.5049    0.72465
 C                     7.51724  -4.88057  -0.09763
 H                     8.06975  -4.67967   0.82877
 H                     7.37624  -5.96429  -0.17293
 H                     8.14693  -4.56674  -0.93955
 O                     5.01766  -2.05768  -0.03452
```

Excitation energies and oscillator strengths:

```
 Excited State   1:      Singlet-A      2.8513 eV  434.84 nm  f=0.0638
<S**2>=0.000
      89 -> 90         0.70401
 This state for optimization and/or second-order correction.
 Total Energy, E(TD-HF/TD-KS) =  -1157.27383604
 Copying the excited state density for this state as the 1-particle RhoCI
density.
```

Excited State 2: Singlet-A 3.2388 eV 382.81 nm f=0.9541 <S2>=0.000**
88 -> 90 0.70251

```
 Excited State   3:      Singlet-A      3.8242 eV  324.21 nm  f=0.1495
<S**2>=0.000
      85 -> 90         0.14361
      87 -> 90         0.68418

 Excited State   4:      Singlet-A      3.8872 eV  318.95 nm  f=0.0002
<S**2>=0.000
      86 -> 90         0.70247

 Excited State   5:      Singlet-A      3.9451 eV  314.27 nm  f=0.0684
<S**2>=0.000
      85 -> 90         0.67980
      87 -> 90        -0.14311

 Excited State   6:      Singlet-A      4.4279 eV  280.01 nm  f=0.0666
<S**2>=0.000
      84 -> 90         0.66493
      89 -> 91         0.19974

 Excited State   7:      Singlet-A      4.6041 eV  269.29 nm  f=0.0006
<S**2>=0.000
      87 -> 92         0.20818
```

```
      88 -> 92         0.65818
      89 -> 92         0.10426

 Excited State   8:      Singlet-A      4.6359 eV  267.44 nm  f=0.0264
<S**2>=0.000
      84 -> 90        -0.20308
      89 -> 91         0.64923

 Excited State   9:      Singlet-A      4.7653 eV  260.18 nm  f=0.0014
<S**2>=0.000
      80 -> 90         0.53629
      81 -> 90        -0.42594
      83 -> 90        -0.11734

 Excited State  10:      Singlet-A      4.9332 eV  251.33 nm  f=0.0021
<S**2>=0.000
      83 -> 90         0.56796
      88 -> 91        -0.38541
```

Tables S3.3. Computational Details for Compound **3**

Sample	Occupied Orbitals	Unoccupied Orbitals
Calculated Structure 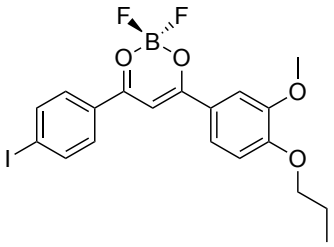	HOMO 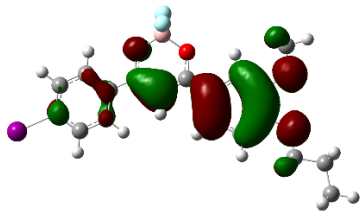	LUMO 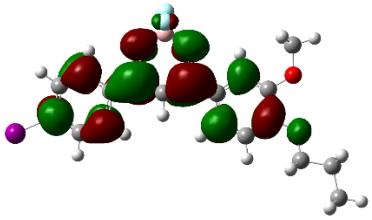
Geometry 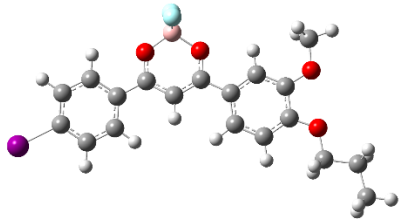	HOMO-1 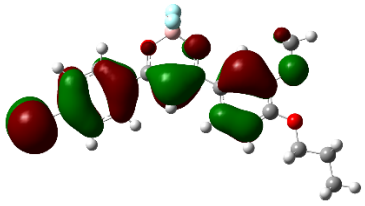	

C	-1.36288	-1.13359	-0.00003
C	-0.1283	-0.47204	0.12447
H	-0.09881	0.59246	0.29231
O	-1.39317	-2.43494	-0.15341
C	1.05819	-1.18605	-0.01612
O	1.04913	-2.48969	-0.16826
B	-0.18823	-3.29237	0.02017
F	-0.21874	-4.29863	-0.93549
F	-0.19414	-3.82033	1.31509
C	2.3941	-0.56219	-0.02093
C	3.53586	-1.3723	0.12071
C	2.56321	0.82689	-0.16829
H	3.42046	-2.44453	0.23349
C	3.8355	1.39551	-0.16653
H	1.70847	1.48003	-0.30683
C	4.81335	-0.81319	0.12816
C	4.95236	0.56942	-0.01481
C	-2.65794	-0.46047	0.00204
C	-3.83962	-1.24108	-0.04038
C	-2.76989	0.93864	0.0392
C	-5.0906	-0.64364	-0.04184
H	-3.74636	-2.31841	-0.06714
C	-4.02228	1.54921	0.03818
H	-1.89157	1.57302	0.05975
C	-5.19172	0.77931	-0.00138
H	3.94551	2.46742	-0.28799
H	5.68133	-1.45299	0.24571
I	6.90813	1.44295	-0.00678
H	-4.08196	2.63036	0.06482

```
 C                    -6.24328  -2.74115  -0.12254
 H                    -5.72898  -3.09491  -1.02372
 H                    -5.75695  -3.15297   0.76946
 H                    -7.28758  -3.05383  -0.14871
 O                    -6.27312  -1.31206  -0.07716
 C                    -6.63448   2.70832   0.03669
 H                    -6.17207   3.10442   0.94994
 H                    -6.14235   3.16218  -0.83311
 C                    -8.1318    2.97868   0.02008
 H                    -8.5628    2.53477  -0.886
 H                    -8.5935    2.47318   0.87743
 C                    -8.43575   4.48141   0.06731
 H                    -9.51713   4.6551    0.05282
 H                    -8.03594   4.94276   0.97887
 H                    -8.00222   5.00539  -0.79358
 O                    -6.4423    1.27946  -0.00609
```

Excited State 1: Singlet-A 2.7686 eV 447.83 nm f=0.7290 <S2>=0.000**

97 -> 98 0.70123

This state for optimization and/or second-order correction.
Total Energy, E(TD-HF/TD-KS) = -1271.79215075
Copying the excited state density for this state as the 1-particle RhoCI density.

Excited State 2: Singlet-A 3.3752 eV 367.33 nm f=0.5772 <S**2>=0.000
95 -> 98 -0.25452
96 -> 98 0.65550

Excited State 3: Singlet-A 3.7024 eV 334.88 nm f=0.0689 <S**2>=0.000
95 -> 98 0.64751
96 -> 98 0.25139

Excited State 4: Singlet-A 4.0119 eV 309.04 nm f=0.0001 <S**2>=0.000
94 -> 98 0.70264

Excited State 5: Singlet-A 4.0237 eV 308.13 nm f=0.0126 <S**2>=0.000
92 -> 98 0.26808
93 -> 98 0.63755

Excited State 6: Singlet-A 4.2658 eV 290.65 nm f=0.0764 <S**2>=0.000
92 -> 98 0.61401
93 -> 98 -0.25003
97 -> 99 0.16769
97 ->100 -0.14374

Excited State 7: Singlet-A 4.4401 eV 279.23 nm f=0.0029 <S**2>=0.000

```
      96 -> 99         0.24859
      96 ->100         0.24976
      97 -> 99         0.48629
      97 ->100         0.35096

 Excited State   8:      Singlet-A      4.5166 eV  274.51 nm  f=0.1114
<S**2>=0.000
      92 -> 98         0.17644
      93 -> 98        -0.12703
      97 -> 99        -0.40370
      97 ->100         0.51162

 Excited State   9:      Singlet-A      4.7706 eV  259.89 nm  f=0.0007
<S**2>=0.000
      95 -> 99         0.13494
      95 ->100         0.12973
      96 -> 99         0.39794
      96 ->100         0.38808
      97 -> 99        -0.24616
      97 ->100        -0.28628

 Excited State  10:      Singlet-A      4.8609 eV  255.06 nm  f=0.0006
<S**2>=0.000
      87 -> 98        -0.12237
      88 -> 98         0.45734
      90 -> 98         0.48697
      91 -> 98        -0.13457
```

Tables S3.4. Computational Details for Compound **4**

Sample	Occupied Orbitals	Unoccupied Orbitals
Calculated Structure 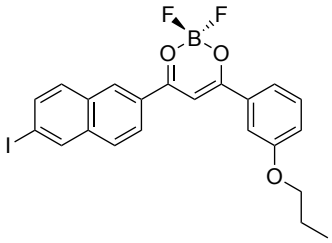	HOMO 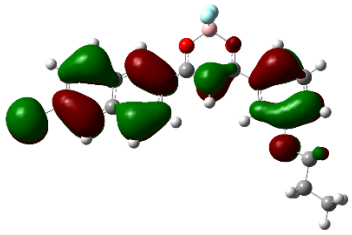	LUMO 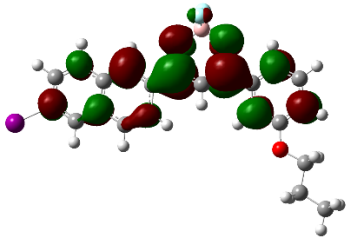
Geometry 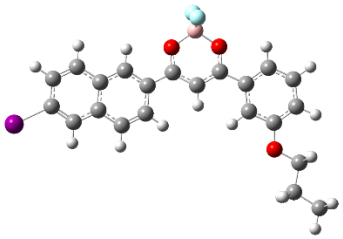	HOMO-1 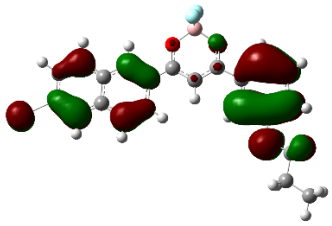	
	HOMO-2 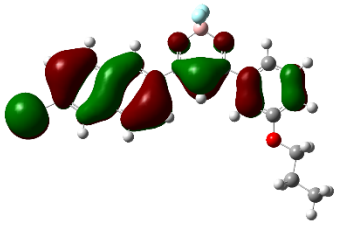	

C	-3.18121	-1.60278	-0.00575
C	-1.99948	-0.86588	0.13227
H	-2.04405	0.18698	0.35971
O	-3.13942	-2.8929	-0.21655
C	-0.76461	-1.4923	-0.06452
O	-0.70115	-2.78231	-0.28258
B	-1.87685	-3.67599	-0.09649
F	-1.85994	-4.64722	-1.08536
F	-1.81852	-4.24135	1.17949
C	-4.52967	-1.01293	0.05626
C	-5.64801	-1.86212	0.18904
C	-4.71715	0.37539	-0.01589
C	-6.92214	-1.3084	0.25632
H	-5.50678	-2.93477	0.24646
C	-6.00471	0.92401	0.04805
H	-3.88501	1.05812	-0.14535
C	-7.11536	0.07715	0.1874
H	-7.78672	-1.95689	0.36591
H	-8.12056	0.47868	0.23959

```
 C                    -7.35747   2.92484  -0.0015
 H                    -7.8602    2.68012   0.944
 H                    -7.97383   2.55249  -0.83104
 C                    -7.1337    4.42556  -0.12336
 H                    -6.59443   4.62875  -1.0573
 H                    -6.48704   4.75553   0.69961
 C                    -8.45563   5.20297  -0.09897
 H                    -9.00307   5.03314   0.83659
 H                    -8.27141   6.27925  -0.18646
 H                    -9.109     4.90767  -0.92941
 O                    -6.0717    2.28164  -0.0381
 C                     0.52278  -0.78215  -0.06119
 C                     1.70148  -1.51963  -0.04085
 C                     0.59318   0.64505  -0.07517
 C                     2.96531  -0.88295  -0.02426
 H                     1.65563  -2.60344  -0.0289
 C                     1.80807   1.28633  -0.06336
 H                    -0.313     1.23892  -0.11475
 C                     3.02636   0.54862  -0.03432
 C                     4.17971  -1.62468   0.00398
 H                     1.84958   2.37207  -0.08153
 C                     4.29391   1.19117  -0.01768
 C                     5.40127  -0.98619   0.01988
 H                     4.13674  -2.71074   0.01234
 C                     5.44191   0.43046   0.00886
 H                     4.33475   2.27568  -0.02544
 H                     6.31976  -1.56244   0.04098
 I                     7.35506   1.40184   0.03654


Excitation energies and oscillator strengths:

 Excited State   1:      Singlet-A      2.8408 eV  436.44 nm  f=0.3556
<S**2>=0.000
     101 ->103        -0.46572
     102 ->103         0.52680
 This state for optimization and/or second-order correction.
 Total Energy, E(TD-HF/TD-KS) =  -1310.91457772
 Copying the excited state density for this state as the 1-particle RhoCI
density.

 Excited State   2:      Singlet-A      2.8921 eV  428.70 nm  f=0.2563
<S**2>=0.000
     101 ->103         0.52638
     102 ->103         0.45931

 Excited State   3:      Singlet-A      3.2847 eV  377.46 nm  f=0.5874
<S**2>=0.000
     100 ->103         0.69191

 Excited State   4:      Singlet-A      3.7260 eV  332.76 nm  f=0.2969
<S**2>=0.000
      99 ->103         0.69475
```

```
 Excited State   5:      Singlet-A      3.9245 eV  315.93 nm  f=0.0000
<S**2>=0.000
      98 ->103         0.70305

 Excited State   6:      Singlet-A      4.3157 eV  287.29 nm  f=0.0720
<S**2>=0.000
      97 ->103         0.66025
     101 ->104         0.14978
     102 ->105         0.12979

 Excited State   7:      Singlet-A      4.3480 eV  285.15 nm  f=0.0005
<S**2>=0.000
      99 ->106         0.12479
     101 ->106         0.16187
     102 ->105         0.13238
     102 ->106         0.65609

 Excited State   8:      Singlet-A      4.3867 eV  282.64 nm  f=0.0513
<S**2>=0.000
     100 ->104         0.22010
     101 ->105         0.10041
     102 ->104         0.56328
     102 ->105         0.28338

 Excited State   9:      Singlet-A      4.4709 eV  277.32 nm  f=0.0325
<S**2>=0.000
      96 ->103        -0.15822
     100 ->104        -0.20368
     101 ->104         0.48472
     101 ->105        -0.14829
     102 ->104         0.28672
     102 ->105        -0.26158

 Excited State  10:      Singlet-A      4.4991 eV  275.58 nm  f=0.0003
<S**2>=0.000
      97 ->103        -0.21566
     100 ->104         0.27752
     101 ->104         0.44533
     102 ->104        -0.26418
     102 ->105         0.28740
```

Tables S3.5. Computational Details for Compound **5**

Sample	Occupied Orbitals	Unoccupied Orbitals
Calculated Structure 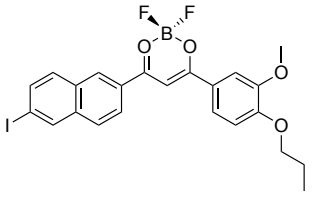	HOMO 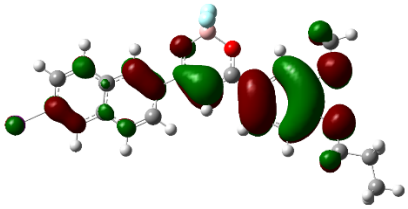	LUMO 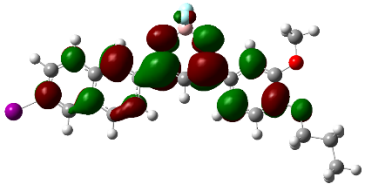
Geometry 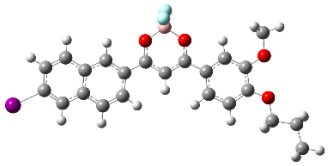	HOMO-1 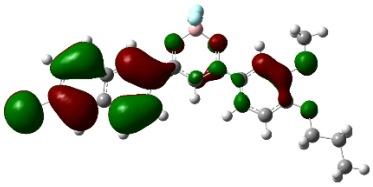	

C	2.51509	1.04754	-0.01113
C	1.27615	0.39205	0.09437
H	1.24105	-0.6742	0.24757
O	2.55541	2.35028	-0.15178
C	0.093	1.11333	-0.04925
O	0.11439	2.41887	-0.19292
B	1.35261	3.21172	0.01588
F	1.39998	4.2271	-0.93043
F	1.34847	3.73025	1.31543
C	3.80674	0.36673	-0.00368
C	4.99274	1.14117	-0.03502
C	3.91134	-1.03295	0.02822
C	6.24064	0.53724	-0.03108
H	4.90518	2.21903	-0.05807
C	5.1607	-1.65008	0.03315
H	3.02972	-1.66297	0.04087
C	6.33431	-0.8862	0.00463
H	5.21452	-2.73164	0.05599
C	7.40432	2.62925	-0.09684
H	6.8976	2.98896	-0.99998
H	6.91426	3.04025	0.79351
H	8.45031	2.93687	-0.11515
O	7.42678	1.19991	-0.05657
C	7.76693	-2.82267	0.04622
H	7.29581	-3.21953	0.9547

```
 H                     7.27891  -3.27115  -0.82869
 C                     9.26289  -3.10084   0.03962
 H                     9.70287  -2.65568  -0.86153
 H                     9.72088  -2.60106   0.90231
 C                     9.5588   -4.60531   0.08319
 H                    10.63935  -4.78456   0.07602
 H                     9.14988  -5.06821   0.98993
 H                     9.12899  -5.12369  -0.78295
 O                     7.58261  -1.39279   0.00678
 C                    -1.24344   0.49549  -0.0674
 C                    -2.36826   1.30641   0.02772
 C                    -1.41257  -0.91876  -0.17983
 C                    -3.67323   0.75597   0.02515
 H                    -2.24841   2.38135   0.11314
 C                    -2.6678   -1.47702  -0.18916
 H                    -0.5495   -1.56725  -0.28011
 C                    -3.83221  -0.66361  -0.08438
 C                    -4.83477   1.57191   0.12936
 H                    -2.78341  -2.55353  -0.28281
 C                    -5.13982  -1.22026  -0.08863
 C                    -6.09695   1.01655   0.12415
 H                    -4.71891   2.64947   0.21274
 C                    -6.23355  -0.38978   0.01391
 H                    -5.25324  -2.29633  -0.17232
 H                    -6.97395   1.64986   0.20364
 I                    -8.20568  -1.23732   0.00987


 Excitation energies and oscillator strengths:

 Excited State   1:      Singlet-A      2.7172 eV  456.29 nm  f=1.0225
<S**2>=0.000
     110 ->111         0.70013
 This state for optimization and/or second-order correction.
 Total Energy, E(TD-HF/TD-KS) =  -1425.43437004
 Copying the excited state density for this state as the 1-particle RhoCI
density.

 Excited State   2:      Singlet-A      3.0353 eV  408.47 nm  f=0.0745
<S**2>=0.000
     107 ->111        -0.10814
     109 ->111         0.68422

 Excited State   3:      Singlet-A      3.3957 eV  365.12 nm  f=0.4452
<S**2>=0.000
     107 ->111        -0.22540
     108 ->111         0.65813

 Excited State   4:      Singlet-A      3.6399 eV  340.63 nm  f=0.0815
<S**2>=0.000
     107 ->111         0.65007
     108 ->111         0.20430
     109 ->111         0.12660
```

```
 Excited State   5:      Singlet-A      4.0419 eV  306.75 nm  f=0.0000
<S**2>=0.000
     106 ->111         0.70238

 Excited State   6:      Singlet-A      4.1029 eV  302.19 nm  f=0.0828
<S**2>=0.000
     105 ->111         0.48387
     109 ->114        -0.10444
     110 ->112         0.49615

 Excited State   7:      Singlet-A      4.2096 eV  294.53 nm  f=0.0351
<S**2>=0.000
     105 ->111         0.48475
     110 ->112        -0.45701
     110 ->114        -0.15242

 Excited State   8:      Singlet-A      4.2990 eV  288.40 nm  f=0.0004
<S**2>=0.000
     109 ->113         0.54326
     110 ->113        -0.42663

 Excited State   9:      Singlet-A      4.4659 eV  277.63 nm  f=0.0563
<S**2>=0.000
     104 ->111        -0.16698
     105 ->111         0.11494
     108 ->112        -0.32152
     109 ->114        -0.30707
     110 ->112        -0.16232
     110 ->114         0.45475

 Excited State  10:      Singlet-A      4.4925 eV  275.98 nm  f=0.0632
<S**2>=0.000
     109 ->112         0.67120
     110 ->114         0.10090
```

Tables S3.6. Computational Details for Compound **6**

Sample	Occupied Orbitals	Unoccupied Orbitals
Calculated Structure 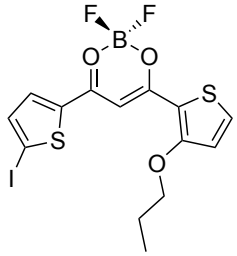	HOMO 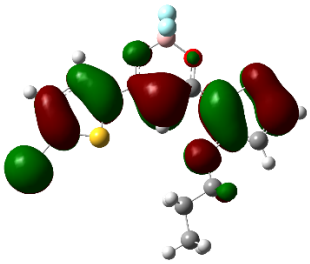	LUMO 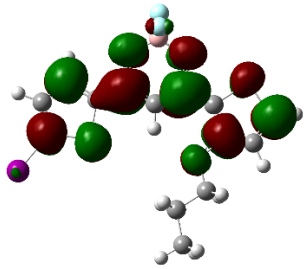
Geometry 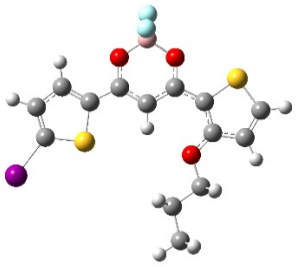	HOMO-1 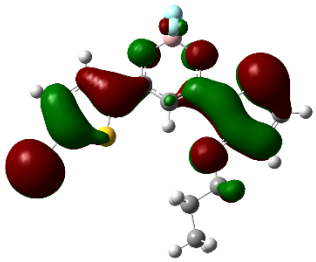	

C	-2.66149	-0.81073	-0.02812
C	-1.28043	-0.56203	0.07368
H	-0.92903	0.45484	0.16069
O	-3.10918	-2.04732	-0.12585
C	-0.38898	-1.62826	-0.0123
O	-0.80808	-2.87212	-0.1131
B	-2.23432	-3.22697	0.11241
F	-2.59016	-4.23158	-0.77839
F	-2.39267	-3.64857	1.43854
C	1.05375	-1.47428	-0.02612
C	1.98366	-2.49856	-0.05153
S	1.84957	0.08871	-0.01157
C	3.32685	-2.04475	-0.05802
H	1.69788	-3.54372	-0.06221
C	3.40594	-0.6711	-0.03752
H	4.19001	-2.69915	-0.07525
I	5.17428	0.47585	-0.03658
C	-3.66749	0.20448	-0.06627
C	-3.54891	1.60566	-0.03455
S	-5.35735	-0.2657	-0.17334
C	-4.80943	2.26908	-0.09638
C	-5.85344	1.38047	-0.17343
H	-4.94166	3.34304	-0.08388
H	-6.90726	1.62302	-0.23015
C	-2.27959	3.64537	0.06388

```
 H                    -2.842     4.01258   0.9306
 H                    -2.74215   4.03005  -0.85278
 C                    -0.81412   4.04143   0.14989
 H                    -0.37843   3.59933   1.05452
 H                    -0.27925   3.61619  -0.70836
 C                    -0.64333   5.56594   0.17437
 H                    -1.15464   6.01214   1.03619
 H                     0.41711   5.8315    0.24135
 H                    -1.04682   6.0291   -0.7345
 O                    -2.34735   2.19731   0.04545


Excitation energies and oscillator strengths:

 Excited State   1:      Singlet-A      2.9410 eV  421.58 nm  f=0.8669
<S**2>=0.000
      91 -> 92         0.70539
 This state for optimization and/or second-order correction.
 Total Energy, E(TD-HF/TD-KS) =  -1798.75520975
 Copying the excited state density for this state as the 1-particle RhoCI
density.

 Excited State   2:      Singlet-A      3.4807 eV  356.20 nm  f=0.2145
<S**2>=0.000
      89 -> 92         0.21567
      90 -> 92         0.66589

 Excited State   3:      Singlet-A      3.8258 eV  324.07 nm  f=0.0793
<S**2>=0.000
      89 -> 92         0.66438
      90 -> 92        -0.20580

 Excited State   4:      Singlet-A      4.0969 eV  302.63 nm  f=0.0004
<S**2>=0.000
      90 -> 93         0.26643
      91 -> 93         0.64175

 Excited State   5:      Singlet-A      4.1163 eV  301.20 nm  f=0.0496
<S**2>=0.000
      88 -> 92         0.69705

 Excited State   6:      Singlet-A      4.2022 eV  295.04 nm  f=0.0001
<S**2>=0.000
      87 -> 92         0.70005

 Excited State   7:      Singlet-A      4.3875 eV  282.58 nm  f=0.0320
<S**2>=0.000
      86 -> 92         0.60383
      91 -> 94         0.34295

 Excited State   8:      Singlet-A      4.5387 eV  273.17 nm  f=0.1309
<S**2>=0.000
      86 -> 92        -0.34008
      91 -> 94         0.58459
```

```
 Excited State   9:      Singlet-A      4.7790 eV  259.44 nm  f=0.0001
<S**2>=0.000
      89 -> 93        -0.19314
      90 -> 93         0.60512
      91 -> 93        -0.27829

 Excited State  10:      Singlet-A      4.9017 eV  252.94 nm  f=0.0044
<S**2>=0.000
      84 -> 92         0.55516
      85 -> 92         0.32699
      90 -> 94        -0.25803
```

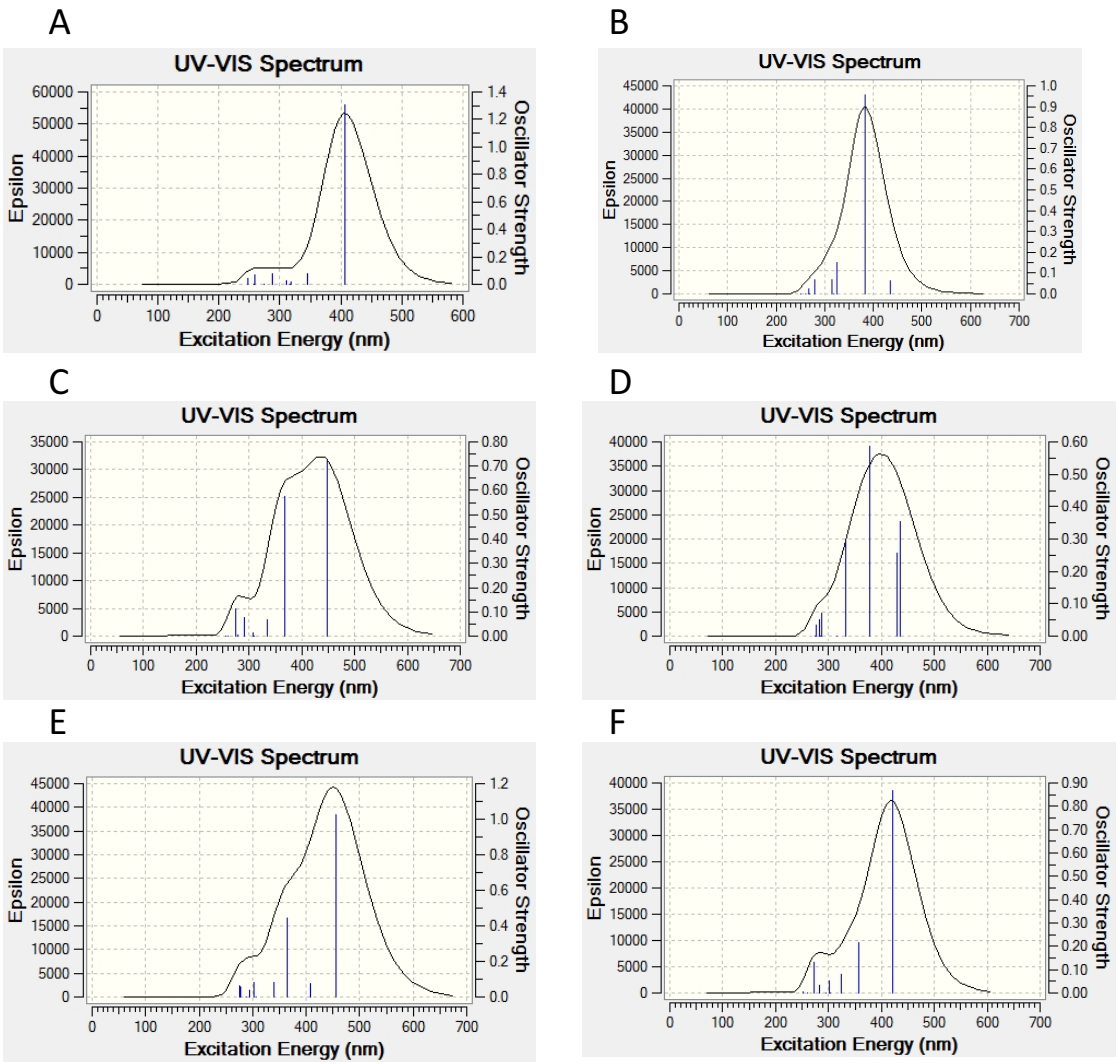

Figure S3.21. Calculated Absorption Spectra of Compounds **1** (A), **2** (B), **3** (C), **4** (D), **5** (E) and **6** (F).

Appendix C

Supporting Information for Chapter 4

Table S4.1. Optical Properties of dtm in PLA Film[a]

Sample	λ_{Ex}[b] (nm)	λ_{F}[c] (nm)	τ_F[d] (ns)	λ_{RTP}[e] (nm)	τ_{RTP}[f] (ms)	S[g] ($\tau_0/\tau_{1\%}$)
dtm[h]	433	464	0.65	585	2.09	1.70

[a]2.5% weight percent dye (mass of dye/ mass of PLA). [b]Maxima of the excitation spectrum monitored at the fluorescence maxima. [c]Fluorescence emission maxima excited at 369 nm. [d]Fluorescence lifetime excited with a 369 nm light-emitting diode (LED) monitored at the emission maximum. All fluorescence lifetimes are fitted to a double-exponential decay. [e]Phosphorescence maxima in the delayed emission spectrum (λ_{ex} = 369 nm from a Xenon flash lamp and with a 0.5 ms delay). [f]Phosphorescence lifetime monitored at the phosphorescence maximum (λ_{Ex} = 369 nm from a Xenon flash lamp). [g]Sensitivity parameter (S = $\tau_0/\tau_{1\%}$ to indicate the amount quenched in the most sensitive range).[1]

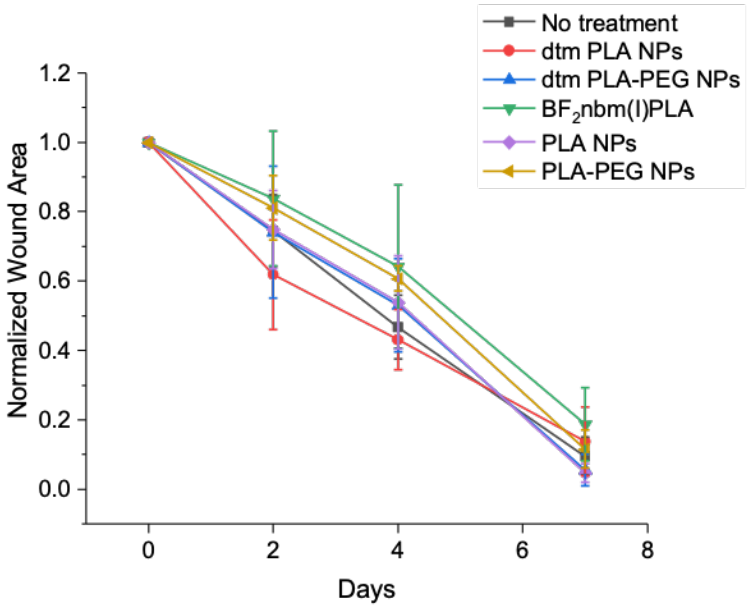

Figure S4.1. Mouse Wound Area Monitored Over Time.

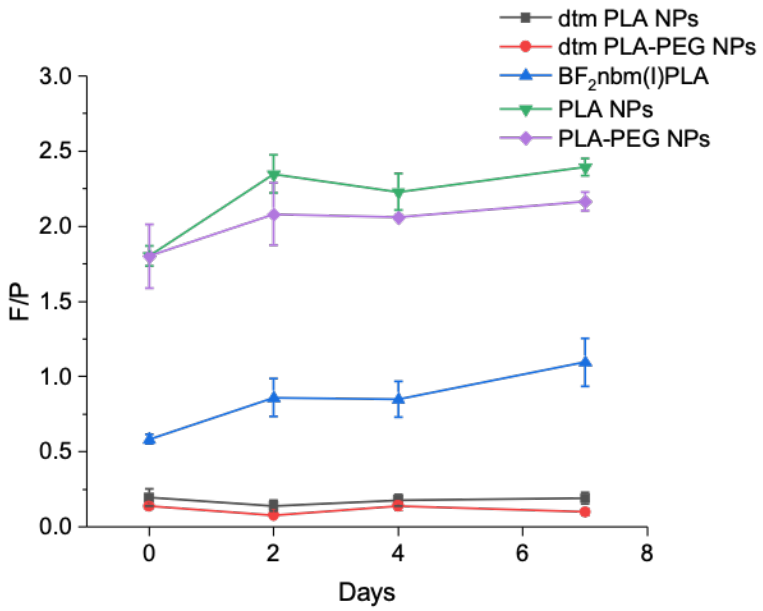

Figure S4.2. F/P Ratios Monitored Over Time

References

(1) Wang, X. D.; Wolfbeis, O. S. Optical Methods for Sensing and Imaging Oxygen: Materials, Spectroscopies and Applications. *Chemical Society Reviews*. 2014, pp 3666–3761.

Appendix D

Supporting Information for Chapter 5

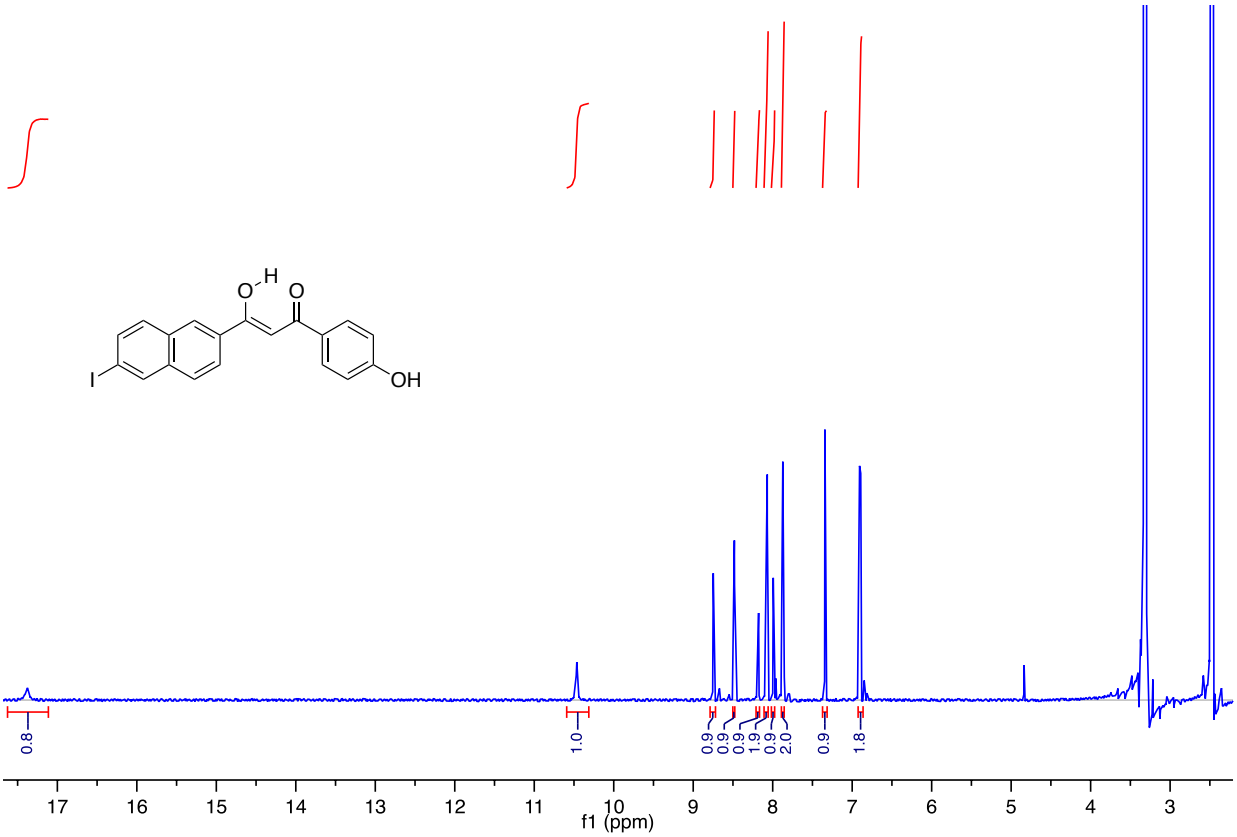

Figure S5.1. *nbm(I)OH.* ^{1}H NMR: (600 MHz, D_6-DMSO) δ11.22 (s, broad, 1H, phenol-O*H*), 8.99 (s, 1H, 1-Np*H*), 8.55 (s, 1H, 5-Np*H*), 8.33 (m, 3H, 2, 6-Ph*H*, 4-Np*H*), (d, J = 6, 1H, 3-Np*H*), 7.95 (m, 2H, 7, 8-Np*H*), 7.87 (s, 1H, COC*H*CO), 7.00 (d, J = 6, 2H, 3, 5-Ph*H*).

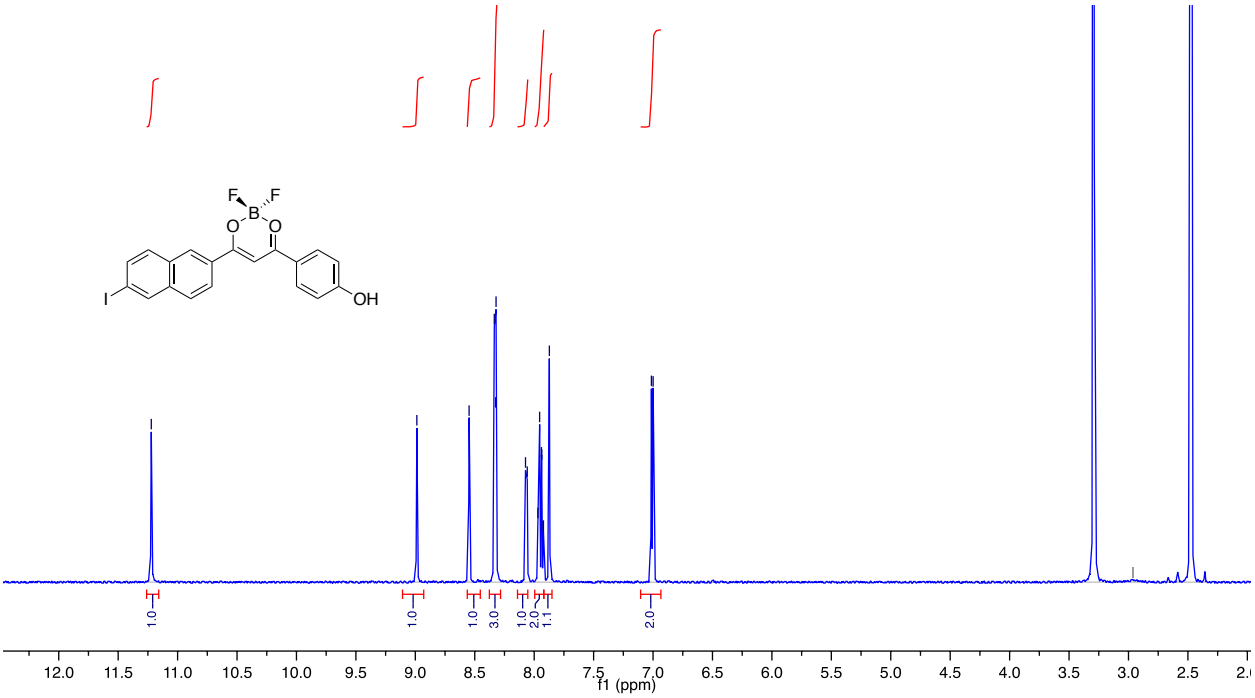

Figure S5.2. *BF_2nbm(I)OH*. ^{1}H NMR: (600 MHz, D_6-DMSO) δ11.22 (s, broad, 1H, phenol-O*H*), 8.99 (s, 1H, 1-Np*H*), 8.55 (s, 1H, 5-Np*H*), 8.33 (m, 3H, 2, 6-Ph*H*, 4-Np*H*), (d, J = 6, 1H, 3-Np*H*), 7.95 (m, 2H, 7, 8-Np*H*), 7.87 (s, 1H, COC*H*CO), 7.00 (d, J = 6, 2H, 3, 5-Ph*H*).

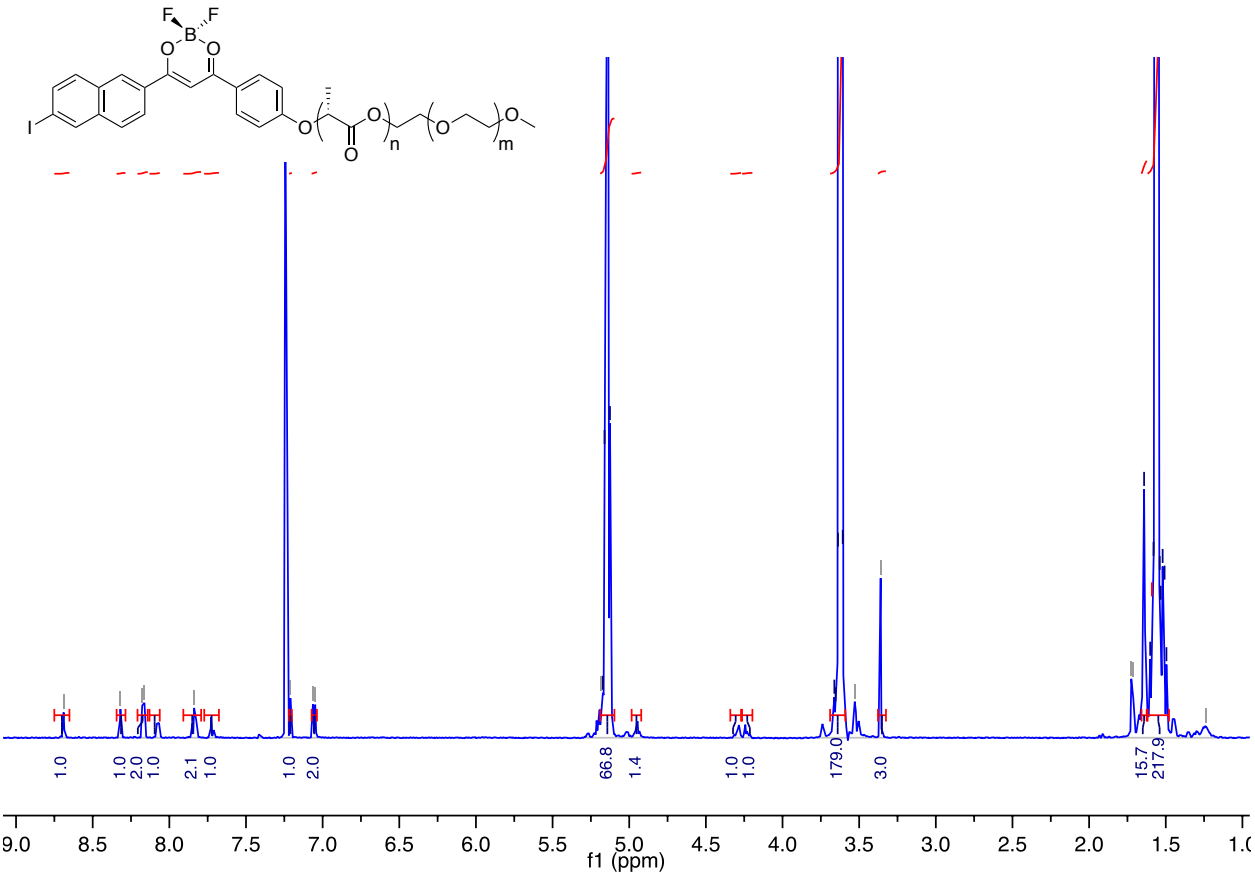

Figure S5.3. *BF_2nbm(l)PLLA-PEG.* ^{1}H NMR: (600 MHz, $CDCl_3$) δ8.69 (s, 1H, 1-Np*H*), 8.32 (s, 1H, 5-Np*H*), 8.17 (d, J = 6, 2H, 2, 6-Ph*H*), 8.09 (d, J =12, 1H, 3-Np*H*), 7.85 (m, H, 7, 8-Np*H*), 7.72 (d, J = 12, 1H, 4-Np*H*), 7.21 (s, 1H, COC*H*CO), 7.06 (d, J = 6, 2H, 3, 5-Ph*H*), 5.17 (q, J = 6, 66H, PLLA-*H*), 3.62 (s, broad, 179H, PEG-OCH_2CH_2-), 3.36 (s, 3H, PEG-OCH_3), 1.55 (m, broad, 217H, PLLA-CH_3).

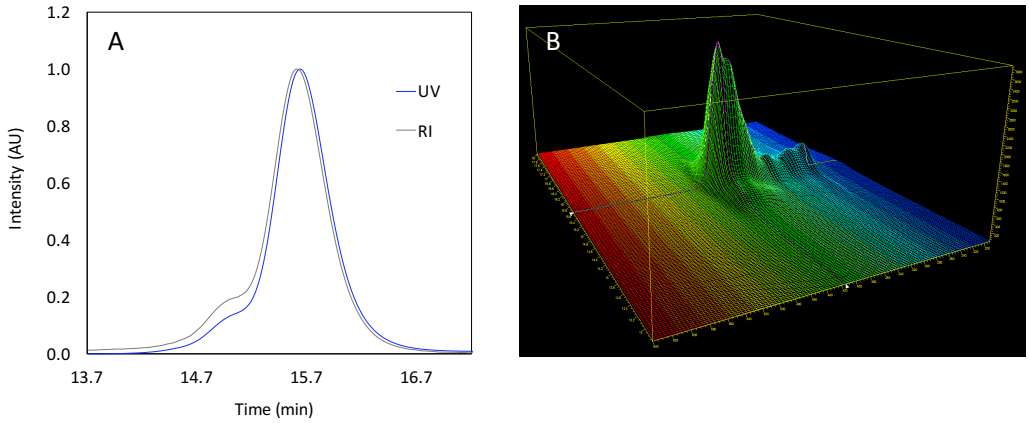

Figure S5.4. GPC Traces of BF_2nbm(I)PLLA-PEG. A) 2D plot of intensity versus elution time (UV = absorbance signal and RI = refractive index. B) 3D chromatogram of the polymer (Y axis = intensity, X axis = absorbance wavelength, Z axis = elution time).

Table S5.1. Polymer Characterization Data and Optical Properties in CH_2Cl_2

Polymer	#	M_n[a] (GPC)	Đ[a]	λ_{abs}[b] (nm)	ε[b] ($M^{-1}cm^{-1}$)	λ_{em}[c] (nm)	Φ_F[d]
BF_2dbmPLLA-PEG	**P1**	10 500	1.05	396	37 000	426	0.68
BF_2nvmPLLA-PEG	**P2**	11 500	1.17	421	32 400	495	0.41
BF_2gvmPLLA-PEG	**P3**	10 600	1.09	424	56 200	502	0.31
BF_2dapvmPLLA-PEG	**P4**	9 300	1.08	536	29 300	623	0.28
BF_2nbm(I)PLLA-PEG	**P5**	7 600	1.05	418	64 500	451	0.04

[a]Average molecular weight data of dye-polymer conjugates determined by GPC in THF. Đ= polydispersity index (M_w/M_n). [b]Absorption maxima and its corresponding extinction coefficient. [c]Fluorescence emission maxima excited at 369 nm, except sample **4** and **5** (λ_{ex} = 385 nm). [d]Relative quantum yield versus anthracene in EtOH as a standard.

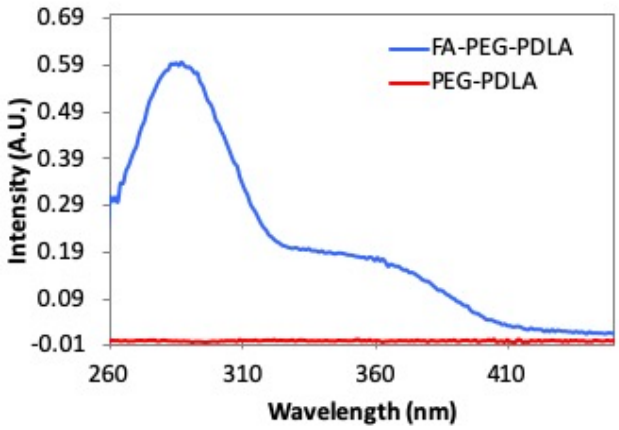

Figure S5.5. UV absorption of folic acid targeted FA-PEG-PDLA and non-targeted PEG-PDLA. Characteristic peaks at around 284 nm and 360 nm demonstrated the successful conjugation of folic acid.

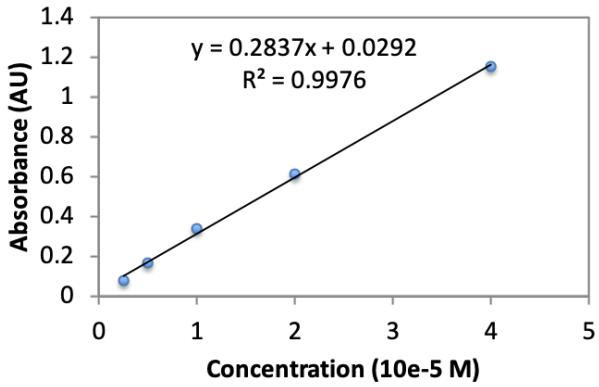

Figure S5.6. Folic acid calibration curve.

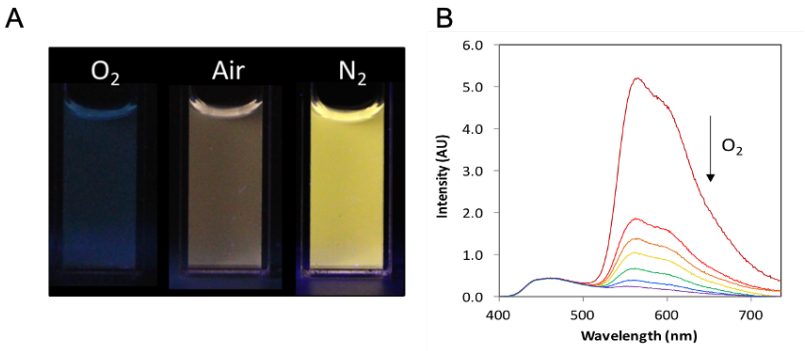

Figure S5.7. Oxygen Calibration of BF_2nbm(I)PLLA-PEG + PDLA-PEG. A) Pictures under UV excitation (λ_{ex} = 369 nm) at various oxygen concentration. B) Total emission showing phosphorescence is quenched with increased oxygen concentration.

Appendix E

Supporting Information for Chapter 6

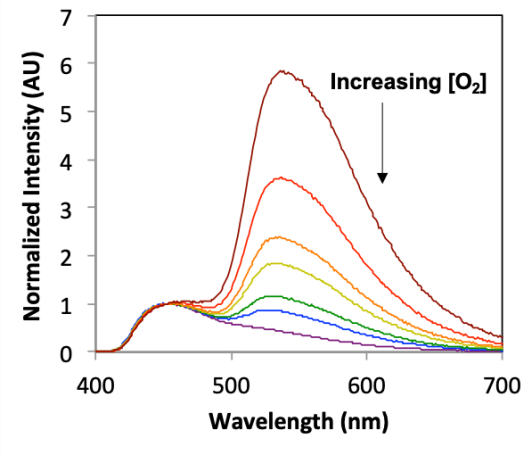

Figure S6.1. Total Emission of O_2 NPs at Varying Oxygen Levels. Oxygen concentration is from 0 to 21 %.

Appendix F

Supporting Information for Chapter 7

Scheme S7.1 Synthetic routine of NHS-BF_2dbmPLA